UNIVERSITY OF SOUTHAMPTON

FACULTY OF PHYSICAL SCIENCES AND ENGINEERING

School of Electronics and Computer Science

Hip Implant Energy Harvester

by

Kantida Pancharoen

Thesis for the degree of Doctor of Philosophy

October 2017

UNIVERSITY OF SOUTHAMPTON

ABSTRACT

FACULTY OF PHYSICAL SCIENCES AND ENGINEERING
DEPARTMENT OF ELECTRONICS AND COMPUTER SCIENCE

Doctor of Philosophy

HIP IMPLANT ENERGY HARVESTER

by Kantida Pancharoen

Failed hip replacements have resulted in increased demand for revision hip surgeries and rising costs in healthcare. To mitigate the problem, instrumented hip prostheses have been proposed to detect the early signs and symptoms of failures in vivo. In the main, batteries and an inductive power link are used to power instrumented hip implants. However, batteries are an unattractive option because of their limited lifetime and the replacing of batteries requiring additional surgery. The use of an electromagnetic inductive link is a potential powering method but requires external drivers to activate implant systems, not preferable for home activity monitoring. Therefore, methods of powering instrumented hip implants by human movement are studied in this thesis.

An electromagnetic vibration energy harvester based on magnetic levitation is presented as suitable for low frequency, high amplitude excitation such as that associated with human motion. The constraints on the size of the harvester are due to the volume of the hip prosthesis which makes designing an effective energy harvester operating at a frequency below 10 Hz a significant challenge. To overcome this, a magnetically levitated electromagnetic vibration energy harvester based on coupled levitated magnets is presented with a nonlinear response, to extend operational bandwidth and enhance the power output of the harvesting device. Experiment results have demonstrated a improvement in the performance of a harvester based on coupled levitated magnets compared with that based on a single levitated magnet. The output voltage across the optimal load 2.66kΩ generated from hip movement is 0.122 V_{rms} (0.66 $V_{p\text{-}p}$) and 0.314 V_{rms} (2.54 $V_{p\text{-}p}$) during walking and running respectively. The power output obtained is 5.61 μW (walking) and 37.07 μW (running). The presented results demonstrate the feasibility of harvesting energy from hip movements to power the instrumentation.

Contents

List of Figures

List of Tables

DECLARATION OF AUTHORSHIP

I, Kantida Pancharoen declare that the thesis entitled 'Hip Implant Energy Harvester' and the work presented in it are my own and have been generated by me as the result of my own original research. I confirm that:

- This work was done wholly or mainly while in candidature for a research degree at this University;
- Where any part of this thesis has previously been submitted for a degree or any other qualification at this University or any other institution, this has been clearly stated;
- Where I have consulted the published work of others, this is always clearly attributed;
- Where I have quoted from the work of others, the source is always given. With the exception of such quotations, this thesis is entirely my own work;
- I have acknowledged all main sources of help;
- Where the thesis is based on work done by myself jointly with others, I have made clear exactly what was done by others and what I have contributed myself;
- Parts of this work have been published as listed in section 1.7 of this thesis

Signed: ……..

Date: ……..

Acknowledgements

I would like to express my sincere appreciation to my supervisors Professor Steve Beeby and Dr Dibin Zhu for their mentoring, encouragement, advice, and valuable supervision to endure this research and the writing of this thesis.

I am thankful for the research facilities and support provided by the School of Electronics and Computer Science (ECS). Special thanks go to Eric Webb of the mechanical workshop for the manufacturing help and fabricating early prototypes. I would like to thank my advisory friends, Narongrit Maneejiraprak and Sangchai Monkronthong, who have contributed and shared valuable experience. Their support and guidance have enabled my thesis to achieve its satisfactory purpose. I would also like to thank the people in the Electronics and Electrical Engineering Laboratory for making my stay in Southampton memorable. I would also like to show my appreciation for the support of all the people I met during the period I was working on this thesis.

I acknowledge the support of the Royal Thai Government through the Office of the Civil Service Commission (OCSC) for the scholarship awarded to pursue my PhD.

I owe special thanks to my parents and my brother for their support, encouragement and persistent confidence in me. Thank you to my boyfriend, Krongboon Singhanat, who have supported and encouraged me in all situations. To whom I owe all my appreciation and unconditional love. This thesis is dedicated to my parents, my brother, and my boyfriend, without whom none of this would have been possible.

Nomenclature

ω_n	Natural frequency of the system [rad/s]
ω_d	External excitation frequency [rad/s]
Φ	Phase angle [degrees]
λ	Flux linkage [Wb]
θ	Electromagnetic coupling
ζ_p	Parasitic damping ratio
ζ_e	Electrical damping ratio
ζ	Total damping ratio
ε	Permittivity of the material [$F \cdot m^{-1}$]
α_{Hci}	Temperature coefficients of Coercivity [%/°C]
α_{Br}	Temperature coefficients of Induction [%/°C]
α	Nonlinear term written by k3/m
μ_0	Permeability of free space [H/m]
A	Acceleration levels [m/s^2]
B	Magnetic flux density [T]
Br	Remanence [T]
C	Capacitance [F]
c	Total damping coefficient [$N \cdot s \cdot m^{-1}$]
c_e	Electrical damping coefficient [$N \cdot s \cdot m^{-1}$]
c_p	Parasitic damping coefficient [$N \cdot s \cdot m^{-1}$]
d	Distance [m]
E	Energy [J]

f	Natural frequency [Hz]
F_b	Elasto-dissipative force [N]
F_{em}	Electromagnetic damping force [N]
F_G	Gravity force [N]
f_r	Linear resonant frequency [Hz]
F_S	Magnetic restoring force [N]
g	Gravity of earth = 9.81 $m \cdot s^{-2}$
H_c	Coercivity [kA/m]
i	Electric current [A]
k	Spring of stiffness [N/m]
k_1	Linear spring stiffness [N/m]
k_3	Nonlinear spring stiffness [N/m]
m	Seismic mass [kg]
M_1	Top levitated magnet of the coupled-magnetically levitated harvester
M_2	Bottom levitated magnet of the coupled-magnetically levitated harvester
P_{avg}	Average power delivered to the electrical load [W]
P_d	Average power dissipated in the damper [W]
$P_{d(inst)}$	Instantaneous power dissipated in the damper [W]
P_{load}	Power across the electrical load [W]
Q	Quality factor
R_C	Coil resistances [Ω]
R_L	Optimal load resistances [Ω]
T	Temperature [°C]
T_c	Curie temperature [°C]

V	Voltage [V]
V_{emf}	Induced voltage in a coil or electromotive force [V]
V_{load}	Load voltage [V]
Y	Amplitude of external sinusoidal vibration [m]
$y(t)$	Input vibration displacement [m]
$z(t)$	Relative displacement of the seismic mass and the base [m]
$\dot{z}(t)$	Displacement velocity of the seismic mass [m/s]
z_0	Quiescent position [m]

Abbreviations

ANM	Asymmetrical Nonlinear Model
CMH	Coupled-Magnetically Levitated Harvester
EVEH	Electromagnetic Vibration Energy Harvesters
FEA	Finite Element Analysis
LM	Linear Model
MLEVH	Magnetically Levitated Electromagnetic Vibration Energy Harvester
NdFeB	Neodymium-Iron-Boron
NPD	Normalised Power Density
NTC	Negative Temperature Coefficient
PD	Power Density
PTFE	Polytetrafluoroethylene
RMS	Root Mean Square
SMH	Single-Magnetically Levitated Harvester
SNM	Symmetrical Nonlinear Model

Chapter 1

Introduction

1.1 General overview

Failed hip replacements have resulted in a demand for revision hip surgeries, which are costly procedures and have a high risk of mortality and complications. To mitigate these issues, in-vivo monitoring of joint replacements has been proposed, using instrumented hip prostheses to detect the early signs and symptoms of failures. An inductive power link and batteries are mainly used to power electronic implant systems including sensing, monitoring and communication systems. However, the limited lifetime of batteries means that additional surgery will be required for battery replacement. The use of an electromagnetic inductive link is a potential powering method but it requires external drivers to activate the implant systems, which are not preferable for home activity monitoring. Therefore, alternative methods for powering instrumented hip implants using energy harvesting from human motion are studied in this research. Energy harvesting is the method of converting unused or wasted energy in the environment into small amounts of electrical energy. An energy harvester operating at low frequencies associated with body motion is presented within the framework of hip implant applications. A comprehensive simulation has been carried out together with a mathematical model to investigate harvester performance. The results are compared with experimental results to validate the harvester modelled and the performance predicted.

1.2 Motivation for hip implant harvesting

The need for hip replacement operations has increased continuously due to a growing ageing population. The number of hip joint replacements is predicted to

increase by about 40% based on the demographic changes affecting the UK population from 1996 to 2026 [1]. With such a huge increase, the need for revision hip replacement surgeries is rising due to the increased amount of hip replacement failures. There were 8,641 cases of hip revisions in 2011 and the number rose to 9,516 cases in 2014 across England, Wales and Northern Ireland [2]. Based on this trend, it is estimated that the number of hip replacement revisions will increase by about 31% by 2030 [3], [4]. Revision surgery is more complicated and needs longer rehabilitation compared with primary hip replacement. This results in difficult surgery and rising healthcare costs [5], [6]. To minimise the need for revision procedures, instrumented hip implants have received much attention as a methodology to detect the failures of hip replacement in-vivo at early stages.

To date, conventional batteries and inductive power systems are the two main methods used to power passive instrumented implants for monitoring and data transmission [7]–[13]. These power sources are not ideal for implants. Batteries have limited power density, limited lifetime, issues of disposal due to toxic chemicals contained inside, and high cost of maintenance [7]. In addition, setting up a power induction coil on the human body is not convenient. It can lead to skin infections, discomfort and restricted activities on the part of patients [14]. To alleviate these problems, kinetic energy harvesting from hip movement has been proposed to power implants. With this approach, the instrumented hip implant can periodically monitor its condition and patients can share relevant information remotely with their physicians while staying at home. It is also possible for doctors to visualise medical parameters in real time, determine appropriate treatments and predict failures in advance. Therefore, overall healthcare quality can improve with reduced healthcare cost.

This work is benchmark research for exploring the feasibility of a practical energy harvesting system for hip implants.

1.3 Instrumented hip replacement overview

Instrumented hip implants have been developed over the past few years as an effective procedure to maximise the outcomes of hip replacement surgery. The electronic instrumentations inside the implants typically comprise of sensory, telemetry and power systems. In-vivo measurement was first introduced by Kilvington and Goodman in 1981 [8]. Four strain gauges and a single channel FM transmitter were used to monitor the prosthesis alignment between the femoral head and stem. This implant system was powered by batteries linked from outside the body of the patient [8]. In 1998, due to the development of a telemetry unit and an inductive powering system, the three-dimension force acting on the head of the prosthesis and the temperature change around the prosthetic neck were measured in-vivo using four strain gauges and an NTC thermistor [9]. The telemetry system was developed to be small and had low power consumption, which resulted in further improvement of the instrumented implant presented in [10], [13]. The improved implant included up to six strain gauges and up to eight thermistors for load and temperature measurement within the implant respectively.

To the present day, it is mainly an electromagnetic induction link that has been used to supply power for instrumented implants tested in-vivo. The power consumption of the system electronics, including sensors, processor, and communications, is between 7mW and 22.5mW [9], [10], [12], [13]. External equipment, e.g. drivers and coils, are needed to power the implantable devices when a measurement is performed. This is inconvenient for the patient and is not consistent with the vision of automated healthcare at home. Progress in electronics has led to a continuous decrease in power consumption of electronic systems [14], making it possible to employ the concept of energy harvesting for the powering of instrumented hip implants. Energy harvesting approaches such as motion-driven electromagnetic harvesting and piezoelectric harvesting have been studied in several works (reviewed in section 2.2) and progress has been made towards practical implementation for in-vivo measurement.

1.4 Research objectives

This research aims to explore the feasibility of harvesting energy from hip movements in order to power instrumentation. The objectives are as follows:

1) Investigate the acceleration level and frequency response of people during walking and running.
2) Identify a practical approach to harvest the energy from low frequency (<10 Hz) vibration associated with body motion.
3) Estimate available power from hip motion considering the different harvesting models, i.e. linear and nonlinear models.
4) Build a simulation model of the harvester designed with mathematical and finite element analysis (FEA) to predict its dynamic behaviour and estimate the power generated.
5) Design an energy harvester structure to operate within the constrained volume inside the artificial hip joint (volume of femoral head and femur is about 8 cm^3 and 20 cm^3 respectively).
6) Validate the performance of the harvester and the simulation predictions through the experimental results.
7) Investigate the temperature dependence of the energy harvester.

1.5 Statement of novelty

The novelties of this work include:

- Development of a magnetically levitated electromagnetic vibration energy harvester (MLEVH) using a coupled magnet for harvesting energy from hip movement within the constrained volume inside the artificial hip joint.
- Operation of the MLEVH under sinusoidal excitation and human motion.
- Design of a simulation model to investigate the behaviour of the MLEVH under sinusoidal excitation and human motion.
- Experimental analysis of damping variation at different acceleration levels.

- Study of temperature effects on the performance of the MLEVH using comprehensive simulation and experimental results.

1.6 Thesis structure

This thesis is organised as follows:

Chapter 2 (Human-powered Energy Harvesting Background) provides an introduction to power generation from the human body and a background of different transduction mechanisms. A literature review of human-powered energy harvesters is presented based on their transduction mechanisms, with a special focus on electromagnetic energy harvesters. Next, strategies to improve power output from low-frequency movement are introduced with some examples of such harvesters. In the final section, existing instrumented hip implants are reviewed together with the methods for powering their electronic systems and power consumption.

Chapter 3 (Power from Hip Motion) describes the main governing theories as a background for designing an appropriate prototype structure for energy harvesting from hip motion. The acceleration and frequency data while walking and running is analysed to identify a suitable operating frequency and specify the input excitation to the harvester model. Energy harvesting devices with linear and nonlinear behaviour are modelled and the achievable output power from human-motion estimated.

Chapter 4 (Harvester Mechanical Design) presents the design of the energy harvester and the modelling of the electromagnetic transduction mechanism. The overall structure of the prototypes are proposed in parallel with the design procedures. The design parameters are then optimised using Comsol simulation. The frequency response of the harvester is also predicted.

Chapter 5 (Simulation and Experimental Validation) demonstrates the results of both simulation and experiments. The dynamic behaviour and general performance, e.g. frequency response, induced voltage, and power output are

provided first using MATLAB Simulink model and Comsol simulation. The results are then compared with the experimental results. The experiment involved testing the harvesters on the shaker to measure the resonant frequency, and determining the optimum load and output voltage. The harvester was then attached to the hip of a participant and the output voltage and power generated recorded during walking and slow running on a treadmill. The results of the simulation and the experiment are discussed at the end of the chapter.

Chapter 6 (Temperature Dependence) investigates the dependence of magnetic properties on temperature, which has an influence on the performance of the MLEVH. The conventional theories are provided to support assumptions. The harvester is experimentally characterised at different ambient temperatures and a number of properties such as magnetic flux density, resonant frequency, induced voltage, and the damping ratio of the harvester are measured. Results from the experiment are discussed and compared with the results from the simulation.

Chapter 7 (Discussion and Conclusion) discusses the harvester's performance and its comparison with state of the art models. The challenges of this work are discussed regarding certain factors, i.e. power efficiency, fabrication, rectification, and energy storage. This chapter concludes and summarises achievements, and outlines further development and recommendations for future work in this research field.

1.7 Published papers

Parts of this thesis have been published as:

1) K. Pancharoen, D. Zhu, and S. P. Beeby, “A Hip Implant Energy Harvester,” *J. Phys. Conf. Ser.*, vol. 557, p. 12038, 2014.
2) K. Pancharoen, D. Zhu, and S. P. Beeby, “Design Optimization of a Magnetically Levitated Electromagnetic Vibration Energy Harvester for Body Motion,” *J. Phys. Conf. Ser.*, vol. 773, p. 12056, Nov. 2016.
3) K. Pancharoen, D. Zhu, and S. P. Beeby, “Temperature dependence of a magnetically levitated electromagnetic vibration energy harvester,” *Sensors Actuators A Phys.*, vol. 256, pp. 1–11, 2017.
4) K. Pancharoen, D. Zhu, and S. P. Beeby, “A Magnetically Levitated

Electromagnetic Vibration Energy Harvester based on Coupled Levitated Magnets," *In preparation*.

Chapter 2

Human-powered Energy Harvesting Background

2.1 Introduction

Energy harvesting is widely considered to be an alternative way for powering electronic devices to minimise the use of batteries which have a finite lifespan. The human body is one promising source of energy which can be harvested from heartbeat, body temperature, blood pressure, and the movement of body parts. This opens up the possibility of powering implantable medical devices without the restriction of battery lifespan. This chapter studies power generation from the human body and reviews the literature on human-powered energy harvesters according to three main transduction mechanisms: electrostatic, piezoelectric, and electromagnetic. Promising transduction mechanisms and the architecture of the harvester applied for implantable devices are discussed regarding size, output power, and operating frequency. With implantable energy harvesters, limited volume and the low resonant frequency required to match human-motion frequency are challenges in generating sufficient energy for implantable devices. The strategies for increasing energy harvested from low-frequency vibrations are discussed in Section 2.4. In addition, works on instrumented hip implants are also reviewed in the last section.

2.2 Power generation from the human body

The human body is an alternative source of energy with a significant amount of harvestable power. The ideal values of power consumed in each activity of daily living are summarised in Table 2.1 [15]. This reveals that considerable power can

be harnessed from human motion. The work performed whilst walking in different joints for a gait cycle of 1 Hz (2 steps/sec) is provided in Table 2.2 [16].

Table 2.1 Energy consumed by the human body derived from [15].

Activity	Kcal/h	Watts
Sleeping	70	81
Sitting	100	116
Eating	110	128
Driving	140	163
Housekeeping	150	175
Swimming	500	582
Mountain Climbing	600	698
Long running	900	1048

Table 2.2 Kinetic energy used during walking in different joints [16].

Activity	Work (J/step)	Power (W)
Elbow	1.07	2.1
Shoulder	1.1	2.2
Hip	19.6	39.2
Knee	24.7	49.5
Ankle	34.9	69.8
Heel strike	1	2

It is seen that most energy can be harvested from the lower body (hip, knee, ankle, and heel strike). Power harvested using electromagnetic transduction mechanisms during walking is estimated in [17]. The calculation shows that a power of 400μW can be generated from the simulated walking frequency of 2 Hz with 2 mm oscillation amplitude. Note that the practical value obtained may be lower than expected because the mechanical damping and the maximum displacement of the proof mass were not considered in the simulation model. Works by [18] show that maximum power densities of 8.7-2100 $\mu W/cm^3$ can be gained from inertial micro power generators for human-powered motion. The amount of power obtained depended on the size of the generator and the body location of the generators mounted. In addition, it was found that the generator mounted in lower-limb locations can produce four times more power than that

mounted in upper-limb locations. Since the power can be harvested from human motions, it is possible to power portable devices and wearable or implantable medical equipment using energy harvesting methods. The power required for some electronic devices are presented in Table 2.3

Table 2.3 power consumption for some electronic devices.

Activity	Power (W)
Cochlear	5.16 mW [19]
Drug pump	400 μW [20]
Neurostimulator	50 μW [21]
Pacemaker	8 μW [22]
Hearing aid	50 μW [23]
Electric wrist watch	1 μW [23]
Travel clock	2 μW [23]

In light of recent advances in microelectronic technology which offers a reduction in power and size, the possibility of fully powering devices from energy produced by the human body has been opened.

2.3 Human-powered energy harvesters

Kinetic energy is a common energy source of the human body, which can be converted into electrical energy. Three main transduction mechanisms used for kinetic energy harvesters are electrostatic, piezoelectric, and electromagnetic. This section gives a review of kinetic energy harvesters categorised by transduction principles. Harvesters designed for human applications in the literature have been reviewed in this section. In addition, some harvesters that have not been designed particularly for humans but their low operating frequencies are also reviewed because they show feasibility to be wearable or implant energy harvesters.

2.3.1 Electrostatic-based energy harvesters

Energy from electrostatic transduction can be generated by exploiting the change in charge of parallel capacitor plates, which is due to the relative movement of two conductive plates. The capacitance C of a capacitor is defined as

$$C = \frac{Q}{V} = \varepsilon \frac{A}{d} \tag{2.1}$$

where Q (Coulomb) is the charge on the plates, V (Volt) is the voltage on the plates, A (m^2) is the area of the capacitor plates, ε ($F \cdot m^{-1}$) is the permittivity of the material between the capacitor plates, and d (m) is the distance between the plates. The electric energy stored in the capacitor is given by

$$E = \frac{1}{2} QV = \frac{1}{2} CV^2 = \frac{1}{2} \frac{Q^2}{C} \tag{2.2}$$

The electrostatic force between the plates is given by

$$F = \frac{1}{2} Q \frac{2d}{\varepsilon A} = \frac{1}{2} \frac{\varepsilon A V^2}{d^2} \tag{2.3}$$

The harvested energy is extracted from the external work done against the electrostatic force between the plates. Electrostatic energy harvesters are compatible with MEMS fabrication technology, which is easily integrated on a chip. Examples of electrostatic energy harvesters designed for human applications are reviewed as follows.

In [24] an electrostatic generator with the structure of honeycomb was presented with the purpose of supplying electrical power for a cardiac pacemaker. The honeycomb structure was made by repeatedly folding the two aluminium-evaporated polyester films (50mm x 30mm x 5μm) which were stuck together with double-sided adhesive tape at 5 mm intervals (Figure 2.1a). This produced a variable capacitor of 1000 cells (50 layers, 20 cells per layer). The initial capacitance was 32nF and could increase to 200nF during operation. The capacitor was suspended between acrylic boards using 8 springs and a mass

attached on top of the acrylic board as shown in Figure 2.1b. The resonator was tuned to the resonant frequency of 4.76 Hz by adjusting the mass to be 0.64 kg for the spring constant of 572 Nm^{-1}. After an initial charging of the capacitor to 24 V, a power of 58 μW was generated from the simulated motion of the goat's heart.

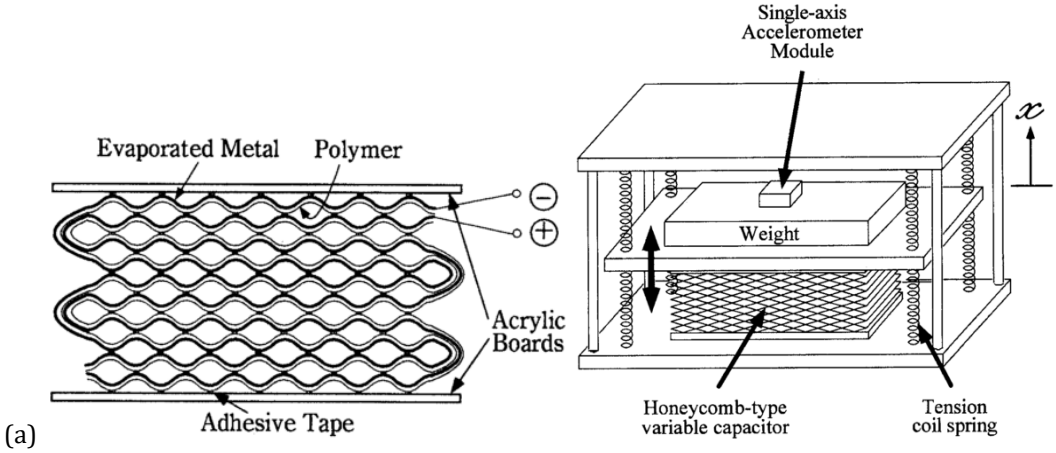

Figure 2.1. (a) Honeycomb structure and (b) Honeycomb-type variable capacitor [24].

Later work from the same team is presented in [25]. The variable-capacitance-type electrostatic generator using the same honeycomb structure was developed to power a cardiac pacemaker. The 12 springs were used to suspend the acrylic boards, which the total spring constant of 1100 Nm^{-1}. The resonant frequency of 6 Hz was tuned by applying the inertial mass of 0.78 kg. After an initial charging voltage of 45 V, the mean power of 36 μW (15 μA at 2.4 V) was generated from the simulated movements of a canine heart, which was enough to supply power for the cardiac pacemaker.

In [26], a non-resonant electrostatic generator was designed for biomedical applications using MEMS fabrication techniques. The prototype consisted of a variable capacitor with one moving plate having a silicon proof mass attached. The device produced an energy of 120 nJ/cycle and output voltages up to 220 V using the charging voltage of 30 V for maximum acceleration of about $40m{\cdot}s^{-2}$. However, the power obtained was significantly below the theoretically predicted values of 2.6μJ/cycle (80μW for operation at 30 Hz). The cause of the discrepancy is

believed to be the result of parasitic capacitances (i.e. viscous air damping) and the tilting motion of the proof mass.

To avoid the need for initial charging, an electrostatic generator using electret polymer film was presented by Arakawa *et al* [27]. High dielectric strength was obtained due to the electret material, which presented a surface charge density up to 0.68 mC/m^2. The power of 6 μW with 200 $V_{p\text{-}p}$ was generated into the optimal load of 1 GΩ at the low excitation frequency of 10 Hz with 1 mm displacement amplitude.

In [28], an electret structure with micro ball bearings was applied in the electrostatic power generator for low-frequency energy harvesting applications. This design offers a long-range movement at low frequency and accommodates miniaturisation. The separation gap was kept constant using micro balls to prevent an electrode from breaking. The electret structure keeps high surface potential with narrow electrode width, which results in a higher power output. This generator produces the power output of 40 μW from an acceleration of 0.4$\boldsymbol{g}$ at a low frequency of 2 Hz.

The main characteristics of each electrostatic generator reviewed are summarised in Table 2.4.

Table 2.4 Summary of electrostatic energy harvesters

Reference	Material	Frequency (Hz)	Acceleration (m/s^2)	Volume (cm^3)	Power (μW)	Power density (μW/cm^3)
[24][a]	Aluminium/polyester	4.76	0.5	-	58	-
[25][a]	Aluminium/polyester	6	1	1	36	36
[26][a,b]	Silicon	10	40	1	24	24
[27][b]	Polymer/glass	10	3.9	800	6	0.0075
[28][b]*	Silicon/glass	2	3.9	5.4	40	7.41

[a] Implantable devices
[b] Portable devices

2.3.2 Piezoelectric-based energy harvesters

Piezoelectric materials have been applied in the area of energy harvesting for many years due to their outstanding capability of converting mechanical energy into electrical energy. An electric current will be produced when piezoelectric materials are placed under mechanical stress. The amount of voltage generated depends on the amount of applied forces, the direction of forces, and the properties of the piezoelectric materials, e.g. the piezoelectric charge coefficients. The materials that are commonly used in the field of energy harvesting are piezoceramic (lead zirconate titanate, PZT), and polymeric materials (polyvinylideneflouride, PVDF). PZT has high piezoelectric properties, but low flexibility; whereas, polymeric materials (e.g. PVDF) offer great flexibility but low piezoelectric properties [29]. To obtain high electrical energy from the materials, various approaches have been presented such as combining the two materials (e.g. PZT and polymer [30]), mixing with specific substances (e.g. nanofillers [31], [32]) or designing new structural models (e.g. multi-layers of PZT, PbTiO3 and ZrO3 [33], [34]). To describe the piezoelectric effect of the materials, the term of piezoelectric charge coefficients d_{ij} has been defined [35]. The *i* direction may refer to static voltage, electric field or surface charge, and the *j* direction can be displacement, applied force or stress. Figure 2.2 shows the system of symbols and notation.

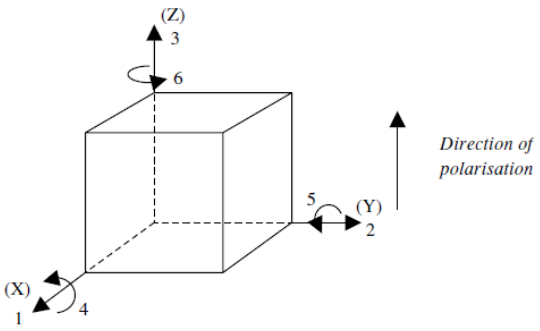

Figure 2.2. Notation of axes [36].

Normally, the piezoelectric charge coefficients used are given as d_{33} for both voltage and force along the *z* axis, and d_{31} for voltage along the *z* axis but force

along the *x* axis. Some examples of work on piezoelectric-based energy harvesters related to human motion are reviewed as follows.

Shoe-mounted generators using piezoelectric elements to convert kinetic energy produced from walking activity into electric energy have been studied widely. Works by Kymissis and Shenck [37], [38] presented a piezoelectric generator using two piezoelectric designs, namely the PVDF stave and PZT dimorph, embedded between shoe insole and sole (Figure 2.3). A stack of PVDF sheets shaped into an elongated hexagon was strained by the bending of the sole, producing a charge through the longitudinal mode (d_{31} mode) of piezoelectric coupling. This arrangement provided an average power of 1.3mW for 250kΩ load at a walking pace of 0.9 Hz. A PZT dimorph was designed to harvest energy from the heel strike by taking advantage of a compressible dimorph and the deformation of transducer under the heel while the heel was hit and lifted. This generated an average power of 8.4mW into a 500kΩ load.

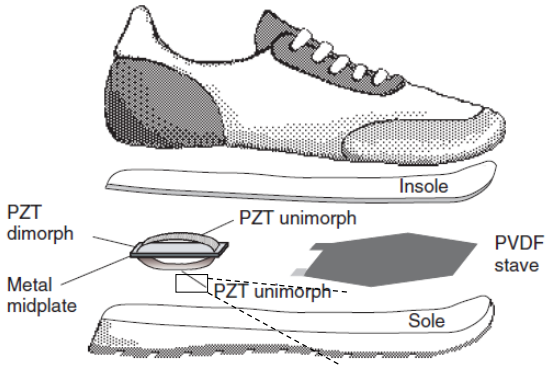

Figure 2.3. Shoe-mounted piezoelectrics: PVDF stave and PZT dimorph [37], [38].

To harness the heel strike, piezoelectric generators placed inside the shoe heel were developed by [39]–[41]. Works by Han *et al* [39] presented a stack of microstructured piezoelectric polymer with approximately 120 film layers (Figure 2.4a) to generate the power output of 4mW per step (a cycle time of 1s for walking) at 130-V load voltages. To harness the energy of heel strikes, Fourie *et al* [40] presented a system of multiple vertical PVDF unimorphs to be inserted inside the heel of a sneaker (Figure 2.4b). A power of 0.06mW was produced into a 470kΩ load at a 1Hz frequency. Another generator presented by [41] used a PZT-

based supporting cantilever with a tip mass at the end (Figure 2.5) to oscillate in response to a heel strike. A harvested power of 378μW was estimated at the resonant frequencies of approximately 35.5 Hz.

(a) 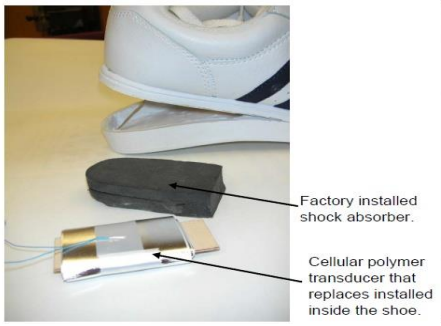

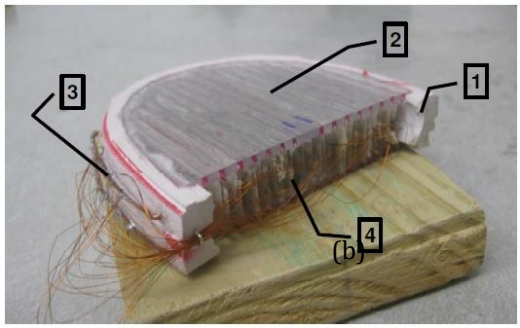

(b)

Figure 2.4. Shoe heels containing (a) the piezoelectric polymer stack of 80μm thick film [39] and (b) 1-rubber cutout, 2-polycarbonate plates, 3-copper terminals, and 4-unimorph strips [40].

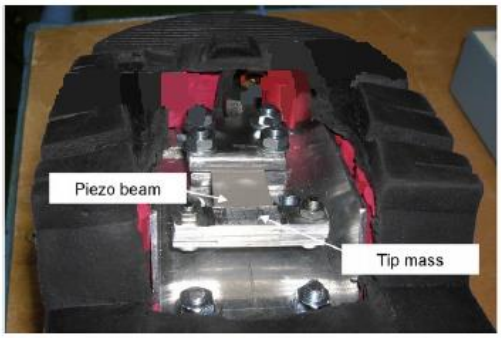

Figure 2.5. Shoe heel with piezoelectric vibrating cantilevers [41].

In [42], a flexible piezoelectric-based material called 'cellular polypropylene (PP) ferroelectret' was presented as a material for powering human-body-worn sensors by exploiting foot strikes during walking. Its properties, such as a relatively high piezoelectric charge constant d_{33} and small Young's modulus compared with the PZT, are suitable for use as material for a wearable energy harvester. Under normal walking conditions, an output peak power of 10.2 μW and energy of 1.12 μJ were generated by a single-layer PP ferroelectret. The power output was boosted by use of a ten-layer PP ferroelectret to 100 μW peak power and an 11.2 μJ energy output. These results are promising for powering wearable electronic devices.

A piezoelectric energy harvester which used impact forces to harness energy from limb motion was presented by Renaud *et al* [43]. Energy is generated when the free-sliding mass collides with the two piezoelectric cantilever beams located at both ends of the frame (Figure 2.7). A power output of 40 μW is estimated from the excitation amplitude of 10 cm at 1 Hz.

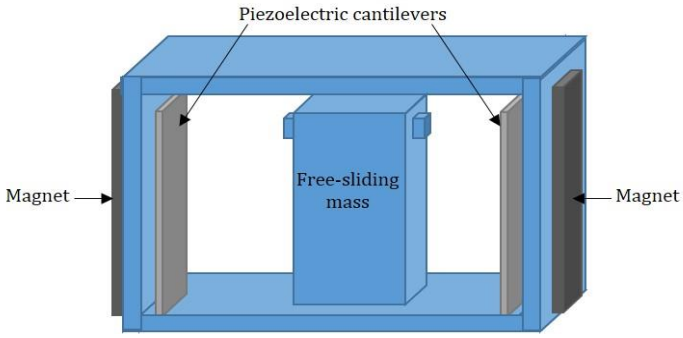

Figure 2.6. Impact-based piezoelectric generators [43].

To monitor failures in prosthetic knee implants, a study of a piezoelectric energy harvester for powering the instrumented electronics of an implant was presented by Platt *et al* [44]. The harvester contained three piezoelectric stacks (each with 145 PZT layers) and was stressed by an axial force across a knee joint to produce energy for a 10 μF storage capacitor and a microprocessor inside the implant. A continuous regulated power of 850μW was able to be delivered into an impedance matched load with a maximum mechanical efficiency of 20% (19% electrical efficiency).

The main characteristics of each piezoelectric generator reviewed are summarised in Table 2.5.

Table 2.5 Summary of piezoelectric energy harvesters

Reference	Material	Frequency (Hz)	Acceleration (m/s^2)	Volume (cm^3)	Power (mW)	Power density ($\mu W/cm^3$)
[37][b]	PVDF	0.9	-	16000	1.3	81.25
[38][b]	PZT	0.9	-	25000	8.4	336.00
[39][b]	piezoelectric polymer	1	-	24000	4	166.67

Reference	Material	Frequency (Hz)	Acceleration (m/s^2)	Volume (cm^3)	Power (mW)	Power density ($\mu W/cm^3$)
[40][b]	PVDF	1	-	540	0.06	111.11
[41][b]	PZT-5A	35.5	-	2267.6	0.378	166.70
[42][b]	PP ferroelectret	0.8	-	-	0.1	-
[43][b]	PZT	1	0.1	1	0.04	0.04
[44][a]	PZT ceramic	1	-	3.6	4.8	1.33

[a] Implantable devices
[b] Portable devices

2.3.3 Electromagnetic-based energy harvesters

The generation of an electric current using electromagnetic induction is one of the most efficient transduction mechanisms for kinetic energy harvesting. In principle, the amount of electricity induced by the movement of the magnet through a conductor (coil) depends on the velocity of relative movement, the strength of magnetic flux density generated by magnets, the number of coil turns and the volume of the coil. According to this fundamental concept, an energy harvesting system can be designed for particular applications.

Electromagnetic vibration energy harvesters designed for low-frequency applications are reviewed in this section, categorised by the design features of the relative movement of a magnet as follows:

1. The moving magnet slides on a shaft or track.
2. The moving magnet moves freely inside the harvester's frame.
3. The moving magnet is suspended with the mechanical spring.
4. The moving magnet is levitated due to the repulsive and attractive magnetic force (magnetic spring).
5. The moving magnet is applied with the principle of diamagnetic levitation.

2.3.3.1 Harvesters using sliding-based magnet moving type

With this type, magnets have been designed to move along a shaft or a rail guide passing through a coil to generate electrical energy. The movement direction of the moving part has been controlled for linear guiding.

Zeng *et al.* [45], [46] proposed the design of a wearable energy harvester to harness electrical power from low-frequency motion of the human foot. The horizontal motion of the foot pushes the centre translator, which consists of several NdFeB permanent magnets stacked and joined by steel spacers. The magnet set moves relative to the outer stator cut in slots for coil winding as in Figure 2.7. The linear movement of a magnet bar is guided using a ball bearing under the bar, slid along a rail and a spring connected to the translator to provide the reciprocating force. Their proposed harvester was able to generate a peak electric power of 674 mW (power density of 3.4 mW/cm^3 with a volume of 200 cm^3) at a horizontal foot motion of 4.5 m/s with a frequency of around 1.75 Hz. Reducing the volume of the harvester was their plan to integrate the generator into a shoe.

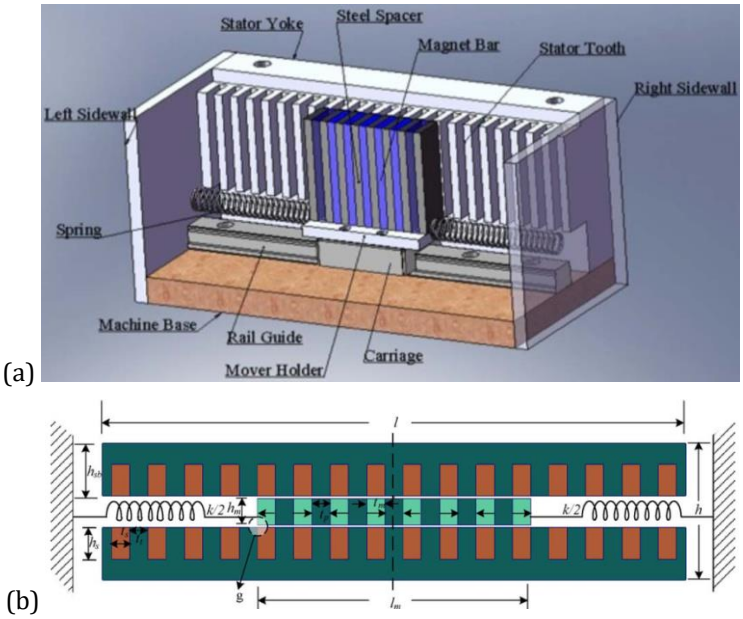

Figure 2.7. (a) A linear magnet energy harvester. (b) The schematic diagram of the harvester by Zeng *et al* [46].

Kwon *et al* [47] presented an electromagnetic energy harvester for low-frequency vibrations by designing a proof mass mounted with copper coils to be the moving part of a generator. The fixed part of the harvester consists of eight NdFeB ring magnets stacked and separated by steel cores on a stainless steel shaft, as in Figure 2.8. The natural frequency of the harvester was shown to be 3.65 Hz, and it was able to generate its maximum power when the load resistance was 680 Ω. Under an acceleration of 0.53 m/s^2 excited in a vertical direction by the shaker, an average power of 0.156 mW was produced. In the event of real field testing at the 3rd Nongro Bridge in South Korea, an average power of 0.12 mW was generated by the harvester from an exciting acceleration of 0.25 m/s^2 at 4.10 Hz. Tuning the natural frequency of the harvester to match the ambient vibration of the bridge and reducing structural damping was their proposed improvement, to increase the amount of power output harvested from low-frequency vibrations on the bridge.

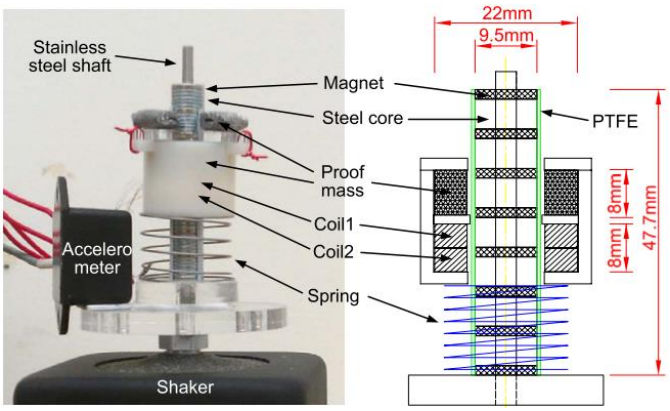

Figure 2.8. The prototype of electromagnetic energy harvester by Kwon *et al* [47].

An inductive multi-coil harvester was proposed by Ylli *et al* [48] to exploit the swing motion of the foot during walking for generating energy. A single seismic mass formed by the three parallel stacks of multi NdFeB magnets and spacers is shown in Figure 2.9. A synchronous movement of the magnet stack through a number of coils induces output voltage. The harvester was able to generate an average power of 1 mW and 2.14 mW at a walking speed of 4 km/h and 10 km/h respectively. The size constraint of a shoe sole is a challenge for their design.

However, the improvement of the simulation model is still ongoing. They will focus on a flexible design for the model with geometrical parameters and new parameters to improve the power output.

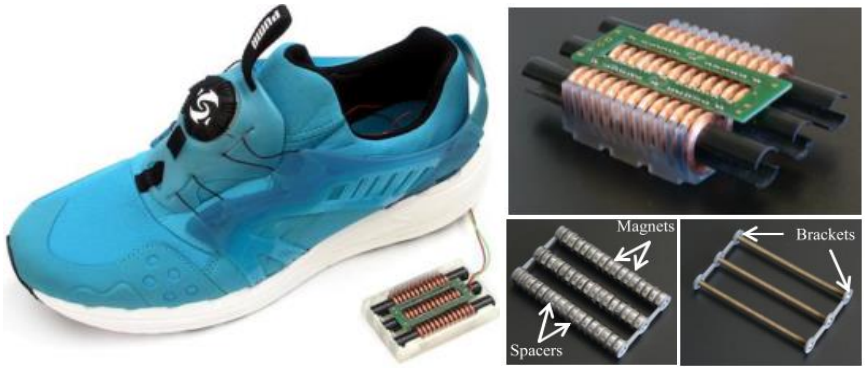

Figure 2.9. The electromagnetic energy harvester for shoe integration by Ylli *et al* [48].

2.3.3.2 Harvesters using impact-based magnet moving type

The free movement of the magnet inside the housing is highlighted. The voltage is induced in a coil due to the variation of magnetic flux density created by the free motion of the magnet. As a result of free motion, contact between magnet and housing or a coil is inevitable.

Choi *et al* [49] developed a vibration energy harvester which takes advantage of the free motion of a spherical permanent magnet to harvest energy under low-frequency vibrations. The proof mass of the harvester comprises a spherical NdFeB magnet enclosed by two shells made of Teflon and SUS to form non-uniform mass distribution as in Figure 2.10. The device was capable of producing a maximum open-circuit voltage of 154.4 mV and an output power of 4.53 μW across a 70Ω load under the vibration frequency of 12 Hz and excitation of 3g (1 g = 9.8 m/s^2).

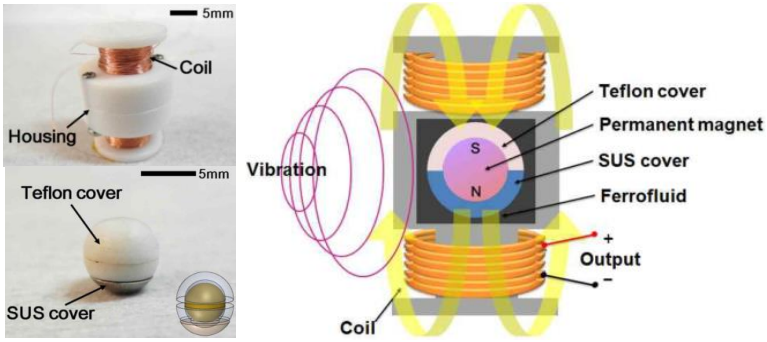

Figure 2.10. Electromagnetic harvesting device using spherical permanent magnet by Choi *et al* [49].

Another electromagnetic harvester proposed by Han *et al* [50] exploited the free movement of a cubic magnet to harvest vibration energy from all directions. A cubic NdFeB permanent magnet acted as a proof mass, freely moving inside a box formed from polyimide substrate and six surfaces of copper coils, as in Figure 2.11. The size and shape of the magnet were optimised, and the harvester could generate an RMS voltage of 4.27 V and a maximum power of 2.45 μW across a 3Ω load at a frequency of 28.86 Hz, under acceleration of 1.17*g*.

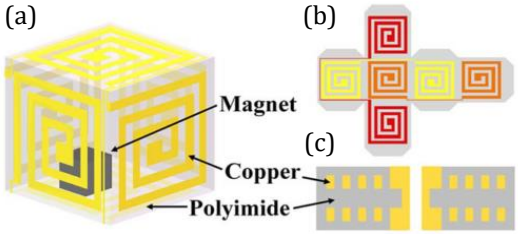

Figure 2.11. (a) A cubic electromagnetic harvester with (b) a planar layout and (c) cross section of the coil [50].

With the proposed harvester in Figure 2.12 [51], the voltage is induced due to free/impact motion of the cylindrical NdFeB magnet through a coil. The RMS power of 71.8μW can be generated at the frequency of 2.5 Hz and an acceleration of 5.2 m/s^2. The large input amplitude results in significant raising power being harvested. However, the impact force exerted on the end stoppers should be of concern. Adding short springs at the end can mitigate the energy loss and improve device stability. A study comparing a free/impact electromagnetic energy harvester (FIEH) with conventional electromagnetic energy harvesters (CEH)

shows that the former is more capable of producing electrical energy from low frequency and large amplitude operation [52]. Without the direct connection of seismic mass with the vibrating frame and spring suspension as in CEH, the free motion of the mass in FIEH allows matching lower frequencies with higher relative amplitude, which results in higher power output at low frequencies.

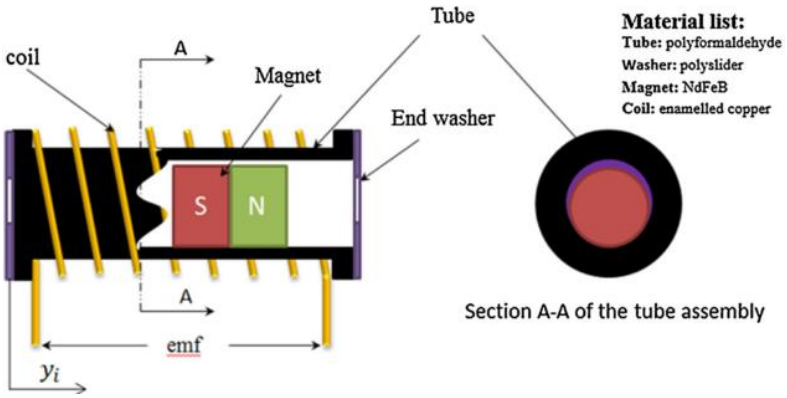

Figure 2.12. The electromagnetic vibration energy harvester with free/impact motion By Haroun *et al* [51].

2.3.3.3 Harvesters using mechanical suspensions

The moving part of the harvesters in this type is suspended by a mechanical spring or a cantilever beam. The vibration energy is typically harvested in one direction.

Khaligh *et al* [53] described a conventional structure of vibration energy harvester as in Figure 2.13. This structure takes advantages of two transduction methods, i.e. piezoelectric and electromagnetic techniques. The four NdFeB permanent magnets mouthed on the top surface of the proof mass are connected to four piezoelectric springs to convert mechanical energy from ambient vibration into electrical energy. The movement of the proof mass not only creates the stress for the piezoelectric mechanism, but also induces a voltage in a fixed copper coil at the centre because of electromagnetic induction. The resonant frequency of the device was reported to be 2 Hz. The overall output power is about 43 mW (power density of 0.293 mW/cm^3 with a volume of 147 cm^3) and piezoelectric and electromagnetic mechanisms generate approximately 6 mW and 37 mW respectively.

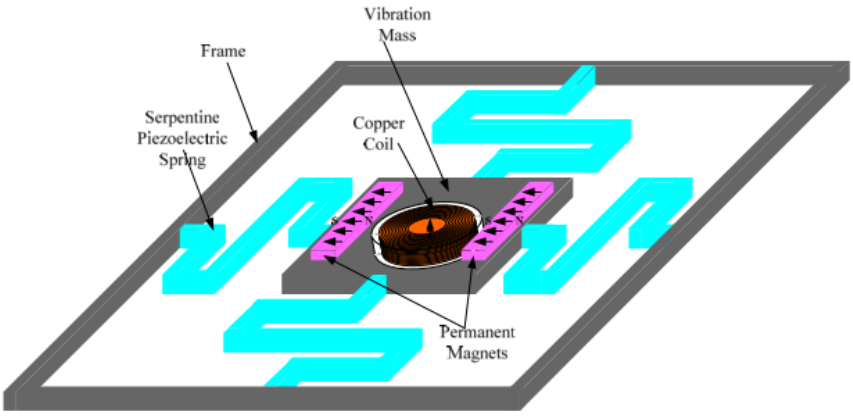

Figure 2.13. A hybrid piezoelectric/electromagnetic energy harvester by Khaligh *et al* [53]

Ooi *et al* [54] reported on an electromagnetic transduction structure with two separate resonators designed to operate over a wide frequency range. The NdFeB permanent magnet and the copper coil are mounted on two separated cantilever beams as in Figure 2.14. The two cantilever structures showed different resonant frequencies of 21.3 Hz and 19.4 Hz respectively. The open-circuit voltage of 259.5Vrms was reported at the exciting frequency of 21.3 Hz and the acceleration of 0.8 m/s^2. However, a low generated power may be obtained in case the device is implemented in unsuitable applications, i.e. a machine which runs at the side frequencies of the harvester. The frequency spectrum of vibration sources is not limited to a certain range.

(a)

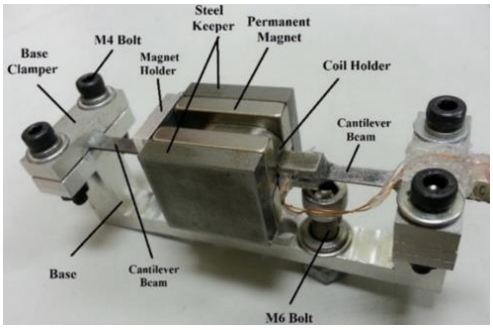

(b)

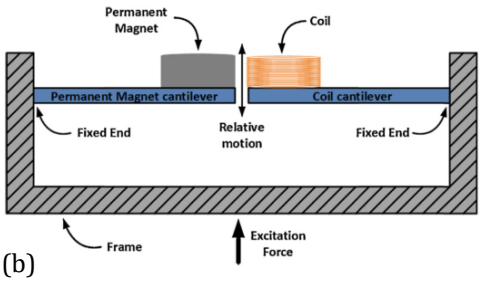

Figure 2.14. (a) Dual-resonator electromagnetic energy harvester and (b) a schematic diagram by Ooi *et al* [54].

Lee *et al* [55], [56] presented the design, fabrication and characterisation of a vibration-based electromechanical energy harvester driven by low-frequency motion. The harvester comprises of a pair of thin flame resistant (FR-4) springs at both top and bottom ends to support a pair of NdFeB permanent magnets fixed by

an aluminium bolt and nuts as in Figure 2.15a. Under the acceleration of 0.2*g*, a maximum power of 490 μW was produced across a load resistance of 1.8 kΩ at the resonant frequency of 12 Hz. Afterwards, the performance of their device was improved by using bigger magnets, changing the material of housing to Teflon, and an increase from one copper coil to three, winding at top, middle and bottom parts as in Figure 2.15b. At the same accelerating level of 0.2*g*, a maximum output power of 1.52 mW can be generated across a load resistance of 5.46 kΩ at a resonant frequency of 16 Hz. The relevant parameters' influence on the reliability of the harvester, i.e. spring fatigue life, needs to be further investigated.

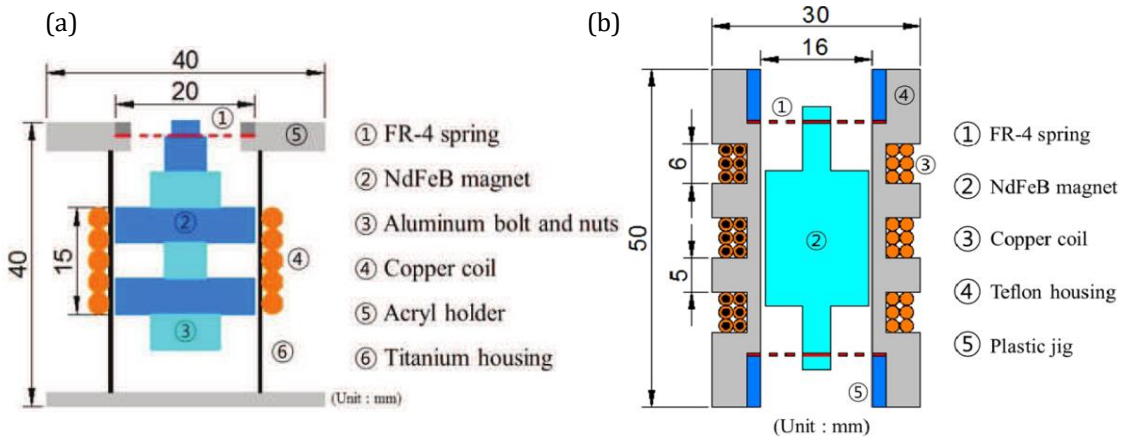

Figure 2.15. Schematic diagrams of electromagnetic energy harvesters presented by Lee *et al* (a) the first-version prototype [55] and (b) the developed prototype [56].

2.3.3.4 Harvesters using magnetic springs

For a harvester of this type, two sets of permanent magnets are deployed. One set acts as the seismic mass while the other provides repulsive force to form a magnetic spring and levitates the seismic mass that vibrates in response to external vibration.

The magnetic spring harvester described by Saha *et al* [57] consists of two opposite polarity circular magnets glued with a soft magnetic pole piece inside a Teflon tube which have two permanent magnets fixed at both ends of the tube and a copper coil wound around the tube, as in Figure 2.16. A maximum power of 14.55 μW across a load of 7.3 kΩ can be produced under an acceleration of 0.38 m/s^2 at a resonant frequency of 8 Hz.

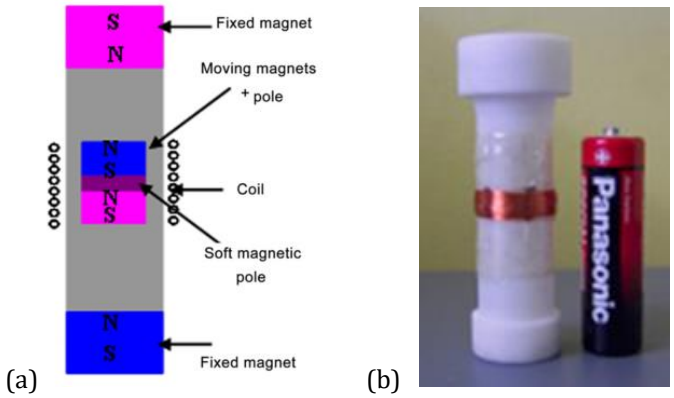

Figure 2.16. (a) Structure of magnetic spring generator and (b) generator prototype by Saha *et al* [57].

Foisal *et al* [58] presented an initial prototype based on a single magnet used as a moving mass between two fixed magnets inside a Teflon tube, as in Figure 2.17. A maximum power of 1.18 mW for an optimum load of 97 Ω can be harvested at a resonance frequency of 9 Hz. Moreover, Foisal *et al* also proposed optimised parameters of the harvester to gain more power based on the same device structure, by increasing the distance between fixed magnets and adjusting the size of the fixed magnet [59]. The maximum power estimated in a Matlab simulation was claimed to be 53.5 mW for 97 Ω load at a resonance frequency of 8.1 Hz. Although it can be seen that work by Foisal *et al* offers higher maximum power than work by Saha *et al* [57] with the comparable size of prototypes, this assumption cannot be made due to testing under different acceleration levels and the missing of some key factors in the paper, i.e. magnet grade and coil diameter.

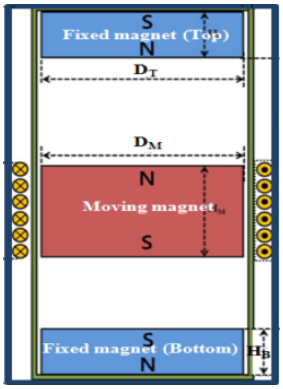

Figure 2.17. Schematic diagram of magnetic spring harvester by Foisal *et al* [58], [59]

The overall structure of the generator described by Munaz *et al* [45] is similar to the devices above by [57]–[59], but this harvester was designed based on a multipole magnet. Three ring NdFeB permanent magnets acting as moving mass are stacked with the same polarisation by having bolts to fix them together without any spacer. It was found that an output power of up to 4.84 mW was obtained across a load resistance of 1 kΩ for a volume of 9.04 cm^3 at a resonance frequency of 6 Hz and under acceleration of 0.5*g*.

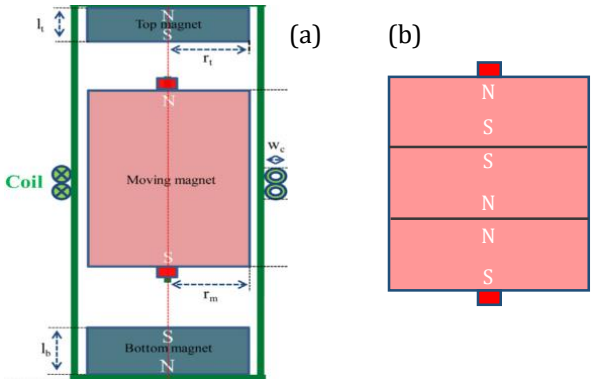

Figure 2.18. Structure of (a) an electromagnetic energy harvester by Munaz *et al* [60] and (b) moving mass formed by three magnets.

For the harvester presented by Berdy *et al* [61], the repulsive force between magnets was also adapted to levitate the moving mass as shown in Figure 2.19. A rectangular permanent magnet is put inside a Teflon box with a guide rail to reduce the contact area between the box and the levitating magnet. In the experiment, the device (its resonance frequency between 6 Hz and 7 Hz) was mounted on an individual's chest to harvest energy. Experimental results show that an average power of 71 μW and 342 μW was obtained across a load resistance of 1000 Ω during walking (4.8 km/h) and running (9.7 km/h) respectively.

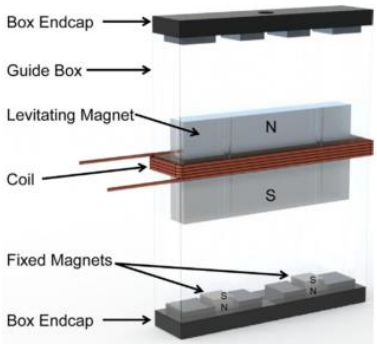

Figure 2.19. An electromagnetic magnetic levitation vibration energy harvester by Berdy *et al* [61].

Zhang *et al* [62] described an electromagnetic energy harvester using a magnetic spring to suspend an array of magnets as in Figure 2.20. A magnet array consists of 2 x 5 magnets levitated due to the repulsive force of a pair of magnets facing each other, with the same pole, and stabilised horizontally by graphite sheets. A total of 16 coils were used to induce an electric current. When exciting the device at its 4 Hz resonant frequency in a backpack during walking, the power output could reach up to 32 mW at 3.58 m/s across a load resistance of 96 Ω.

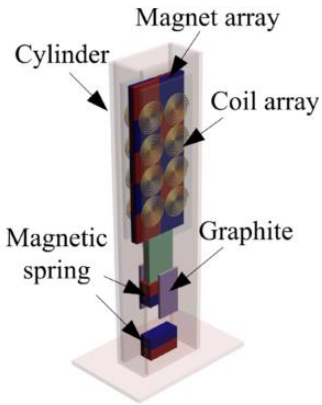

Figure 2.20. Structure of a hand-held electromagnetic energy harvester by Zhang *et al* [62]

2.3.3.5 Harvesters using diamagnetic levitation

A diamagnetic sheet is the main structure for these types of harvesters. The technique of diamagnetic levitation is applied by levitating the magnet to float stably in the middle of the diamagnetic sheets. Except for force repelled from the diamagnetic sheets, there is also an attractive force from the fixed magnet at the top which helps uplift the floating magnet. The floating magnet moving in response to the external vibration induces a voltage in a coil which is typically mounted on the diamagnetic sheet.

Wang *et al* [63], [64] presented a structure of graphite diamagnetic plates to levitate a NdFeB cylindrical magnet which balances the weight of the floating magnet by using a NdFeB disc magnet placed at the top of the overall structure, as in Figure 2.21. The electrical energy can be extracted from the relative motion of the floating magnet and copper coils engraved in the graphite sheets. A power of

0.74 μW can be generated at a frequency of 2.7 Hz across a load resistance of 1870 Ω. The low power output obtained is due to the small available range of displacement and loss from the effect of eddy currents. Optimization of coil and magnet geometry, harvester size, and ways to mitigate eddy currents were later reported in [65]. As a result, an RMS power output of 1.72 μW was reported under a peak acceleration of 0.081 m/s^2 at a frequency of 2.1 Hz.

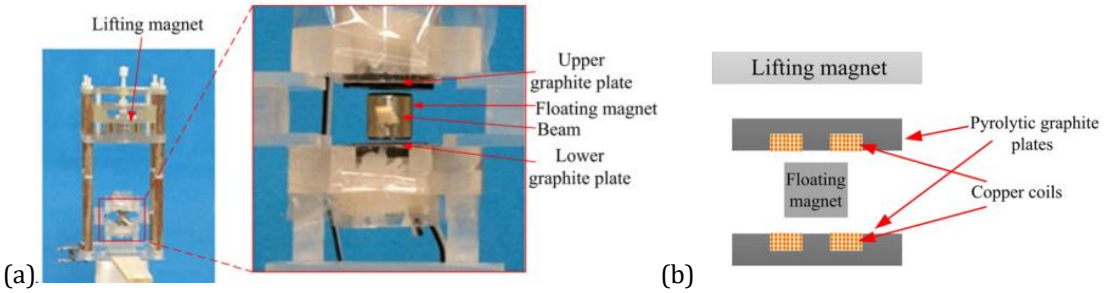

Figure 2.21. (a) A magnetically levitated vibration energy harvester and (b) schematic diagram by Wang *et al* [63], [64].

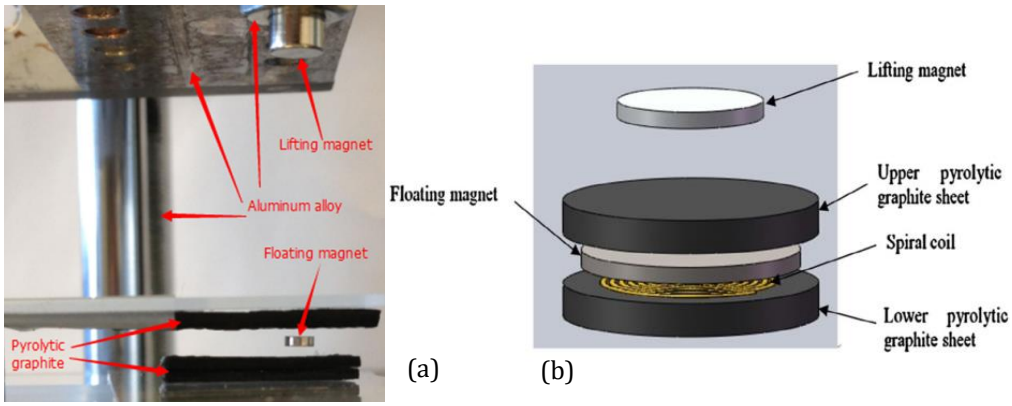

Figure 2.22. (a) A vibration harvester using diamagnetic levitation and (b) schematic diagram by Ye *et al* [66].

Another electromagnetic vibration energy harvester based on diamagnetic levitation was proposed by Ye *et al* [66]. The overall structure of their proposed device was similar to works in [63], [64] except for the dimensions, the magnetic properties of the magnet, and the geometry and size of the magnet, coil and graphite sheets. At a natural frequency of 6.93 Hz, the peak power of 66.7 μW can be generated across a load resistance of 45.94 Ω

2.3.3.6 Summary

Electromagnetic vibration energy harvesters that can be implemented for the purpose of harnessing energy from human motion during routine activities, i.e. walking and running have been reviewed and categorised into five types:

1. Harvesters using a sliding-magnet moving type
2. Harvesters using a freely movable magnet
3. Harvesters using mechanical suspensions
4. Harvesters using magnetic springs
5. Harvesters using diamagnetic levitation

Such harvesters can harvest electrical energy from vibrations with low frequencies (< 20 Hz) and high amplitudes. The main characteristics of the mentioned electromagnetic harvesters are summarized in Table 2.6.

Although the free motion of moving mass in the first two types is a benefit for power harvesting at low frequencies, energy loss due to friction and impact force acting on parts of the harvester are significant factors that reduce the power generated and device lifetime. Considering that long-term usability is one of the most important requirements for harvesters implanted in the hip prosthesis, electromagnetic vibration energy harvesters based on mechanical springs such as harvesters mentioned in Section 2.3.3.3 are not ideal for hip implant application. This is due to the inevitable issue of spring fatigue that may reduce the longevity of the harvesters. By comparison, magnetic springs are an attractive alternative as a base structure for energy harvesters for hip implant applications. All harvesters mentioned in Section 2.3.3.4 and 2.3.3.5 take advantage of the repulsive force between magnets to suspend the moving magnet instead of using mechanical springs. Although the technique of diamagnetic levitation in Section 2.3.3.5 promises zero friction, which can potentially benefit the hip implant application, one disadvantage that should be pointed out is that the displacement of moving mass is limited within the narrow gap between the diamagnetic sheets (<10 mm) due to the limited ability of such sheets to support the weight of the floating

magnet. As a result, the power obtained from this type of harvester is low owing to the restricted movement space for the floating magnet and the limited size and thus magnetic field strength of the magnet. Therefore, an electromagnetic vibration energy harvester based on a magnetic spring, as in Section 2.3.3.4, is believed to be a suitable solution for hip implant applications. This structure has low friction, no spring fatigue issue and the capability to work under external vibrations with low frequency and high amplitude such as human motion.

In the literature, it can be seen that adding arrays of magnets or coils, i.e. the works in [47], [55], [56], [60], [62] is one of the procedures that increases the amount of power generated. However, such arrays should be optimised properly considering the volume available for the displacement of moving magnets for particular applications. To illustrate, it has been stated in [48] and [60] that redundant magnets used to form a single moving mass result in low output power due to the displacement of moving mass being decreased. Furthermore, lowering the friction loss occurring during the operation of the harvester can increase the output power as well. For example, an attempt to reduce contact between the inner surface of the plastic box and moving magnet in [61] by adding a small guide rail led to an increment in output power by 25% to 50% according to the experiment results. Also, the magnet shape and size, as well as the overall volume of the harvester, have a significant influence on the power generation. For example in [59], the authors increased the length of harvester by 4 mm (9.5% increased) and decreased the size of the top magnet. The power output was found to be improved by about 45 times compared to the old design [17]. The effect of magnet shape on the performance of a harvester has also been proven by the experiment in [51] whereby different frictional characteristics of each magnet shapes result in the particular amount of power gained. For instance, Coulomb's friction presented in a ball magnet is lower than that of the cylindrical magnet which affects the power generation.

As a result of these aforementioned procedures, there are various feasible ways to develop a model of an electromagnetic-based energy harvester that will prove

suitable for hip implant harvesting and achieve enough power for powering small monitoring devices, which is the main objective of this project. To address this challenge, an efficient method and structure to harvest energy at low frequencies within the size constraints of a hip prosthesis are investigated in Section 2.4.

Table 2.6 Summary of electromagnetic vibration energy harvesters

Ref.	Freq. (Hz)	Velocity (m/s)	Acceleration (m/s^2)	Moving mass (g)	Power (mW)	Volume (cm^3)	Power density (mW/cm^3)
[46][b]	1.75	4.5	-	145	674	200	3.4
[47][b]	3.65	-	0.53	-	0.156	-	-
[48][b]	-	1.11 2.78	-	-	1 2.14	46.69	0.021 0.046
[49][a,b]	12	-	29.42	-	0.00453	3.40	0.0013
[50][a,b]	28.86	-	11.47	-	0.00245	1	0.00245
[51][a,b]	2.5	-	5.2	-	0.0718	0.763	0.0941
[53][b]	2	-	-	-	43	147	0.293
[54][b]	21.3	-	0.8	-	259.5Vrms	-	-
[55][b]	12	-	1.96	-	0.49	-	-
[56][b]	16	-	1.96	27.5	1.52	-	-
[57][b]	8	-	0.38	27	0.01455	12.7	0.0011
[58][b]	9	-	4.9	-	1.18	7.39	0.16
[59][b]	8.1	-	4.9	-	53.5	-	-
[60][b]	6	-	4.9	-	4.84	9.04	0.535
[61][b]	6 - 7	1.33 2.69	-	-	0.071 0.342	6.83	0.01 0.05
[62][b]	4	3.58	-	-	32	120	0.267
[63], [64]	2.7	-	-	8	0.00074	-	-
[65]	2.1	-	0.081	6	0.00172	-	-

Ref.	Freq. (Hz)	Velocity (m/s)	Acceleration (m/s^2)	Moving mass (g)	Power (mW)	Volume (cm^3)	Power density (mW/cm^3)
[66]	6.93	-	-	0.19	0.0667	-	-

[a] Implantable devices
[b] Portable devices

2.3.4 Discussion

A summary of the energy harvesters in the literature review is presented in Figure 2.23, Figure 2.24 and Figure 2.25 regarding power output, power density and normalised power density versus the frequency of operation respectively. Some energy harvesters reviewed are not included in these charts because either operating frequency or volume of the device and acceleration were not reported in the publications. The filled symbols in the diagram represent the harvesters with volumes less than 10 cm^3.

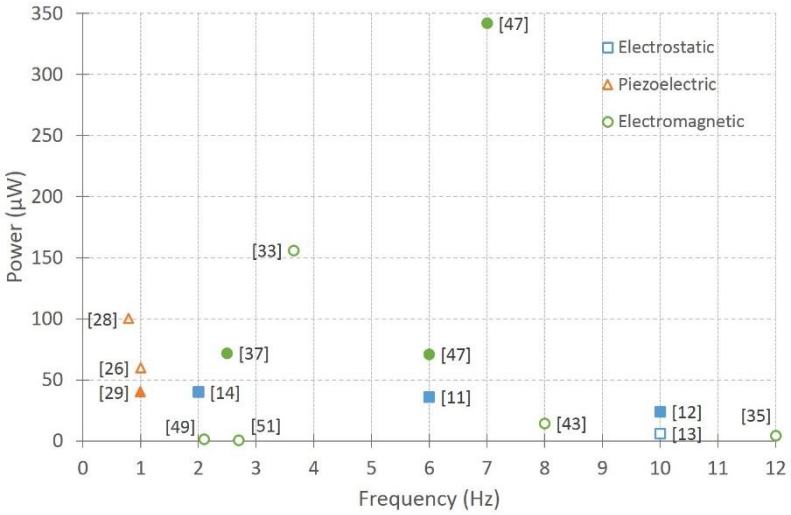

Figure 2.23. Power output versus operating frequency of the energy harvesters.

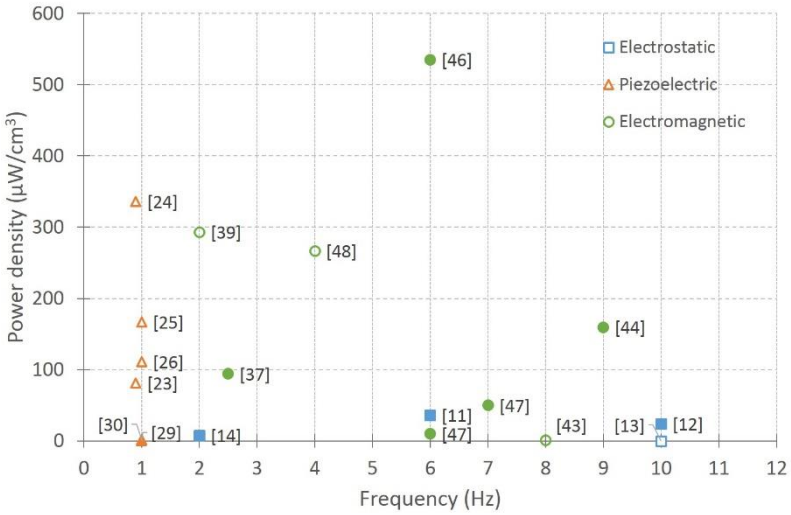

Figure 2.24. Power density versus operating frequency of the energy harvesters.

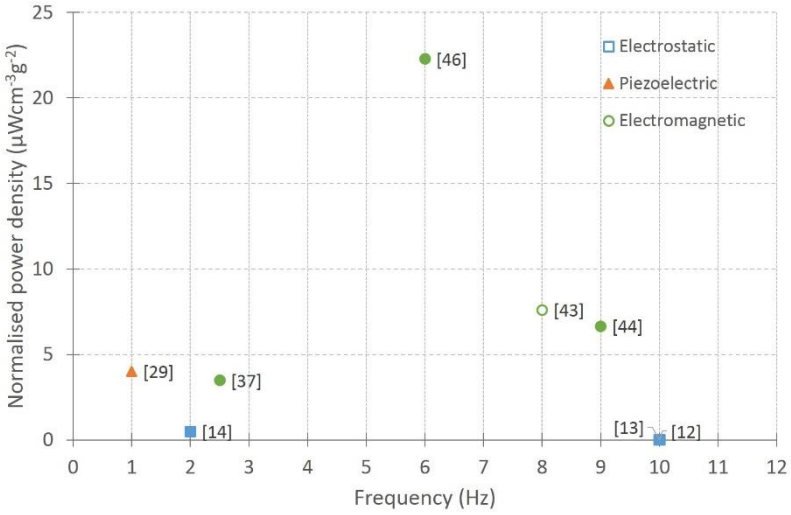

Figure 2.25. Normalised power density versus operating frequency of the energy harvesters.

Figure 2.23, Figure 2.24 and Figure 2.25 show that the electrostatic energy harvesters have low power output and minimal power density compared to other types of harvester. This makes this transduction mechanism less competitive with other mechanisms. Both piezoelectric and electromagnetic harvesters provide a relatively high power density. A relatively higher power output is given by the electromagnetic harvesters, whereas the piezoelectric harvesters offer lower operating frequency (close to 1 Hz). Note that most of the piezoelectric harvesters are designed to be applied inside shoes which undergo direct impact from foot strikes, so their performance may degrade when placed at other locations, e.g. the

hip, where such impact is not available. Considering the miniature devices (filled symbols: volume less than 10 cm^3), the electromagnetic harvesters give a superior performance. Some of them offer high power density at a low operating frequency of less than 3 Hz, which is close to the frequency of human motion. The electromagnetic harvesters could have an advantage over the piezoelectric harvesters due to their high output and feasibility to be designed for hip motion which has lower impact force and smaller amplitude displacement than foot motion.

To harness energy from hip movements for powering electronic systems implanted inside hip prosthesis, the electromagnetic mechanism is thought to be a practical choice compared to other transduction mechanisms such as piezoelectric and electrostatic. No smart materials are needed for the electromagnetic harvesters which require only copper coils and permanent magnets. Some piezoelectric materials such as PZT contain lead which is toxic to the human body. In addition, the low output impedances (few Ω's to kΩ's) of electromagnetic energy harvesters result in high output current and require no external voltage sources, which is needed for most electrostatic energy harvesters [46], [67]–[69]. Compared to the piezoelectric and electrostatic harvesters, the electromagnetic harvesters have high power density with a low-cost design. However, the constraints of available volume may affect design trade-offs for electromagnetic harvester performance due to the potential large scale in the structural devices.

2.4 Strategies to increase energy harvested from low-frequency vibrations

Hip implant energy harvesting takes advantage of human motion during routine activities, e.g. walking or running, to generate electrical energy for powering other microsystems within the hip prosthesis. In principle, the maximum power can be produced when the excitation frequency matches the resonance frequency of the device [70]. According to variation and instability of the frequencies of human

movements, extracting maximum power from hip movements is not always possible due to the unsuitability of the vibration condition. This leads to lower power output than expected. In addition, the limited size of the implantable devices can result in a small amount of power generated. To overcome such problems and increase the performance of the devices in real applications, several solutions have been proposed such as frequency tuning techniques [71]–[74], frequency up-conversion techniques [75]–[81], and techniques to widen the operational bandwidth of harvesters [82]–[91].

The frequency tuning techniques involve mechanisms that tune the resonance frequency of a harvester to match the ambient vibration frequency at all times by mechanical or electrical methods. Possible solutions include varying the centre of gravity of the inertial mass, changing the dimensions of the structure, changing spring stiffness and adjusting the electrical loads of the harvester [92]. However, frequency tuning requires an additional system that results in a more complex design and additional power consumption. If not designed properly, the power consumption of the frequency tuning technique may exceed the power output generated by the harvester [93].

How to harvest energy and maximise the power generated by low-frequency excitation such as hip motions, frequency up-conversion techniques and strategies to widen bandwidth, are reviewed in this section.

2.4.1 Frequency up-conversion

Ashraf *et al* [75] designed the structure of the energy pumping energy harvester using elastic beams. The inner structure, as in Figure 2.26a, acts as a high-frequency resonator which consists of the coil on the PVC beam being sandwiched by four magnets. This structure attached to the frame is supported by two flexible beams to form a low-frequency resonator, as in Figure 2.26b. A low-frequency vibration is pumped to a high frequency by an oscillation of a low-frequency structure excited high-frequency structure. The peak power of 20.9 mW and

average power of 5.02 mW across a 3 kΩ load was produced under 1*g* acceleration at a resonance frequency of 10.3 Hz.

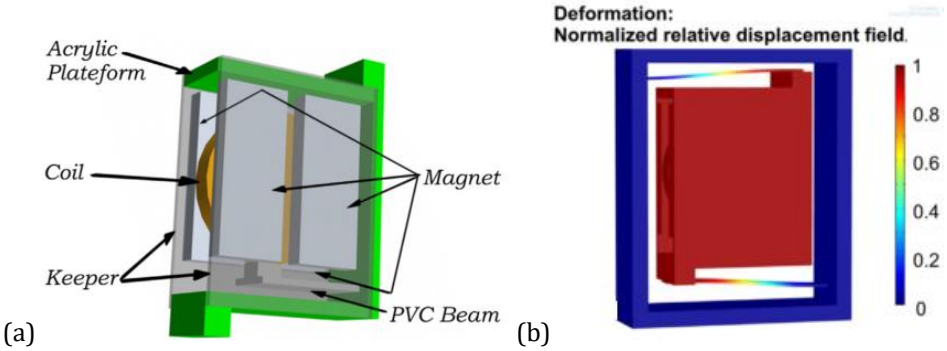

Figure 2.26. Design of the energy pumping frequency harvester by Ashraf *et al* (a) the structure of high-frequency oscillator and (b) the complete harvester vibrated in high frequency [75].

The electromagnetic energy harvesting systems proposed by Rahimi *et al* [76] have a main structure comprising of a cantilever beam with a pick-up coil and magnets placed on a support, as in Figure 2.27. The magnet excited under an ambient low-frequency vibration oscillates in an up and down direction. It touches and excites the cantilever to vibrate at its resonance frequency. The impact of the two parts is the key to this frequency up-conversion technique. A higher frequency oscillation is generated when the generating beam is released. A power output of 128 μW is generated at an external vibration frequency of 2 Hz and an acceleration of 72m*g*. However, physical contact between two beams is not a reliable solution for implementation of a harvester that requires high durability.

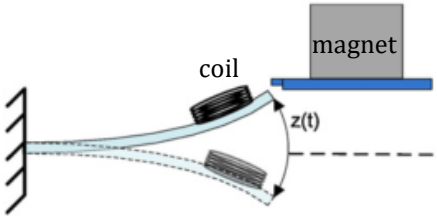

Figure 2.27. The system of electromagnetic energy harvesting by Rahimi *et al* [76].

Halim *et al* [77] presented a non-resonant frequency up-converted electromagnetic energy harvester that exploits the free movement of a non-magnetic ball inside a cylinder (Figure 2.28) to force the movement of the magnet. To illustrate, the impact of the non-metallic ball on magnets at the top and bottom

of the cylinder excites the magnet to move relative to the copper coil wound around the cylinder and vibrate at a higher frequency. An average power of 104 μW across a 17 Ω load was produced at a frequency of 15 Hz under 20 m/s^2 acceleration. A power density of 14.56 $\mu W/cm^3$ was reported.

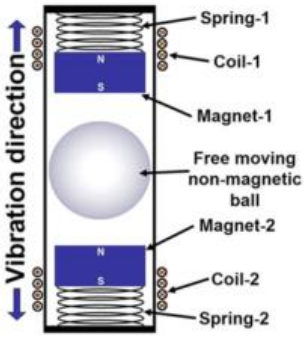

Figure 2.28. Schematic of a frequency up-converted electromagnetic energy harvester by Halim *et al* [77].

Halim *et al* [78] proposed another frequency up-converting electromagnetic energy harvester that uses the impact of a spherical ball to drive the magnet inside a rectangular frame, as in Figure 2.29, to oscillate at a high frequency. Instead of the direct impact mentioned in [77], the transverse impact of a metallic ball is applied. The ball moved freely in a rectangular channel, pushing the proof mass with a magnet mounted to vibrate at a higher resonant frequency. With a hand motion excitation of about 2*g* at a frequency of 5.8 Hz, an average power of 103.55 μW across an 85 Ω load was generated with a power density of 5.4 $\mu W/cm^3$.

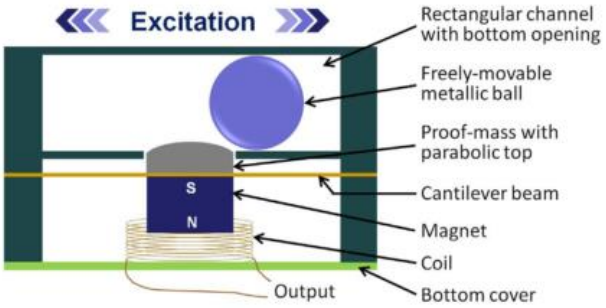

Figure 2.29. Model of an electromagnetic energy harvester by Halim *et al* [78].

Turkyilmaz *et al* [79] presented an electromagnetic micro-power generator to harvest energy from low-frequency vibrations with the capability to tune a resonance. The model consists of two diaphragms with different resonance

frequencies. The magnet mounted on the top diaphragm has a resonance frequency in the range of 1-30 Hz and resonates with ambient vibration. The repulsive force pulls and releases the lower magnet attached to a high-frequency diaphragm which has a resonance frequency in the range of 20-200 Hz, achieving the technique of frequency up-conversion. The resonance frequency of the diaphragms can be tuned to match a broad range of exciting frequency vibrations by adjusting the rubber springs that fix the diaphragms to a common frame. An average power of 3.21 μW across 2.1 Ω was reported by converting the input frequency of 13 Hz to 200 Hz at 7.5 mm peak to peak vibrations.

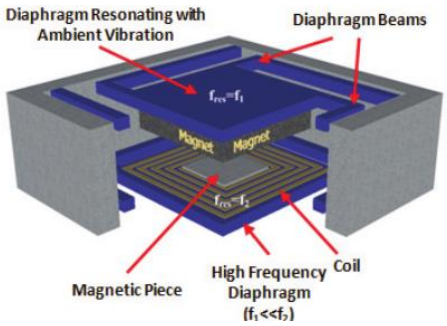

Figure 2.30. Structure of an electromagnetic micro-power generator by Turkyilmaz *et al* [79].

Zorlu *et al* [80] presented a design for a magnet and coils on resonating cantilever beams for electromagnetic power generation. The frequency up-conversion technique is achieved by two resonating structures: a diaphragm with a permanent magnet and cantilever beams with coils, as shown in Figure 2.31. The diaphragm is oscillated by external vibration which leads to the resonance of the magnet. The movement of the magnet attracts and releases cantilever beams resulting in the frequency conversion. Experimental results showed that the proposed system generated RMS voltage of 6.94 mV and an average power of 1.2 nW by converting environmental vibrations of 10 Hz (frequency motion of magnet) to 63 Hz (frequency of cantilevers). Although increasing the number of cantilevers is possible to improve the generated power, the difference in the natural frequency of the cantilever and asynchronous release of the cantilever may be an obstacle to achieve expected output.

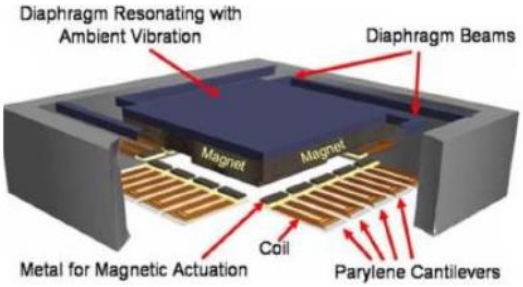

Figure 2.31. Structure of an electromagnetic energy harvest for low frequency by Zorlu *et al* [80].

Tang *et al* [81] presented a repulsive driven frequency up-converting generator that converts low-frequency to high-frequency vibrations by the two-stage vibratory structure, as shown in Figure 2.32. According to the magnetic force of attraction and repulsion, the movement of inertial mass with actuation magnet excited by ambient vibration induces electromechanical coupling in both Frequency Increased Generators (FIG) located beside the mass. Results showed the power density of 1.11 μW/cm^3 and average power output of 158 μW were obtained at an input frequency of 0.5 Hz under an acceleration of 1*g*. The movement of the central mass is key in this work and presents electromechanical coupling as a power generation. Non-contact magnetic repulsion was used in this generator.

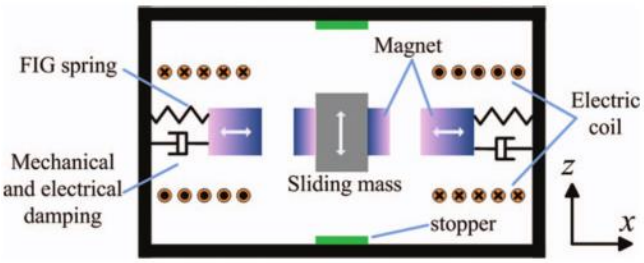

Figure 2.32. Schematic of a repulsively driven frequency-increased generator by Tang *et al* [81].

2.4.2 Widening bandwidth of the harvester

Yuksek *et al* have developed a broadband electromagnetic energy harvester by using multi impact oscillations to broaden the response bandwidth of the harvester [82]. Two low-frequency cantilevers mounted with impact masses at their ends, as in Figure 2.33, were designed to respond to external vibration at different frequencies (25 Hz and 50 Hz). The copper coil attached to the free end

of the high-frequency cantilever is excited by the impact action of masses on low-frequency cantilevers and vibrates relative to the magnet. As a result, voltage is induced by electromagnetic induction. At 2*g* acceleration, a wide bandwidth response from 10 to 63 Hz was reported. The bandwidth can be changed to 10-51 Hz and 10-58 Hz at accelerations of 0.5*g* and 2*g* respectively by adjusting the frequency of impact cantilevers to 25 Hz and 45 Hz respectively. A maximum power of 85 μW was generated under 5*g* acceleration at 30 Hz for 2.68Ω load resistance.

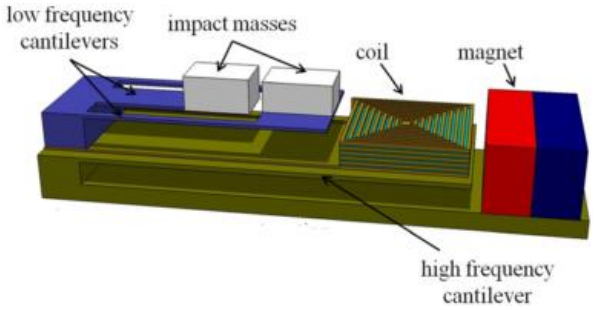

Figure 2.33. A schematic of electromagnetic energy harvester by Yuksek *et al* [82].

A wide bandwidth electromagnetic generator was developed by Sari *et al* [83] consisting of a series of cantilevers, which have various lengths and hence resonant frequencies (Figure 2.34). The small length increment for each cantilever results in the overlapping frequency spectrum of the cantilevers, which leads to a widened bandwidth and an increase in the overall power generated. Electromagnetic induction was used for power generation. The cantilever array sputtered with coils is excited by the external vibration and moves relative to the fixed magnet. A continuous power of 0.5μW was generated at 20mV between 3.3 and 3.6 kHz of exciting vibration.

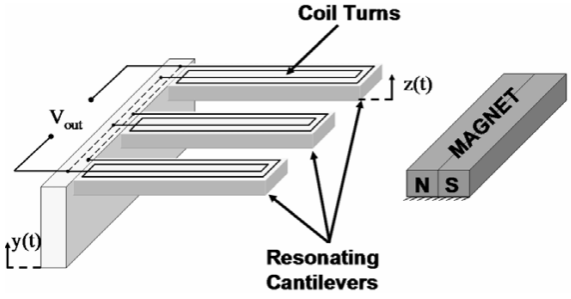

Figure 2.34. Electromagnetic micro power generator by Sari et al [83].

Another vibration energy harvester described by Podder *et al* [84] applied a cantilever structure for low operational frequency. The device consists of four NdFeB permanent magnets bonded at the end of a cantilever around a fixed copper coil and a pair of magnets placed in opposition, as in Figure 2.35. Apart from the fact that a low-frequency vibration can be exploited by the electromagnetic conversion in the middle of the structure, the operational frequency range of the device is widened as well, owing to bi-stability produced by the repulsive force between magnets at the end of cantilever. A peak power of 22 μW for 1 kΩ load was reported at A frequency of 35 Hz under 0.5*g* acceleration.

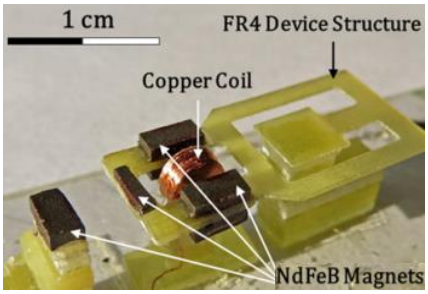

Figure 2.35. Electromagnetic bistable vibration energy harvester by Podder *et al* [84].

To widen the bandwidth of harvesters, a structure employing a pair of coupled oscillators was proposed by Petropoulos *et al* [85]. The two proof masses with the two linear springs connected in series to the frame. The analysis showed that the frequency response was flat over a wider operating range. Another coupled oscillator was proposed by Abed *et al* [86] aiming to take advantage of the nonlinearities and the modal interaction to improve the device performance. The arrays of levitated magnets introduced a nonlinear effect, which widened the bandwidth of the device with a bandwidth of 190% and normalised power of 20.2 $mWcm^{-3}g^{-2}$ over an operating frequency range of 4.6-14.5 Hz. The effect of nonlinearities has been exploited by many works [87]–[91] to extend harvester bandwidth.

2.4.3 Discussion

Frequency up-converting techniques and techniques to widen harvester bandwidth have been applied to improve harvester efficiency and generate more output power (summarised in Table 2.7). However, to implement those techniques in hip implant harvesters, some potential limitations need to be considered. First, the operating frequencies of those harvesters mentioned [75], [78]–[80], [82], [84] are quite high (10- 35 Hz) and not in the range of human motion. To operate under low-frequency vibration, designing a hip implant harvester applying such techniques is still the main challenge for this work. Furthermore, most techniques mentioned above rely on physical contact-impact between parts. This may lead to serious failures when devices are used over a long period. Especially in the case of a hip implant harvester, long-term usability is a significant consideration for any design. Thus, techniques that have no physical contact between parts in the system, such as methods of non-contact magnetic repulsion as presented in [79] or the nonlinear structures using magnetic springs, seem to be suitable for hip implant harvesters. Although the frequency up-conversion techniques and the strategies to widen bandwidth, i.e. using an array of structures, lead to an increase in overall output power, complexity of design and fabrication seem to be significant problems to overcome regarding the constrained volume of a hip prosthesis. Thus, techniques should be optimised with serious consideration of minimum physical contact between components, size constraints and fatigue reduction, in order to achieve a reliable energy harvester for hip implant applications.

Table 2.7 Summary of electromagnetic vibration energy harvesters applied the techniques to gain high power.

Ref.	Input Freq. (Hz)	Output Freq. (Hz)	Power (mW)	Acceleration (m/s^2)	Volume (cm^3)	Power density (mW/cm^3)
[75]	10.3	-	5.02	9.81	27.38	0.183
[76]	2	100	0.128	0.71	21	0.061

[77]	<6	15	0.104	20	7.16	0.0146
[78]	5.8	315	0.104	19.61	19.2	0.054
[79]	13	200	0.0032	1.78	-	-
[80]	10	63	$12e^{-6}$	5.88	0.46	$2.6e^{-6}$
[81]	0.5	54.8	0.158	9.81	141.8	0.011
[82]	30	-	0.085	49.03	-	-
[83]	3.5	-	0.0005	-	1.4	$3.6e^{-4}$
[84]	35	-	0.022	4.9	-	-

2.5 Instrumented hip implant applications

Instrumented hip implants have been receiving much attention as an effective approach to reduce failures in hip replacement. A better understanding of the mechanics and functions of the human hip joints, e.g. contact forces, torques, and frictions, could be gained to improve quality and more functional hip prostheses, which will result in more efficient hip implant operations.

The first study on the loading in the hip joint was carried out in 1974 by Carlson *et al* [7]. The implant was instrumented with 14 pressure transducers mounted on the inner surface of a hollow ball (Figure 2.36a) to measure the pressure distribution between the cartilage-covered surface of the hip socket and the surface of the hip prosthesis. The signals measured were transmitted to external equipment by a 16-channel radio telemetry device located inside the hollow ball (Figure 2.36b). Electric power required to operate the telemetry device was approximately 500mW, which was supplied externally through an electromagnetic induction link. This instrumented implant was tested in-vitro. The actual pressure distribution over the joint surface was not able to interpolate due to lacking information of some parameters, e.g. the muscle forces acting across the joint, even adding some transducers. A full evaluation of the measuring system awaits implementation in a human hip.

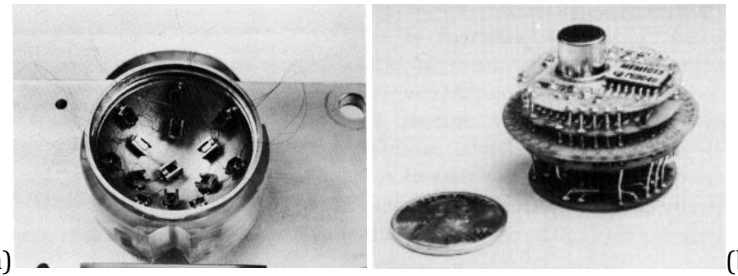

(a) (b)

Figure 2.36. (a) Pressure transducers mounted inside the hollow ball of the prosthesis and (b) assembled 16-channel telemetry device for sealing within the ball of the prosthesis [7].

Work by Carlson *et al,* as aforementioned, was remodelled in 1999 by McGibbon *et al* [11]. The number of transducers was decreased to 13 semiconductor strain gauges (Figure 2.37). The same telemetry system (16-channel telemetry device) was applied and powered by electromagnetic induction links. The implant was tested in vivo to measure contact pressure distributed on the prosthesis head. According to the data measured, the relation between the repetitive pressure and cartilage degeneration in patients was able to conclude.

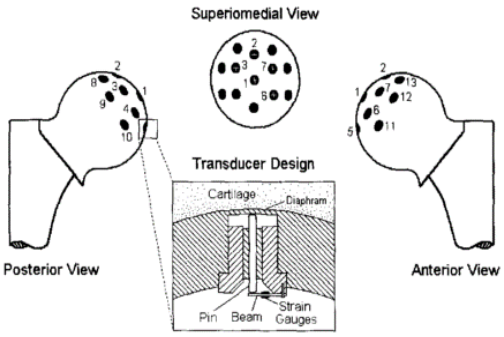

Figure 2.37. Cross-section of pressure transducer instrumented in femoral head prosthesis [11].

In 1981, another instrumented hip implant was proposed by Kilvington and Goodman to monitor the offset of the femoral head of hip prosthesis [8]. This aimed to decrease head load and improve the stem alignment of a hip prosthesis. The axial load were sensed by four strain gauges mounted within the thickened neck of the prosthesis, as shown in Figure 2.38. The gauge output was transmitted via the signal wires attached to the strain gauges and passed through an incision in the skin to connect with the telemetry box, which consisted of 3 x 1.35 V batteries, 2 reed switches, and an oscillator chip. This implant was tested in vivo in a female patient for 40 days only due to losing the signal of gauge output. The

inappropriate silicone used for encapsulating strain gauges resulted in the presence of acetic acid to corrode such gauges and solder connections.

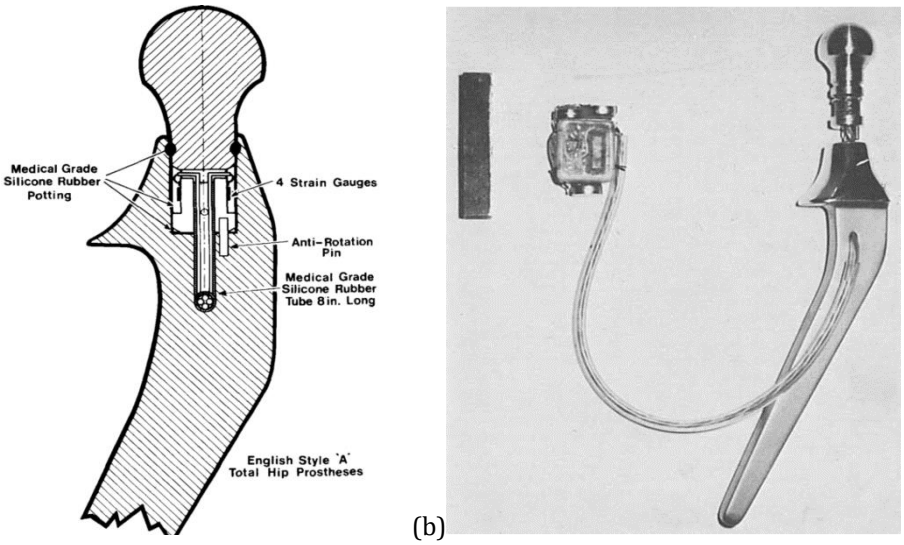

(a) (b)

Figure 2.38. (a) Cross-section view of the prosthesis (b) Complete instrumented prosthesis by Kilvington and Goodman [8].

In the early 1990s, Graichen and Bergmann developed a new instrumented hip implant due to a clinical problem, the high loosening rate of artificial hip joints [9]. Three semiconductor strain gauges with an NTC resistor were mounted in the neck of a hip prosthesis to measure three-dimensional forces and determine the temperature behaviour during the measuring process. The in-vivo measurement was performed and transmitted the measured signals using a four-channel telemetric transmitter, which powered inductively via the internal and external coil. A power of only 7 mW was required according to the low duty cycle (0.05) of the transmitter and the low power consumption of the sensor system.

The increase in the temperature in the hip implants during walking found from previous experiments led to consideration that risk of hip loosening may relate to the high implant temperature. Then, Graichen *et al* developed the eight-channel telemetry transmitter using a bipolar integrated circuit to function with multi-channel telemetry for temperature and load measurements [10]. Three strain gauges and 8 NTC resistors, as shown in Figure 2.39, were applied for in-vivo measurements. With that development, forces acting on prosthesis head and

temperature distribution within the implant were able to be monitored together in real time. The power consumption per a telemetry unit was about 10mW.

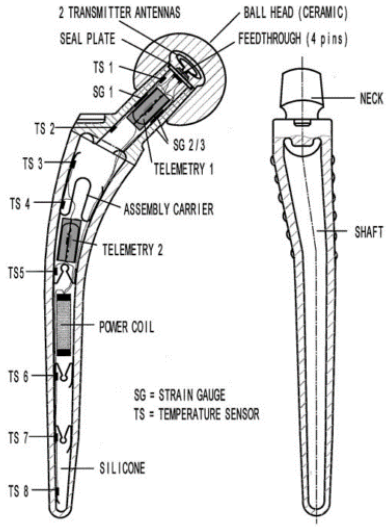

Figure 2.39. Cross-section schematic of instrumented hip implants by Graichen *et al* [10].

In 2007, further development of a new telemetry chip by [94] introduced an improved 9-channel telemetry transmitter with a programmable integrated circuit using BICMOS technology. More accurate measuring results, smaller dimensions, and less power consumption were provided. With this new telemetry system, Damm *et al* proposed another model of instrumented implant (Figure 2.40) to measure the 3-axis forces and moments between the head prosthesis and acetabular cup in-vivo using six semiconductor strain gauges [13]. Its ability to measure forces and moments acting within the joint was acceptable with an accuracy of 1.9% for forces and 1.5% for moments. The electronic instruments were powered inductively by the external magnetic field and required the power of only 5 mW for telemetry circuit.

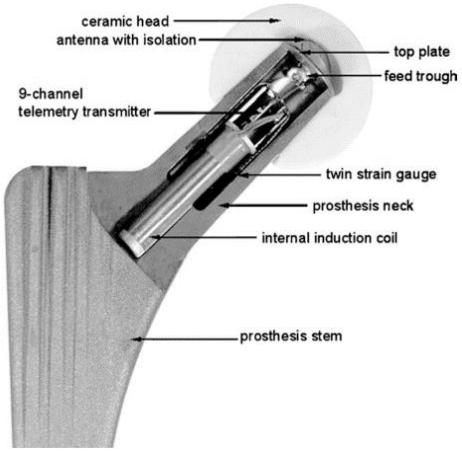

Figure 2.40. Model of the instrumented hip implant by Damm *et al* [13].

To detect implant loosening, an instrumented hip implant with vibration analysis technique was presented by Puers *et al* [12]. A miniaturise capacitive accelerometer and microcontroller circuits embedded in the prosthetic head (Figure 2.41) were used for in-vivo measurements to monitor the response of the prosthetic femur when applying mechanical vibrations to a femur bone. The mechanical interface between the prosthesis and the femur could be analysed for the risk of implant loosening. Similar to previous works, the method of inductive power link was selected to power the system which consumed a power of 22.5 mW.

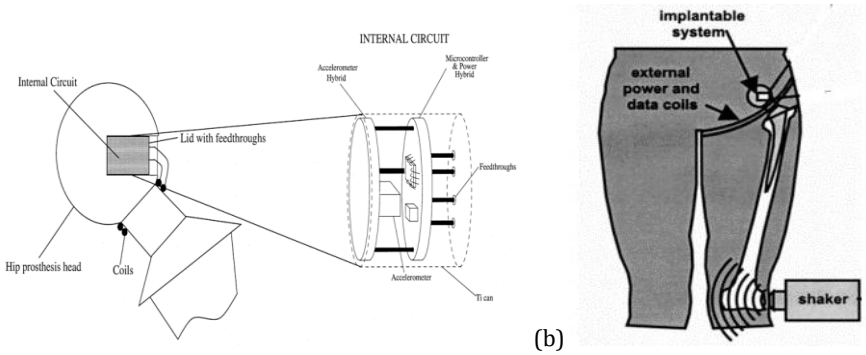

(a) (b)

Figure 2.41. (a) Model of the implantable system. (b) A system to detect hip prosthesis loosening [12].

In 2010, kinetic energy harvesting was introduced by Morais *et al* as a method for powering hip implants [95]. Motion-driven electromagnetic harvesting was the concept for the power source of their device. The prototype for this harvester is

illustrated in Figure 2.42. The movement of magnets inside a Teflon tube during the gait cycle induced an electric current in two coils which mounted around the tube. The maximum power obtained from the harvester was 1.53 mW with a 1000Ω load. For the first in-vitro experiment in 2010, the total energy stored in the capacitors was 1760μJ. It was enough to supply the instrumented system which required energy of about 825μJ over a period of 25 ms. Afterwards, the energy storage circuits were modified in 2011 resulting in higher usable energy up to 1912.5 μJ under normal walking conditions [96].

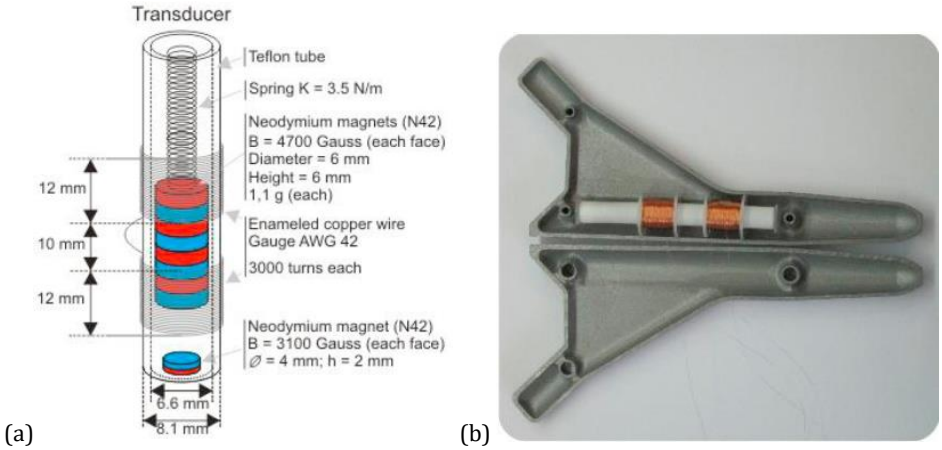

Figure 2.42. (a) Model of energy harvester. (b) location of harvester inside a hip prosthesis model [95].

An energy harvesting method was also proposed by Silva *et al* to power instrumented implants [3]. Three energy harvesting mechanisms were implemented on hip prosthesis: translation-based electromagnetic harvester, rotation-based electromagnetic harvester and piezoelectric harvester, as shown in Figure 2.43 [97], [98]. The amplitude movement and axial force occurring on the prosthesis during the human gait cycle were harvested to produce energy. The amount of power that can be harvested from each transduction concept was not mentioned in this paper. However, their device can enable operation of a Bluetooth protocol (BLE112 from Bluegiga) up to 50 seconds, and a specific communication protocol from Texas Instrument (SimpliciTi) up to 110s. Also, the translation-based generator was expected to be the most efficient transducer and generate the most power among these three proposed methods due to its larger

movement amplitude and larger relative movement velocity between magnets and coil.

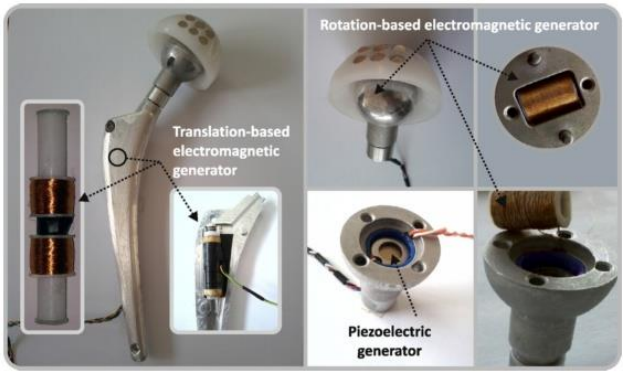

Figure 2.43. Three energy harvesting systems located in hip prosthesis prototype [98].

2.5.1 Discussion

A summary of the instrumented hip implants in the literature is provided in Table 2.8. In the literature, batteries, power induction systems and energy harvesting systems are presented to be a power source for the implants. Although batteries were selected for powering the instrumented implant at an early stage, their problems such as toxic hazards and low energy storage density [7] are not suitable for long-term applications. Considering that medical devices require high reliability [99], the use of batteries as a power source does not guarantee a long-term use of the instrumented implants. Also, the problem of power shortage may occur when using the battery-based supply system. According to the increase in the number of sensors, transducers and actuators to overcome the failure of hip implants [100], the system may require more energy to operate. Then, the inductive powering method has been proposed to be another option [9]–[13]. Although such problems from batteries are mitigated by using the inductive power links, the full-operation constraint of instrumented implants has been presented and yet to be addressed. The external component required for the inductive-powering supply system, i.e. the outer coil wrapped around the patient's thigh, the power oscillator, and the microcontroller system (data link) must exist nearby to monitor and process the data from sensor systems. This limits the activities of patients and not practical for home health monitoring [101].

Therefore, the studies of kinetic energy harvesting system are presented for powering instrumented hip implants as works by [95], [96], [98], [102]. Their in-vitro experimental results showed that such power supply system had high enough efficiency for powering their electronic implants. For in-vivo measurements, concerns have been raised which question the ability to generate sufficient power for the electronic implant. The poor mobility of patients appears to reduce the performance of kinetic energy harvesting system and lower the amount of energy harvested.

Table 2.8 Summary of recent instrumented hip implants

Features	Method for power supply	The instrumented implant requiring power supply	Components inside body	Components outside body	Test	Electric power needs/Available Energy
Carlson *et al.*, 1974 [7]	Inductive powering	• 14 pressure transducers • 16-channel telemetry device	• Secondary coil • Circuitry	• 100kHz power oscillator • primary coil	In vitro	500mW
Kilvington and Goodman, 1981 [8]	Batteries 3x1.35 V batteries (Duracell mercury WH 3T2)	• 4 strain gauges • FM transmitter system	• 3 batteries and 2 reed switches: outside prosthesis (inside transmitter system housing)	• Magnet	In vivo	not reported
Graichen and Bergmann, 1991 [9]	Inductive powering	• 3 semiconductor strain gauges • Thermistor NTC • 4-channel telemetric transmitter	• Secondary coil • Regulation systems	• 4kHz power oscillator • primary coil	In vivo	7mW
Graichen and Bergmann, 1999 [10]	Inductive powering	• 3 semiconductor strain gauges • 8 temperature sensors NTC • 2 eight-channel telemetric transmitter	• Secondary coil • Regulation systems	• 3.5-4.5kHz power oscillator • primary coil	In vivo	10mW
McGibbon *et al.* 1999 [11]	Inductive powering	• 13 semiconductor strain gauge • Thermistor • 16-channel telemetry device	• Secondary coil • Circuitry	• 100kHz power oscillator • primary coil	In vivo	not reported

Features	Method for power supply	The instrumented implant requiring power supply	Components inside body	Components outside body	Test	Electric power needs/Available Energy
Puers *et al.* 2000 [12]	Inductive powering	• capacitive accelerometer • microcontroller • 10-11.5MHz RF transmitter	• Secondary coil • Circuitry	• 750kHz power oscillator • primary coil	In vivo	22.5mW
Damm *et al.* 2010 [13]	Inductive powering	• 6 semiconductor strain gauges • NTC thermistor • 9-channel telemetric RF transmitter	• Secondary coil • Regulation systems	• power oscillator • primary coil	In vivo	5mW for telemetry circuit
Morais *et al.*, 2010-11 [95], [96]	Motion-driven electromagnetic harvesting	• RF transmitter • Circuitry	• Electromagnetic generator • Rechargeable battery	• 125kHz power oscillator • ASK receiver	In vitro	108.9μW or 1001.88μJ
Silva *et al.*, 2012-13 [97], [98]	• Motion-driven electromagnetic harvesting • Inductive powering • Piezoelectric harvesting	• RF transmitter • Circuitry	• 2 Electromagnetic generators • Inductive generator • Piezoelectric transducer • 2 supercapacitors	• 125kHz power oscillator • ASK receiver	In vitro	not reported

2.6 Summary

Instrumented hip implants have been developed for a period aiming to increase the longevity and success rate of hip replacement surgery. The sensor and monitoring system within the transmitting devices has been embedded in hip prostheses for these purposes. The batteries and inductive power links are used conventionally for powering the implanted systems, which are not entirely compatible with a patient's daily living activities. Then, energy harvesting devices have emerged to improve home healthcare technologies and offer a better quality of life for patients.

This chapter has investigated the feasibility of human-powered energy harvesting devices for hip implant applications. It has been shown that a huge amount of energy is contained within the human body, which can be harvested from movements during daily living activities. A large amount of power could be achieved from lower body locations, i.e. hip, knee, ankle, and heel strike due to the large displacement. To convert kinetic energy into electrical energy, three main transduction mechanisms can be used for a kinetic energy harvesting device, which are electrostatic, piezoelectric, and electromagnetic transducers. The high power density and longevity of electromagnetic energy harvesting devices with a low-cost design have made them an attractive choice for hip implant applications. However, the effect of size on the performance of electromagnetic energy harvesting devices is unavoidable. The volume constraints of hip prostheses has limited device design to being small-scale, which results in a reduction of device performance. Next, the strategies to increase the power generated have been studied, which are frequency up-conversion and bandwidth widening. According to the size limitations of the device, complex structures for frequency up-conversions and generator arrays are not an option. The more practical solution for this constraint is to employ nonlinear structures, which can be realised by using magnetic springs. Their larger bandwidth, due to the effect of shifting the resonant frequency, is preferable for the random excitation of human movements.

This is promising for an increase in the overall output power. However, the complicated mathematical modelling of nonlinear devices should be given careful consideration for practical design and implementation.

Chapter 3

Power from Hip Motion

3.1 Introduction

Kinetic energy harvesting from the human body uses motion associated with human activities to generate energy. Several transduction mechanisms, as mentioned in Section 2.3, have been employed to convert kinetic energy into electrical energy. According to Chapter 2. the magnetically levitated electromagnetic vibration energy harvesters include devices which are suitable for harvesting energy from the random motions of a human, which are characterised by high amplitude displacement with a broad range of low frequencies (<10 Hz). The nonlinear response of the harvesting system is promising for a wide operating bandwidth which potentially enhances the power output of the harvesting devices.

In this chapter, the general model of kinetic energy transduction is studied first to define the parameters that influence the harvested energy. Vibration spectra containing information of frequency and level of acceleration during walking and running are analysed. Different models of harvesting devices are studied concerning the acceleration of hip movements during walking, to validate the suitability of nonlinearities for the purposes of a hip-implant energy harvesting device.

3.2 Kinetic energy harvesting

The kinetic energy harvester is typically modelled as a conventional second-order spring and mass system, as in Figure 3.1.

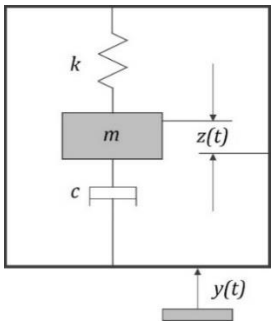

Figure 3.1 Model of the second-order spring-mass system [70].

The system consists of a seismic mass, m, attached to a spring of stiffness, k. The damping coefficient, c, represents total energy losses within the system containing parasitic losses, c_p, and electrical loss, c_e. The governing equation describing the motion of the system is given by [70]

$$m\ddot{z}(t) + c\dot{z}(t) + kz(t) = mg - m\ddot{y}(t) \tag{3.1}$$

where *z(t)* is the relative displacement of the seismic mass and the base, and the vibration displacement *y(t)* is the input to the system exciting a movement of the mass. The steady state solution for relative displacement, *z(t)*, is

$$z(t) = Zsin(\omega t - \phi) \tag{3.2}$$

where

$$Z = \frac{\omega^2 Y}{\sqrt{\left(\frac{k}{m} - \omega^2\right)^2 + \left(\frac{c\omega}{m}\right)^2}} \tag{3.3}$$

with the phase angle

$$\phi = \tan^{-1}\left(\frac{c\omega}{(k - \omega^2 m)}\right) \tag{3.4}$$

The natural frequency of the system ω_n is defined as

$$\omega_n = 2\pi f = \sqrt{k/m} \tag{3.5}$$

The instantaneous power dissipated in the damper is

$$P_{d\ (inst)} = c(\dot{z}(t))^2 = c\omega^2 Z^2 \cos^2(\omega t - \phi) \tag{3.6}$$

The harvested energy per cycle is

$$E = \int_{t=0}^{T} c(\dot{z})^2\, dt = c\omega^2 Z^2 \int_{t=0}^{T=2\pi/\omega} \cos^2(\omega t - \phi)\, dt = \pi c \omega Z^2 \tag{3.7}$$

where $T=2\pi/\omega$. The average power dissipated within the damper is

$$P_d = \frac{E}{T} = \frac{c\omega^2 Z^2}{2} \tag{3.8}$$

Substituting (3.3) and writing in near dimensionless form, it results

$$P_d = \frac{m\zeta Y^2 \left(\frac{\omega}{\omega_n}\right)^3 \omega^3}{\left[1 - \left(\frac{\omega}{\omega_n}\right)^2\right]^2 + \left[2\zeta\left(\frac{\omega}{\omega_n}\right)\right]^2} \tag{3.9}$$

where the total damping ratio $\zeta=c/2m\omega_n$. In the condition that the excitation frequency matches the natural frequency of the system, $\omega=\omega_n$, the power dissipated can be simplified to (3.10) and maximum power can be attained.

$$P_d = \frac{mY^2\omega^3}{4\zeta} \tag{3.10}$$

According to the proportion of the acceleration levels, A, and the displacement amplitude of the excitation, Y, in a natural frequency, $A=\omega^2 Y$. Equation (3.10) can be rewritten as

$$P_d = \frac{mA^2}{4\omega^3\zeta} \tag{3.11}$$

As aforementioned, the power dissipated in the damper is influenced by the mass, the external excitation, and the system damping. For practical devices, the amount of power flowing into the device is limited by the relative displacement of the moving mass to its housing. The maximum power is achieved when the moving-mass displacement is at its maximum value. The damping ratio has contributed to

maintaining the maximum displacement of the moving mass. For example, for small excitation forces, low damping will result in large displacement which leads to larger harvested power. If a large excitation force is applied, the displacement of moving mass could be controlled within its allowable displacement value by controlling its damping. This potentially leads to maximum power absorbed from the environment. In the case of miniaturised devices, the maximum displacement is small. Thus, the damping of the small devices should allow the displacement amplitude of moving mass to approach its maximum value, which leads to the maximum harvested power. Also, matching the natural frequency of the devices with the excitation frequency will maximise harvested power according to Eq. (3.9). To design the harvesting devices for the low-frequency excitation of human motion will be a challenge due to the design constraints of harvester size, which makes it difficult to achieve a very low natural frequency.

Note that the harvestable power mentioned in this chapter is the power flowing from the environment into the device. The power delivered to the electrical load will be discussed in Chapter 4 and is subject to further constraints.

3.3 Theoretical background of a nonlinear harvesting device

The harvesting devices characterised by nonlinear structure using a magnetic spring have been presented as a promising approach to harvest energy under intermittent excitation such as human motion. The power can be harvested over a larger bandwidth due to the effect of hard/soft spring on the dynamic behaviour of the systems. The equation of motion in Eq. (3.1) is applied to the nonlinear behaviour of the spring force, F_s, using Duffing's equation which given by

$$F_s = k_1 z(t) + k_3 z^3(t) \tag{3.12}$$

where k_1 and k_3 are linear and nonlinear spring stiffness respectively. Then, the equation described the motion of the nonlinear system can be written as

$$m\ddot{z}(t) + c\dot{z}(t) + k_1 z(t) + k_3 z^3(t) = mg - m\ddot{y}(t) \tag{3.13}$$

The spring force given in Eq. (3.13) using Duffing's equation describes the nonlinear behaviour of the harvesting devices. With the hard-spring effect, which has a positive cubic nonlinearity ($k_3>0$) in Eq. (3.13), the bandwidth increases as the frequency increases. On the other hand, the soft-spring effect, which has a negative cubic nonlinearity ($k_3<0$) in Eq. (3.13), is characterised by an increase in bandwidth with decreasing frequency. The variation of the resonant frequency as a function of amplitude is shown in Figure 3.2. The bandwidth is broadened in one direction, i.e. shifting to the right or shifting to the left, for hardening or softening nonlinearity respectively.

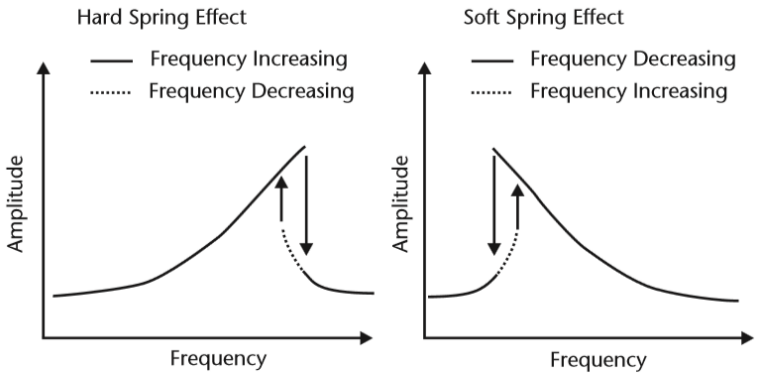

Figure 3.2 The effect of hardening and softening nonlinearities [107].

According to the broadband frequency spectrum of human motion, multi-degree-of-freedom harvesters are introduced to achieve wider bandwidth for enhancing harvester performance [86], [108]–[110]. The multiple degrees of freedom system are illustrated in Figure 3.3.

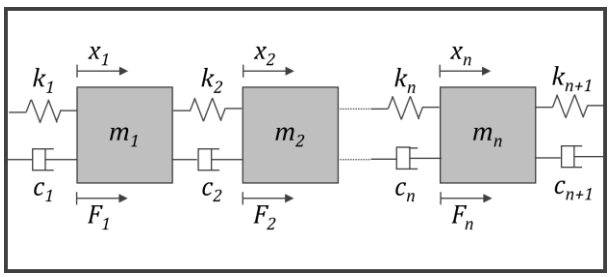

Figure 3.3 A n-DOF spring-mass-damper system.

More than a single resonant frequency can be obtained by using two or more vibrating masses, *m*. There are *n* resonant frequencies in the response of a n-degree-of-freedom (n-DOF) system [111]. Each resonant frequency has its own mode shape and can be tuned close to each other which results in a wide resonant bandwidth and displacement amplification.

3.4 Evaluation of hip-motion signal

How to design the electromagnetic vibration energy harvester for hip implant applications, and the energy sources, i.e. hip motion during walking and running, are studied in this section. Their general information such as the vibration spectra containing information of frequency and the acceleration level are analysed. Then, the maximum displacement of the inertial mass and the available power are simulated regarding the different harvesting models. Information obtained here will be applied to optimise the design of the electromagnetic vibration energy harvester in Chapter 4.

3.4.1 Frequency responses

In this section, analyses were divided into two parts based on the sources of collected data, which are from hip-replacement patients and non hip-replacement patients. The collected data was processed in Matlab by applying Fast Fourier Transform (FFT) for frequency domain analysis. Then, the frequency components could be investigated. Matlab code for FFT is provided in Appendix A.

3.4.1.1 Hip-replacement patients

The frequency responses of the patients' hip movement during gait cycles (free walking) were analysed with the data of contact forces acting on the acetabular ball of hip prostheses. The Orthoload team [103] collected this hip forces data by using the instrumented hip implants (reviewed in Chapter 2 [10], [13], [94]) for in-vivo measurements. There are 27 data sets from a group of six hip-replacement patients. An example of numerical and video data is provided in Appendix B. The

measured signal was sampled 250 times in a second. The duration of the signal is 3s. Figure 3.4 shows the spectra of the hip-motion signal analysed from the contact force data of one patient (data set of kwr0250b). Spectra of all 27 datasets are provided in Appendix C. The main parameters of the FFT are defined as the number of samples acquired = 750 and the frequency resolution = 0.33.

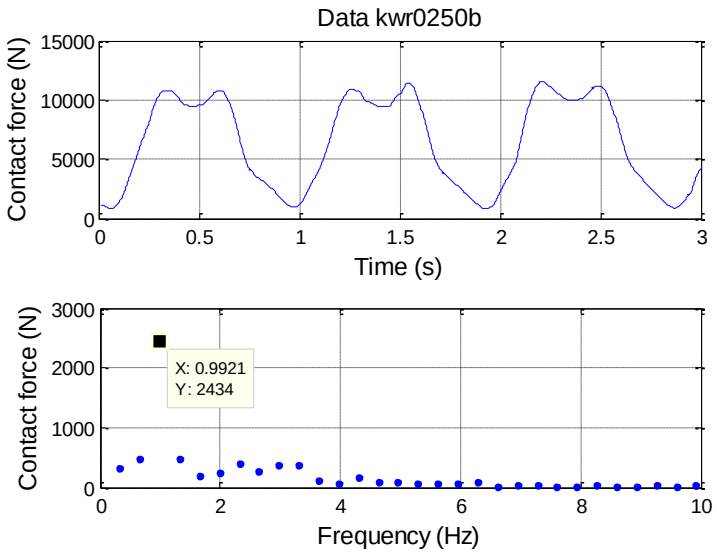

Figure 3.4 The spectra of hip motion during walking analysed from the data set of kwr0250b.

As can be seen in Figure 3.4, the movements of the hip during walking consists of several frequency components. The frequency spectra shows that the energy is contained in the low-frequency range (below 5 Hz). The dominant frequencies and average contact forces on the hip prosthesis of patients during walking are summarised in Table 3.1. An average of the dominant frequencies is 0.91 Hz calculated by ignoring the frequency which associates the patient stumbles (kwrwn2, pflwfs and pflwn1). The average contact force on the femoral head of the hip prosthesis is about 1814 N when walking.

Table 3.1 Analysed data of walking hip motions from 6 patients.

Data sets	Body weight (N)	Dominant frequency (Hz)	Average contact force (N)
kwr0140d	690	0.974	1559
kwr0641b	702	1.078	1383
kwr0641c	702	0.992	1390
kwr0340b	740	0.815	1576

Data sets	Body weight (N)	Dominant frequency (Hz)	Average contact force (N)
kwr0250b	720	0.992	1606
kwrwn2	700	0.623	1771
pfl0692b	1010	1.211	2374
pflwfs	970	1.374	2115
pflwn1	980	1.866	2205
rhr0117c	600	0.841	1452
rhr0530a	700	0.957	1820
rhr0191a	600	0.852	1692
rhr0449a	700	0.866	1848
ebl5078a	610	0.9415	1922
ebl4425a	650	1.106	1599
ebl4435a	650	1.312	1671
jb5101a	490	0.734	1882
jb5128d	490	0.713	1534
jb4535a	510	1.147	1780
ibl440b	800	0.659	2048
ibl303a	800	0.794	1920
ibl303b	800	0.804	2056
ibl659b	800	0.61	2064
ibl612a	800	0.892	2072
ibl216b	800	0.669	1920
ibl735b	820	0.868	2189
ibl482c	840	0.888	2192
	Average	**0.905**	**1814**

3.4.1.2 Non hip-replacement patients

Acceleration data was also collected from 22 non hip-replacement patients by instrumenting the wireless tri-axial accelerometer at the hip ideally located above the top of the femur as in Figure 3.5 [104]. The measured signal was sampled 128 times in a second. The duration of the signal is 30s. The set of acceleration data was analysed by Matlab to investigate the frequency components during free walking and running on a treadmill. An example of analysis results is shown in Figure 3.6. Spectra of all 22 datasets are provided in Appendix C. The FFT

parameters are defined as the number of samples acquired = 3840 and the frequency resolution = 0.033.

Figure 3.5 The wireless tri-axial accelerometer mounted on the hip [104]

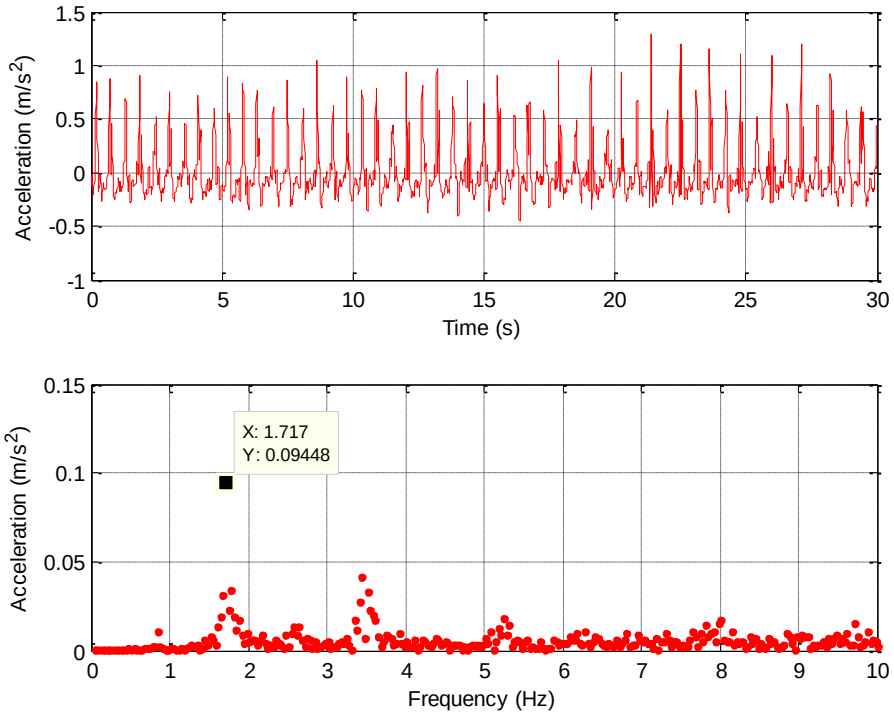

(a)

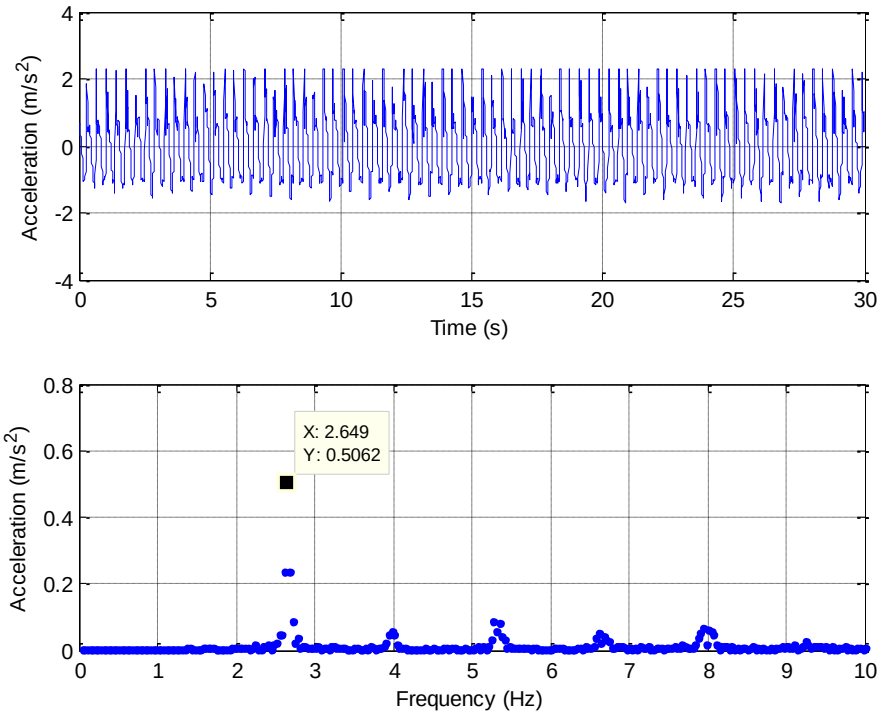

(b)

Figure 3.6 An example of acceleration data and frequency response during (a) walking and (b) running analysed by Matlab.

The dominant frequencies of hip movement during walking and running of 22 non hip-replacement patients are plotted in Figure 3.7. It is apparent that the dominant walking frequencies are scattered in the range of 1.5 - 2 Hz, while the dominant running frequencies (2.5-3.5 Hz) are roughly twice the walking dominant frequencies. Table 3.2 summarises the dominant frequencies and accelerations of non hip-replacement patients during walking and running. It shows that the acceleration levels of the dominant frequency of hip movements are about 0.06 m/s^2 peak (≈0.01$\boldsymbol{g}$) during walking and 0.48 m/s^2 peak (≈0.05$\boldsymbol{g}$) during running.

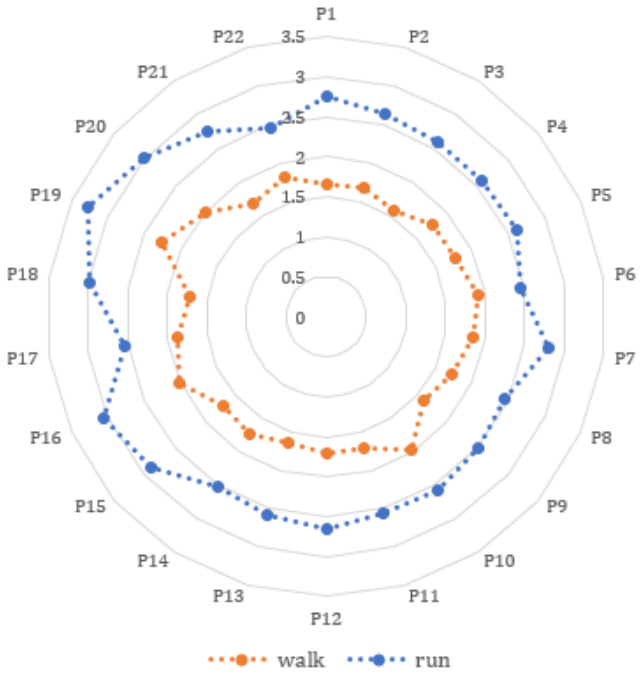

Figure 3.7 The dominant frequencies during walking and running of 22 non hip-replacement patients.

Table 3.2 The acceleration levels of 22 non hip-replacement patients during walking.

Data	Walking			Running		
	Frequency	Acceleration level (m/s^2)		Frequency	Acceleration level (m/s^2)	
	(Hz)	RMS	Peak	(Hz)	RMS	Peak
P1	1.65	0.028	0.040	2.75	0.44	0.62
P2	1.68	0.026	0.037	2.65	0.36	0.51
P3	1.58	0.028	0.039	2.58	0.31	0.43
P4	1.75	0.023	0.032	2.58	0.35	0.50
P5	1.78	0.023	0.033	2.62	0.41	0.58
P6	1.92	0.043	0.061	2.45	0.45	0.63
P7	1.85	0.059	0.083	2.82	0.33	0.47
P8	1.72	0.067	0.094	2.45	0.24	0.34
P9	1.62	0.030	0.042	2.52	0.35	0.50
P10	1.98	0.111	0.158	2.58	0.35	0.50
P11	1.72	0.034	0.048	2.55	0.23	0.33
P12	1.72	0.031	0.043	2.65	0.35	0.50
P13	1.65	0.019	0.026	2.58	0.24	0.33
P14	1.75	0.065	0.092	2.52	0.33	0.47
P15	1.72	0.033	0.047	2.88	0.43	0.61
P16	2.02	0.040	0.057	3.05	0.39	0.54
P17	1.88	0.061	0.086	2.55	0.50	0.71

Data	Walking			Running		
	Frequency (Hz)	Acceleration level (m/s²)		Frequency (Hz)	Acceleration level (m/s²)	
		RMS	Peak		RMS	Peak
P18	1.72	0.038	0.054	2.98	0.24	0.35
P19	2.25	0.123	0.174	3.28	0.49	0.69
P20	1.98	0.039	0.056	3.02	0.30	0.43
P21	1.68	0.027	0.038	2.75	0.19	0.27
P22	2.48	0.017	0.024	2.35	0.25	0.35
Average	**1.82**	**0.044**	**0.062**	**2.69**	**0.34**	**0.48**

3.4.2 Power harvested from the harvesting devices

The usable power harvested from hip motion is estimated using Matlab Simulink by considering the three types of spring-mass harvesting devices as in Figure 3.8, namely the linear model (LM), the symmetrical nonlinear model (SNM), and the asymmetrical nonlinear model (ANM). The harvesting systems using the mechanical spring and the magnetic spring are described by the linear model and the nonlinear model, respectively. The symmetrical nonlinear model is the model in which the inertial mass experiences magnetic-spring forces from both ends. The asymmetrical nonlinear model' is the model in which the magnetic-spring force is applied from the bottom end only. In this section, power available provided by these three mentioned models is analysed.

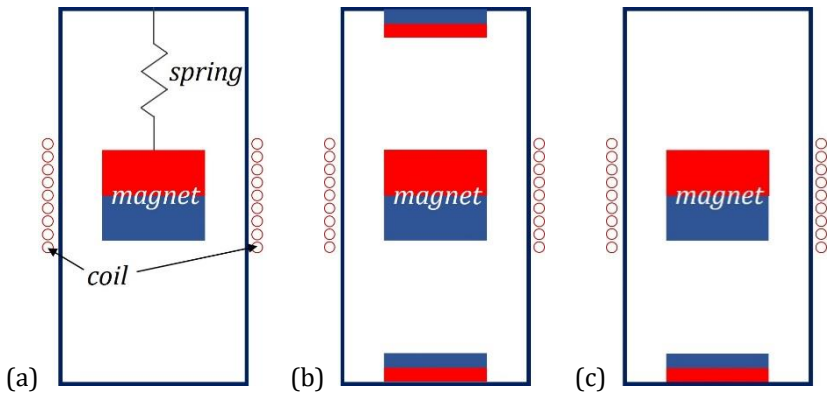

Figure 3.8 The spring-mass harvesting systems as (a) the linear model, (b) the symmetrical nonlinear model, and (c) the nonlinear asymmetrical model.

The Simulink model in Figure 3.9 has been developed based on Eq. (3.13) to estimate available power in the systems. To analyse LM which is governed by the equation of motion in Eq. (3.1), the nonlinear stiffness k_3 in the model is set to zero. The input of the model is the excitation acceleration of hip movements in time domain during the walking of non hip-replacement patients, as presented in Section 3.4.1.2. The relative displacement, *z(t),* can be obtained by integrating the displacement velocity, *ż(t)*. According to Eq. (3.6), the power dissipated in the damper can be estimated by multiplying the dot product of the displacement velocity and the damping coefficient, *c*. The simulation parameters are in Appendix F.

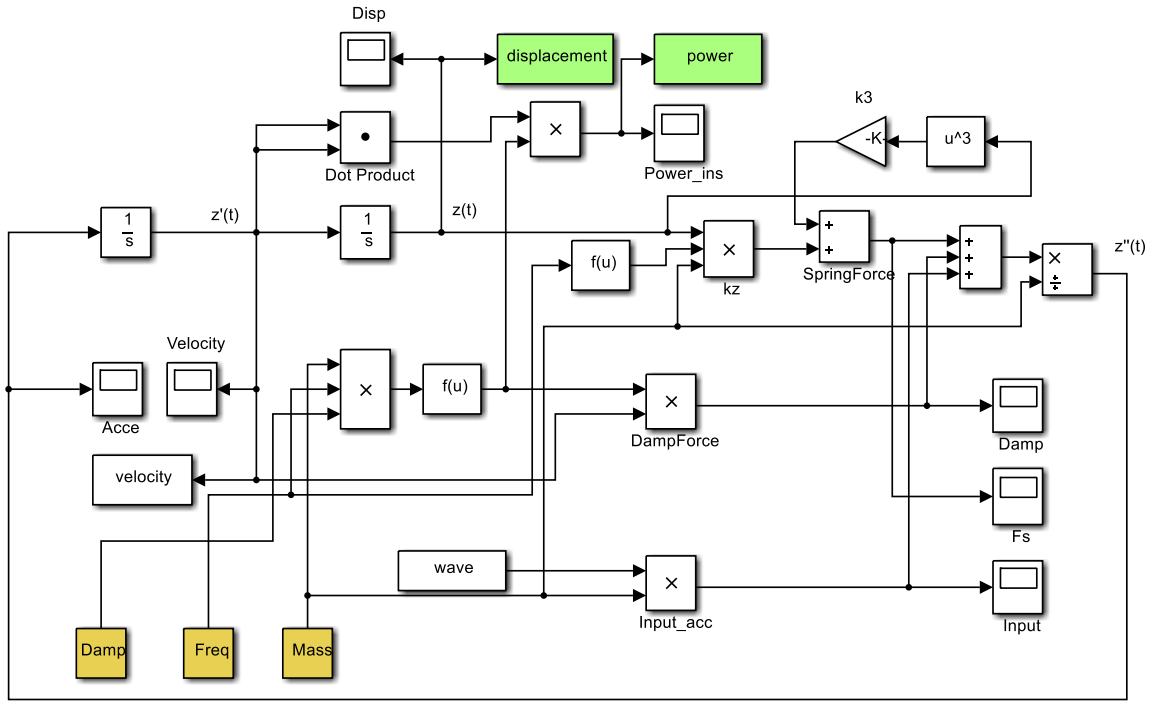

Figure 3.9 The Simulink modelled for power and displacement estimation.

3.4.2.1 Linear harvesting model

The results simulated by Simulink model are presented in Figure 3.10 and Figure 3.11. The simulation results show that the maximum displacement amplitude of the moving mass is at the frequency of 2 Hz (Figure 3.10) as well as the maximum power dissipated in the damper (Figure 3.11). This correlates with the dominant frequencies of the non hip-replacement patients during walking, about 1.79 Hz.

The results also show that the weight of moving mass influences the amount of power harvested. Increasing weight of moving mass increases the output power (Figure 3.11a). The increasing damping ratio results in the decrease in the moving-mass displacement (Figure 3.10), and hence decreases the power harvested (Figure 3.11b).

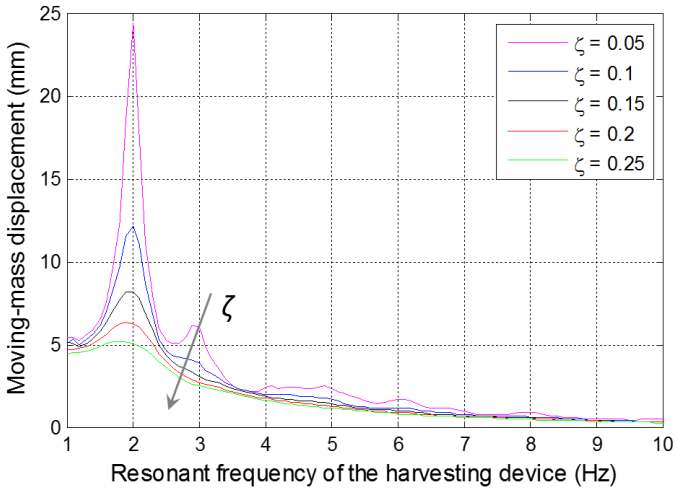

Figure 3.10 The maximum moving-mass displacement of LM during hip movements with various damping ratio.

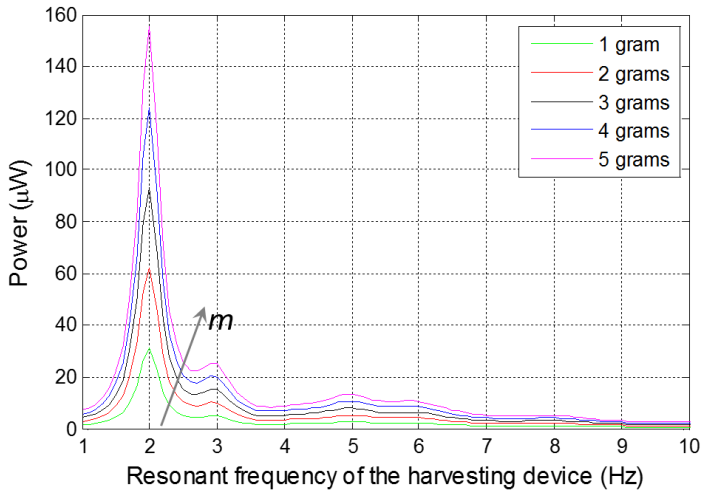

(a)

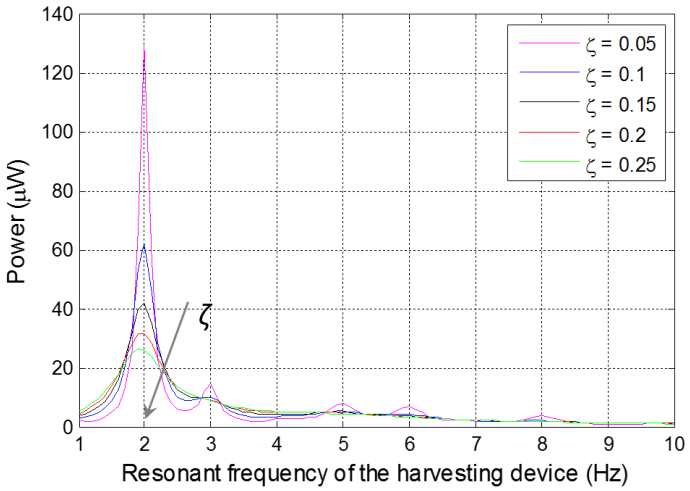

(b)

Figure 3.11 The power available of LM during hip movements with (a) various moving-mass weight at fixed ζ=0.1 and (b) various damping ratio when the mass weight is 2 grams.

For LM, maximum power can be harvested from the hip movements when the resonant frequency of the harvester matches the natural frequency of the excitation signal. If the linear harvester operates out of the frequency range of the excitation signal, the harvested power is significantly lower. However, the harvester designed for operating at the low frequency (about 2 Hz) might become rather bulky for human-powered energy harvesting devices according to Eq. 3.5.

3.4.2.2 Symmetrical nonlinear harvesting model

The effect of nonlinearities on the frequency response of the harvesting devices is studied in this section. Nonlinearity offers the advantage of wider bandwidth which suits the wide frequency range associated with the hip movements. SNM is simulated by the Simulink for the potential harvestable power compared with LM.

For SNM, the moving mass will suddenly experience strong magnetic forces when moving close to the top and bottom magnets. The variations of the magnetic force with the displacement are illustrated in Figure 3.12.

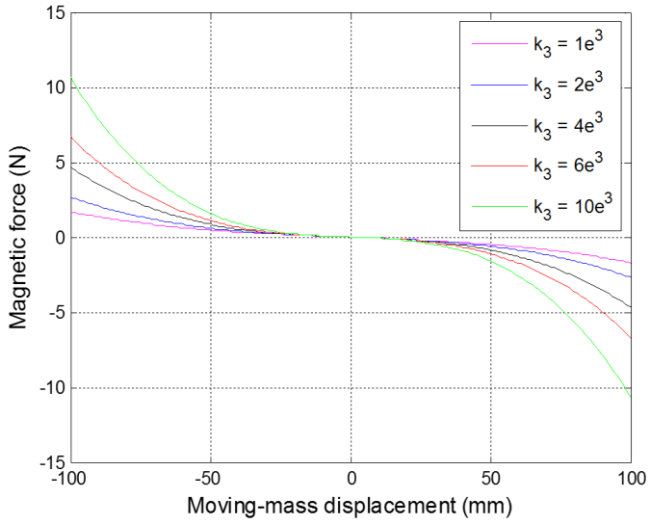

Figure 3.12 The magnetic force on the moving magnet versus the displacement modelled for the SNM.

Figure 3.12 shows that the magnetic force increases as the moving mass approaches the fixed top and fixed bottom magnets. Furthermore, it is clear that the magnetic force increases with the rising of nonlinear stiffness, k_3. The moving mass used for the simulation is 2 grams with a damping ratio of 0.1. The input for the model is the acceleration of hip movements during walking, the same as used in LM. The linear resonant frequency, k_1, was fixed at 2 Hz. The results are presented in Figure 3.13 with the different nonlinear stiffness, k_3=1e^3 N/m^3 to k_3=10e^3 N/m^3.

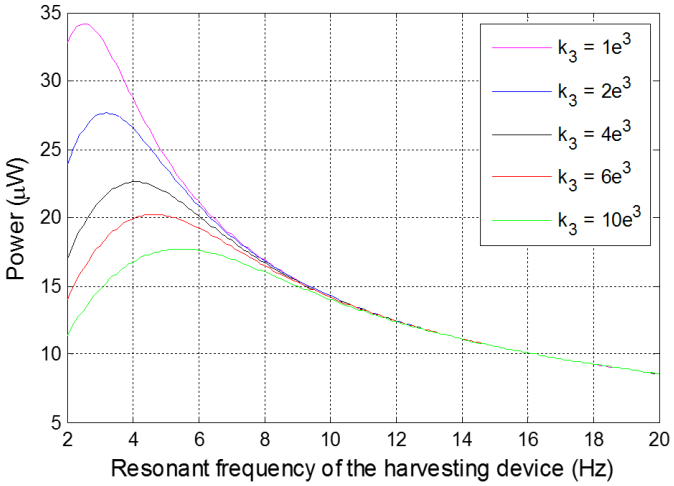

(a)

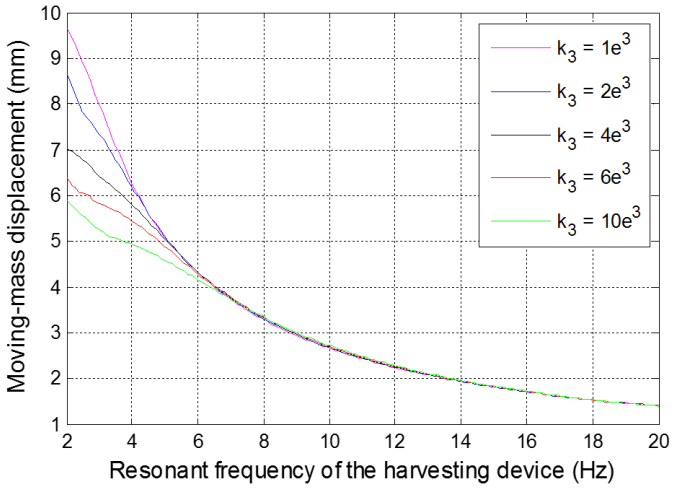

(b)

Figure 3.13 Analysed results of the SNM at fixed ζ=0.1 and *m*=2 grams: (a) the harvestable power and (b) the relative displacement of seismic mass from the hip movements during walking SNM.

Figure 3.13a shows that the effect of the nonlinearities increases with the increasing k_3, which results in the wider bandwidth of the harvesting device but with a lower peak of power response. The maximum power harvested is not at the same dominant frequency of hip movements (2 Hz). It is shifted from the frequency of 2 Hz due to the influence of nonlinearities. Figure 3.13b shows that the displacement amplitude of the moving mass is high at the low resonant frequency, and decreases with the increasing resonant frequency of the harvesting device.

Compared with LM, the frequency bandwidth of SNM is wider than that of LM, but the peak is lower because the maximum displacement of the moving mass is suppressed as the magnetic force gets stronger when the moving mass moves closer to the front ends of the device. For a given resonant frequency, the maximum moving-mass displacement of SNM is lower than that of LM. The increased bandwidth of SNM may not result in more available power compared to the peak of power response in the linear model. Note that the comparison of LM and SNM are based on the same simulation parameters, i.e. the damping ratio and the linear stiffness, in order to investigate their characteristic behaviour. For a given external excitation, the same maximum power as obtained from a linear

harvesting device is also possible for the nonlinear harvesting device by optimising the linear stiffness and the load resistance [105], [106].

3.4.2.3 Asymmetrical nonlinear harvesting model

As reported previously, the device with LM can harvest the largest amount of power from hip movements when its resonant frequency is matched with the walking dominant frequency (2 Hz), but a large-scale harvesting device has to be designed to achieve this low resonant frequency. If the resonant frequency of the harvesting device with LM does not match the dominant frequency of the hip movements, the generated power is significantly decreased. The harvesting device with SNM operates over a wide range of frequency due to nonlinearities. This implies that more power could be harvested even when the resonant frequency of the device does not match the dominant frequency of the hip movements. However, the maximum power harvested by SNM is smaller compared with that harvested by LM. Then, the harvesting device with ANM is studied.

A performance comparison between SNM and ANM was performed using the condition of the harvester size constraints. The maximum moving-mass displacement was limited up to 7 mm. SNM which has the k_3=4e^3 N/m^3 (black line in Figure 3.13) was chosen for a comparison. Its maximum power harvested (22.6 μW) from walking was at a resonant frequency of 4.1 Hz with a maximum displacement of 5.8 mm. For ANM, the change of the magnetic forces with the moving-mass displacement is different from the magnetic-forces profile of SNM. The moving mass of ANM experiences a repulsive force only from the bottom end and relies on gravity when it moves far apart from the equilibrium. The magnetic-force profiles of SNM and ANM is presented in Figure 3.14.

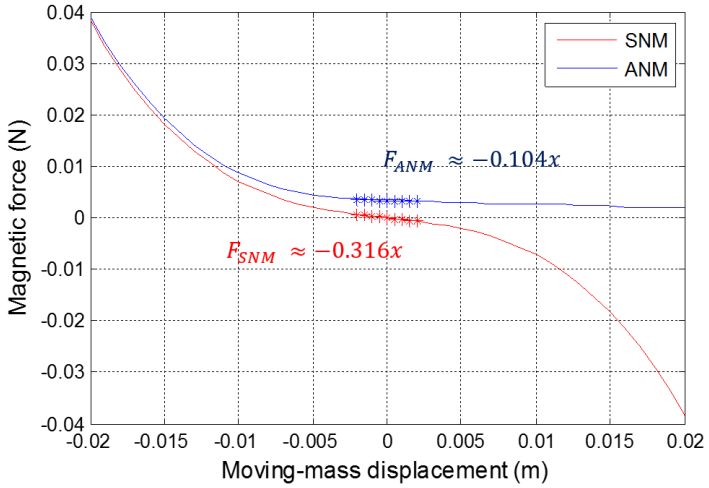

Figure 3.14 The magnetic force on the moving magnet (m=2 grams) versus the displacement of SNM and ANM.

Removing the fixed top magnet of SNM results in a continuous decrease in the magnetic force on the moving mass when it moves away from the bottom fixed magnet, as shown in Figure 3.14 (blue line). The resonant frequencies of SNM and ANM were approximated using the curve fitting:

$$F = kx \tag{3.14}$$

where F is the magnetic force on the moving mass and x is the moving-mass displacement. Using (3.5), the resonant frequencies of SNM and ANM are about 4 Hz and 2.3 Hz respectively. The force profile of both models (Figure 3.14) was applied in the simulation to investigate the power generated and the moving-mass displacement under the hip movement during walking. The results are presented in Figure 3.15.

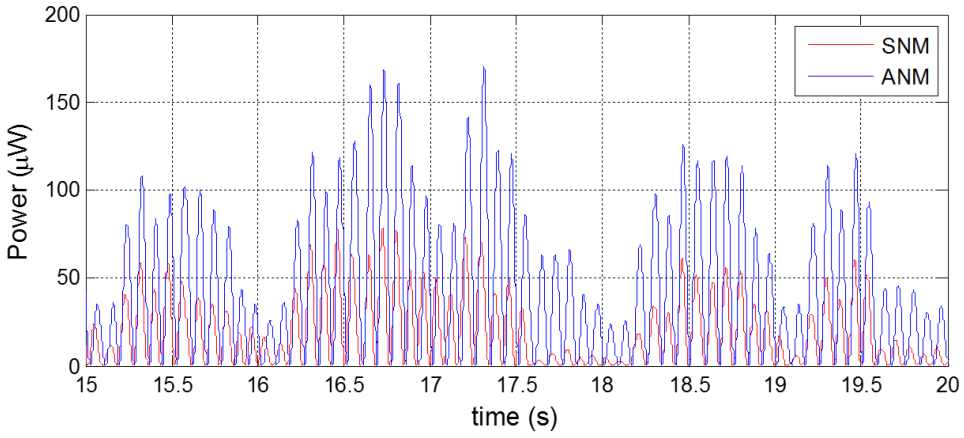

(a)

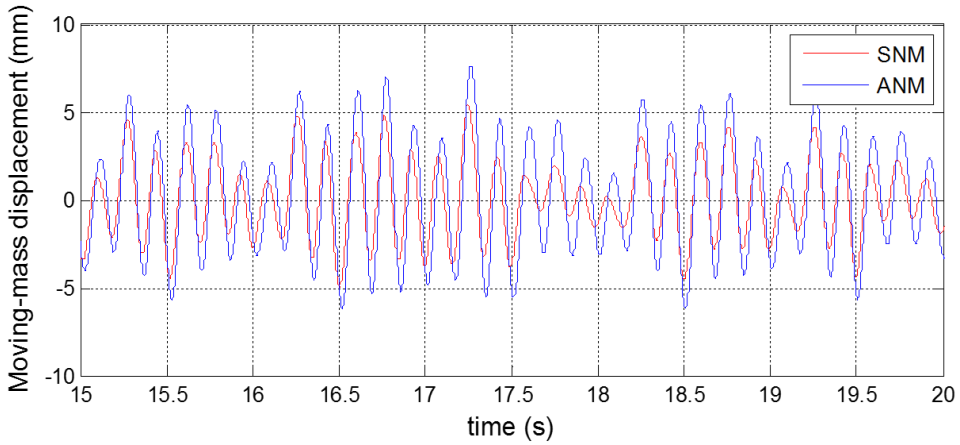

(b)

Figure 3.15 Analysed results compared between SNM and ANM (a) the instantaneous power harvested from hip movement and (b) the relative displacement of seismic mass during hip movements.

Figure 3.15 shows the instantaneous power and the moving-mass displacement of SNM and ANM over a period of time. The average power generated and the maximum displacement were calculated to be 22.6 μW and 6 mm for SNM, and 42.3μW and 7 mm for ANM. Without magnetic force from the top fixed magnet, the moving-mass displacement increases due to the reduction in the effective spring stiffness and hence the resonant frequency is decreased. The higher the maximum displacement of the moving mass and the lower the operating frequency explain the larger power harvested in comparison with SNM. Then, to harvest energy from a broadband low-frequency environmental vibrations within the condition of volume constraints, ANM is thought to be the most suitable for the hip-implant energy harvesting device.

3.5 Summary

After analysing data from hip movements during walking and running, it is found that excitation frequency ranges between 0.5 and 5 Hz. Overall, the analysed results show that the dominant frequency range of hip movements during walking and running is below 5 Hz. This implies that most of the harvestable energy is contained in this frequency range. Therefore, the operating frequency of the harvester should be designed to cover this frequency range for maximum power.

The linear and nonlinear models of energy harvesting systems are established using Matlab Simulink to study their performance in terms of output power and mass displacement. For the linear model, the analyses show that the matching between the excitation frequency and the resonant frequency of the harvester results in the maximum harvested power. However, larger harvesters have to be designed for the low excitation frequency of human body motions, which is not for implantable devices. Outside the operating frequency range, the performance of the linear energy harvester will be significantly worse, i.e. power harvested is significantly decreased. Then, nonlinear devices can be considered to take advantage of their nonlinear effects, normally exhibiting a wide range of operating frequency.

For the nonlinear harvesting device, the power can be harvested over a wide bandwidth of frequencies due to the effect of shifting the resonant frequency. Low operating frequencies are possible within a small volume of the harvesting device due to the nonlinear restoring force of the magnetic spring. Although the wide bandwidth may result in the reduction of the maximum power harvested, there is feasibility in improving the harvested power by designing the harvesting device with asymmetric nonlinear structures, optimising the linear stiffness and the load resistance matching.

Chapter 4

Harvester Mechanical Design

4.1 Introduction

The designing of a kinetic energy harvesting device for hip implant applications is a challenge due to volume constraints and the low operating frequencies required. The nonlinear structure studied in Chapter 3 has the potential to overcome such difficult challenges. The nonlinear harvester is able to work under a broad range of frequencies, which is suitable for the frequent change in excitation frequency associated with human motion. In this work, a magnetic spring instead of a conventional spring is used. Such a structure will eliminate mechanical fatigue issues and make it easier to achieve a low resonant frequency within a small device volume [112].

This chapter presents the two configurations of magnetically levitated electromagnetic vibration energy harvesters which are the single-magnetically levitated harvester (SMH) and the coupled-magnetically levitated harvester (CMH). The nonlinear effect introduced by these harvesters is expected to have broader bandwidth, which is a benefit regarding harvesting performance. In an attempt to lower the operating frequency range of the device, CMH is proposed for comparison with SMH. Their dynamic behaviour is studied, aiming to determine the most suitable structure for hip implant energy harvesting. An overview of the harvesters is provided in Section 4.2 and followed by discussion of design parameters including harvester volume, moving-mass configuration, spacer thickness, and coil specification. Mathematics and mechanical models with the frequency characteristics of the harvesters are provided in Section 4.4 and 4.5.

4.2 Design structure overview

The structures of SMH and CMH are shown in Figure 4.1. For CMH, the two movable magnets are arranged in a Borosilicate glass tube with likepoles facing each other and levitated by the bottom fixed magnet. The top levitated magnet set (M_1) consists of two 4 mm-diameter NdFeB cylindrical magnets with a ferromagnetic spacer placed between them to concentrate magnetic flux, and two cylindrical Tungsten pieces (1 mm in thickness). All the components are glued together. The bottom levitated magnet set (M_2) consists of an NdFeB cylindrical magnet and two 4 mm-diameter cylindrical Tungsten pieces (1 mm in thickness). The tube is 20 mm in length with an outer diameter of 7 mm. Two coils wound from 30μm-diameter enamelled copper wire are wrapped around the outside of the glass tube at positions near each movable magnet set. Teflon tape of 0.1 mm thickness is wrapped around the movable masses to reduce the friction between the masses and the inner surface of the tube. The bumpers made from crepe rubber are glued at the inner surface of the top lid, at the bottom of the M_1, and at the top surface of the fixed magnet to mitigate destructive impacts between the moving masses and top/bottom of the tube. The voltage will be induced in coils due to the magnetic flux change created by the oscillating magnets. For SMH, its structure is almost the same as CMH apart from that it does not have the bottom magnet set M_2 and the bottom coil.

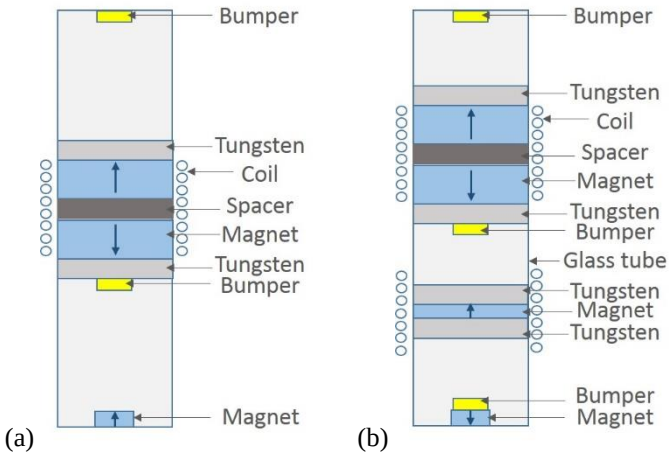

Figure 4.1. Structure of (a) SMH and (b) CMH.

The harvesters are characterised by the parameters listed in Table 4.1, which are obtained from Section 4.3. The component parameters such as the thickness of magnets to form a moving mass, the coil length, and the position of the coil have been investigated in that section given the size constraints of the harvester. The fabricated harvesters are shown in Figure 4.2.

Table 4.1 model parameters of SMH and CMH

Parameter	Value	Unit
Housing length, L_H	21	mm
Glass tube length, L_T	20	mm
Coil length, L_C	5	mm
Length of M_1, L_{M1}	13.4	mm
Length of M_2, L_{M2}	2.5	mm
Moving mass, M_1	1.52	g
Moving mass, M_2	0.59	g
Moving mass of SMH	1.53	g
Volume of SMH	0.829	cm^3
Volume of CMH	0.887	cm^3

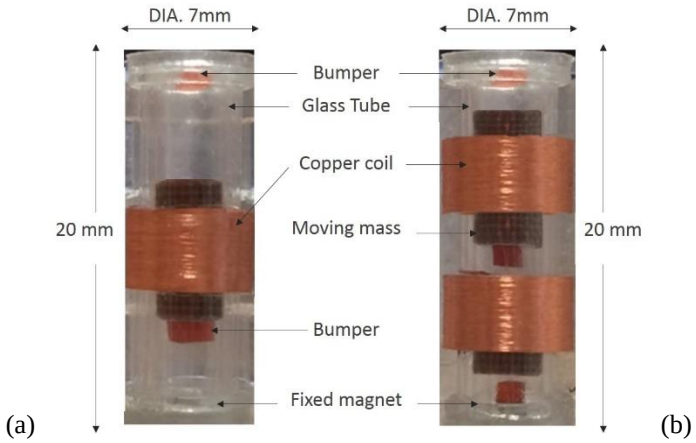

Figure 4.2. Fabricated electromagnetic-based harvester of (a) CMH and (b) SMH.

4.3 Optimal design parameters

4.3.1 Harvester volume

The prototype of the harvesters shown in Figure 4.2 is designed to be 2 cm in length with a diameter of 7 mm due to the volume constraints of the hip prosthesis

presented in Figure 4.3. The volume of the harvesters proposed does not affect the strength of the entire hip prosthesis according to the simulation result of SolidWorks in Figure 4.4. The simulation was performed by applying a force of 2 kN on the femoral head of the Titanium hip prosthesis to investigate the stress distribution. It shows that the hip prosthesis with the harvester embedded can withstand high stress without permanent deformation (yield strength of 810 N/mm^2). A weight of up to 2000 N could be handled without any severe sign of fracture.

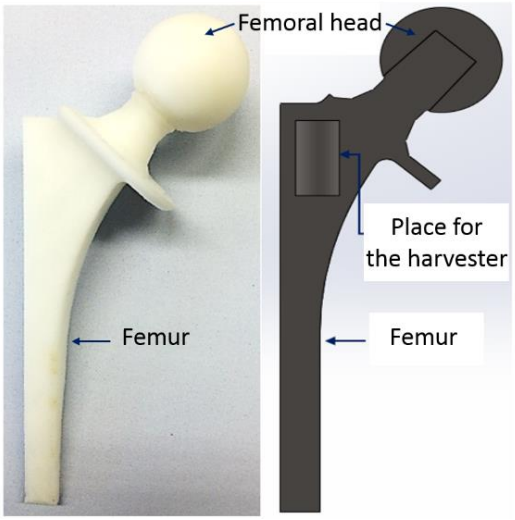

(a) (b)

Figure 4.3 (a) 3D-printing model of hip prosthesis and (b) Cross-section of a hip prosthesis.

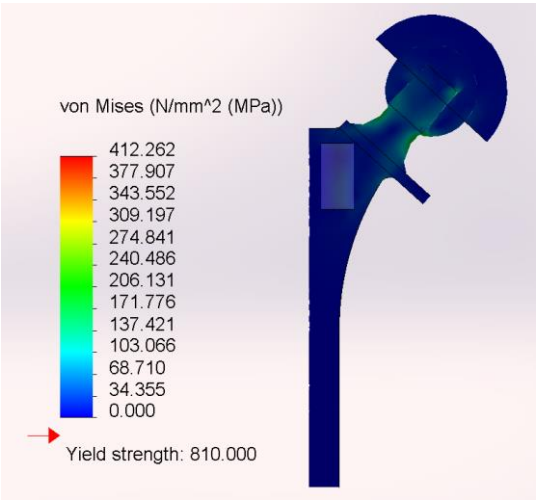

Figure 4.4 Stress on the hip prosthesis simulated by SolidWorks.

4.3.2 Seismic-mass arrangement

Two configurations of the moving mass are proposed in this section to find a suitable arrangement that can induce more voltage in a coil. Figure 4.5 shows the two arrangements of a moving mass: the moving mass using a single magnet and the moving mass consisting of a coupled magnet with a spacer joined between them. COMSOL Multiphysics is used to simulate the magnetic flux density and the flux links in the coil around those two moving masses.

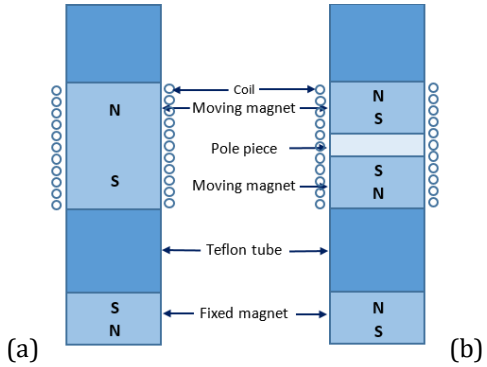

Figure 4.5 The prototype with (a) a single magnet and (b) a coupled magnet forming a seismic mass.

The magnetic flux variation of two different moving masses is presented in Figure 4.6. The magnetic flux density of the moving mass formed by a single magnet (0.91 T) is higher than that of the moving mass formed by a coupled magnet (0.72 T). However, the magnetic flux density in the coil induced by a coupled-magnet moving mass is stronger than that induced by a single-magnet moving mass. As in Figure 4.6, the magnetic flux induced in a coil (red arrows) has been concentrated by the mild-steel spacer used in a coupled-magnet moving mass. This results in stronger magnetic flux density in the coil of the prototype with a coupled magnet than that of the prototype with a single magnet. The average flux density in the coil is 0.067 T induced by a single-magnet moving mass and 0.075 T induced by a coupled-magnet moving mass.

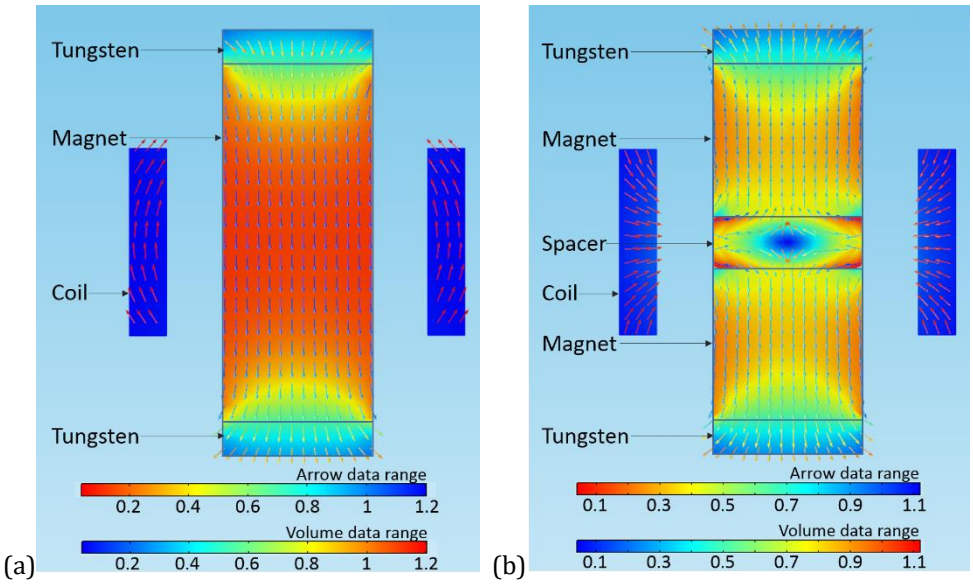

Figure 4.6 The simulation results of magnetic flux density of (a) a single-magnet moving mass and (b) a coupled-magnet moving mass.

Next, the moving masses were moved axially through the coil to simulate the magnetic flux linking in the coil. The maximum change in the flux linkage is preferred to increase the electromagnetic coupling, which leads to the inducing of a high voltage referred to in (4.7). The variation of flux linkage with the magnet position with respect to the centre of the coil is shown in Figure 4.7. The slope of the flux linkage obtained from the moving mass using a coupled magnet (orange area in Figure 4.7) is higher than that obtained from the moving mass using a single magnet (blue area in Figure 4.7). This suggests that the prototype using a coupled magnet as a moving mass has potential to induce a higher voltage in a coil due to providing the higher electromagnetic coupling. Note that the location of the coil has to be adjusted in accordance with the quiescent position of the moving magnet to keep the moving magnet oscillating around the maximum slope of the flux linkage characteristic (details in Section 4.3.4.3).

Because a strong magnetic flux induced in a coil and a potential high coupling coefficient can be obtained using a coupled magnet, the coupled magnet has been chosen to form the moving mass for the prototype in this report.

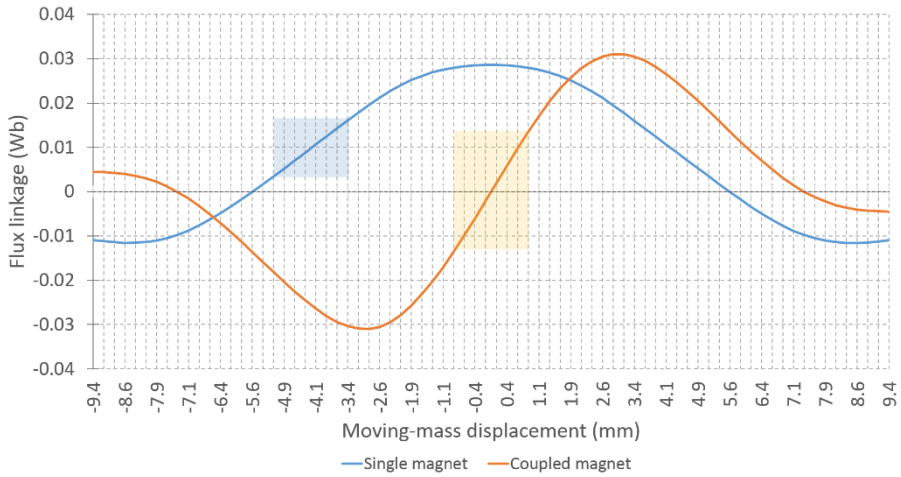

Figure 4.7 The flux linkage versus moving magnet displacement along the guide induced by a single-magnet moving mass and a coupled-magnet moving mass.

4.3.3 Spacer thickness

According to the previous section, the coupled-magnet configuration is selected to be the moving mass of the prototype. In order to join such magnets together and concentrate magnetic flux, a ferromagnetic spacer was placed between them. The material of the spacer is mild steel. It acts like a pole piece which helps to prevent saturation of the pole and to offer the magnetic flux a low reluctance path [57]. For instance, magnetic flux density of such magnets will be captured and concentrated to the area of interest by the spacer. This mitigates the magnetic flux losses in the magnetic circuit. In Figure 4.8, the magnetic flux density of a spacer and a magnet and the flux induced in a coil are simulated with the variation of the spacer thickness. It shows that the flux concentrated in the spacer is higher than its saturated flux density (≈1.8T) when the thickness is less than 0.4 mm and starts to become stable after a thickness of 2.4 mm. So, the proper spacer thickness is expected to be in between 0.4 – 2.4 mm. Spacer that is too thick is not suitable for forming a moving mass for a small harvester. Using thick spacer means the size of the moving mass increased. Increasing the size of the moving mass results in the decrease in the volume available for the displacement of moving mass, which leads to low induced voltage. In Figure 4.8, the highest flux density is induced in a coil

when using the spacer thickness of 1.4 mm, which makes it an appropriate thickness for the spacer.

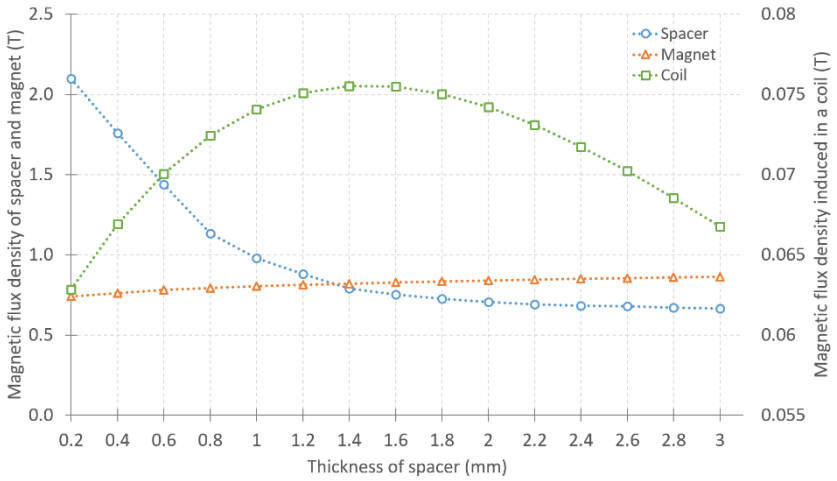

Figure 4.8 The magnetic flux density of spacer, magnet and coil with the variation of spacer thickness.

4.3.4 Coil specification

Finite element analysis (FEA) in COMSOL Multiphysics was used to predict the voltage induced in a coil. The simulations were carried out by letting the moving mass slides through the centre of the coil (the velocity of 0.31 m/s) to simulate the varying flux gradients intersecting the coil, which is the voltage induced in one moving stroke.

4.3.4.1 Coil wire diameter and coil turns

From the manufacturing process of a cylinder coil winding, the average coil fill factor of 0.64 was obtained. Assuming constant coil length of 5 mm, the induced voltage and the power output can be estimated using COMSOL to define the suitable diameter of coil wire and coil turns. The diameter of coil wire was varied from 10 µm – 40 µm with the variation of coil turns from 1000 turns to 5000 turns. The change in the voltage induced with the coil wire diameter and the coil turns are shown in Figure 4.9a. Given a load resistance equal to the coil resistance, the power output was calculated, as shown in Figure 4.9b. The results are summarized in Table 4.2.

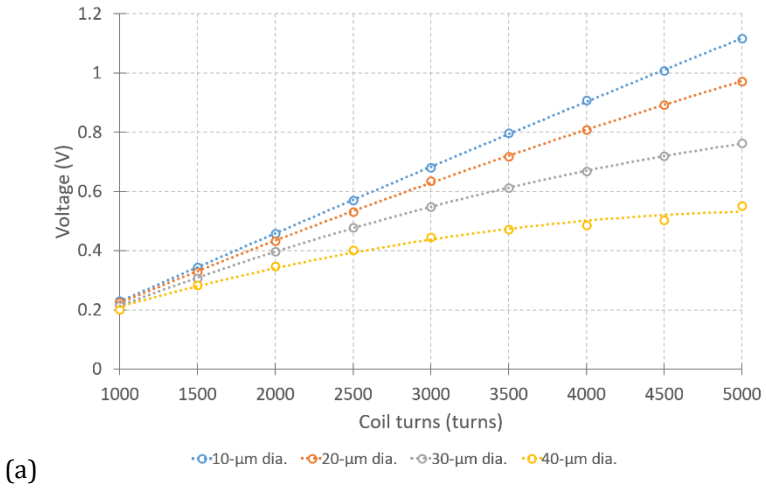

(a)

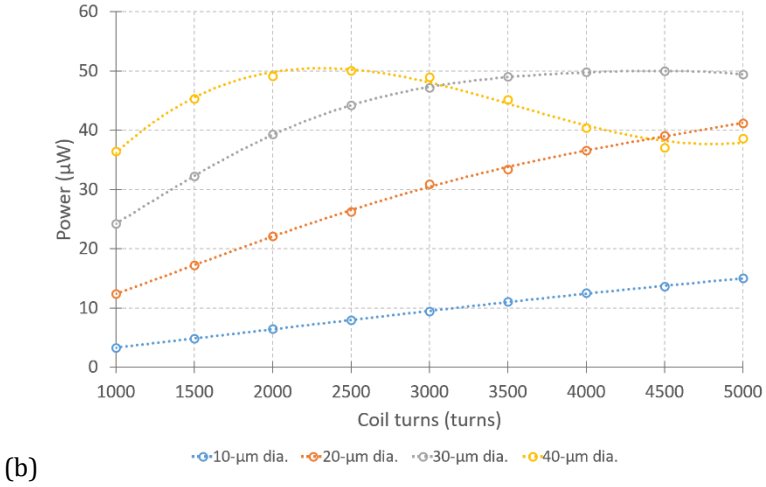

(b)

Figure 4.9 The simulation results of (a) RMS voltage induced and (b) power output with variations in the coil wire diameter and the coil turns.

High voltage inducement and high power output are preferred for the energy harvesting device for efficiency reasons. Figure 4.9a shows that increasing coil turns and the decreasing diameter of coil wire lead to an increase in voltage induced. However, this also results in increased coil resistance (Table 4.2a) which affects the amount of power output obtained. To gain a high level of induced voltage while achieving high power output, the coil is made of 4500 turns of 30-µm copper wire. The voltage induced of the coil parameters chosen is still in the high range (>0.7 V) compared with others in Table 4.2b, and also gains high power output, as shown in Table 4.2c.

Table 4.2 the simulation results of (a) coil resistance, (b) voltage induced and (c) power output for optimising coil wire diameter and coil turns

a) Coil resistance (Ω)									
Coil diameter	Coil turns								
	1,000	1,500	2,000	2,500	3,000	3,500	4,000	4,500	5,000
10 μm	4040	6080	8147	10217	12301	14398	16508	18632	20769
20 μm	1032	1570	2120	2688	3266	3863	4468	5094	5736
30 μm	474	734	1006	1293	1594	1912	2242	2585	2943
40 μm	279	441	616	806	1010	1229	1462	1708	1969
b) Voltage induced (Vrms)									
Coil diameter	Coil turns								
	1,000	1,500	2,000	2,500	3,000	3,500	4,000	4,500	5,000
10 μm	0.23	0.34	0.46	0.57	0.68	0.80	0.91	1.01	1.12
20 μm	0.23	0.33	0.43	0.53	0.64	0.72	0.81	0.89	0.97
30 μm	0.21	0.31	0.40	0.48	0.55	0.61	0.67	**0.72**	0.76
40 μm	0.20	0.28	0.35	0.40	0.44	0.47	0.49	0.50	0.55
c) Power output (μW)									
Coil diameter	Coil turns								
	1,000	1,500	2,000	2,500	3,000	3,500	4,000	4,500	5,000
10 μm	3.3	4.8	6.4	7.9	9.4	11.0	12.5	13.6	15.0
20 μm	12.4	17.2	22.1	26.3	30.9	33.4	36.6	39.1	41.2
30 μm	24.2	32.2	39.3	44.2	47.2	**49.0**	**49.8**	**49.9**	**49.4**
40 μm	**36.4**	**45.3**	**49.1**	**50.1**	**49.0**	45.2	40.4	37.0	38.6

4.3.4.2 Coil length

The length of the coil was varied from 1 mm to 9 mm with the different sizes of the moving mass formed by 1-pair magnet to 6-pair magnets, as shown in Figure 4.10.

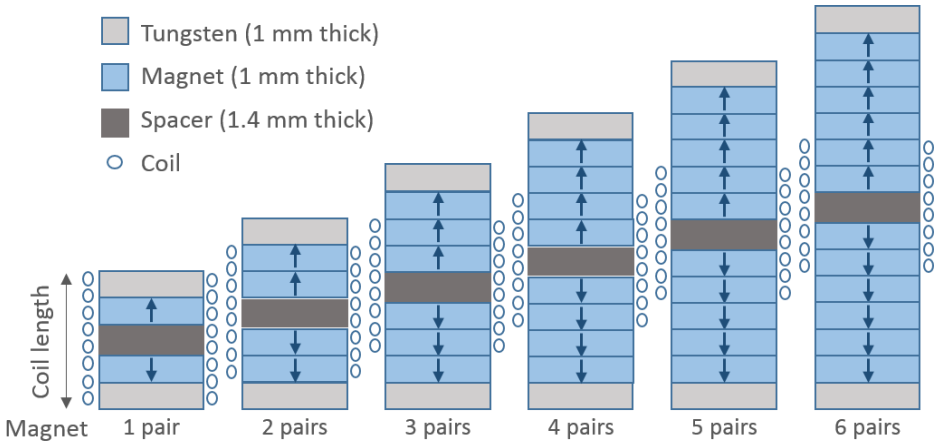

Figure 4.10 The configurations of the moving magnet used for the simulation

Providing a constant coil fill factor of 0.64, the values and dimensions of the coil given for the simulation are listed in Table 4.3. The change in the voltage induced with the thickness of magnets and the coil length is shown in Figure 4.11a. Given a load resistance equal to the coil resistance, the power output was calculated as shown in Figure 4.11b.

Table 4.3 coil parameters

Parameter	Value	Unit
Coil fill factor, F_C	0.64	-
Wire diameter, d	30	μm
Wire resistivity (copper), ρ	1.6×10^{-8}	Ωm
Coil outer radius, R_o	4.5	mm
Coil inner radius, R_i	3.5	mm
Coil length, L_C *(varying)*	1-9	mm

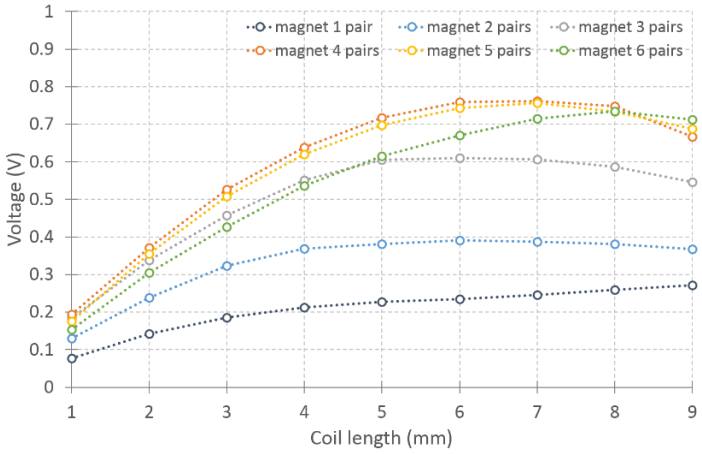

(a)

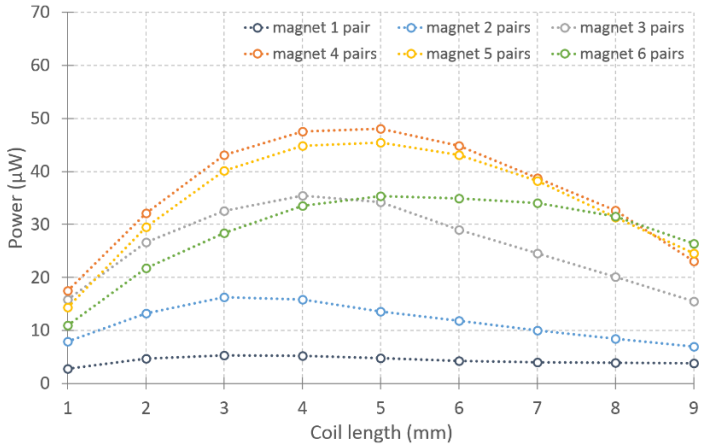

(b)

Figure 4.11 The simulation results of (a) RMS voltage induced and (b) power output with variations in the thickness of magnets and coil length.

As mentioned in Section 4.3.3, too large moving-mass size results, relating to the low voltage induced, are due to the size constraints of the harvester which has low displacement space for moving mass. Besides this, the increasing length of the coil leads to an increase in coil resistance, which affects the level of power output. This means that even though high induced voltage can be achieved due to increasing coil length, the amount of power output obtained may still be low due to high coil resistance. In Figure 4.11, the largest induced voltage is generated by the moving mass consisting of two 4 mm-thickness magnets (magnet 4 pairs). Power output increases initially with the increasing length of the coil but decreases beyond a coil length of 5 mm. A further increase in the number of magnets and coil length results in lower output power. Then, the optimum length of the coil and thickness of the magnets are 5 mm long coil and 4 mm thick magnets. This was optimised for SMH with consideration of the space available for the displacement of the moving mass. For a fair comparison, the same size of magnets has been applied to CMH to form M_1.

4.3.4.3 Coil position

With the optimised dimension of the coil and moving magnet from the previous section, the flux linkage in the coil and the electromagnetic coupling coefficient, θ, calculated by COMSOL (Figure 4.12) were investigated to maximise the power

output of the harvester. This can be performed by adjusting the location of the coil related to the position of the moving magnet, to keep the moving magnet oscillating around the maximum flux linkage gradient (yellow area in Figure 4.12) which maximises the coupling coefficient.

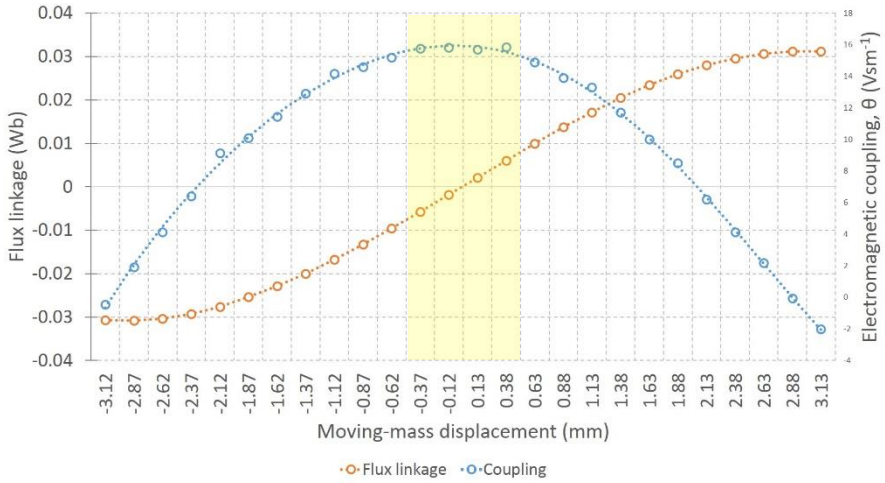

Figure 4.12 Flux through the coil as a function of moving magnet displacement when the coil is centred at z = 0.

According to Figure 4.12, the greatest change in flux linkage is when the moving mass and the coil are centred, implying that the coil should be located at the quiescent position of the moving magnet.

4.4 Electromechanical model of the prototypes

4.4.1 Coupled magnet harvester

Spring-mass-damper systems are used for modelling CMH. Figure 4.13 shows a schematic diagram of CMH.

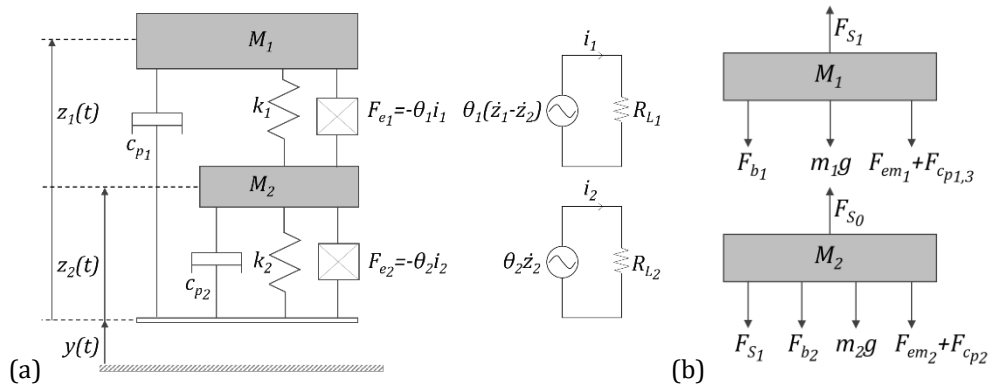

Figure 4.13 (a) Schematic and (b) Free-body diagram of CMH

The governing equation of each movable magnet (M_1 and M_2) can be written as

$$m_1\ddot{z}_1(t) + c_{p_1}\dot{z}_1(t) + F_{b_1} - F_{S_1} + F_{em_1} + m_1 g = -m_1\ddot{y}(t) \tag{4.1}$$

$$m_2\ddot{z}_2(t) + c_{p_2}\dot{z}_2(t) + F_{S_1} + F_{b_2} - F_{S_0} + F_{em_2} + m_2 g = -m_2\ddot{y}(t) \tag{4.2}$$

where $z(t)$ is the relative displacement of the seismic mass m and the base, c_p is the parasitic damping coefficient, F_b is the elastic-dissipative force due to the bumpers, F_S is the magnetic restoring force, $y(t)=Y\cos(\omega_d t)$ is the external excitation, and F_{em} is the electromagnetic damping force which is due to the change of flux inducing a current in the coil. It can be written as

$$F_{em_1} = \theta_1 i_1 \quad \text{and} \quad F_{em_2} = \theta_2 i_2 \tag{4.3}$$

where i is the electric current generated by the device and θ is the electromagnetic coupling which may be written as the displacement derivative of the flux linkage, $d\lambda/dz$. Applying Kirchhoff's law to the electrical circuit (Figure 4.13), the electric current passing through the electric load can be expressed as

$$i_1(t) = \theta_1\left(\frac{\dot{z}_1(t)-\dot{z}_2(t)}{R_{L_1}+R_{C_1}}\right) \quad \text{and} \quad i_2(t) = \theta_2\left(\frac{\dot{z}_2(t)}{R_{L_2}+R_{C_2}}\right) \tag{4.4}$$

where R_L and R_C are the optimal load and coil resistances respectively, and $\dot{z}(t)$ is the velocity of the relative motion. By substituting (4.4) into (4.3), the electromagnetic damping force can be written as

$$F_{em_1} = {\theta_1}^2 \left(\frac{\dot{z_1}(t)-\dot{z_2}(t)}{R_{L_1}+R_{C_1}}\right) \quad \text{and} \quad F_{em_2} = {\theta_2}^2 \left(\frac{\dot{z_2}(t)}{R_{L_2}+R_{C_2}}\right) \tag{4.5}$$

This allows an electrical damping coefficient, c_e, to be given by

$$c_{e_1} = \frac{{\theta_1}^2}{R_{L_1}+R_{C_1}} \quad \text{and} \quad c_{e_2} = \frac{{\theta_2}^2}{R_{L_2}+R_{C_2}} \tag{4.6}$$

The voltage induced in a coil (electromotive force (*emf*)) is proportional to the electromagnetic coupling and the velocity of the moving magnet.

$$V_{emf_1} = -\theta_1\left(\dot{z_1}(t) - \dot{z_2}(t)\right) \quad \text{and} \quad V_{emf_2} = -\theta_2 \dot{z_2}(t) \tag{4.7}$$

where V_{emf} is the induced voltage. The instantaneous power dissipated within the damper is

$$P_{inst_1} = \frac{{\omega_d}^2}{2}\left(c_1 {\dot{z_1}}^2(t)\right)(1-\cos(2\omega_d t)) \tag{4.8}$$

$$P_{inst_2} = \frac{{\omega_d}^2}{2}\left(c_2 {\dot{z_2}}^2(t)\right)(1-\cos(2\omega_d t)) \tag{4.9}$$

The load voltage and the instantaneous power can be determined by

$$V_{load} = V_{emf}\frac{R_L}{R_L+R_C} \tag{4.10}$$

$$P_{load} = \frac{V_{load}^2}{R_L} \tag{4.11}$$

where ω_d is the external exciting frequency, Y is the amplitude of external sinusoidal vibration, and φ is the phase angle.

The governing equations of the motion presented in (4.1) and (4.2) were implemented in a MATLAB/Simulink model to evaluate the induced voltage and the output power from (4.7),(4.10),(4.11) and also to study the dynamic behaviour of the harvester. The detailed description of the model is provided in the next chapter.

4.4.2 Single magnet harvester

SMH is also modelled using a conventional second-order spring and mass system, as in Figure 4.14.

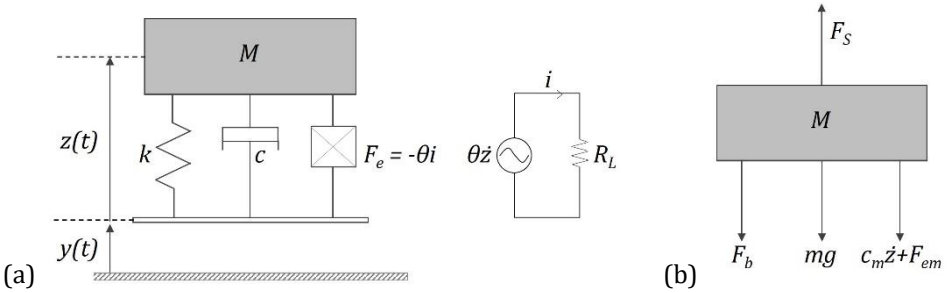

Figure 4.14 (a) Schematic and (b) Free-body diagram of SMH

The governing equation described the motion of the moving magnet M is given by

$$m\ddot{z}(t) + c_p\dot{z}(t) + F_b - F_S + F_{em} + mg = -m\ddot{y}(t) \qquad (4.12)$$

This is similar to the equation of motion of CMH's moving magnet M_1. Then, other parameters such as the electromagnetic damping force, the induced voltage, and the harvested power can be described by the equation related to the moving magnet M_1 of CMH. In the next chapter, the equation of motion of SMH will be applied in the Matlab/Simulink model to study its dynamic behaviour and compare with the behaviour of CMH.

4.5 Frequency response of the prototypes

Apart from the Matlab/Simulink model, the system response of SMH and CMH can be estimated numerically by solving the equation of motions as presented in (4.1), (4.2), and (4.12). An overview of the moving-mass displacement amplitude versus frequency response will be presented roughly in this section by ignoring the boundary condition related to the size constraints of the harvester.

4.5.1 Single magnet harvester

To estimate the moving-mass displacement and frequency response of SMH, the equation of motion in (4.12) was written as the Duffing equation given by

$$\ddot{z} + c\dot{z} + \omega_0^2 z + \alpha z^3 = F\cos(\omega_d t + \phi) = A_1\cos(\omega_d t) + A_2\sin(\omega_d t) \quad (4.13)$$

where α is the nonlinear term written by k_3/m, ω_0^2 represents the linear term given by k/m, and the amplitude of the applied force $F = (A_1^2+A_2^2)^{1/2}$. The first approximation of the solution is assumed to be

$$z = A\cos(\omega_d t) \quad (4.14)$$

where the initial condition of $z(0) = A$ and $\dot{z}(0) = 0$. Substituting (4.14) into (4.13) to determine the exciting frequency ω_d and using trigonometric identity,

$$\cos^3(\omega t) = \frac{3}{4}\cos(\omega t) + \frac{1}{4}\cos(3\omega t) \approx \frac{3}{4}\cos(\omega t) \quad (4.15)$$

we obtain

$$\left[(\omega_0^2 - \omega_d^2)A + \frac{3}{4}\alpha A^3\right]\cos(\omega_d t) - c\omega A\sin(\omega_d t) = A_1\cos(\omega_d t) + A_2\sin(\omega_d t) \quad (4.16)$$

Equating the coefficient of $\cos(\omega_d t)$ and $\sin(\omega_d t)$ on both sides of (4.16),

$$(\omega_0^2 - \omega_d^2)A + \frac{3}{4}\alpha A^3 = A_1 \quad (4.17)$$

$$c\omega_d A = A_2 \quad (4.18)$$

Squaring and adding (4.17) and (4.18),

$$\left[(\omega_0^2 - \omega_d^2)A + \frac{3}{4}\alpha A^3\right]^2 + (c\omega_d A)^2 = F^2 \quad (4.19)$$

The response curves of SMH under the external forces given by (4.19) are presented in Figure 4.15 and Figure 4.16. The linear and nonlinear stiffness substituted in (4.19) is from curve fitting in Figure 5.4. The damping ratio, ζ, is introduced to describe the frequency response of the system which depends on the damping coefficient c, mass m, and the oscillating frequency ω_0 written by $c=2m\omega_0\zeta$.

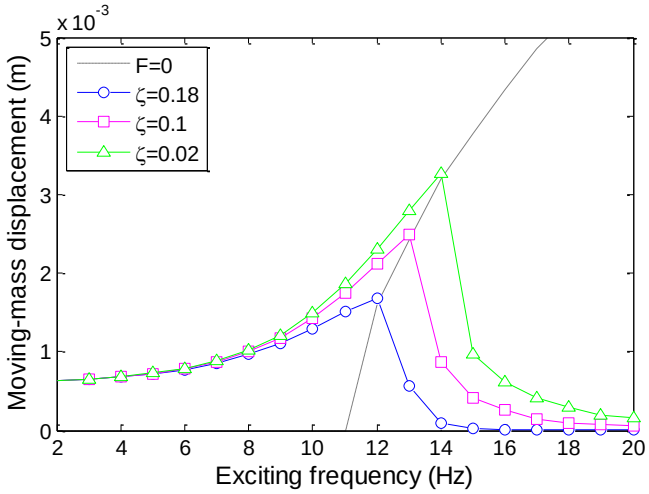

Figure 4.15 The response curves of SMH under the external force of 0.3***g*** with various damping ratio.

Figure 4.15 was plotted by varying the damping ratio from 0.02 to 0.18 under the excitation level of 0.3***g***. It shows that the maximum amplitude of moving-mass displacement decreases with increasing damping ratio. This result reflects a higher rate of energy transfer as the damping ratio increases. The resonant frequency is shifted toward a higher range of frequency corresponding to the increase in the damping ratio. The nonlinearity, the excitation force and the damping ratio influence the effect of the frequency shifting referred to in (4.19).

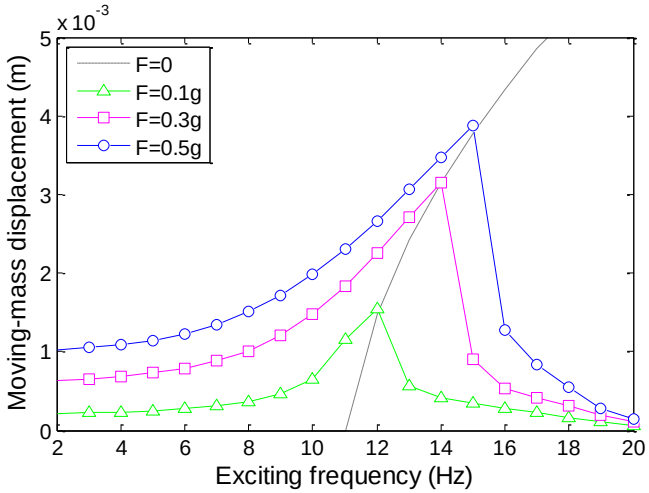

Figure 4.16 The response curves of SMH under external forces with a damping ratio of 0.06

Figure 4.16 was plotted using the damping ratio of 0.06 with the excitation acceleration of 0.1***g***, 0.3***g***, and 0.5***g***. It shows that the displacement amplitude of the moving mass bends to the right as the excitation frequency ω_d is increased. A

nonlinear hardening response is exhibited. The effect of shifting the resonant frequency results in a larger bandwidth, which depends on the nonlinearity, the damping ratio, and the excitation acceleration.

4.5.2 Coupled magnet harvester

The equation of motions in (4.1) and (4.2) is written as the Duffing equation given by

$$m_1\ddot{z}_1+c_1\dot{z}_1 + k_1(z_1 - z_2)+k_{13}(z_1 - z_2)^3 = 0 \tag{4.20}$$

$$m_2\ddot{z}_2 + c_2\dot{z}_2 + k_2z_2 + k_{23}z_2^3 - k_1(z_1 - z_2)-k_{13}(z_1 - z_2)^3 = Fcos(\omega_d t) \tag{4.21}$$

The non-dimensional expressions for (4.20) and (4.21) are given by

$$\mu\ddot{w} + \mu\gamma(\gamma w + \varepsilon\gamma w^3) + \mu\gamma(2\zeta_0\dot{w}) + \mu\gamma(2\zeta_0\dot{u}) = -\mu\ddot{u} \tag{4.22}$$

$$\ddot{u} + 2\zeta_2\dot{u} + u + \eta u^3 - \mu\gamma(\gamma w + \varepsilon\gamma w^3) = F_0\cos(\Omega\tau) \tag{4.23}$$

where the parameters substituted are given by

$$u_0 = \frac{m_1 g}{k_2}, \quad \mu = \frac{m_1}{m_2}, \quad \omega_1^2 = \frac{k_1}{m_1}, \quad \omega_2^2 = \frac{k_2}{m_2}, \quad \gamma = \frac{\omega_1}{\omega_2}, \quad \Omega = \frac{\omega_d}{\omega_2},$$

$$w = \frac{z_1 - z_2}{u_0}, \quad \zeta_1 = \frac{c_1}{2m_1\omega_1}, \quad \zeta_2 = \frac{c_2}{2m_2\omega_2}, \quad \varepsilon = \frac{k_{13}u_0^2}{k_1}, \quad \eta = \frac{k_{23}u_0^2}{k_2}, \quad F_0 = \frac{F}{k_2 u_0},$$

$$u = \frac{z_2}{u_0}, \qquad \tau = \omega_2 t,$$

Transforming (4.22) and (4.23) into a set of four-first-order differential equations:

$$\left.\begin{aligned} \dot{u} &= r \\ \dot{r} &= F_0\cos(\Omega\tau) - 2\zeta_2 r - u - \eta u^3 + \mu\gamma(\gamma w + \varepsilon\gamma w^3) \\ \dot{w} &= s \\ \dot{s} &= -F_0\, cos(\Omega\tau) + 2\zeta_2 r + u + \eta u^3 - \gamma(\mu + 1)(\gamma w + \varepsilon\gamma w^3) - 2\gamma\zeta_1 s \\ &\quad - 2\gamma\zeta_1 r \end{aligned}\right\} \tag{4.24}$$

The steady-state responses of the moving masses, m_1 and m_2, are assumed to be

$$u = acos(\Omega\tau + \phi) \tag{4.25}$$

$$\dot{u} = -a\Omega sin(\Omega\tau + \phi) \tag{4.26}$$

$$w = bcos(\Omega\tau + \theta) \tag{4.27}$$

$$\dot{w} = -b\Omega sin(\Omega\tau + \theta) \tag{4.28}$$

where a and b are the unknown response amplitudes. ϕ and θ are the corresponding phase angles. Transforming (4.24) using the assumptions of the averaging method [113], [114],

$$\dot{a}cos(\Omega\tau + \phi) - a\dot{\phi}sin(\Omega\tau + \phi) = 0 \tag{4.29}$$

$$-\dot{a}sin(\Omega\tau + \phi) - a\dot{\phi}cos(\Omega\tau + \phi) = f_1/\Omega \tag{4.30}$$

$$\dot{b}cos(\Omega\tau + \theta) - b\dot{\theta}sin(\Omega\tau + \theta) = 0 \tag{4.31}$$

$$-\dot{b}sin(\Omega\tau + \theta) - b\dot{\theta}cos(\Omega\tau + \theta) = f_2/\Omega \tag{4.32}$$

where

$$f_1 = a(\Omega^2 - 1 - \eta a^2 \cos^2(\Omega\tau + \phi))\, cos(\Omega\tau + \phi) + 2\zeta_2 a\Omega sin(\Omega\tau + \phi) + F_0 cos(\Omega\tau) + \mu\gamma f_3 \tag{4.33}$$

$$f_2 = b\Omega^2 cos(\Omega\tau + \theta) + \dot{a}\Omega sin(\Omega\tau + \phi) + \left(a\Omega^2 + a\Omega\dot{\phi}\right)cos(\Omega\tau + \phi) - \gamma f_3 - 2\gamma\zeta_1\left(-b\Omega sin(\Omega\tau + \theta)\right) - 2\gamma\zeta_1\left(-a\Omega sin(\Omega\tau + \phi)\right) \tag{4.34}$$

$$f_3 = \gamma b(1 + \varepsilon b^2 \cos^2(\Omega\tau + \theta))\, cos(\Omega\tau + \theta) \tag{4.35}$$

The expressions of the time change rates are written from (4.29)-(4.32) as

$$\dot{a} = -\frac{f_1}{\Omega} sin(\Omega\tau + \phi) \approx -\frac{1}{2\pi}\int_0^{2\pi/\Omega} f_1 sin(\Omega\tau + \phi)\, d\tau \tag{4.36}$$

$$\dot{\phi} = -\frac{f_1}{a\Omega} cos(\Omega\tau + \phi) \approx -\frac{1}{2\pi a}\int_0^{2\pi/\Omega} f_1 cos(\Omega\tau + \phi)\, d\tau \tag{4.37}$$

$$\dot{b} = -\frac{f_2}{\Omega} sin(\Omega\tau + \theta) \approx -\frac{1}{2\pi}\int_0^{2\pi/\Omega} f_2 sin(\Omega\tau + \theta)\, d\tau \tag{4.38}$$

$$\dot{\theta} = -\frac{f_2}{b\Omega} cos(\Omega\tau + \theta) \approx -\frac{1}{2\pi b}\int_0^{2\pi/\Omega} f_2 cos(\Omega\tau + \theta)\, d\tau \tag{4.39}$$

Equation (4.36)-(4.39) are evaluated to obtain

$$\dot{a} = -\frac{1}{\Omega}\left[\frac{F_0}{2} sin(\phi) + \zeta_2 a\Omega + \mu\gamma b\left(\frac{\gamma}{2}\left(1 + \frac{3}{4}\varepsilon b^2\right) sin(\phi - \theta)\right)\right] \tag{4.40}$$

$$\dot{\phi} = -\frac{1}{a\Omega}\left[\frac{F_0}{2}cos(\phi) + \frac{1}{2}a\left(\Omega^2 - 1 - \frac{3}{4}\eta a^2\right) + \mu\gamma b\left(\frac{\gamma}{2}\left(1 + \frac{3}{4}\varepsilon b^2\right)cos(\phi - \theta)\right)\right] \tag{4.41}$$

$$\dot{b} = -\frac{1}{\Omega}\left[\frac{\dot{a}\Omega}{2}cos(\phi - \theta) - \frac{a\Omega^2 + a\Omega\dot{\phi}}{2}sin(\phi - \theta) + \gamma\zeta_1 b\Omega + \gamma\zeta_1 a\Omega cos(\phi - \theta)\right] \tag{4.42}$$

$$\dot{\theta} = -\frac{1}{b\Omega}\left[\frac{b\Omega^2}{2} + \frac{a\Omega^2 + a\Omega\dot{\phi}}{2}cos(\phi - \theta) + \frac{\dot{a}\Omega}{2}sin(\phi - \theta) - \frac{\gamma^2 b}{2}\left(1 + \frac{3}{4}\varepsilon b^2\right) + \gamma\zeta_1 a\Omega sin(\phi - \theta)\right] \tag{4.43}$$

The response amplitudes and phase angles remain unchanged in the steady-state motion, thus their derivatives are equal to zero, $\dot{a} = \dot{\phi} = \dot{b} = \dot{\theta} = 0$. Equation (4.40)-(4.43) are simplified into

$$\frac{F_0}{2}sin(\phi) + \zeta_2 a\Omega + \mu\gamma b\left(\frac{\gamma}{2}\left(1 + \frac{3}{4}\varepsilon b^2\right)sin(\phi - \theta)\right) = 0 \tag{4.44}$$

$$\frac{F_0}{2}cos(\phi) + \frac{1}{2}a\left(\Omega^2 - 1 - \frac{3}{4}\eta a^2\right) + \mu\gamma b\left(\frac{\gamma}{2}\left(1 + \frac{3}{4}\varepsilon b^2\right)cos(\phi - \theta)\right) = 0 \tag{4.45}$$

$$-\frac{a\Omega^2}{2}sin(\phi - \theta) + \gamma\zeta_1 b\Omega + \gamma\zeta_1 a\Omega cos(\phi - \theta) = 0 \tag{4.46}$$

$$\frac{a\Omega^2}{2}cos(\phi - \theta) + \frac{b\Omega^2}{2} - \frac{\gamma^2 b}{2}\left(1 + \frac{3}{4}\varepsilon b^2\right) + \gamma\zeta_1 a\Omega sin(\phi - \theta) = 0 \tag{4.47}$$

Squaring and adding (4.46) and (4.47) to cancel out the trigonometric terms give

$$\left(\frac{a\Omega^2}{2}\right)^2 + (\gamma\zeta_1 a\Omega)^2 = (\gamma b\Omega\zeta_1)^2 + \frac{b^2}{4}\left(\Omega^2 - \gamma^2\left(1 + \frac{3}{4}\varepsilon b^2\right)\right)^2 \tag{4.48}$$

Substituting (4.46) and (4.47) into (4.44) and (4.45) gives

$$\frac{{F_0}^2}{4}+\left(\mu\gamma b\left(-\frac{\gamma^2\zeta_1}{\Omega}\left(1+\frac{3}{4}\varepsilon b^2\right)\right)\right)^2 = \left(\zeta_2 a\Omega+\frac{\mu\gamma^3 b^2}{a\Omega}\left(1+\frac{3}{4}\varepsilon b^2\right)(\zeta_1)\right)^2 + \left(\frac{a}{2}\left(\Omega^2-1-\frac{3}{4}\eta a^2\right) - \frac{\mu\gamma^2 b^2}{2a\Omega^2}\left(1+\frac{3}{4}\varepsilon b^2\right)\left(\Omega^2-\gamma^2\left(1+\frac{3}{4}\varepsilon b^2\right)\right)\right)^2 \quad (4.49)$$

The solutions can be reached from the relationship between the steady-state response amplitudes of the system governed by (4.48) and (4.49). The moving-mass displacement amplitude of CMH (M_1 and M_2) under different excitation forces (0.1$\boldsymbol{g}$, 0.2$\boldsymbol{g}$ and 0.3$\boldsymbol{g}$) with a fixed damping is presented in Figure 4.17.

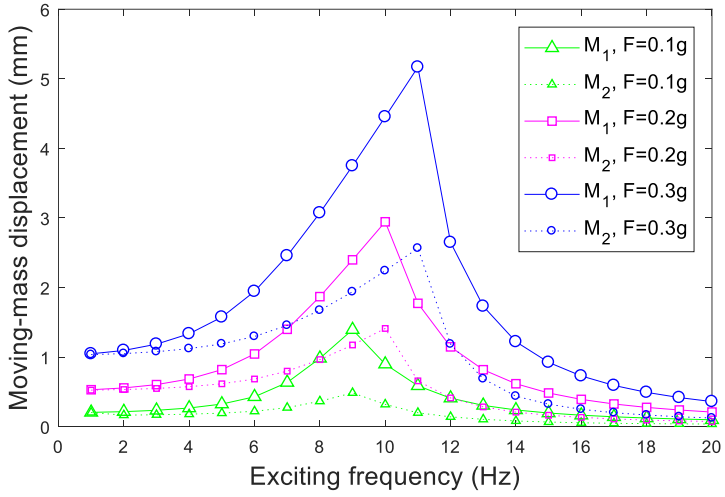

Figure 4.17 The moving-mass displacement of CMH under the different forces with a damping ratio of ζ_1=0.08 and ζ_2=0.1.

In Figure 4.17, the nonlinear hardening response of CMH is exhibited and shows a synchronised displacement between M_1 and M_2. Increasing the acceleration levels results in broadening the frequency response of CMH, as occurred with SMH. At the acceleration of 0.1-0.3$\boldsymbol{g}$, the operating frequency of CMH is around 9-12 Hz, which is rather low compared with that of SMH (12-14 Hz). However, it should be noted that these numerical results are analysed without the boundary condition

to investigate the displacement response versus frequency of the moving mass. With the size constraints of the harvesters, the moving-mass displacement is limited. Collision is inevitable, thus influencing the frequency response of the harvesters. A complete simulation will be provided in the next chapter to estimate the actual dynamic behaviour of the harvesters.

4.6 Conclusion

With the aim of achieving high power output, the structure of a harvester should be designed carefully, considering a number of parameters, i.e. the range of operating frequency to match the external exciting vibration, the factor by which to reduce the level of total damping ratio, and the proper size of moving mass within the limited available volume of a device. Moreover, dimensions of the coil also influence the amount of energy harvested. Using a small diameter coil wire means more coil turns can induce a higher voltage within the same size constraints. However, reduced diameter of coil wire increases coil resistance, which leads to a decreasing output current and power output. Therefore, the coil should be carefully designed to induce high voltage and also achieve high power output.

The electromagnetic vibration energy harvesters, SMH and CMH, presented in this chapter, have been designed regarding the constrained volume of the hip prosthesis. The number of magnets forming a moving mass, the thickness of the spacer, and the coil configuration have been optimised to benefit the harvesting performance. The nonlinear regime of the designed harvesters offers the ability to harvest energy in a wide frequency band. This is suitable for hip implant harvesting which exploits the unpredictable vibrations during walking. The additional moving mass applied in CMH influences the bandwidth of the device. It is over a lower range of frequency compared with the bandwidth of SMH. According to the low excitation frequency range of human motion, it is believed that CMH has the potential to harvest more energy than SMH.

Chapter 5

Simulation and Experimental Validation

5.1 Introduction

This chapter begins by applying the theoretical model discussed in the previous chapter with a simulation model, to study the behaviour of the proposed harvesters: the single-magnetically levitated harvester (SMH) and the coupled-magnetically levitated harvester (CMH). The performance of these harvesters is discussed and compared regarding output power from both harmonic excitation and human motion through experimental and simulation results. Some conclusions are drawn in the final section.

5.2 Simulations

5.2.1 MATLAB simulink model

To investigate the dynamic behaviour of SMH and CMH in response to external vibrations, a MATLAB/Simulink model has been developed based on equation (4.1) and (4.2) for CMH, and equation (4.12) for SMH. The simple block diagram in Figure 5.1 is an overall view of CMH model. The simulation parameters are presented in Table 4.1 (more parameters detailed in Appendix F). The diagram for SMH is provided in Appendix D.

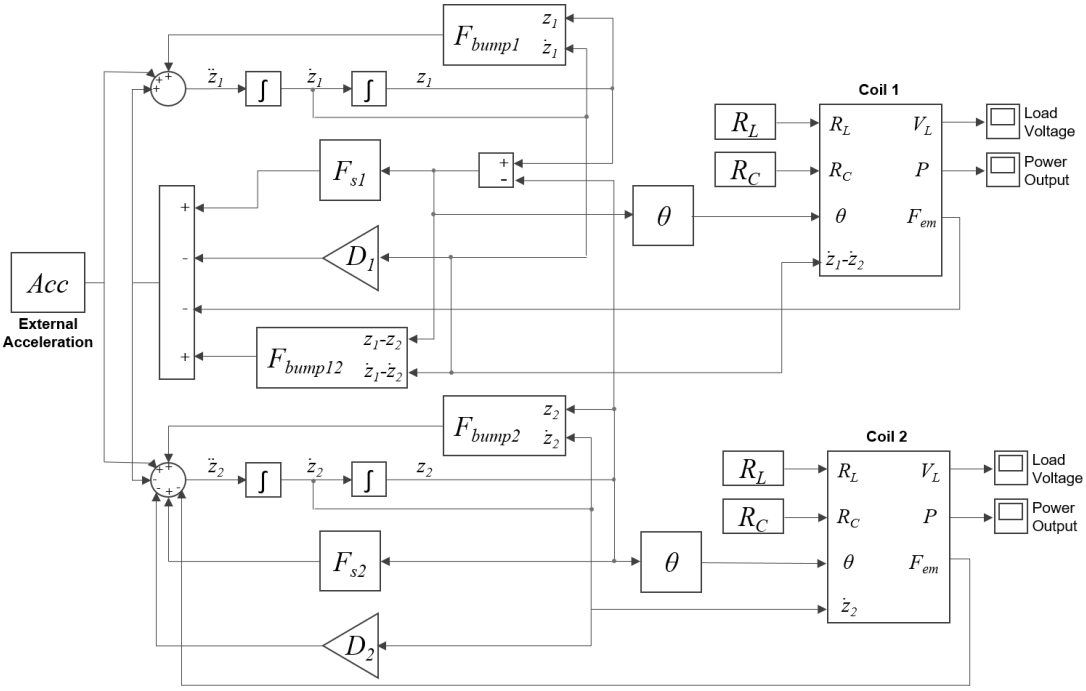

Figure 5.1 Block diagram of the Matlab/Simulink model for CMH.

The magnetic restoring force F_S and the electromagnetic coupling θ between moving magnets and coils were calculated using finite element analysis (FEA) in Comsol Multiphysics® to be implemented in a Simulink model as lookup tables. Figure 5.2 and Figure 5.3 show F_S and θ as a function of moving-mass displacement. In Figure 5.1, the F_S *and* θ were extracted from the lookup table corresponding to the displacement of the moving magnet to calculate V_{emf}, V_{load}, and P_{load} referred to in equations (4.7), (4.10), and (4.11) respectively.

The relation between the magnetic restoring force of CMH and moving-mass displacement is carried out by cubic fitting in Matlab. The fitting results on the F_S of the top movable magnet (M_1) and the bottom movable magnet (M_2) of CMH are shown in Figure 5.2 as:

$$F_{S_{M1}} = -1.38\text{e}^6 z^3 + 1115.7z^2 - 5.94z + 0.0006 \quad (5.1)$$

$$F_{S_{M2}} = -1.74\text{e}^6 z^3 + 6547z^2 - 14.39z - 8.5\text{e}^{-5} \quad (5.2)$$

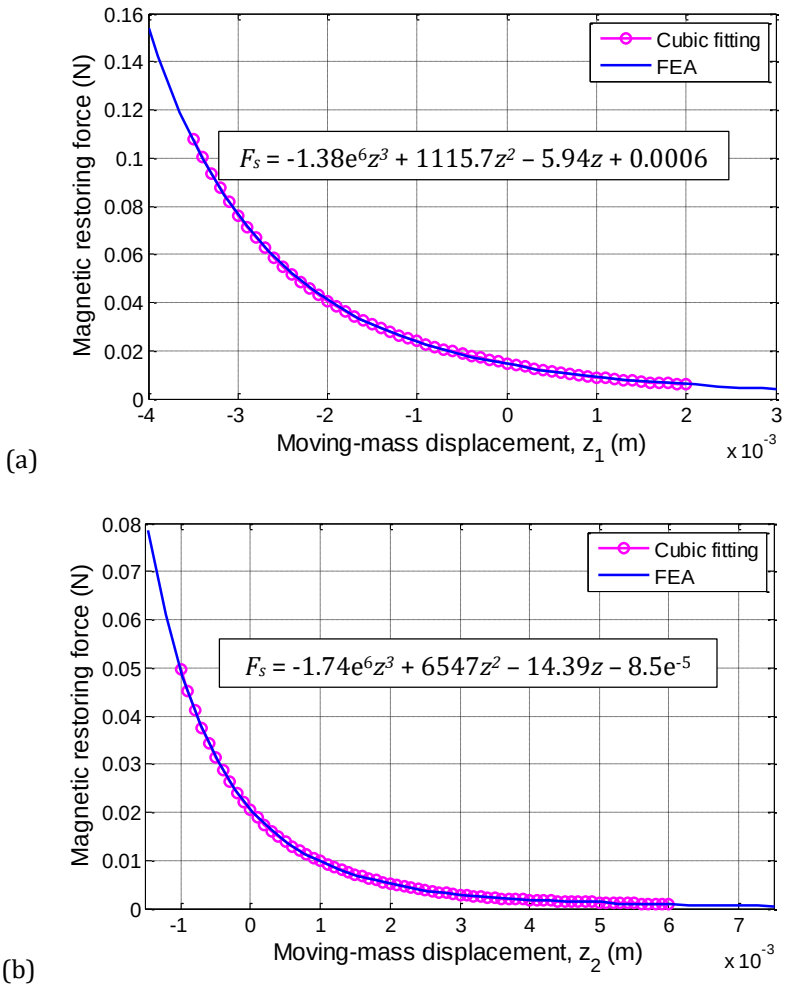

Figure 5.2 Magnetic restoring force of (a) top movable magnet M_1 and (b) bottom movable magnet M_2 of CMH.

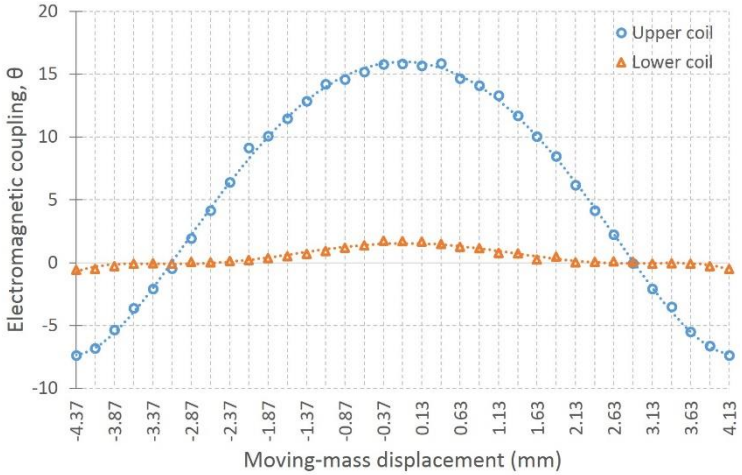

Figure 5.3 Electromagnetic coupling of CMH.

The linear resonant frequency of M_1 and M_2 can be calculated from the fitting results in Figure 5.2, which is

$$F_{S_{M1}} = 5.94z_1 \text{ and } F_{S_{M2}} = 14.39z_2 \tag{5.3}$$

from

$$f_r = \frac{1}{2\pi}\sqrt{\frac{k}{m}} \tag{5.4}$$

Substituting k_1=5.94 N/m, m_1=1.52e^{-3} kg, k_2=14.39 N/m, and m_2=0.59e^{-3} kg into (5.4). The linear resonant frequencies of M_1 and M_2 are 9.95 Hz and 13.14 Hz, respectively. The force from M_1 exerted on M_2 reduces the height of M_2 making it closer to the bottom fixed magnet, which results in harder spring stiffness. The high level of electromagnetic coupling in the upper coil (Figure 5.3) is due to the stronger magnetic flux density generated by M_1, which has a larger size. The magnetic restoring force on the moving magnet of SMH is in Figure 5.4. Substituting m=1.53e^{-3} kg into (5.4), the predicted linear resonant frequency of SMH can be calculated as 10.86 Hz. The electromagnetic coupling of SMH is the same as that presented in Figure 5.3 for the upper coil.

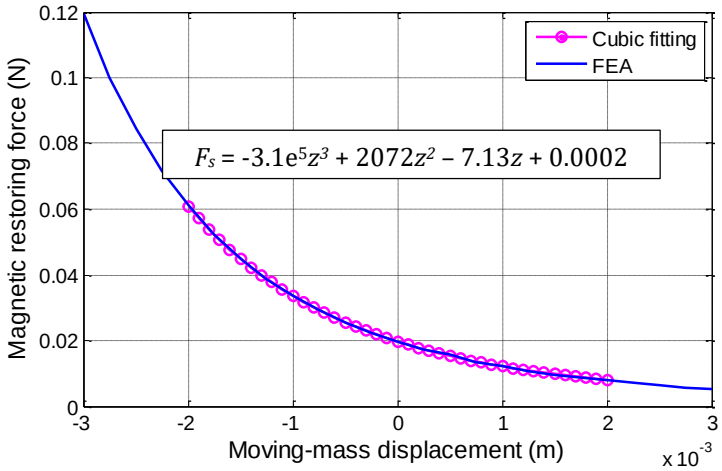

Figure 5.4 Magnetic restoring force of SMH.

The collision of the moving magnets with the frame is unavoidable due to the small size of the harvesters (2 cm in length). The elastic spring forces due to the bumpers, F_{bump}, are included in the Simulink model, calculated using the following conditions:

$$F_{bump_1} = -k_b(z_1 - S_U) - c_b\dot{z}_1 \qquad if \quad z_1 \geq S_U \tag{5.5}$$

$$F_{bump_{12}} = -k_b(z_1 - z_2 - S_M) - c_b(\dot{z}_1 - \dot{z}_2) \quad if \quad z_1 - z_2 \leq S_M \tag{5.6}$$

$$F_{bump_2} = -k_b(z_2 - S_L) - c_b\dot{z}_2 \qquad if \quad z_2 \leq S_L \tag{5.7}$$

where k_b and c_b are the spring and damping constants of the bumpers, S_U is the gap between the upper bumper and M_1, S_M is the gap between M_1 and M_2, and S_L is the free space between M_2 and the lower bumper. The displacement of the moving magnets (z_1 and z_2) were used to define the conditions in which the moving magnets hit the bumpers. Forces F_{bump1}, F_{bump2} , and F_{bump12} represent the collisions between M_1 and the upper bumper, M_2 and the lower bumper, and M_1 and M_2 , respectively.

The bumpers are fabricated from crepe rubber to reduce energy loss. However, energy loss is still present and is proportional to the velocity of the moving masses, as presented in (5.5)-(5.7). The parasitic damping coefficients c_p applied in the Simulink model were calculated from the decaying waveforms of the open circuit voltage of the harvester, as presented in Section 5.3.2.1. These were obtained at low

amplitudes in order to avoid collisions between the moving magnets and the bumpers. More detail is provided in Section 5.3.1. After these parameters had been defined, the induced voltage and the power output of the harvester could then be simulated using the Simulink model presented in Figure 5.1.

5.2.2 Simulation results

5.2.2.1 Sinusoidal excitation

The voltage induced in a coil of SMH and CMH are simulated under sinusoidal excitations at accelerations of 0.1$\boldsymbol{g}$, 0.3$\boldsymbol{g}$ and 0.5$\boldsymbol{g}$ (1$\boldsymbol{g}$ = 9.8 ms^{-2}). The results are presented in Figure 5.5. The voltage induced in the lower coil of CMH is not included in this section but will be mentioned in Section 5.4.

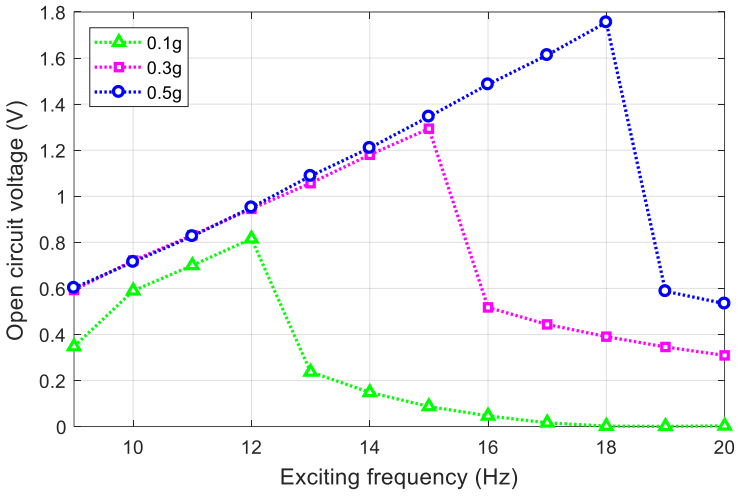

(a)

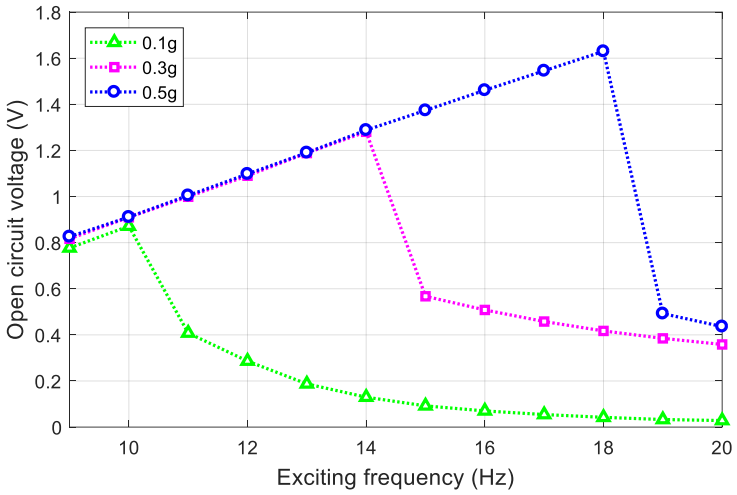

(b)

Figure 5.5 The RMS voltage induced in a coil of (a) SMH and (b) CMH simulated by Matlab/Simulink.

Figure 5.5 shows that both SMH and CMH configurations demonstrate nonlinear behaviour. The higher the amplitude, the stronger the nonlinearity becomes, which broadens the bandwidth of the devices. According to these simulation results, it is found that the bandwidth of CMH is wider than that of SMH by about 15%, 22%, and 38% under excitations of 0.1$\boldsymbol{g}$, 0.3$\boldsymbol{g}$, and 0.5$\boldsymbol{g}$ respectively. This is defined by the 3-dB bandwidth, where the induced voltage has dropped by 0.707 or $1/\sqrt{2}$ of the maximum voltage. Table 5.1 details the bandwidth of the devices under different acceleration amplitudes.

Table 5.1 The operating bandwidth of SMH and CMH at different levels of acceleration.

Levels of Acceleration	Operating bandwidth (Hz)		Percentage increase (%)
	SMH	CMH	
0.1$\boldsymbol{g}$	2.62	3.00	14.62
0.3$\boldsymbol{g}$	3.76	4.57	21.73
0.5$\boldsymbol{g}$	4.21	5.83	38.46

Figure 5.6 shows the displacement of the moving masses in SMH and CMH devices. The collision between the moving magnet and the bumper can be observed at acceleration levels of 0.3$\boldsymbol{g}$ and 0.5$\boldsymbol{g}$. The collisions increase the effective stiffness resulting in an increase in bandwidth. The available space for moving-mass displacement for SMH is 3.2 mm and 2.4 mm for CMH. The more limited the space

available for moving-mass, the broader the bandwidth (Table 5.1) but this may occur at the expense of the output-power.

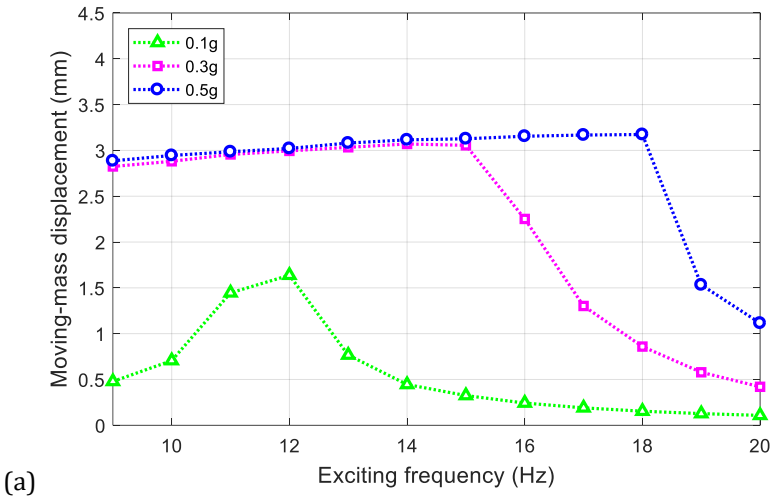

(a)

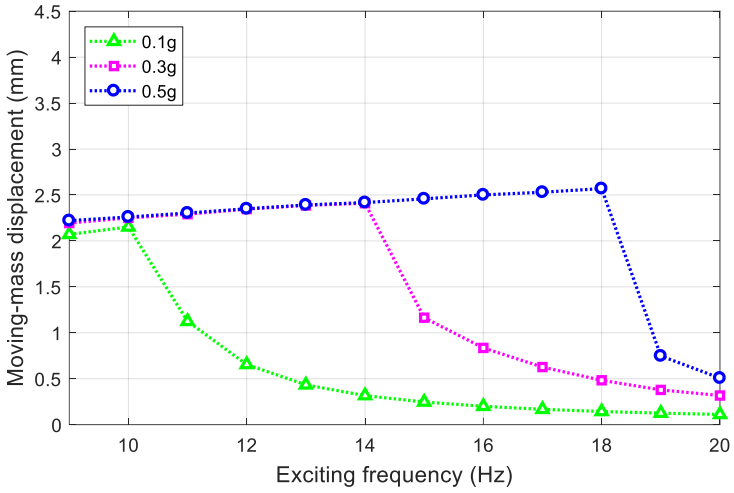

(b)

Figure 5.6 The displacement amplitude of the moving mass for (a) SMH and (b) CMH simulated by Matlab/Simulink.

5.2.2.2 Hip-motion excitation

The acceleration at the hip of a fit and healthy individual walking and running were applied to the Simulink model to estimate the harvester output during realistic excitation conditions. The coil voltage when walking and running obtained from the simulation is compared with the experiment results in Figure 5.7 for SMH and Figure 5.8 for CMH, and summarised in Table 5.2. The results show that CMH generates

higher voltage at lower acceleration, i.e. walking; whereas, SMH has better performance when the user is running.

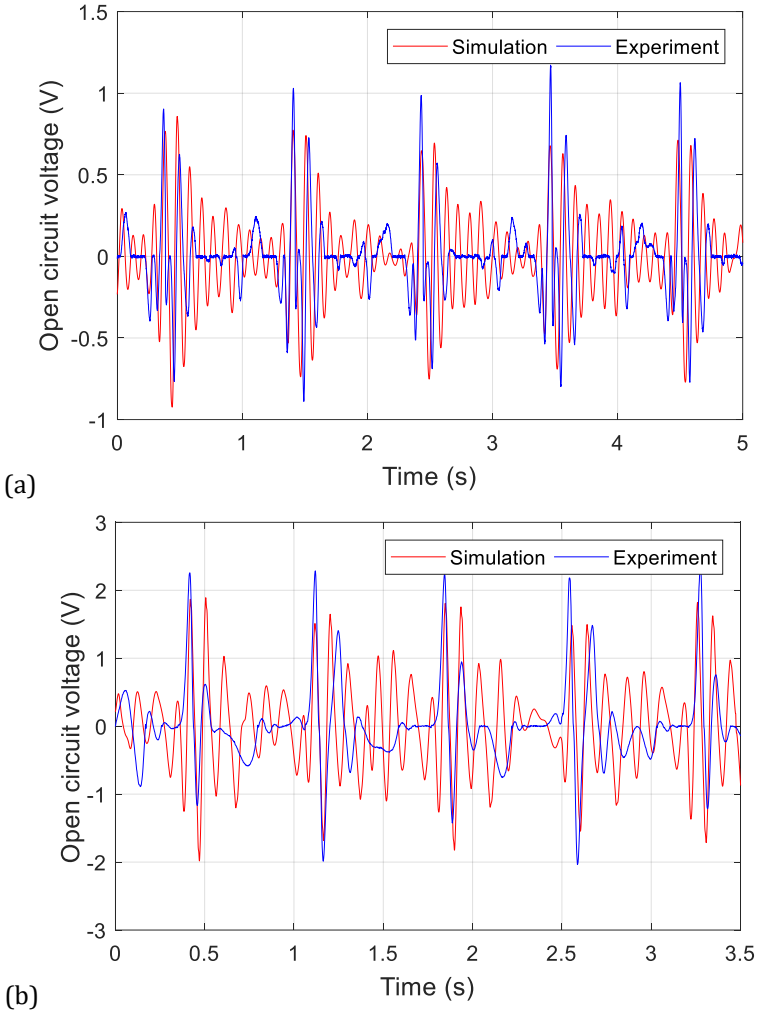

Figure 5.7 The variation of the voltage induced in a coil versus time during (a) walking and (b) running on a treadmill of SMH.

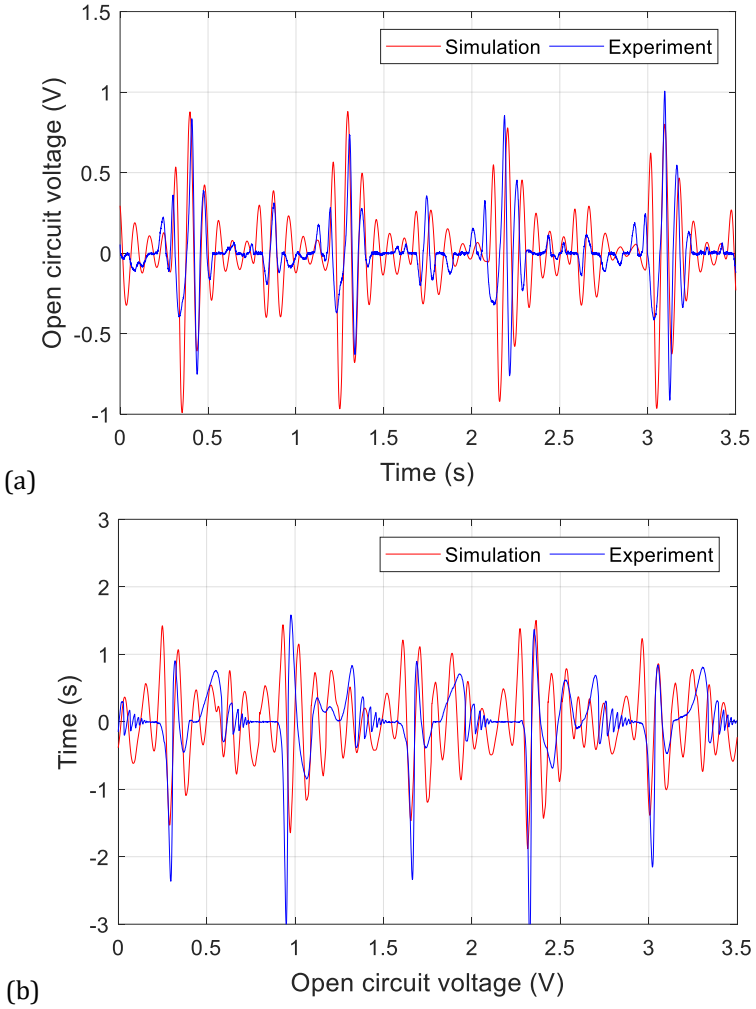

Figure 5.8 The variation of the voltage induced in a coil versus time during (a) walking and (b) running on a treadmill of CMH.

Table 5.2 The open circuit voltage of SMH and CMH during walking and running.

	SMH		CMH	
Acceleration	Simulation (Vrms)	Experiment (Vrms)	Simulation (Vrms)	Experiment (Vrms)
Walking	0.252	0.243	0.268	0.256
Running	0.685	0.669	0.617	0.608

The coil voltage waveforms from the simulation do not perfectly synchronise with the experiment. The amplitude of the simulated RMS voltage during walking and running is marginally higher than the experiment results. The reason for this can be explained

by the damping parameters used in the simulation model and the effect of collisions. The damping parameters were calculated from the decaying waveforms generated by constant sinusoidal excitation. This underestimates the overall damping during walking and running since the actual footstep generates an impulse excitation, which results in the collisions between the mass and bumpers causing an increase in the damping compared with the sinusoidal excitation.

5.3 Experiments

5.3.1 Experimental procedures

The experiments have been separated into three sections with Section 5.3.2.1, presenting the damping analysis observed under various excitations from 0.1$\boldsymbol{g}$ to 0.5$\boldsymbol{g}$. The electrodynamic shaker (ET-126B) was stopped abruptly in order to record the attenuated impulse response of the harvester, as shown in Figure 5.9, which enables the harvester's damping factor to be calculated using equation (5.8) [115].

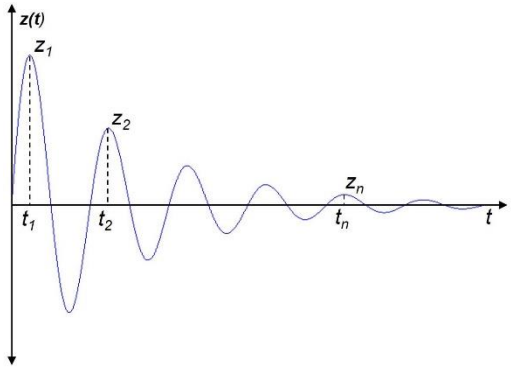

Figure 5.9 Example of an underdamped impulse response [115]

$$\zeta = \frac{\alpha}{\sqrt{4\pi^2 + \alpha^2}} \tag{5.8}$$

where ζ is the damping ratio, and α is defined as $\alpha = \frac{1}{n} ln \frac{z_1}{z_{n+1}}$. The parasitic damping, ζ_p, and total damping, ζ, can be determined from the open loop and loaded impulse

response, respectively. According to the relationship of the damping in (5.9), the electrical damping ratio, ζ_e, can be calculated.

$$\zeta_e = \zeta - \zeta_p \tag{5.9}$$

The dynamic behaviour of the two harvesters under harmonic excitation is presented in Section 5.3.2.2. The harvesters were tested on an electrodynamic shaker in a vertical direction under sinusoidal acceleration with levels of 0.1$\boldsymbol{g}$, 0.3$\boldsymbol{g}$, and 0.5$\boldsymbol{g}$ to investigate the bandwidth, voltage and power output of the harvesters. Section 5.3.2.3 presents results from mounting the harvesters at the hip of an individual when walking (2.6 km/h) and slow running (7 km/h) on a treadmill. The output voltage and power at optimum load resistance are presented in this section.

5.3.2 Experimental results

5.3.2.1 Decaying oscillations

The open-loop and closed-loop impulse response of the harvesters were recorded at acceleration levels of 0.1$\boldsymbol{g}$, 0.2$\boldsymbol{g}$, 0.3$\boldsymbol{g}$, 0.4$\boldsymbol{g}$, and 0.5$\boldsymbol{g}$. The driving force is applied for 10 seconds and then stopped. The linear resonant frequency of the harvesters can be determined from the impulse response of the harvester at low amplitudes with no collisions between the moving magnets and the bumpers. The FFT of the impulse response is shown in Figure 5.10.

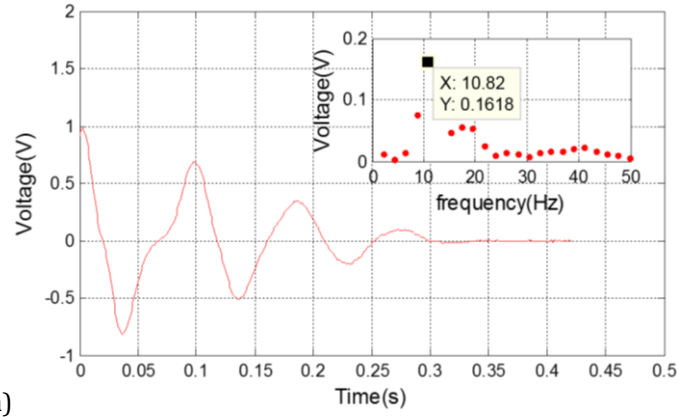

(a)

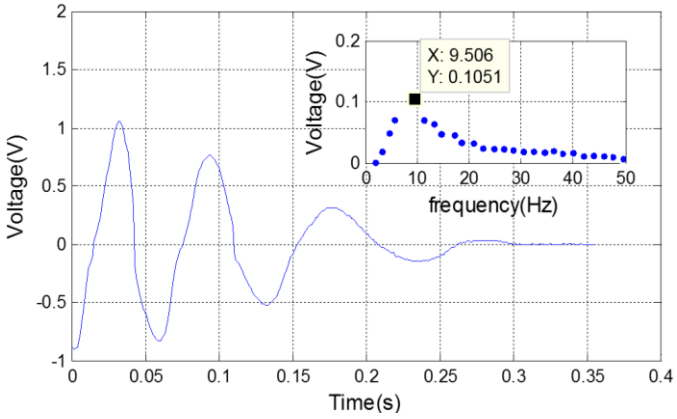

(b)

Figure 5.10 The impulse response of (a) SMH and (b) CMH at the driving vibration of 0.1***g***.

From Figure 5.10, with no collisions, the most significant damping mechanism is viscous damping, as shown by the exponential decay in the amplitude. Dry friction is also present but if this was dominant it would result in a linear decay. From the FFT, the linear resonance frequencies of CMH and SMH are 10.82 Hz and 9.51 Hz respectively, which are close to the simulated values presented in Section 5.2.1 (10.86 Hz and 9.95 Hz). The lower linear operating frequency provided by CMH could be more beneficial to harvesting performance from human motion.

The parasitic damping ratio can be obtained under open circuit conditions from equation (5.8). The total damping ratio is obtained when connected to an optimum load. Equation (5.9) can then be used to obtain the electrical damping ratio. The dependence of the damping ratio on acceleration levels is shown in Table 5.3.

Table 5.3 Damping parameters of the harvesters at different acceleration levels.

Acceleration level	Single-magnetically levitated harvester (SMH)			Coupled-magnetically levitated harvester (CMH)		
	ζ	ζ_p	ζ_e	ζ	ζ_p	ζ_e
0.1g	0.104	0.059	0.045	0.145	0.097	0.047
0.2g	0.105	0.060	0.045	0.162	0.115	0.048
0.3g	0.116	0.071	0.046	0.166	0.118	0.048
0.4g	0.121	0.075	0.046	0.169	0.122	0.047
0.5g	0.122	0.076	0.046	0.170	0.124	0.046
Average	0.114	0.068	0.046	0.162	0.115	0.047

According to Table 5.3, electrical damping is relatively unaffected by acceleration levels. The observed increase in parasitic damping at accelerations of 0.3$\boldsymbol{g}$-0.5$\boldsymbol{g}$ for SMH and 0.2$\boldsymbol{g}$-0.5$\boldsymbol{g}$ for CMH can be attributed to the collisions of the moving magnet and bumpers. Referring to Table 5.3, it can be estimated, from the average values of the ζ and ζ_e, that 40% and 30% of the total dissipated power is transferred to the electrical domain for SMH and CMH harvesters respectively.

5.3.2.2 Sinusoidal excitation

The voltage and power output were recorded across a varying load resistance (1.5 kΩ to 4 kΩ) in order to find the optimal load. The optimum resistance was the same for all acceleration levels, Figure 5.11 presents the result at 0.3$\boldsymbol{g}$.

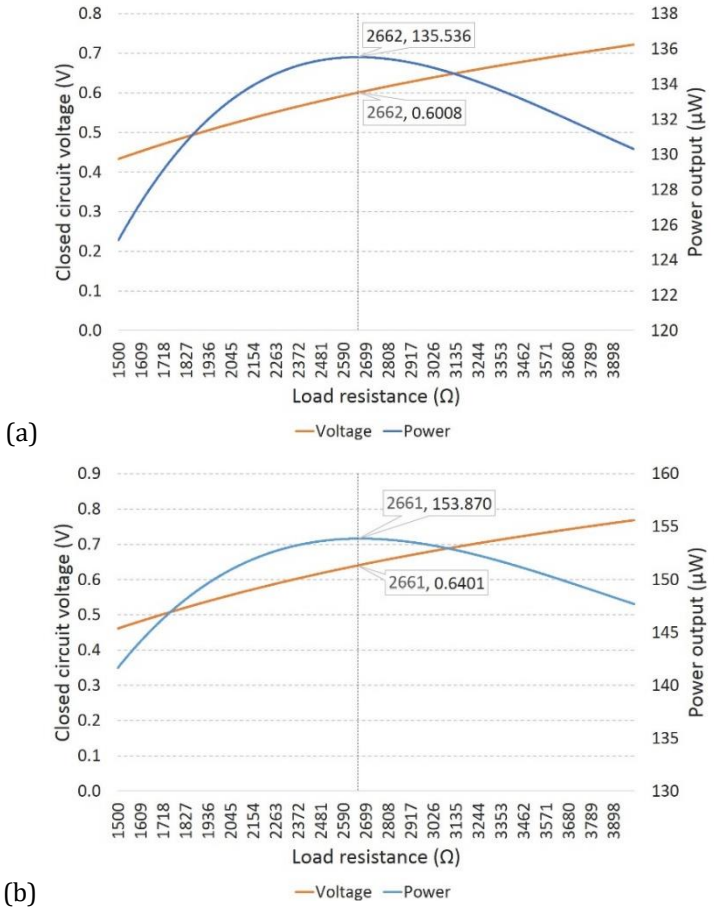

Figure 5.11. The closed circuit voltage (Vrms) and power output across the varying load resistance of (a) SMH and (b) CMH under the acceleration level of 0.3$\boldsymbol{g}$.

The optimum load resistance of the two harvesters are 2662Ω for SMH and 2661Ω for CMH, which closely match the coil resistance of 2558Ω. This is due to large parasitic damping ($\zeta_p >> \zeta_e$), as shown in Table 5.3. Equation (5.10) demonstrates the relationship between load resistance and damping under the matching condition when $c_e = c_p$ is required for maximum power output [70], [116]. The relatively large parasitic damping results in the maximum power output at a load resistance close to the coil resistance ($R_L \approx R_C$).

$$R_L = R_C + \frac{\theta^2}{c_p} \tag{5.10}$$

In order to characterise the nonlinear behaviour of the harvesters, the coil voltage of the two harvesters across the optimal load resistance was measured by sweeping the frequency up and down across a range of 8 - 20 Hz. The results are presented in Figure 5.12. The voltage and power output at the resonant frequencies under different acceleration amplitudes are summarised in Table 5.4.

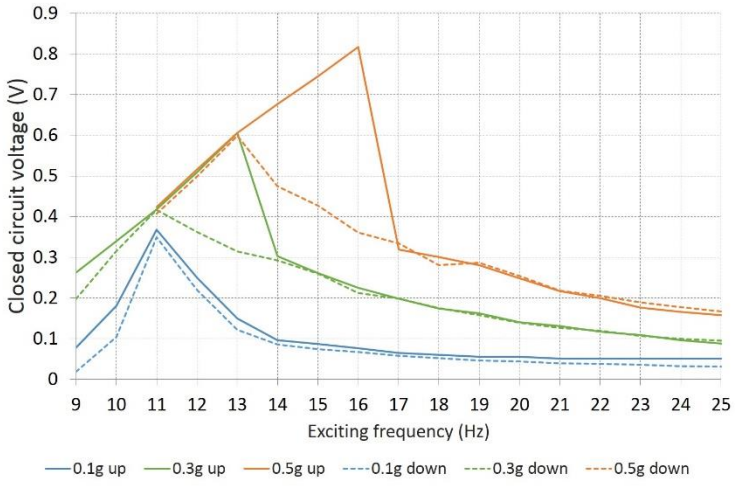

(a)

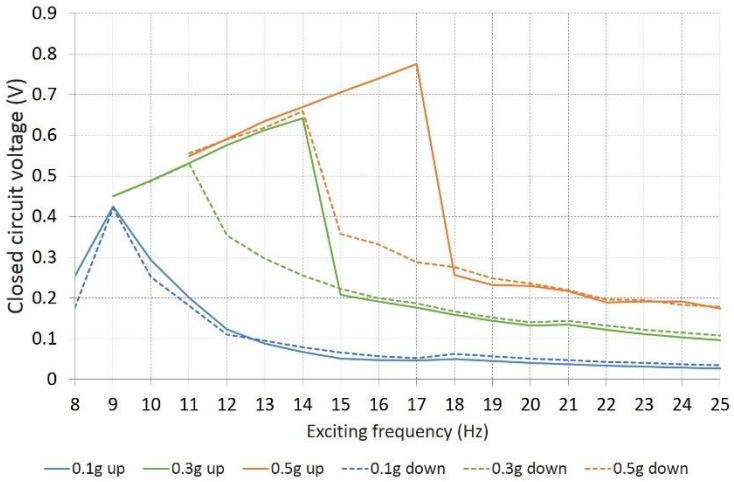

(b)

Figure 5.12 The hysteresis effect of the load voltage (Vrms) at various acceleration levels for (a) SMH and (b) CMH (solid line=up sweep and dash line=down sweep).

Table 5.4 Maximum voltage and power output of the harvesters at different acceleration levels.

Acceleration level	Single-magnetically levitated harvester (SMH)		Coupled-magnetically levitated harvester (CMH)	
	Voltage (Vrms)	Power (μW)	Voltage (Vrms)	Power (μW)
0.1*g*	0.368	50.9	0.425	67.9
0.3*g*	0.605	137.7	0.642	154.9
0.5*g*	0.816	250.4	0.775	225.8

In Figure 5.12, the resonant frequencies change with increasing acceleration amplitudes, shifting from 9 Hz to 17 Hz and 11 Hz to 16 Hz for CMH and SMH, respectively. The two harvesters did not demonstrate nonlinear behaviour at 0.1$\boldsymbol{g}$ due to high damping. At higher acceleration levels, the frequency response indicates a hard nonlinearity which produces hysteresis in the response. The hysteresis regions are broader in a frequency up-sweep as the acceleration amplitudes increase. The operating frequency of CMH is lower than that of SMH. This lower operating frequency implies that CMH is more suitable for harvesting energy from low-frequency excitation, e.g. human movement.

5.3.2.3 Hip-motion excitation

The average voltage and power output of SMH and CMH across a load resistance of 2.66kΩ were recorded during walking (2.6 km/h) and running (7 km/h) on a treadmill, as presented in Table 5.5.

Table 5.5 Closed circuit voltage and output power harvested during walking and running.

	Closed circuit voltage (Vrms)		Output power (μW)	
	Walking	Running	Walking	Running
SMH	0.107	0.346	4.32	45.02
CMH	0.122	0.314	5.61	37.07

Results in Table 5.5 are consistent with the simulation results in Section 5.2.2.2. While CMH offers higher voltage and power output during walking, SMH is better when running. However, the output of CMH can be improved by including the lower coil.

Figure 5.13 shows the load voltage of CMH at the upper and lower coils. The synchronisation of the waveforms enables the upper and lower coils of CMH to be connected in series, to improve the measured load voltage and power output. Then, the upper and lower coils of CMH were connected in series to measure the load voltage and power output generated during walking and running on a treadmill.

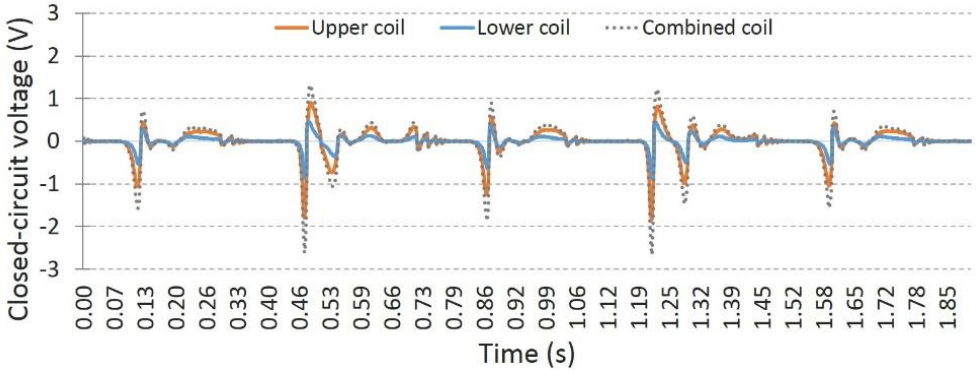

Figure 5.13. Closed circuit voltage output of CMH from the upper and lower coil.

The voltage increases from 0.122 to 0.170 Vrms during walking and from 0.314 to 0.448 Vrms during running. However, due to the increase in total coil resistance, the

power generated by the serial-coil connection only shows a small increase to 5.63 μW and 39.4 μW during walking and running respectively. The improved output voltage will be beneficial in rectifying electronics, resulting in reduced electrical losses. Also, there is the possibility of optimizing the bottom coil magnet arrangement, which may provide further improvement.

5.4 Discussion

Under sinusoidal excitation, the dynamic behaviour of the harvesters simulated using FEA and Matlab/Simulink are consistent with the experiment results, as presented in Figure 5.14 and Figure 5.15, which are comparisons of open-circuit and closed circuit voltage under various excitations.

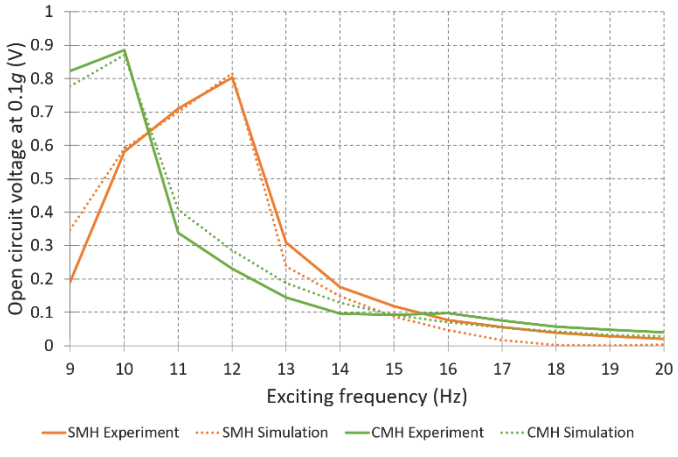

(a)

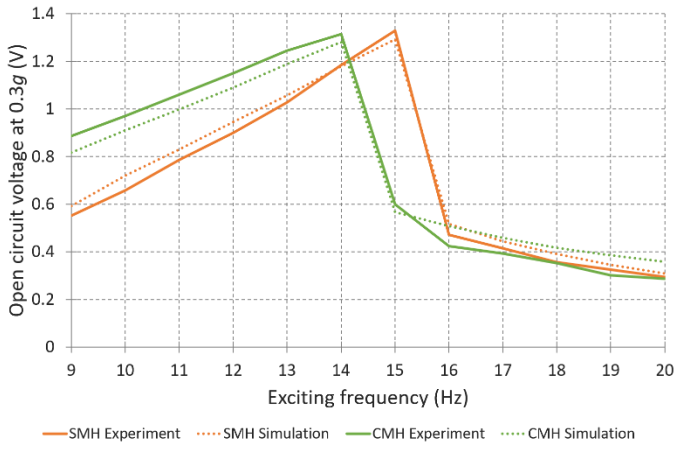

(b)

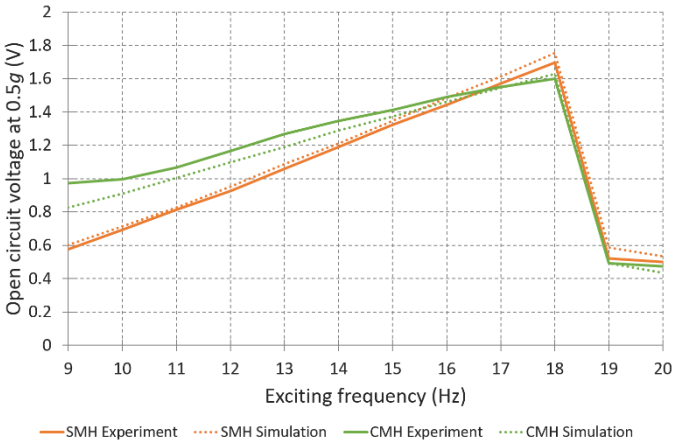

(c)

Figure 5.14. The simulation and experimental comparisons of the open-circuit voltage (Vrms) under the sinusoidal excitations of (a) 0.1***g***, (b) 0.3***g***, and (c) 0.5***g***.

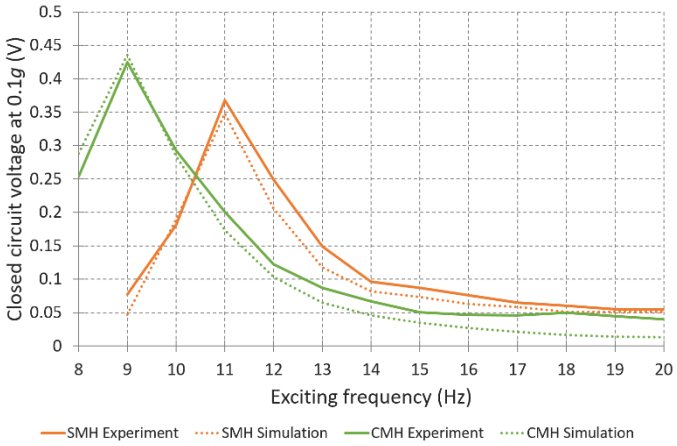

(a)

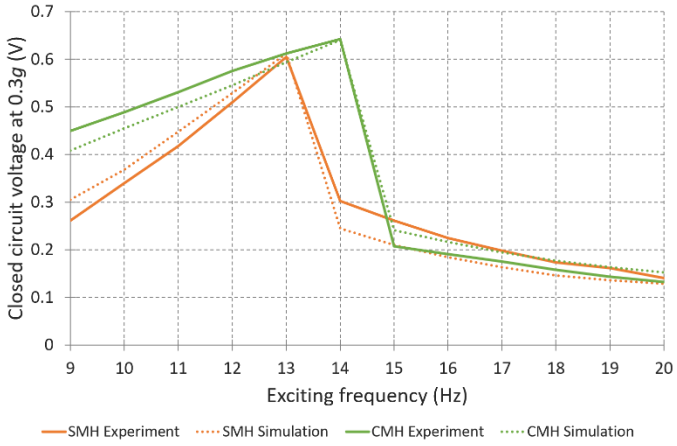

(b)

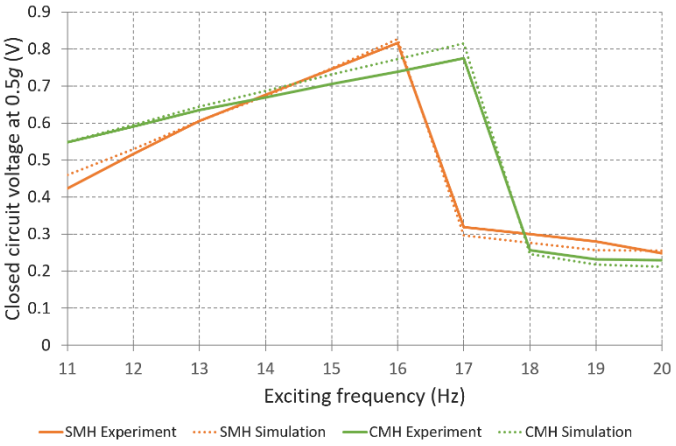

(c)

Figure 5.15. The simulation and experimental comparisons of the closed circuit voltage (Vrms) under the sinusoidal excitations of (a) 0.1***g***, (b) 0.3***g***, and (c) 0.5***g***.

These results are in good agreement and also confirm the validity of the simulation model. This can aid with the optimisation of the harvester design and predictions relating to harvested power. However, this model still needs further development, especially when used under dynamic excitation such as human motion. Referring to the results presented in Section 5.2.2.2, the amount of induced voltage simulated during walking and running is still over-predicted. The variation of parasitic mechanical damping with velocity could be accounted for by the restricted use of the model. Future studies on the characteristics of damping force and the energy of collisions in correspondence with random excitation, are required to enhance the efficiency of the simulation model.

5.5 Summary

This chapter has investigated the dynamic behaviour of the single-magnet harvester (SMH) and the coupled-magnet harvester (CMH) with simulations and experiments. The experiment results provide a complete validation of the theoretical and dynamic models and could be used to design and optimize the behaviour of future harvesters.

The work presented in this thesis shows the feasibility of harvesting useful energy from hip movement using SMH and CMH. CMH demonstrates better performance than SMH at a low acceleration level. Compared with SMH, output power of CMH under a low excitation level of 0.1$\boldsymbol{g}$ and hip movement during walking increases from 50.9 to 67.9 μW and from 4.3 to 5.6 μW, respectively. However, the unavoidable collisions due to size constraints have limited the efficiency of CHM under high acceleration levels. SMH exhibits better performance in response to high levels of excitation due to more space being available for moving-mass displacement. Although the limited displacement and velocity result in the reduction of output power, especially at high-amplitude excitation, the voltage induced in the lower coil of CMH can be exploited to enhance harvester performance. It is worth mentioning that collisions between moving magnets and end bumper can increase the operation bandwidth of both energy harvesters.

This study investigates a way to broaden the frequency bandwidth within a compact harvester design. Using two coupled moving magnets ensures that the operating frequency of the device is lower. This approach is useful for harvesters driven by low-frequency excitation.

Chapter 6

Temperature Dependence of the Harvester

6.1 Introduction

The strength of the magnets naturally has a large influence on the dynamic characteristics and output power of the electromagnetic vibration energy harvesters. However, it can be affected by ambient temperatures which vary from applications to applications. The effect of temperature on the electromagnetic transducers has been carried out by many works especially in the processes of design and fabrication. Glynne-Jones *et al*. [119] addressed the compatibility of the operating temperature and the magnet type to maintain strong flux density for a high degree of coupling. Neodymium-Iron-Boron (NdFeB) has been chosen for their electromagnetic generator to be compatible with the car engine application, which has a working temperature of up to 120°C. In [120] the authors reported on a method for improving the fabrication process of the electromagnetic energy harvester using buried NdFeB and concluded that the process temperatures should be maintained below 60°C to avoid the demagnetisation of the magnetic film, which otherwise would cause deterioration in the performance of the final device. These highlighted the importance of considering the temperature effects when designing and fabricating the electromagnetic transducers. Despite this interest, the temperature effect on the performance of the electromagnetic vibration energy harvesters has not been well studied.

Although the effect of temperature on the harvesters proposed in this work is least important due to the limited temperature range of human applications (0°C – 40°C), the characterisation of electromagnetic energy harvesters under various ambient

temperatures still need to be fully understood in order to develop for further applications. Therefore, the temperature dependence of a magnetically levitated electromagnetic vibration energy harvester is investigated in this chapter regarding the fundamental properties such as the variation of magnetic flux density, the resonant frequency, damping ratio, quality factor and open circuit output voltage.

6.2 General background

Temperature is a significant parameter that greatly affects the variation of magnetic properties as carried out by many researchers. Works by Hu *et al* [121] show that the coercivity of permanent magnets alters with different temperatures. Refer to [122], magnets start to lose their magnetism when they are operated at an ambient temperature that exceeds their Curie temperature. Also, the temperature-dependent equations given by [123] indicate that the magnetic characteristics of permanent magnets such as the remanence and coercivity decrease with rising ambient temperature. Luo *et al* [124] have highlighted that the effect of temperature should be considered alongside the grade of magnet used because the low Curie temperature of some magnets leads to a limited operating temperature range close to room temperature that may not be applicable to other applications. Example specified temperature ranges for different types of applications include 0°C to 70°C for commercial, -20°C to 85°C for industrial, -40°C to 125°C for automotive and -55°C to 125°C for the military. Typical temperature properties for a range of magnet materials are provided in Table 6.1.

Table 6.1 Typical Temperature properties of magnet materials [125], [126].

Properties	Neodymium magnets	Samarium Cobalt Magnets	Alnico Magnets	Ferrite Magnets
Max. Operating Temperature	80°C	300°C	450°C	250°C
Min. Operating Temperature	-138°C	-273°C	-75°C	-20°C
Curie Temperature	310°C	700°C	800°C	450°C
Temp. coefficients of Induction, α_{Br}	-0.12%/°C	-0.05%/°C	-0.03%/°C	-0.2%/°C
Temp. coefficients of Coercivity, α_{Hci}	-0.6%/°C	-0.3%/°C	-0.02%/°C	+0.27%/°C

The influence of temperature on magnetic properties highlights the impact of temperature variations on the characterisation of all electromagnetic energy harvesters. The change of magnetic flux density, the resonant frequency, damping ratio/quality factor, the velocity of relative motion, open circuit output voltage and the optimal load resistance are all affected by temperature. To investigate the performance and fundamental properties of the magnetically-levitated energy harvester, a comprehensive set of experimental and simulation results are provided. Figure 6.1 shows the electromagnetic harvester used in this work. It represents a standard configuration demonstrated in several devices in the literature [57]–[62], [127], with some variations in the design and arrangement of the moving-mass components.

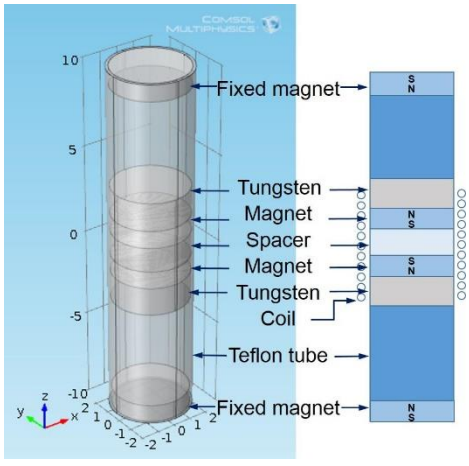

Figure 6.1 Model of magnet levitated harvester.

It consists of two fixed magnets at the top and bottom of a Teflon tube. The tube contains a moving mass consisting of two cylindrical magnets with a ferromagnetic spacer placed in between them to join the magnets and concentrate the magnetic flux. The magnets have been aligned with like-poles facing each other and levitated by the repulsive magnetic force. The voltage is induced in a stationary copper coil due to the variable and moving magnetic field that intersects it. The magnet chosen for this harvester is NdFeB permanent magnets which has a high magnetic coercivity, high resistance to being demagnetised, and strong mechanical strength [128]–[130]. The magnetic flux density generated by the magnets at different temperatures was simulated as shown in Figure 6.2.

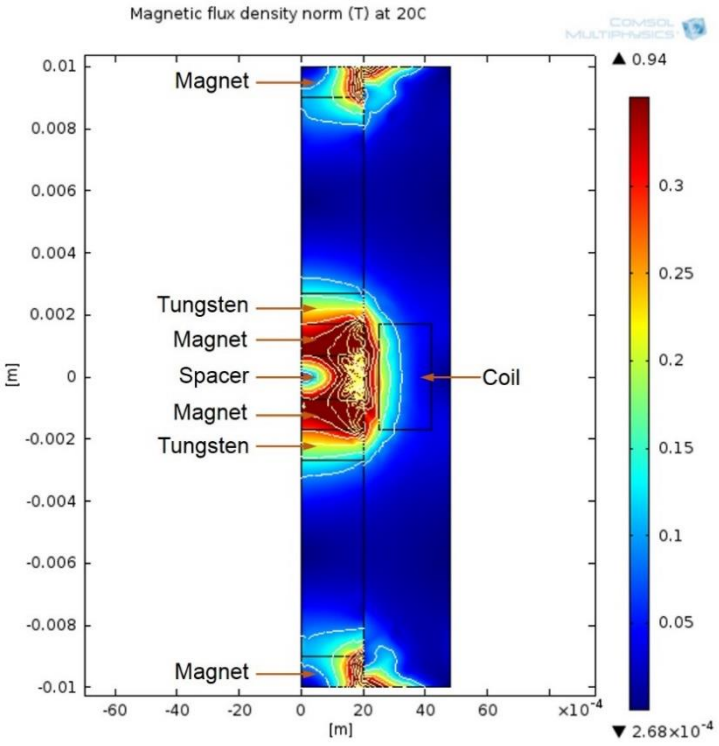

(a)

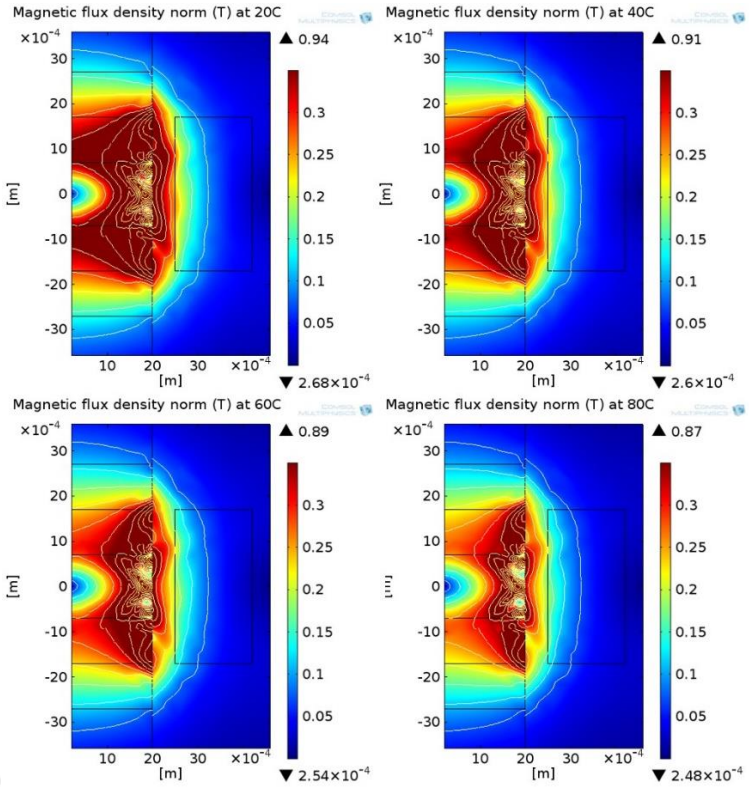

(b)

Figure 6.2 (a) The magnetic flux density of the harvester with (b) zoomed view around the moving magnet and a stationary copper coil at a temperature of 20°C,40°C, 60°C, and 80°C.

The nonlinear behaviour is due to the interaction between the fixed and moving magnets. The magnetic forces are nonlinearly varying with separation distance which results in a nonlinear magnetic spring. The properties of the magnetic spring are determined by the properties and strength of the magnets. Thermal demagnetisation of the permanent magnets will reduce the performance of the harvester and change the dynamic behaviour of the magnetically levitated energy harvester. These effects will be explored using both simulation and experimental analysis. Moreover, the results can be adapted for other types of devices.

The characteristics of a magnetic material are usually shown by its hysteresis plot, which illustrates the ability to retain its magnetisation. The hysteresis behaviour is indicated by magnetic parameters such as coercivity (H_c) and remanence (B_r). The ability of the magnet to resist demagnetisation is specified by the value of coercivity

(H_c) with higher values meaning it is harder to magnetise or demagnetise the material [131]. The residual magnetisation after the removal of the external magnetic force used to polarise the magnet is denoted by the remanence (B_r) [132]. The higher the remanence, the larger the magnetic flux density (B) produced by the magnet. This correlation can be described by equation (6.1) which is an estimate of the magnetic flux density, B, produced by a cylindrical magnet [133].

$$B(S) = \frac{B_r}{2}\left(\frac{(S+L)}{\sqrt{(S+L)^2+R^2}} - \frac{S}{\sqrt{S^2+R^2}}\right) \tag{6.1}$$

where S is the distance from a pole face on the symmetrical axis (m), L is the length of magnet (m), and R is the radius of magnet (m). The relationship of remanence (B_r) and the coercivity (H_c) can be presented by [134]

$$B_r \approx \mu_0 H_c \tag{6.2}$$

where $\mu_0 = 4\pi\times10^{-7}$ H/m is the permeability of free space and the coercive field $\mu_0 H_c$ is about 4-8% less than B_r. The information about the variation in these properties can be acquired by observing the demagnetisation curves in the second quadrant of the hysteresis loop [135]. The temperature coefficient of the remanence α_{B_r} has been used to estimate the change in remanence with temperature as expressed in % change per degree C by

$$\alpha_{B_r} = \frac{1}{B_r}\cdot\frac{\Delta B_r}{\Delta T} \quad [\%/°C] \tag{6.3}$$

where T is temperature. The remanence at different temperatures can be estimated by multiplying the temperature coefficients with the temperature difference to obtain the percentage changes in expected B_r. The Curie temperature, T_c, is another parameter to limit the operating temperature range of each magnetic material. Above this temperature, the permanent magnetic properties will be lost. For NdFeB

magnets, the Curie temperature varies depending upon the grade but typically ranges from 300 to 400°C, which is lower than some other rare-earth magnet such as Samarium-Cobalt ($T_c \cong$ 700 – 800°C) [118]. The practical maximum operating temperature will be less than the Curie temperature, and hence the relatively low T_c limits their applications [136] [137]. In order to apply NdFeB magnets properly in particular applications, the temperature dependence of their magnetic properties should be appreciated.

6.3 Magnetically levitated harvester

A conventional second-order spring, mass and damper system is also used to model this magnetically-levitated harvester and further characterised using the nonlinear model due to nonlinear vibration of a magnetic spring. The governing equation is same as the equation given for SMH mentioned in Chapter 4, which is

$$m\ddot{z}(t) + (c_p + c_e)\dot{z}(t) + kz(t) + k_3 z^3(t) = mg - m\ddot{y}(t) \tag{6.4}$$

The Duffing equation is assumed to describe the nonlinear behaviour of the spring force. The first order and third order terms are considered as dominant terms, as shown in equation (6.5).

$$F_S = \sum_{i=0}^{n} k_n z^n \approx k_1 z(t) + k_3 z^3(t) \tag{6.5}$$

where F_s *is* the magnetic restoring forces, k and k_3 are linear and nonlinear spring stiffness respectively, and $z(t)$ is the relative displacement of the seismic mass m and the base. The system characteristics can be analysed by the key parameters of conventional second-order spring, mass and damper system as follows:

$$\omega_n = \sqrt{k/m} \tag{6.6}$$

$$\zeta = \frac{c}{2m\omega_n} = \frac{c_m + c_e}{2m\omega_n} \tag{6.7}$$

$$Q = 1/\zeta \tag{6.8}$$

where ω_n is the natural frequency of the device, ζ is the total damping ratio, and Q is the Quality factor. These parameters are the key considerations for any further analysis (either analytical or numerical) of a magnetically levitated electromagnetic vibration energy harvester. The analysis of the energy harvester often involves determining the power transferred to the electrical load and the optimal load condition. Due to the complexity of nonlinear behaviours, the analysis can be achieved with the following simplifications [105], [138]:

$$R_{L\_opt} = R_C + \frac{\theta^2 c_m \omega_d^2}{(k - m\omega_d^2)^2 + (c_m\omega_d)^2} \tag{6.9}$$

$$\begin{aligned} P_{L_{opt}} &= \frac{1}{8}\frac{(a\theta m\omega_d)^2}{R_C((k - m\omega_d^2)^2 + (c_m\omega_d)^2) + c_m(\theta\omega_d)^2} \\ &= \frac{1}{8}\frac{a^2m^2}{c_m}\left(1 - \frac{R_C}{R_{L\_opt}}\right) \end{aligned} \tag{6.10}$$

where R_{L_opt} is the optimal load resistance, P_{L_opt} is the power transferred to an optimal load, R_C is the coil resistance, ω_d is the external exciting frequency, and a is the excitation acceleration levels. In the case of the levitated harvester, magnetic forces are acting in the place of a mechanical spring. Hence, the magnetic properties of the magnets will have a prominent effect on the characteristics of the harvester. In this chapter, we show the effects of the ambient temperatures on the key parameters of the levitated harvester caused by the changes of mechanical and magnetic properties. The link between the key parameters and temperature is the magnetic force, and

therefore the approximate model of the magnetic force (F_M) between two cylindrical magnets is given here for further reference [139].

$$F_M = \frac{3(\pi M R_1^2 L_1)^2}{8}[g(d) - g(d + L_2)], \tag{6.11}$$

where

$$g(x) = \left(\frac{1}{x^4} - \frac{R_2^2 + 3x^2}{3(R_2^2 + x^2)^3}\right) \tag{6.12}$$

The equation of the magnetic force composes of the geometrical constants R_1, R_2, L_1 and L_2 of each cylindrical magnet where R represents the radius and L represents the length of the magnet (m). The function of F_M can be separated into two parts:

1) A constant term $\gamma = \frac{3(\pi M R_1^2 L_1)^2}{8}$
2) The function in terms of the relative distance between the two magnets, d.

The constant (γ) shows a second order relationship with magnetisation M ($\gamma \sim M^2$). This explicitly shows the connection between F_M and the temperature, since the magnetisation can be expressed by the terms of the temperature-related quantity B_r as $B_r = \mu_0 M$ [140]. Moreover, if B_r is assumed to vary linearly with temperature T in equation (6.3), F_M should vary quadratically with temperature. The second part of F_M is expressed by the function $f(d)$ in terms of the relative displacement between the associated magnets. Therefore F_M can be transformed into a polynomial expansion.

$$F_M = \gamma \sum_{i=0}^{n} \acute{k}_i d^n \tag{6.13}$$

For the levitated devices, the magnetic forces are modelled as the nonlinear restoring spring force F_S. Hence F_S is then represented by the total magnetic force of F_{M1} and F_{M2} as seen in Figure 6.3.

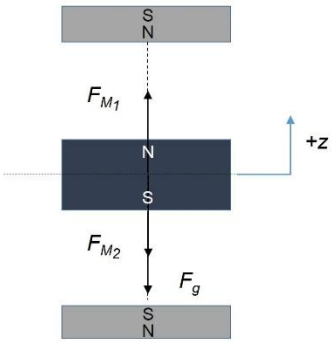

Figure 6.3 Free-body diagram of force on the moving magnet.

The relative displacements between magnets d_1 and d_2 can be given by an offset of the relative displacement z between the seismic mass and the base. So, F_S can be rewritten in the form of polynomial expansion in terms of z.

$$F_S = F_{M_1} - F_{M_2} = \gamma \sum_{i=0}^{n} \tilde{k}_i z^n \tag{6.14}$$

Assuming that the Duffing equation can closely explain the nonlinear behaviour of the device, F_S should be able to approximately fit into the polynomial form described in equation (6.5).

$$F_S = \gamma \sum_{i=0}^{n} \tilde{k}_i z^n \approx \gamma \tilde{k}_1 z + \gamma \tilde{k}_3 z^3 = kz + k_3 z^3 \tag{6.15}$$

According to the equation (6.15), all stiffness coefficients of the nonlinear spring contain the constant termγ, derived from the magnetic force, therefore they can be rewritten in the quadratic form of the temperature. The experiment presented in section 6.5 will experimentally test this hypothesis for the relationship between the spring stiffness coefficients and temperature proposed in this section.

6.4 Experiment procedures

The Neodymium magnet used in this work is the sintered N35 grade NdFeB permanent magnets with a diameter of 4 mm and a thickness of 1 mm. Its magnetic properties are given in Table 6.2.

Table 6.2 Magnetic properties of N35 NdFeB magnets at room temperature [117], [118].

Properties	Parameter	Value	Unit
NdFeB magnet grade	-	N35	-
Remanence	B_r	1170-1220	mT
Coercive Force	H_c	≥ 868	kA/m
Intrinsic Coercive Force	H_{ci}	≥ 955	kA/m
Max. energy product	$(BH)_{max}$	263-287	kJ/m^3
Max. Operating Temperature	-	80	°C
Temp. coefficient of remanence	α_{B_r}	-0.12	%/°C
Temp. coefficient of coercivity	α_{H_c}	-0.6	%/°C

For the purposes of simulation, the values of remanence B_r at different temperatures obtained from the N35 magnet datasheet have been applied to the simulation model using COMSOL to calculate parameters, e.g., magnetic flux density, magnetic forces, and induced voltage. Although the value of remanence B_r provided in the datasheet was only stated at room temperature (20°C); the values at the temperature of 30°C, 40°C, 50°C, 60°C, 70°C, and 80°C can be calculated by using equation (6.3) and the temperature coefficient of remanence, α_{Br}, mentioned in Table 6.2. The values of remanence B_r at different temperatures are presented in Table 6.3.

Table 6.3 The remanence of N35 NdFeB magnets at different temperatures.

Temperature (°C)	20	30	40	50	60	70	80
Remanence, B_r (Tesla)	1.20	1.18	1.17	1.15	1.14	1.13	1.11

To study the temperature effect on the characteristics of the magnetically levitated harvester, the experiments have been separated into three sections. In section 6.5.1, static measurements of the magnetic flux density B of a N35 cylindrical magnet from

room temperature to 80 °C are presented. This includes direct measurement of B on the top surface of the magnet using a Gauss meter model GMET H001. The variation of the quiescent position (z_0) and the magnetic forces (F_S) on the floating magnet at different temperatures are also presented. The quiescent position, z_0, was quantified to compare with the experimental results by calculating the position at which the magnetic forces, F_S, on the levitating magnet is equal the gravitational force, F_G, as given by

$$F_S(z_0) = F_{M_1}(z_0) - F_{M_2}(z_0) = mg \tag{6.16}$$

The quiescent position (z_0) is one of the parameters used to indicate the strength of magnetic field under various ambient temperatures. Section 6.5.2 presents measurements of the dynamic properties of the harvester taken in an environmental chamber. The harvester shown in Figure 6.1 was tested on a shaker table located within the chamber in order to measure the resonant frequency and the output voltage of the harvester generated under various ambient temperatures. These measurements include stopping the shaker abruptly in order to record the attenuated impulse response of harvester, which enables the harvester's damping factor to be calculated. This section also demonstrates how the velocity changes with temperature and discusses the variation in the voltage induced due to the change in velocity and magnetic flux density. The effect of the temperature on the value of the optimal load resistance is clarified as well. Section 6.5.3 presents the influence of magnetic hysteresis on the performance of the levitated harvester. The ambient temperature of the harvester was cycled in an environmental chamber between the temperature of 20°C and 80°C. This heating and cooling processes take 30 minutes per cycle. The change in the resonant frequency of the harvester after temperature cycling is recorded at 1 cycle, 5 cycles, 10 cycles, 15 cycles, 20 cycles, 30 cycles, 40 cycles, and 50 cycles.

6.5 Results and Discussion

6.5.1 Static characterization of magnets and harvester

The magnetic flux density *B* of the magnet was measured at temperatures from 20°C to 80°C. Figure 6.4 shows the deterioration of magnetic flux density with rising temperature as measured by the experimentally and predicted by the simulation. There is a clear decrease in the magnetic flux density versus increasing temperature. The effect of this decrease can be identified when observing the inertial mass position in the magnetically levitated harvester at different temperatures as shown in Figure 6.5.

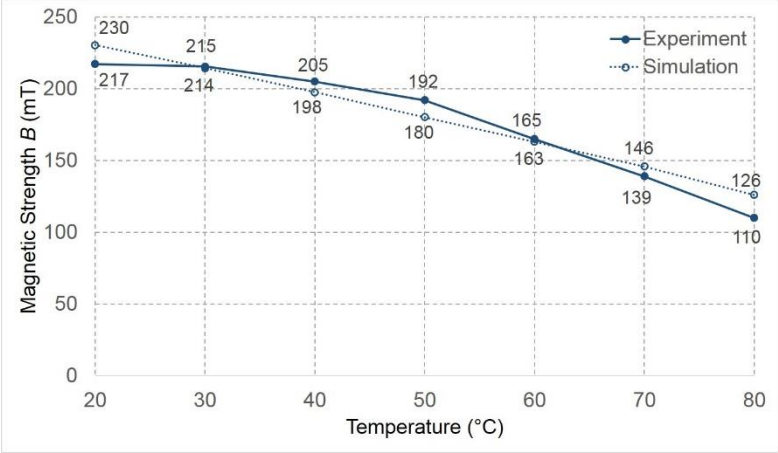

Figure 6.4 Temperature dependence of N35 NdFeB magnetic flux density.

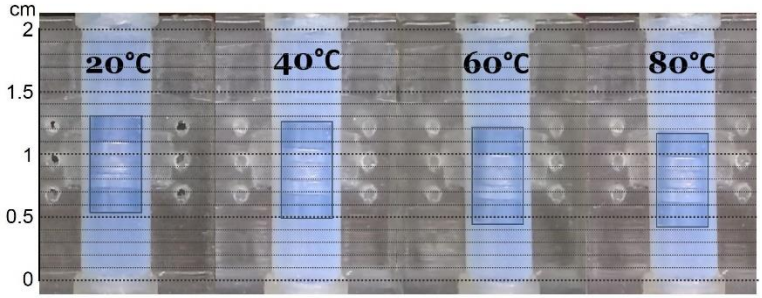

Figure 6.5 The quiescent position of moving mass at different temperature.

The initial moving-mass position decreases with increasing temperature. It can be described by the relation of magnetic flux density and magnetic force as expressed in equations (6.11). The reduced magnetic flux density of magnets due to the increased temperature reduces the magnitude of the force between moving mass and fixed bottom magnet which results in the reduced height of the quiescent position as illustrated in Figure 6.5. The quiescent positions calculated using equation (6.16) plus Comsol simulation are compared with the measurement results in Figure 6.6. The results from measurement and calculation are comparable and show a small offset of 0.3 mm approximately. The offset is caused by the parameters used in the simulation, e.g., remanence B_r, which was an approximated value taken from the range of the values provided in the datasheet.

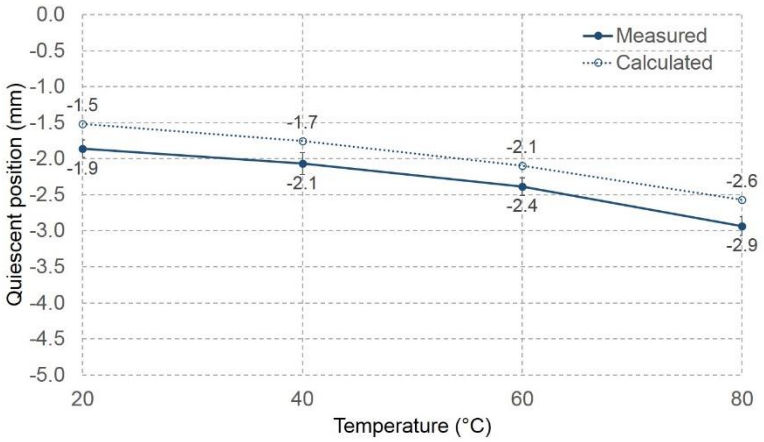

Figure 6.6 Measured and calculated the quiescent position of the levitating mass at different temperature.

Figure 6.7 shows the simulation results of the total forces (F_S-F_G) on the levitated mass versus relative displacement, z, at different temperatures. The net force increases as the moving mass approaches the fixed top or fixed bottom magnets. Furthermore, it is clear that the net force decreases with the rising temperature.

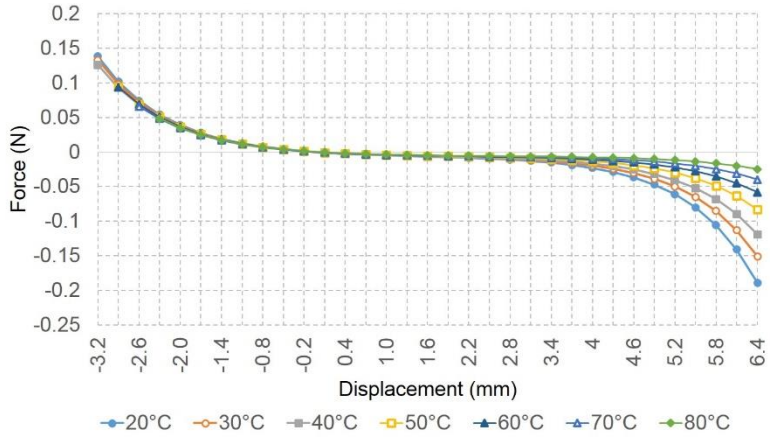

Figure 6.7 The total forces on moving magnet at different temperatures.

6.5.2 Dynamic characterisation of the harvester

The fabricated harvester (Figure 6.8) consists of two NdFeB cylindrical magnets pieces (Ø4 mm x 1 mm thickness) fixed in position at the top and bottom of the Teflon tube (Ø4.32 mm ID x 0.51 mm wall x 20 mm length). The coil is wound from Ø50 µm copper wire with 1,100 coil turns, and this is positioned mid-way along the length of the tube. The moving mass was composed of two cylindrical Tungsten pieces (Ø4 mm x 1 mm thickness), two NdFeB magnets and a ferrite spacer with the same diameter of Ø4 mm as shown in Figure 6.1. The harvester was tested on an electromagnetic shaker located inside an environmental chamber for temperature control.

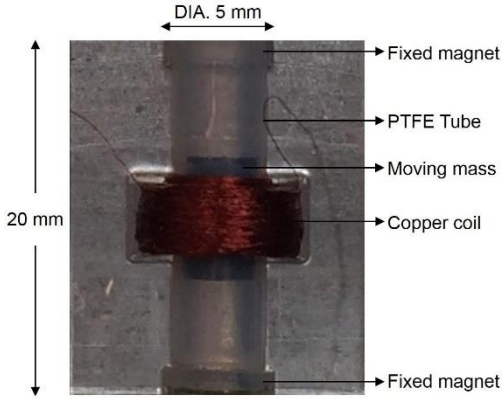

Figure 6.8 Fabricated magnetically levitated electromagnetic harvester.

6.5.2.1 Mechanical damping factor

The mechanical damping factor was measured when the harvester is open circuit to minimise electrical damping. It was determined by monitoring the decay in the harvester output after stopping the driving vibrations. The dependence of damping ratio with temperature is shown in Figure 6.9.

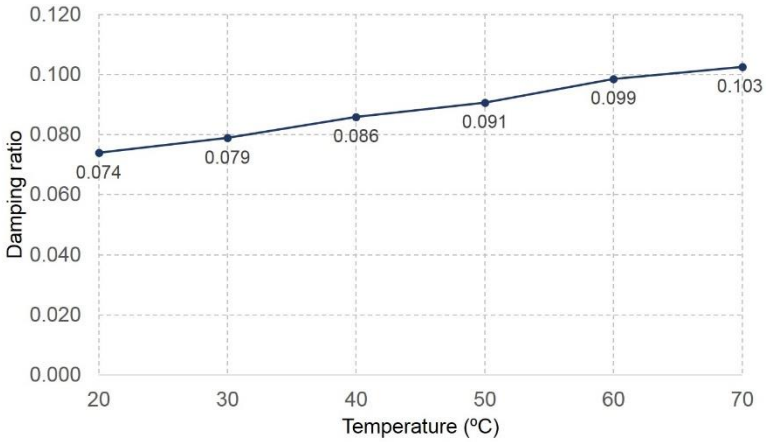

Figure 6.9 Variation of damping ratio with temperature.

The damping ratio is linearly increasing with the rising temperature. This is due to the increasing friction between the moving mass and inner surface of the tube. This is due to the unequal thermal expansion coefficients of the materials used in the harvester construction. The thermal expansion coefficient of Teflon tube (PTFE) is quite high; 143.3×10^{-6}/°C, when compared with other material as in Table 6.4 and this causes a reduction in the gap between the moving mass and the tube wall as the temperature increases.

Table 6.4 The coefficient of thermal expansion of materials used in harvester fabrication [141]–[143].

Material	Value	Unit
NdFeB	3.4	10^{-6}/°C
Tungsten	4.9	10^{-6}/°C
Mild steel	13	10^{-6}/°C
PTFE	143.3	10^{-6}/°C

This result is arguably more unforeseen than the previous results but is very important for the operation of the harvester. The level of damping reflects the level of unwanted mechanical losses, and these losses increase at higher temperatures. The effect on the harvester of the increased losses is described as follows.

6.5.2.2 Resonant frequency and spring stiffness

To measure the resonant frequency of the harvester, it was excited at 500 m$\boldsymbol{g}$ (1$\boldsymbol{g}$ = 9.8m/s^2) in the vertical direction in the temperature range of 20°C to 80°C. The measured resonant frequencies at different temperatures were compared with the simulation results as presented in Figure 6.10

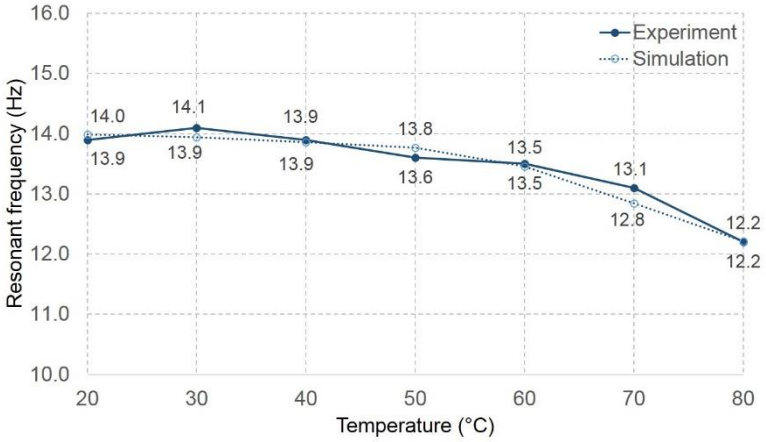

Figure 6.10 Variation of resonant frequency with temperature.

To predict the resonant frequency of the harvester, the linear and nonlinear spring stiffness (k and k_3) at different temperatures are estimated by curve fitting on the net forces simulated in Figure 6.7 (see Appendix E for details). The polynomial expansions of F_s from curve fitting can be aligned with the assumption of the nonlinear spring force described in equation (6.5). The spring stiffness parameters estimated from the fitting equations are presented in Table 6.5. Any variation in magnetic force results in the change of spring stiffness. For a fixed moving magnet displacement, a reduction in the magnetic forces will lead to a lower spring stiffness, which lowers the resonance frequency of the energy harvester according to (6.6).

Table 6.5 The spring stiffness of the harvester at different temperatures.

Temperature (°C)	20	30	40	50	60	70	80
Linear spring stiffness, k (N/m)	7.49	7.44	7.35	7.26	6.94	6.32	5.71
Nonlinear spring stiffness, k_3 (N/m^3)	$8.3e^{-5}$	$8.1e^{-5}$	$8.5e^{-5}$	$5.9e^{-5}$	$4.6e^{-5}$	$3.5e^{-5}$	$2.5e^{-5}$

The polynomial fit has been applied to the stiffness-temperature curve to show the effect of temperature on the spring stiffness, k as shown in Figure 6.11. This relation can be expressed in quadratic and cubic forms as

$$\text{Quadratic fitting: } k = -0.0007T^2 - 0.042T + 6.9 \quad (6.17)$$

$$\text{Cubic fitting: } k = -6.9e^{-6}T^3 + 0.00034T^2 - 0.0054T + 7.5 \quad (6.18)$$

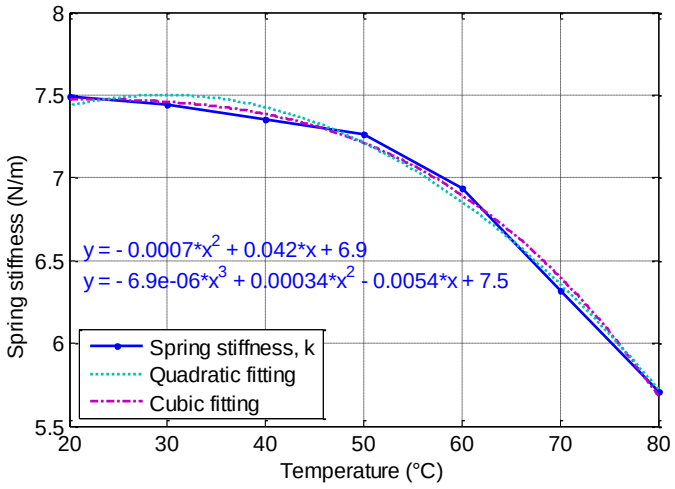

Figure 6.11 The spring stiffness estimated from curve fitting at different temperatures.

According to the results from curve fitting, the quadratic form has given an acceptable approximation in comparison to the cubic form. The norms of residuals for cubic and quadratic fitting are 0.15423 and 0.11562 respectively. The dominant terms of both equations are the 1st order and the 2nd order. Therefore, this confirms the hypothesis that the function of spring stiffness, k. can be expressed in quadratic form as mentioned in section 6.3.

In Figure 6.10, the resonant frequency reduces as the temperature is increased. This is due to the reduction in the magnetic forces as the consequence of the lower magnetic field as mentioned in (6.11) resulting in reduced spring stiffness as the relation in (6.15). This is a serious consideration for resonant energy harvesters tuned to a target frequency present in the environment. The change in resonant frequency could lead to a significant drop in the output of the harvester.

6.5.2.3 Open circuit voltage

The electromotive force (*emf*) or voltage induced in a coil is proportional to time-rate change of magnetic flux linkage through a coil, given by [144]

$$V_{emf} = -\theta \dot{z}(t) = -NBl\dot{z}(t) \tag{6.19}$$

where V_{emf} is induced voltage, N is number of coil turns, B is the flux density, A is the area of the coil, l is length of a coil, and $\dot{z}(t)$ is the velocity of the relative motion which can be determined from (6.4) as

$$\dot{z}(t) = \frac{\omega_d Y \sqrt{1 + \left(2\zeta \frac{\omega_d}{\omega_n}\right)^2}}{\sqrt{\left(1 - \left(\frac{\omega_d}{\omega_n}\right)^2\right)^2 + \left(2\zeta \frac{\omega_d}{\omega_n}\right)^2}} \sin(\omega_d t - \phi) \tag{6.20}$$

where Y is the amplitude of external sinusoidal vibration, and ϕ is the phase angle. At resonance the induced voltage simplifies to

$$V_{emf} = -NBl\frac{\omega_n Y}{2\zeta} \tag{6.21}$$

Equation (6.21) succinctly summarises the effects of the change in magnetic and dynamic properties of the harvester on the output voltage. It is clear the magnetic flux density, B, has a direct effect on the induced voltage. The reduction in magnetic flux density due to the dependence of the remanence B_r (Eq. (4.3)) on temperature also

reduces the spring constant, which in turn reduces the resonant frequency. The fall in the resonant frequency reduces the relative velocity of the magnets, and this also reduces V_{emf}. The increase in the damping ratio with temperature will also reduce the velocity. The combined effect of the increasing damping ratio and decreasing resonant frequency on the relative velocity is shown in Figure 6.12(a). The net effect on the induced voltage of these factors is shown in Figure 6.12(b).

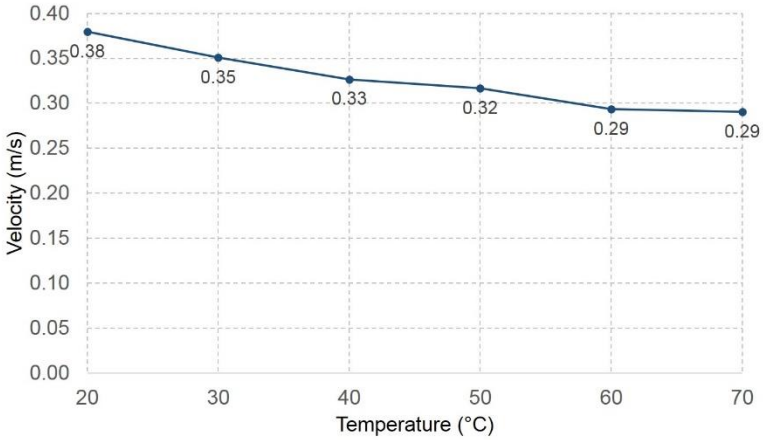

(a)

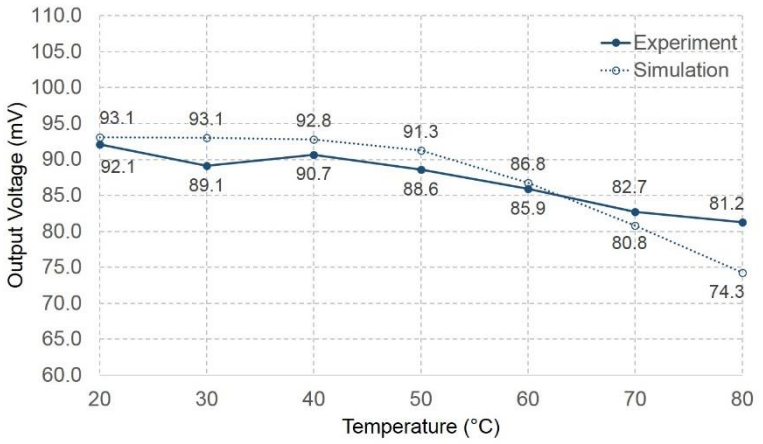

(b)

Figure 6.12 Variation of (a) velocity and (b) Output voltage with temperature.

Figure 6.12(b) shows the open circuit output voltage generated by the energy harvester when excited by an electromagnetic shaker under different temperatures. The excitation level was fixed at 500 m$\boldsymbol{g}$ and the excitation frequency was varied to

maintain resonance across the temperature range. The induced voltage is decreasing with rising temperature, which is consistent with the simulation result.

Since both B and velocity affect the induced voltage then, provided constant coil parameters, the decrease in B and velocity will both contribute to the lower induced voltage. Simplifying the harvester model as in Figure 6.3 to describe the amount of voltage induced under the influence of B, it implies that the direct effect of the change in the magnetic flux density B is the most significant effect on the open circuit output voltage. Using the equations (6.5), (6.6) and rewriting (6.21) (see Appendix E for details), the induced voltage is given by

$$V_{emf} = \frac{-NB^2 l R_1^2 L_1 \pi}{\mu_0} . f(x) \tag{6.22}$$

where

$$f(x) = \sqrt{\frac{3Y[g(d) - g(d + L_2) - g(D - d - L_1) - g(D - d - L_1 + L_2)]}{4m\zeta}} \tag{6.23}$$

where D is the distance between fixed magnets, and function g is a function whose output value is dimensionless. It can be noted that the open circuit output voltage is proportional directly to the square of magnetic flux density.

6.5.2.4 Optimal load resistance

The effect of temperature on the values of the optimal load resistance R_{L_opt} at which the maximum power is obtained for a given frequency is presented in this section. The harvester was shaken at its resonant frequency, and the value of the optimal load resistance was recorded for different ambient temperatures. The results are presented in Figure 6.13. These results show good agreement with the results calculated using equation (6.9).

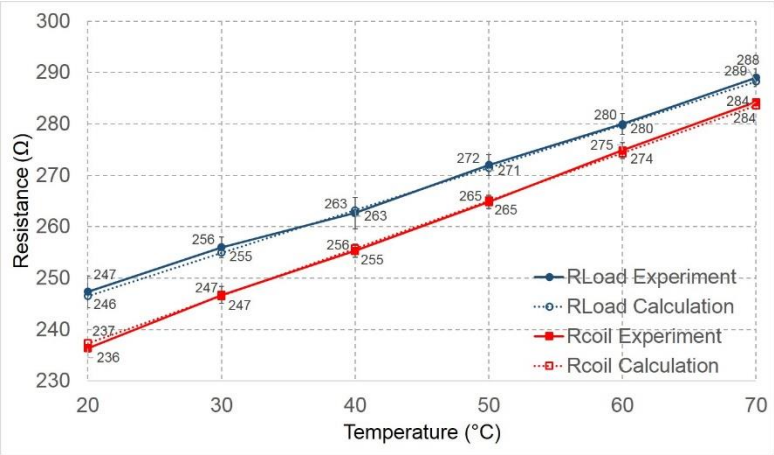

Figure 6.13 Variation of optimal load and coil resistances with temperature.

The results from Figure 6.13 confirm that the relationship between the coil resistance R_C and the temperature can be expressed by a linear model as follows [145].

$$R_C(T) = R_{C\_ref}\left[1 + \alpha_C\left(T - T_{ref}\right)\right] \tag{6.24}$$

where R_{C_ref} is the coil resistance at reference temperature T_{ref}, usually 20°C, and α_C = 3.9×10^{-3}/°C is the temperature coefficient of resistance of copper. The values of coil resistance R_C increases with the temperature and can be further used to evaluate the optimal load resistance according to (6.9). At resonance, the expression in (6.9) can be simplified to

$$R_{L\ opt} = R_C + \frac{\theta^2}{c_p} \tag{6.25}$$

The increasing value of R_C with the rising temperature affects the change in the values of R_{L_opt} as shown in Figure 6.13. The values of R_{L_opt} increase with increasing temperature as well and come close to the values of R_C at high temperature (>70°C). It can be described by the relation presented in (6.25). As the temperature rises, the value of c_p increases while the values of θ decrease due to the reduction in magnetic flux density B, resulting in the convergence of R_{L_opt} to the value of R_C. As a result, the ratio between R_{L_opt} and R_C approaches unity and the power delivered to the load will

be decreased with increasing temperature according to (6.10). This is shown in the results presented in Figure 6.14.

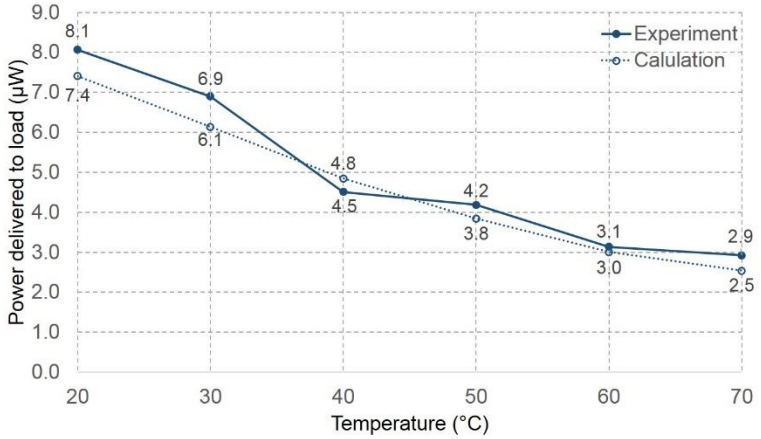

Figure 6.14 Variation of power transferred to load with temperature.

6.5.3 Temperature cycle test

The influence of hysteresis behaviour of a magnet on the levitated harvester is investigated in this section by recording the resonant frequency of the harvester after every 5 cycles of temperature cycling between 20°C and 80°C. The results are presented in Figure 6.15. After one cycle, the resonant frequency of the harvester decreases from 14.0 Hz to 12.0 Hz and then maintains this level (about 12 Hz) for all subsequent cycles.

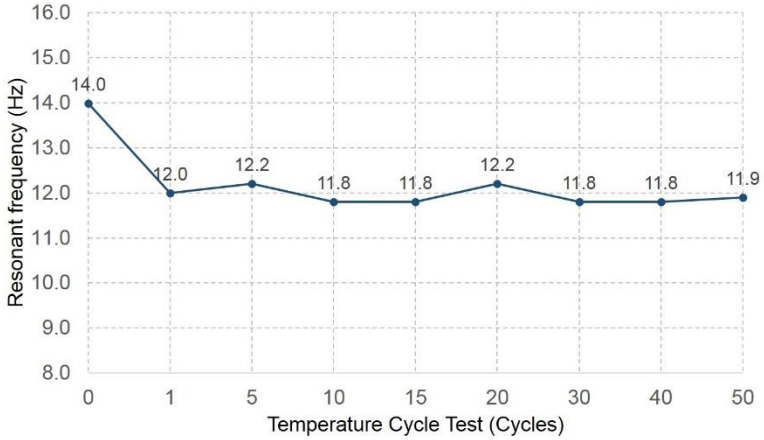

Figure 6.15 Variation of damping ratio with temperature.

When the temperature of the harvester was cooled down back to room temperature, the original strength of magnets was not recovered because the maximum temperature in the cycle test reached the maximum operating temperature of the Neodymium magnets which is 80°C. However, the resonant frequency of the harvester does not degrade further because the temperature cycling is within the same range of temperature (20°C - 80°C).

6.6 Conclusion

This chapter presents the influence of temperature on the performance of magnet levitated electromagnetic energy harvesters. Parameters investigated include magnetic flux density, resonant frequency, damping ratio, open circuit output voltage, the velocity of the relative motion and the load resistance. Both simulation and experimental results show that these properties vary with ambient temperatures.

The magnetic flux density reduces as the temperature increases which results in lower resonant frequency, lower relative velocity, lower open circuit output voltage and higher damping ratio. These parameters start to decline significantly since 50°C which is 30 degrees lower than the maximum operating temperature of the magnets used in the harvester. Varying resonant frequencies with temperature can lead to harvesters being de-tuned from the target vibration frequency, which could mean the harvester is no longer tuned to the application. The increasing damping ratio with the increasing ambient temperature indicates higher parasitic damping from increased mechanical losses. Decreasing magnetic field strength and increased damping ratios will also reduce output power even if the harvester's resonant frequency still matches the environmental vibration frequency. The effect of temperature on the value of the optimal load resistance can lead to a drop in the harvested power. This means the harvester is no longer matched to achieve the maximum harvested power. The specified maximum operating temperature of the magnets was found to lead to partial demagnetisation. When cycling from room to the maximum specified

temperature, the magnetic field was initially found to fall but remained constant thereafter. Harvesters were found to operate beyond the specified maximum operating temperature of the magnet but suffer from a reduced magnetic strength. These results highlight the importance of taking operating temperature into consideration when designing an electromagnetic energy harvester.

Chapter 7

Discussion and Conclusion

7.1 Summary

The main objective of this research is to develop power generation methods for sensor and communication systems within a hip replacement joint. To achieve the objective, the walking behaviour of hip-replacement patients and people with no hip conditions were first investigated in order to find out the frequency range and the excitation levels of people during walking and running which are important in designing the device structures. According to the low-frequency movements of human motion, the vibration energy harvesters operated at low frequencies (<20 Hz) have been reviewed with the focus on the electromagnetic vibration energy harvesters which offer high power density, low-cost fabrication and require no external voltage sources. Among the energy harvesters reviewed, the structure designed to avoid physical impact between components is believed to be suitable for the hip implant harvester due to consideration of reliability and durability of the device. The use of magnetic spring to levitate the moving magnet avoids the issue of spring fatigue in mechanical spring and is also suitable for harvesting energy over a wide frequency range due to its nonlinear behaviour. A broad frequency range of body motion would be covered, which implies more power be generated. For the hip implant applications, the volume constraint has a great influence on the electromagnetic harvester's performance, i.e. the power generated by small energy harvesters may not be high enough to power the monitoring system inside hip prosthesis. Therefore, methods to widen the bandwidth of the harvester and frequency up-conversion techniques have been reviewed to improve output power and device efficiency under low-frequency excitation. Minimum physical contact between components, size constraints and

the fatigue reduction are still the issues that need to be considered to maintain the reliability of the harvester.

Within the constrained volume of the hip prosthesis, two configurations of the magnetically levitated electromagnetic vibration energy harvesters were presented which are the single-magnetically levitated harvester (SMH) and the coupled-magnetically levitated harvester (CMH). Comprehensive results have been obtained to show that employing the coupled levitated magnets is a way to shift the operating frequency of the harvester to the lower range closed to the range of human motion (< 10 Hz). This is beneficial for more effective energy harvesting. Compared with SMH, the output power gained from CMH under a low sinusoidal vibration level of 0.1$\boldsymbol{g}$ and hip movement during walking were increased from 50.9 to 67.9 μW and from 4.32 to 5.61 μW, respectively. CMH outperforms other demonstrated harvesters in the literature with the highest normalized power density of 79.5 kgs/m^3.

Referring to the performance analysis, the proposed harvesters have some limitations due to the small volume available for the displacement of moving magnets. The limited displacement and velocity result in reduction of output power especially at high-amplitude excitation, e.g. running, where the parasitic damping is a dominant influencing factor. Integrating the bumpers to avoid the destructive collisions or packaging the harvester in vacuum could be a solution to increase the harvesters' performance.

The MATLAB/Simulink model with the FEA software has been developed as a tool for optimisation of the harvester design and prediction of the harvested power. A good agreement between the experimental measurements and the simulation result is found under the sinusoidal excitation. This validates the model to be used for further design constraints. However, the developed model might not be completely transferable to estimate the harvester performance under the intermittent excitation such as human movements. The variation of the parasitic mechanical damping with the velocity could be accounted for the restricted use of

the model. Future studies on the characteristic of the damping force in correspondence with the random excitation are required to enhance the efficiency of the simulation model.

The temperature dependence of a magnetically levitated electromagnetic vibration energy harvester was studied for further works in applications that vary in temperature. The investigation highlights that the performance of the harvester is largely dependent upon the strength of magnets which varies with ambient temperature. The reduction of magnetic flux density with the rising temperature has an effect on performance of magnet levitated electromagnetic energy harvesters such as resonant frequency, open circuit voltage and potentially output power. The harvester could be de-tuned from the target vibration frequency due to the variations in resonant frequency with temperature, and lead to a drop in the induced voltage and the harvested power. The operating temperature should be taken into consideration when designing an electromagnetic energy harvester.

This work is the first step towards enhancing the energy harvesting technique for hip implant applications and has raised many questions in need of further study. For in vivo experiments, more broadly research is also needed to determine specific materials avoiding the problem of toxic hazards in long-term implantations.

7.2 Research findings and achievements

This thesis demonstrates a feasible approach for a way to harvest energy from hip movement. The two electromagnetic energy harvesters use nonlinear behaviour to generate power from low-frequency excitation such as human hip motion. The value of research contribution lies in the modelling, design and implementation of the energy harvesting device for the instrumented hip implants. The summary of findings and achievements is as follows:

General insight

- The electromagnetic transduction mechanism is the preferred choice for the hip implant energy harvesting devices due to the high power density, the longevity and the ease of fabrication with a low-cost design.
- The performance of the electromagnetic harvesters is the size dependent. The size constraint of the hip implant applications results in the low power generated.
- The frequency spectra of the acceleration waveforms collecting from the hip-replacement patients (27 subjects) and the people without hip conditions (22 subjects) are dominant in the range of 0.7 - 2 Hz (walking) and 2.5 - 3.5 Hz (running). Most of harvestable energy is contained in the low-frequency range.
- The resonant electromagnetic energy harvester is not suitable for the hip implant applications because a large-scale structure has to be designed to operate at the low-frequency range of human body motions.
- The electromagnetic energy harvesters with a nonlinear structure using magnetic spring are preferred for the broad frequency excitations of hip motion due to the wide operating frequency range and the feasibility to operate at low-frequency range within a small volume of the harvester.

Harvester prototypes

- Two different configurations of the magnetically levitated electromagnetic energy harvester were designed: the single-magnetically levitated harvester (SMH) and the coupled-magnetically levitated harvester (CMH).
- The moving mass consisting of coupled magnets with like-poles facing each other and the spacer to join the magnets were found to provide a higher change rate of flux linkage in comparison with the moving mass using a single magnet. More voltage can be induced when using coupled magnets.

- Within the constraint volume of hip prosthesis, the harvester size is designed to be fit in a cylinder 2 cm in length and with a diameter of 7 mm. The optimal length of the coil and the optimal thickness of the magnets were determined to be 5 mm and 4 mm, respectively.
- The linear resonant frequencies of SMH and CMH are estimated to be 11 Hz and 9.95 Hz respectively.
- The operating bandwidth of CMH is wider than that of SMH referred to Table 5.1.
- For SMH, the closed circuit voltage generated at the optimal load of 2.66kΩ is 0.107 V_{rms} (0.41 V_{p-p}) and 0.346 V_{rms} (2.77 V_{p-p}) during walking and running respectively. The power output obtained is 4.32 μW (walking) and 45.02 μW (running).
- For CMH, the closed circuit voltage generated at the optimal load of 2.66kΩ is 0.122 V_{rms} (0.66 V_{p-p}) and 0.314 V_{rms} (2.54 V_{p-p}) during walking and running respectively. The power output obtained is 5.61 μW (walking) and 37.07 μW (running).
- CMH shows a higher voltage and a larger power generated compared to SMH at low acceleration level, i.e. walking, while SMH generates more power at high acceleration level, i.e. running.
- Experiment results show that at high acceleration levels, the unavoidable collision due to the size constraints has limited the efficiency of CMH harvesters.

7.3 Comparison with state of the art

A comparison of the proposed harvesters (SMH and CMH) with the selected electromagnetic vibration energy harvesters (EVEHs) from chapter 2 is presented diagrammatically in Figure 7.1 and Figure 7.2. All of the selected harvesters were designed for operating in a low-frequency range (<20 Hz). Most of them are cylindrical type magnetic energy harvesters except for [146], [147] and [75] which are magnetically sprung block type energy harvester. The details are summarised

in Table 7.1 with the performance matrics, i.e. the power density (PD) and the normalised power density (NPD). The PD is defined as the power output divided by the volume of the harvester, which is a commonly used metric in the literature due to the data required to calculate it being simple to obtain. However, it does not accounted for the characteristics of the vibration source. The harvesters excited under higher accelerations will have higher PD. To include the source effect, the NPD was proposed. It is the power output divided by the volume of the harvester and normalised to the acceleration level [148], which can be expressed as

$$NPD = P/A^2V \tag{14}$$

where P is the power output, A is the acceleration level, and V is the volume of the harvester. The NPD provides fairer comparison as the source and scale dependences have been considered. However, some other factors related to harvester effectiveness have not been considered, e.g. bandwidth, excitation frequency, and characteristic of the excitation source. Dividing the power output by the acceleration squared and the volume seems to favour larger devices, low frequency, and low acceleration. Nevertheless, the NPD can still be treated as a guide to indicate the relative performance level for the different harvesters analysed (low operating frequency (<20Hz) and the small volume of the device (<30 cm^3)).

Table 7.1 Comparison of the harvesters from literature.

Reference	Freq. (Hz)	Power (mW)	Acceleration (m/s^2)	Mass (g)	Volume (cm^3)	PD ($\mu W/cm^3$)	NPD (kgs/m^3)
SMH (This work) [a]	11	0.0508	0.981	1.53	0.83	61.3	63.71
CMH (This work) [a]	9	0.0679	0.981	2.11	0.89	76.5	79.50
Saha [57] [b]	8	0.0146	0.38	27	12.7	1.2	7.93
Foisal [58] [b]	9	1.18	1.6	3	7.389	159.7	62.38
Munaz [60] [b]	6	4.84	4.9	11.5	9.04	535.4	22.30
Berdy [61][146] [b]	6.7	0.41	0.981	7.7	7.7	53.3	55.33
Zhang [147] [b]	5.5	4.3	4.905	-	26	165.4	6.87
Sun [149] [b]	3.33	50	7.848	39.4	31.8	1572.3	25.53
Gutierrez [150] [b]	8.2	0.101	1.962	4.53	3.12	32.4	8.41
Lee [56] [b]	16	1.52	1.96	27.5	35.34	43.0	11.20
Ashraf [75] [b]	10.3	5.02	9.81	47	27.38	183.4	1.91

[a] Implantable devices
[b] Portable devices

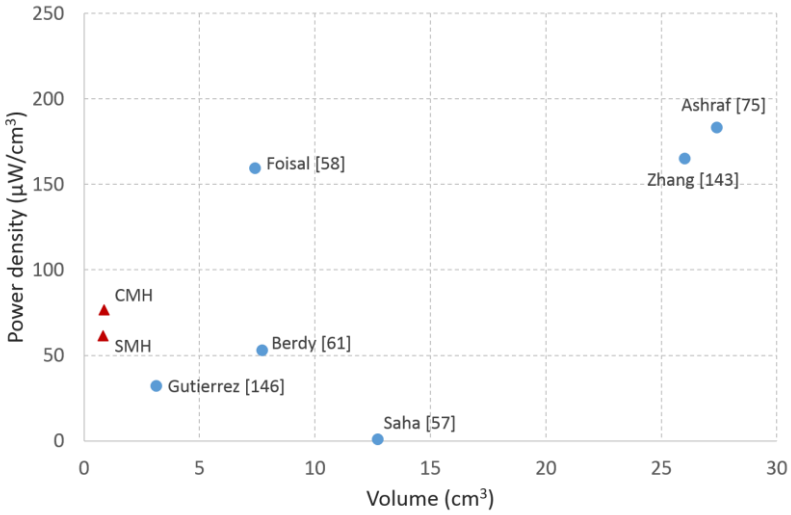

Figure 7.1. Power density versus volume of the harvesters.

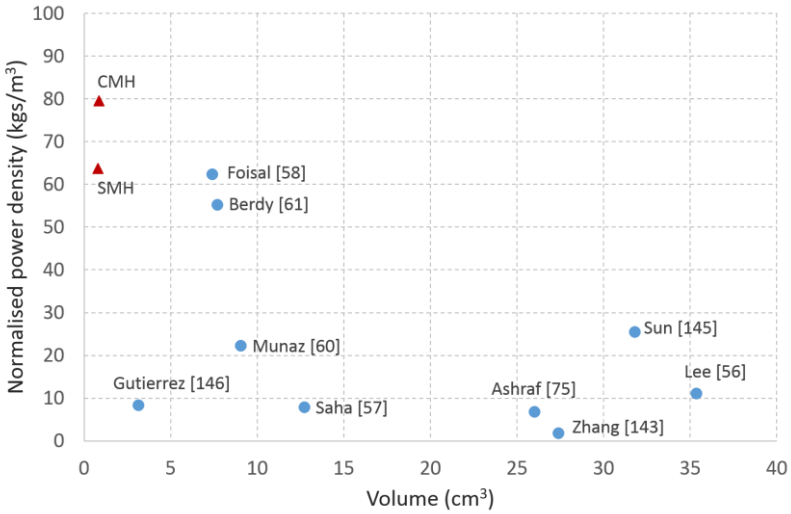

Figure 7.2. Normalise power density versus volume of the harvesters.

The PD is plotted against volume in Figure 7.1 for the EVEHs and the harvesters investigated in this thesis. In comparison with others, CMH and SMH harvesters demonstrate a comparable PD but possess the smallest volume. However, if the driving acceleration is taken into account, CMH and SMH harvesters outperform other EVEHs as illustrated in Figure 7.2. The coupled-magnetically levitated harvester (CMH) achieves the highest NPD with the smallest volume of 0.83 cm^3.

7.4 Challenge

To become a practical energy harvester for implantable applications, the challenges for the miniature energy harvesting devices are the power efficiency, fabrication, rectification, and energy storage. The remaining challenges are discussed in more detail below and inform the future work required in this area.

7.4.1 Power generation and efficiency

Performance of the electromagnetic vibration energy harvesters depends largely on the size of the harvester. The smaller the harvester, the lower the power generated. The reduced size of moving magnet due to form factor constraint of the hip implant harvesting devices results in the low output power, which is an inevitable problem for the miniature devices. Then, to achieve a maximum output power, matching the operating frequency of the harvesters with the ambient vibration frequency is recognized as being the most important consideration. However, designing a miniature energy harvester to be suitable for human movement applications that have a low operating frequency (<10Hz) is the main challenge. Also, human movement is an intermittent excitation. The harvesters designed with broad bandwidth, non-linear or non-resonant are preferred to capture the widest range of input frequencies from body motion and activities. Moreover, to improve the efficiency of the devices, an approach to mitigate parasitic losses is needed for future studies. The collision is unavoidable in the miniature devices designed for human movement applications, which has a large displacement. Further work on material integration for a perfectly inelastic collision, would help for enhancing the efficiency and stability of the devices.

7.4.2 Fabrication

The mechanical damping is recognized as being the most important factor that limits the efficiency of the miniature harvesters. For a magnetically levitated electromagnetic vibration energy harvester, the gravitational force and the air gap between the inner surface of the housing and the moving mass may induce the

viscous damping torque during the displacement of moving mass, which leads to the rotational motion of the moving mass. This causes the moving mass to decelerate and impede the vertical movement. In [61] the authors carried out an approach to reduce the tilt by adding the small guide rails on the inner surface of the housing. The power output was reported to improve by 50 percent according to their experiment results. In order to minimise the mechanical damping for energy efficiency, approaches to reduce the friction also need to be developed e.g. the low-friction materials and possibly lubricants. Also, the harvester in a vacuum is beneficial to mitigate losses due to air damping. Lowering the mechanical losses will lead to an improvement of the harvesting performance.

The constraint of the material and special packaging for bio-implanted applications cannot be ruled out. The problem of high corrosion and toxicity due to metal-ion release are also found in the fabricated materials used in this work, i.e. the copper and tungsten [151]–[153]. Other biocompatible materials such as gold could be applicable for fabricating the harvesting device, but with cost consideration. Encapsulation is another viable solution for any implantable devices to protect the device from body fluid penetration and avoid the toxicity problems. Various biocompatible materials have been applied for packaging the implantable devices, e.g. silicone, epoxy, titanium and glass. The silicone and the polymer-based epoxy encapsulations are suitable for short-term human contact (up to 6 months) because they could be swelled and dissolved inside the human body [8], [154], [155]. For the long-term implantation, the titanium and the glass encapsulations are preferable [156]. Finally, further studies that take reliability into account will need to be undertaken to ensure a long operating life span of the implantable devices.

7.4.3 Rectification and multiplier circuit

Voltage rectification is required for most kinetic energy harvesters due to the time-varying voltages generated. However, the low levels of output voltage generated from some human-powered energy harvesting devices could lead to an

additional challenge for subsequent rectification and voltage step-up circuits. Generating a voltage that exceeds the threshold voltage of the Schottky diodes, which have low voltage-drop characteristic (>0.23 V), can be problematic for some harvesters. Various approaches have been put forward to overcome this limitation. For instance, work by [76] presented an interface ASIC (Application-Specific Integrated Circuit) based on boot-strap rectification (BSR) technique as a passive rectifier to reduce the threshold voltage of the diodes. The voltage efficiency of rectifier stays above 70% for input voltage peak values above 0.2V. Apart from the bootstrapping circuits, precharged floating gate transistors [157] or different biasing arrangements [158] can also be applied to reduce the threshold voltage. In addition, the AC–DC conversion with voltage conditioning could be employed to achieve the required voltage rectification, conversion, and regulation. For example, the direct AC–DC converters proposed by [159] with the combination of a boost and a buck–boost converter reported a conversion efficiency of 61% with amplitude less than 0.5V is rectified. Moreover, the challenge of the start-up process should be taken into consideration especially for harvesting energy from low and intermittent excitation as mentioned in [160]. The decoupling filters and the input-power dependent power gating were demonstrated to improve the system operation under intermittent excitation. The start-up speed and the load cycles were increased with an improvement of 67% in the start-up time and a 50% increase in the operational frequency of the load. All of these interface circuits were addressed as a challenge for further research.

7.4.4 Energy storage

Due to the intermittent power generated from the random vibration source such as human motion, the energy storage devices would be needed to provide a steady power supply for the system. The storage component chosen is typically a high capacity supercapacitor or a rechargeable battery. The high energy densities of the batteries are preferable, but their limited number of charging cycles make them a less favourite choice particularly for the implantable medical devices. Supercapacitors have some advantages in comparison with batteries such as up to

a million charge-discharge cycles, fast charging time, wide temperature range and high power density (W/kg) [23]. However, there are some challenging issues for the miniature low-power harvesting systems with the intermittent vibration sources, i.e. the start-up phase, the charging time and the size of supercapacitors. The multiple start-up attempts may have occurred because the power could not be generated over a certain period of time. To complete the start-up phase, the size of storage element should be large enough which lead to prohibitively long charging time to achieve the required level of voltage. Further studies, which take the power conditioning circuit and the voltage regulator into account, will need to be undertaken in order to shorten the charging time of the supercapacitors and enable the system to work at a lower super-capacitor voltage. The size and capacitance of a supercapacitors should be considered to provide an acceptable charging time and operating duty cycle and be suitable for the volume available in particular applications.

7.4.5 Temperature

Although the effect of temperature on the performance of a magnetically levitated electromagnetic vibration energy harvester is least important in the human applications due to the limited working temperature (0°C – 40°C), the importance of considering temperature in the processes of packaging should be highlighted. Titanium encapsulation material has long been used in medical implants such as cardiac pacemakers as well as in the replacement hip, and knee joints due to the durability, resistance to corrosion, and a strong mechanical hardness [12], [94], [161]. However, a high-temperature laser welding technique (Titanium melting point >1600°C) is required for sealing the titanium encapsulation [162], [163]. This process may disrupt the magnetic strength especially in the small-size device, and results in compromising the device performance. Then, to minimize the risk of damaging the device during the welding process, the titanium housing would be substantially larger than the actual size of the device. Within the size constraints of the applications, glass encapsulation could be an option due to the cold-welding techniques which able to maintain the temperature inside the

implant's cavity to be less than 80°C [164]–[166]. Smaller implants are enable and also eliminate the heat damage to the encapsulated device.

7.5 Recommendations

Magnetically levitated electromagnetic vibration energy harvesters optimized for harvesting energy from the hip movement have been presented. The results so far have been very promising and could be useful for other low-frequency applications as well as when the excitation frequency varies with time. However, this work has raised many questions that need further study to advance the research. It is recommended that further research should be undertaken in following areas:

Simulation model

To predict the performance of the harvester, the simulation model plays an important role in the design process. However, in this work, some parameters applied in the simulation model still have to be determined experimentally, i.e. the mechanical damping parameter. Then, further work is needed to advance the simulation model, i.e. including the theoretical model of friction effect, air flow, and the pneumatic effect. Also, further studies on the variation of the damping under intermittent excitation should be carried on to establish a unified approximation model for a nonlinear energy harvester driven by random broadband vibrations. This could eventually lead to the accurate prediction for the characteristic and dynamic behaviour of the prototype before fabricating the real device.

Parasitic damping

The excessive parasitic damping has decreased the overall efficiency of the harvester. Packaging the harvester in vacuum and integrating the efficient bumper to conserve the kinetic energy could minimize the parasitic losses in this work. However, more work should be done to enhance the performance of the

harvesters e.g. using low-friction materials or designing the harvester to avoid the physical contact between the harvester components.

Materials

To develop the harvester for the implantable applications, further investigation needs to be carried out to establish the suitable material with the biocompatibility. The low-friction materials are preferred for the harvester housing to reduce the parasitic damping which influences the harvester performance. One of the biocompatible materials used in healthcare is Teflon or Polytetrafluoroethylene (PTFE) [167] which also offers the low friction coefficients. However, the PTFE is not an option to be the main material for the harvester housing because it is not rigid enough. Instead, a low friction coating by the biocompatible plastics such as the PTFE or Fluorinated Ethylene Propylene (FEP) may be an alternative choice. The other rigid material selected for the housing could be coated with such materials to mitigate the friction effects. Apart from the material of the harvester housing, the bumper material also needs to be carefully considered since the collision is unavoidable in the miniature harvester driven by the high-amplitude excitation. The properties of suitable material selected could provide a perfectly inelastic solution which leading to the increase in the power generation. More studies on the materials for fabricating the harvester, would help to enhance the harvester performance.

Interface circuits

Given the overall performance of the proposed prototypes, further studies should focus on the interface circuits i.e. the power condition circuit, the rectification, and the multiplier circuit to rectify the low AC voltage generated. The standard interface circuits may not have high enough efficiencies to transmit energy to the load. To overcome the challenge, the techniques mentioned in section 7.4.3 could be adapted to suit all requirements. The prospect of being able to develop more effective interface circuitry, serves as a continuous impulse for future research on the low-power harvesting systems.

Generator reliability

Since the harvester will be implanted within the hip prosthesis, it is necessary to consider the reliability and durability of harvesting device. Physical contact between components inside the harvester should be investigated for reliability prediction. A portion of the magnet could be fractured due to the hard collision, which leads to the degradation of the magnet performance (field loss). To enhance the reliability and extend the life-time of the harvesting device, this should be taken into consideration.

Appendix A
Matlab code for fast fourier transform

Code for analysing the frequency response of each subject.

```
[type,sheetname] = xlsfinfo('Data_HipSignal.xlsx');
m = size(sheetname,2);

for k=1:m

   Sheet = char(sheetname(1,k));
   [Bdata] = xlsread('Data_HipSignal.xlsx',Sheet);
   A=Bdata(:,2);

   %% Number of samples:
   N = size(A,1);        % assumes data is an N x 1 column vector

   %% Compute the time domain:
   Fs = 200;                % samples per second
   dt = 1/Fs;               % seconds
   t = dt*(0:N-1)';
   T = N*dt;

   %% two-sided spectrum, centered on DC
   X = fftshift(fft(A))/N;

   %% Compute the frequency domain:
   dF = Fs/N;
   f = (-Fs/2:dF:Fs/2-dF)';

   %% Plot the time domain signal:
   figure;
   subplot(2,1,1);
   plot(t,A);
   title(['\fontsize{12}Data ',Sheet])
   grid on
   xlabel('\fontsize{12}Time (s)');
   ylabel('\fontsize{12}Contact force (N)');
   xlim([0 3.5]);

   %% Plot the magnitude response:
   subplot(2,1,2);
   plot(f,abs(X),'.');
   grid on
   xlabel('\fontsize{12}Frequency (Hz)');
   ylabel('\fontsize{12}Contact force (N)');
   xlim([0 10]);ylim([0 3000]);

end
```

Appendix B
Numerical and video data of the patients

I. Numerical data

This is an example data of contact forces on the acetabular ball of hip prostheses collected by Orthoload team [103].

Data File: KWR0140D.AKF
Measurement Programm: 5.0.9
----------MEASURING INFOS----------
Diagram Title #1 Forces at Hip Joint
Diagram Title #2 Relative to Femur
Comment #1 HIP JOINT Walking free; Velocity: normal
Comment #2 Pat: KWR, Side: Right, 8 Month PO
BodyWeight [N]: 690.0
Implant Type: Hip Joint
Axes Directions X, Y, Z: Medial, Anterior, Superior
Axes Origin: Center of Femoral Head
Angle of Rotation (Deg): Z = -2.0 X = 9.0 Y = 0.0
Displacement X, Y, Z (mm): 0.0 0.0 0.0
Activity Code: HIPJOINT 1P_1_7_1 2P_1_3_1
----------DATA----------
Number of Data Sets = 770
Number of analog channels = 0
Time-Offset(sec) = 0.02
Max. Force (N, sec): 1639.17 2.583

Time [s] [N]	-Fx [N]	-Fy [N]	-Fz [N]	Fres -	Marker [0/1]
0.000	00152.56	-00012.35	00261.07	00302.63 -	0
0.004	00150.23	-00010.74	00256.05	00297.06 -	0
0.008	00147.56	-00008.96	00250.04	00290.47 -	0
0.013	00145.12	-00007.13	00243.51	00283.56 -	0
0.017	00142.95	-00005.45	00236.49	00276.39 -	0
0.022	00140.88	-00003.91	00229.24	00269.10 -	0
0.026	00138.42	-00002.47	00221.54	00261.24 -	0
0.031	00135.33	-00001.16	00213.26	00252.58 -	0
0.035	00131.93	00000.11	00204.84	00243.65 -	0
0.040	00128.62	00001.15	00196.51	00234.86 -	0
0.044	00125.81	00001.88	00188.49	00226.63 -	0
0.049	00123.43	00002.20	00181.04	00219.12 -	0
0.053	00121.22	00002.11	00173.94	00212.02 -	0
0.058	00118.86	00001.93	00167.02	00205.01 -	0
0.062	00116.91	00001.56	00160.53	00198.60 -	0
0.067	00115.69	00000.99	00154.88	00193.32 -	0
0.071	00115.17	00000.02	00150.19	00189.26 -	0
0.076	00114.80	-00001.27	00146.43	00186.07 -	0
0.080	00113.50	-00001.98	00142.22	00181.97 -	0

⋮

II. Video data

This is the loads data of a patient provided by Orthoload team [103]. The contact forces on the femoral head of the hip prosthesis have been recorded and monitored real time during patient's walking.

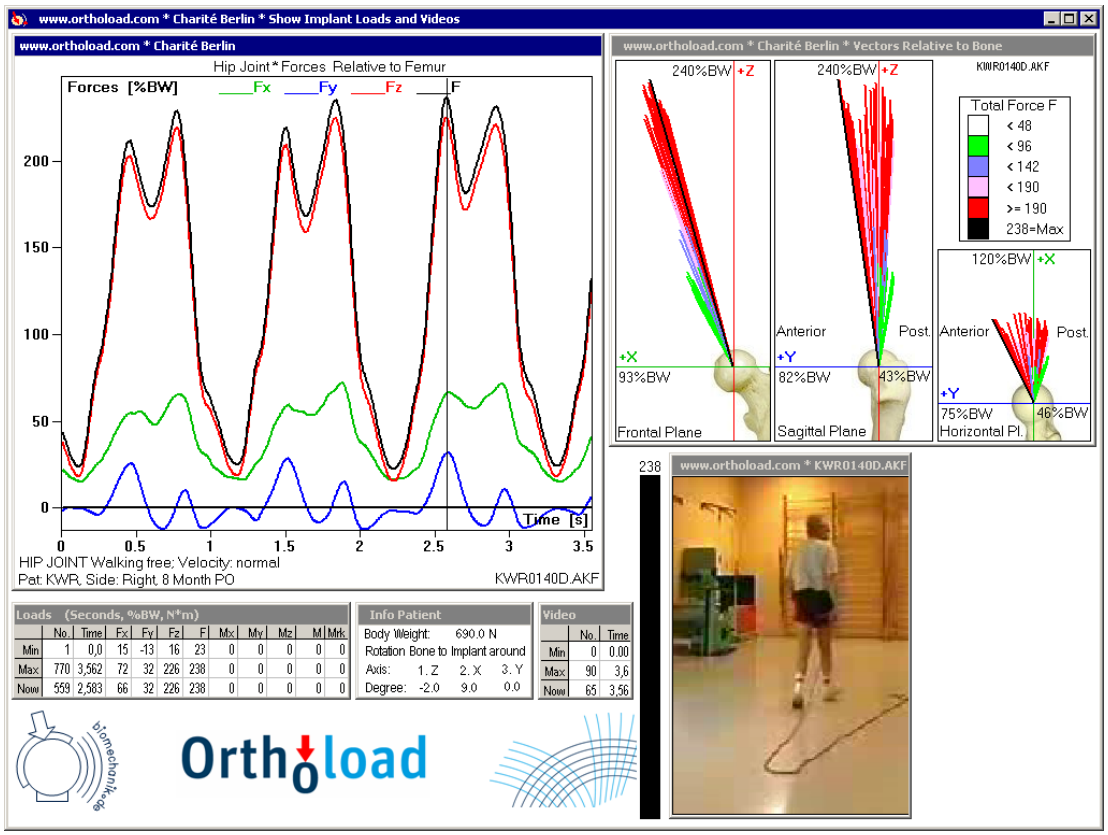

Appendix C
Spectra of the hip-motion signal

I. Hip-replacement patients

The spectra of the hip-motion signal during walking analysed from a group of six hip-replacement patients.

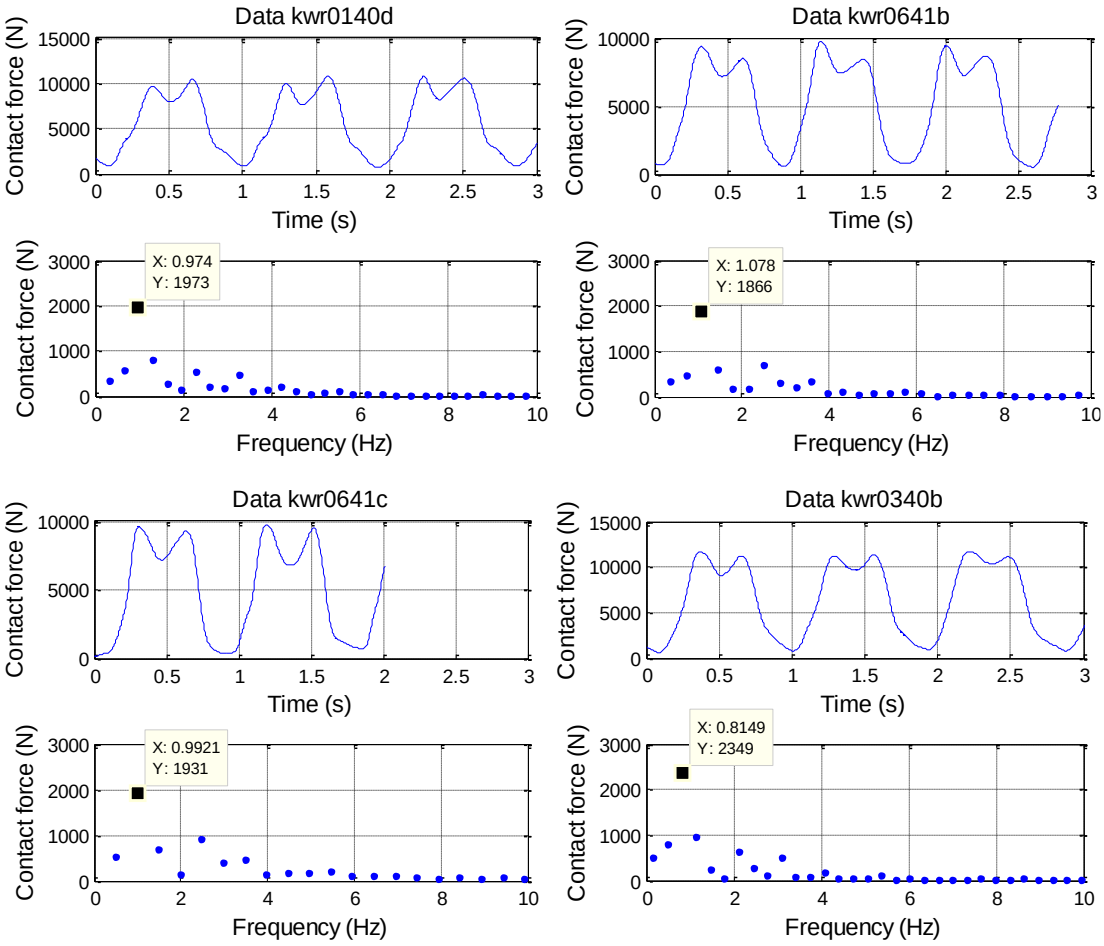

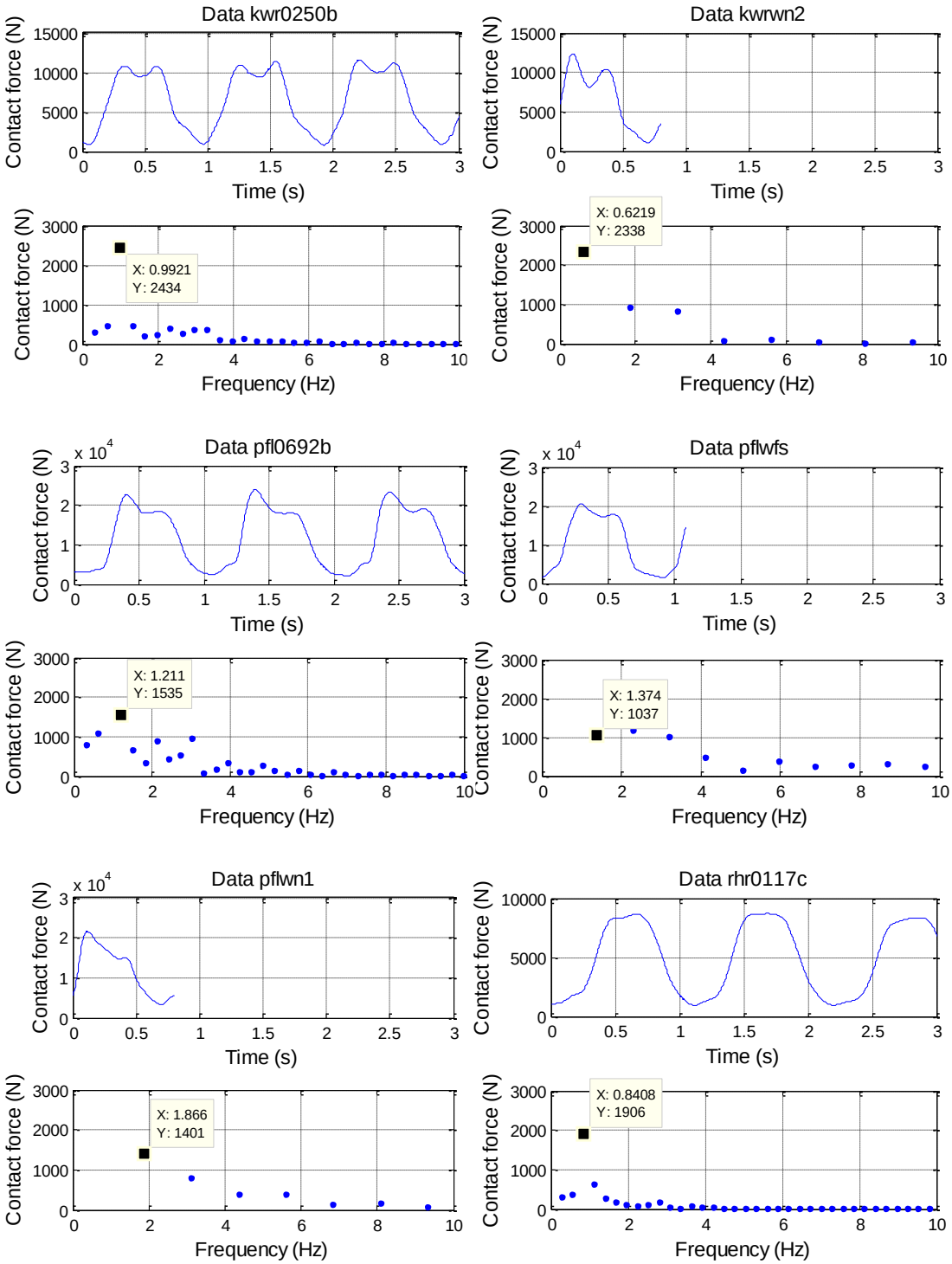
Data kwr0250b
Contact force (N)
Time (s)
X: 0.9921
Y: 2434
Frequency (Hz)
Data kwrwn2
X: 0.6219
Y: 2338
Data pfl0692b
x 10^4
X: 1.211
Y: 1535
Data pflwfs
X: 1.374
Y: 1037
Data pflwn1
X: 1.866
Y: 1401
Data rhr0117c
X: 0.8408
Y: 1906

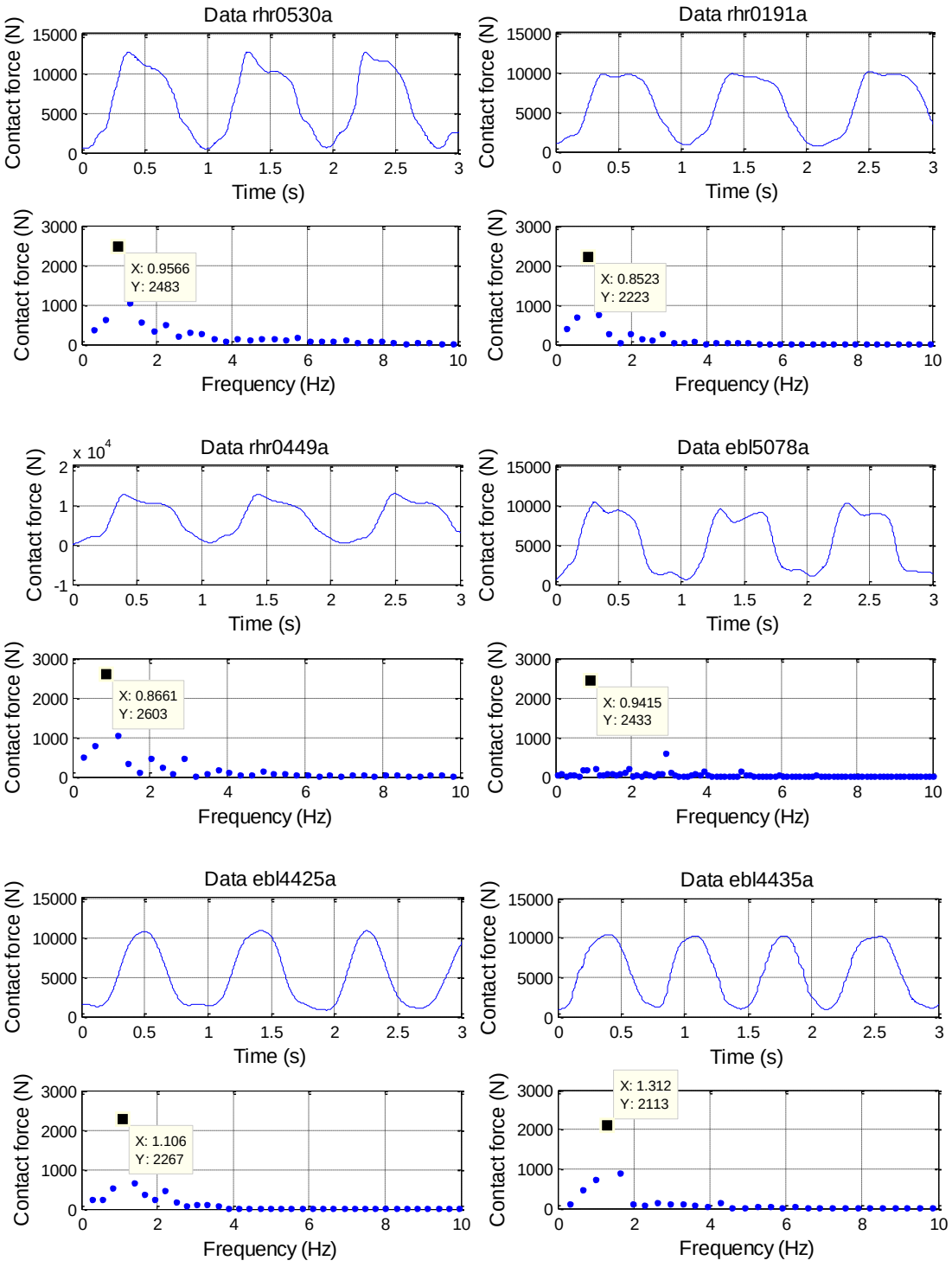
Data rhr0530a
Contact force (N)
Time (s)
X: 0.9566
Y: 2483
Frequency (Hz)
Data rhr0191a
X: 0.8523
Y: 2223
Data rhr0449a
x 10^4
X: 0.8661
Y: 2603
Data ebl5078a
X: 0.9415
Y: 2433
Data ebl4425a
X: 1.106
Y: 2267
Data ebl4435a
X: 1.312
Y: 2113

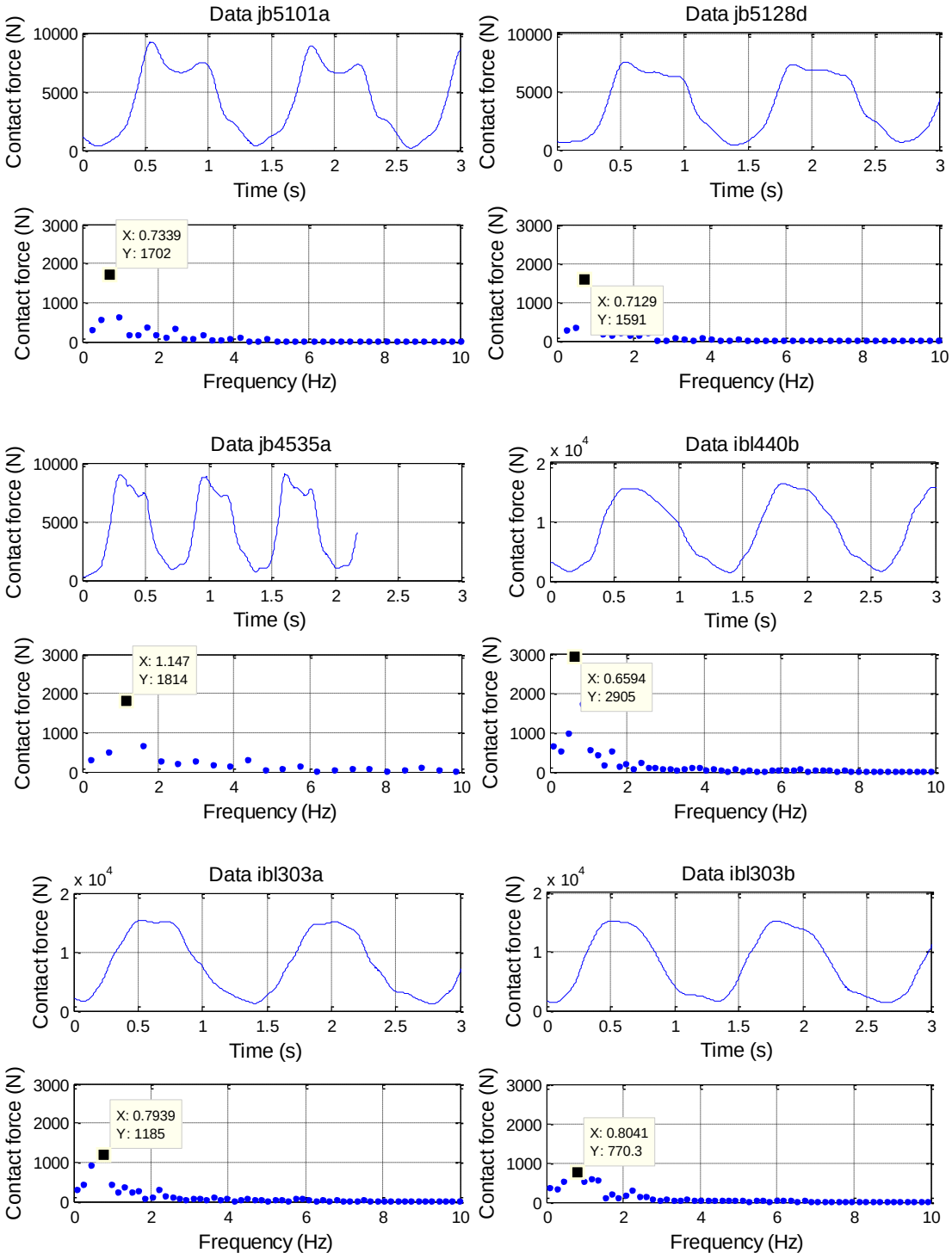
Data jb5101a
Contact force (N)
Time (s)
X: 0.7339
Y: 1702
Frequency (Hz)
Data jb5128d
X: 0.7129
Y: 1591
Data jb4535a
X: 1.147
Y: 1814
Data ibl440b
x 10^4
X: 0.6594
Y: 2905
Data ibl303a
X: 0.7939
Y: 1185
Data ibl303b
X: 0.8041
Y: 770.3

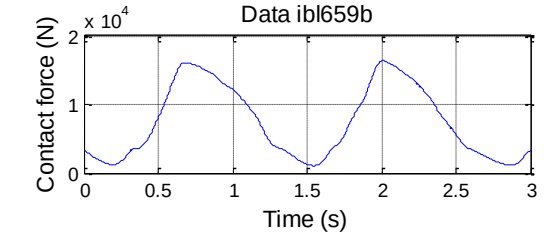
Data ibl659b
x 10^4
Contact force (N)
Time (s)

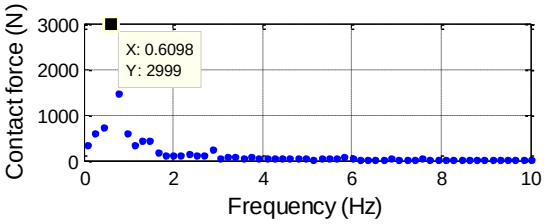
X: 0.6098
Y: 2999
Contact force (N)
Frequency (Hz)

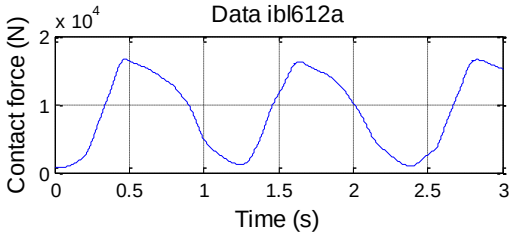
Data ibl612a
x 10^4
Contact force (N)
Time (s)

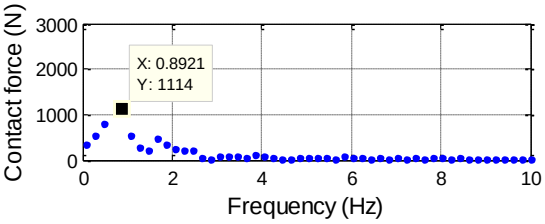
X: 0.8921
Y: 1114
Contact force (N)
Frequency (Hz)

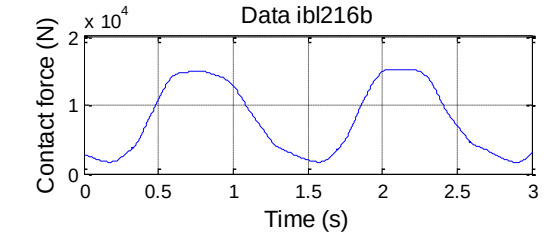
Data ibl216b
x 10^4
Contact force (N)
Time (s)

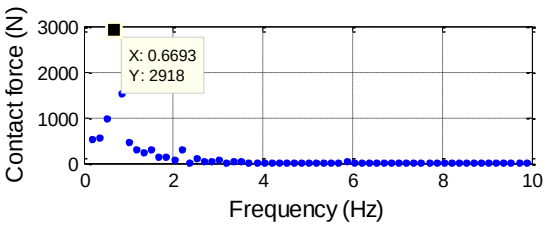
X: 0.6693
Y: 2918
Contact force (N)
Frequency (Hz)

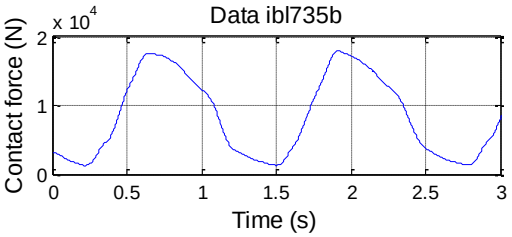
Data ibl735b
x 10^4
Contact force (N)
Time (s)

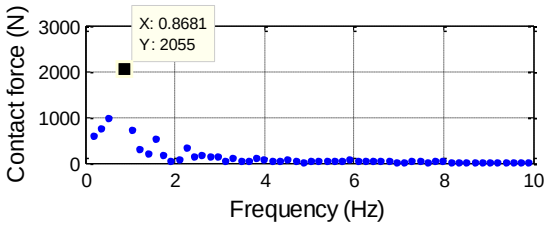
X: 0.8681
Y: 2055
Contact force (N)
Frequency (Hz)

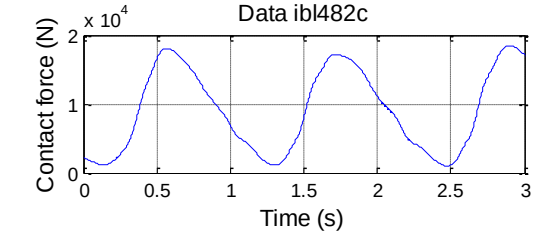
Data ibl482c
x 10^4
Contact force (N)
Time (s)

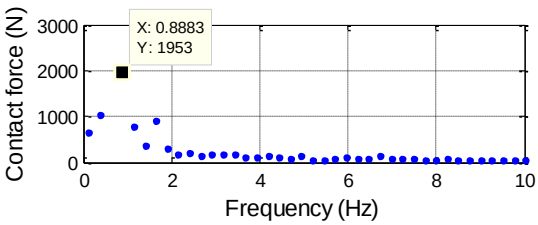
X: 0.8883
Y: 1953
Contact force (N)
Frequency (Hz)

II. Non-hip replacement patients

i. Hip-motion signal during walking

The spectra of the hip-motion signal during walking analysed from 22 non-hip replacement patients.

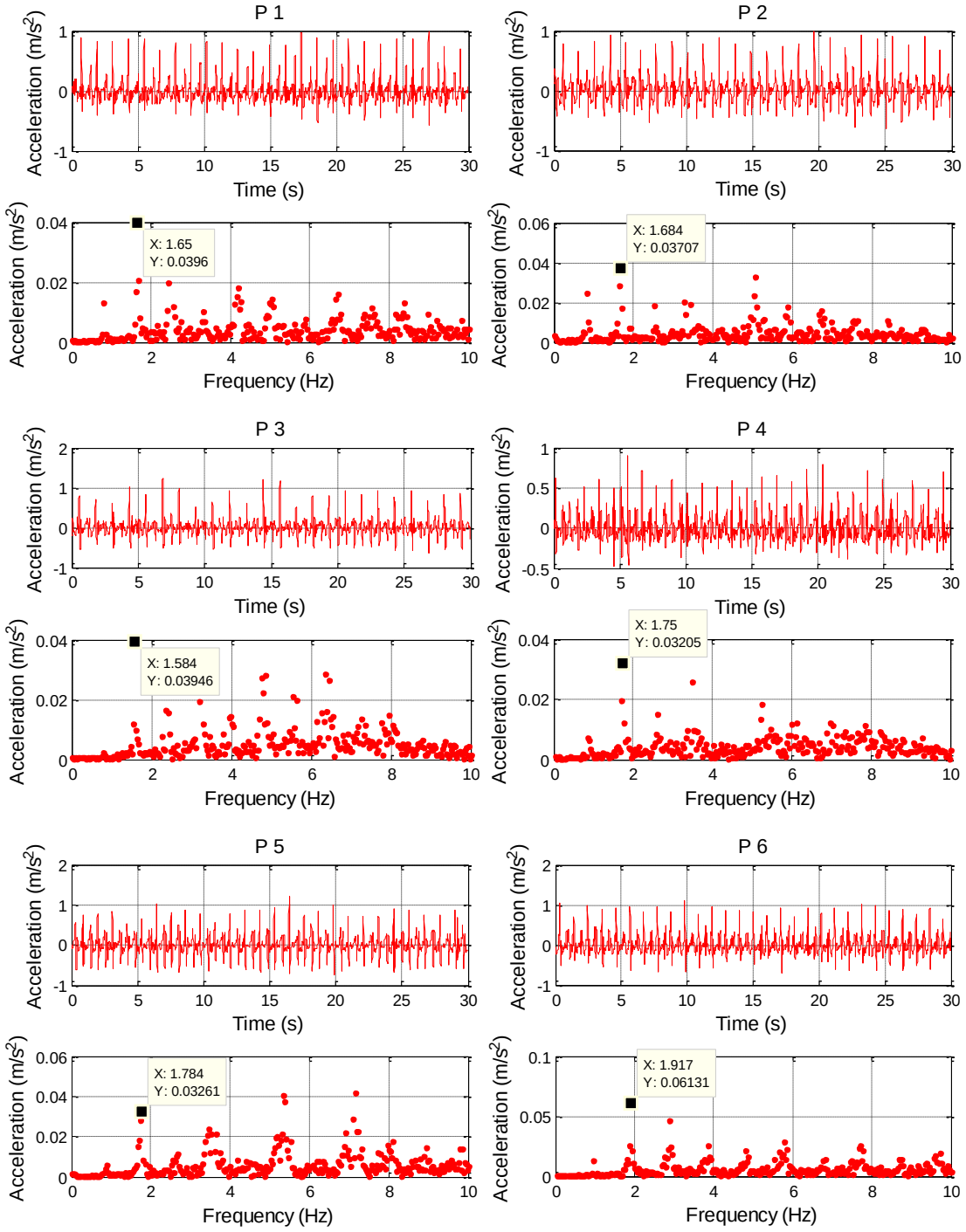

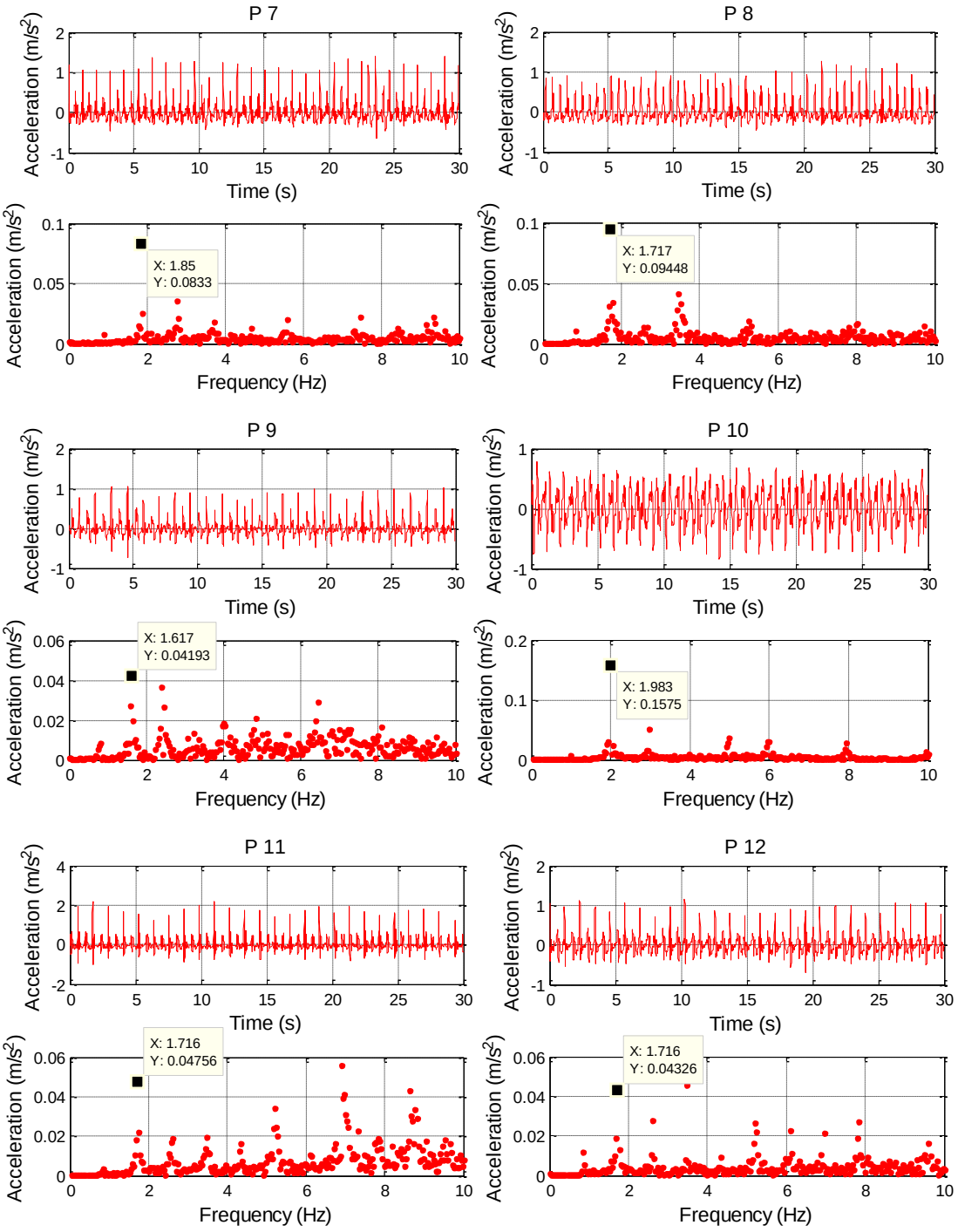
P 7
Acceleration (m/s²)
Time (s)
X: 1.85
Y: 0.0833
Frequency (Hz)
P 8
X: 1.717
Y: 0.09448
P 9
X: 1.617
Y: 0.04193
P 10
X: 1.983
Y: 0.1575
P 11
X: 1.716
Y: 0.04756
P 12
X: 1.716
Y: 0.04326

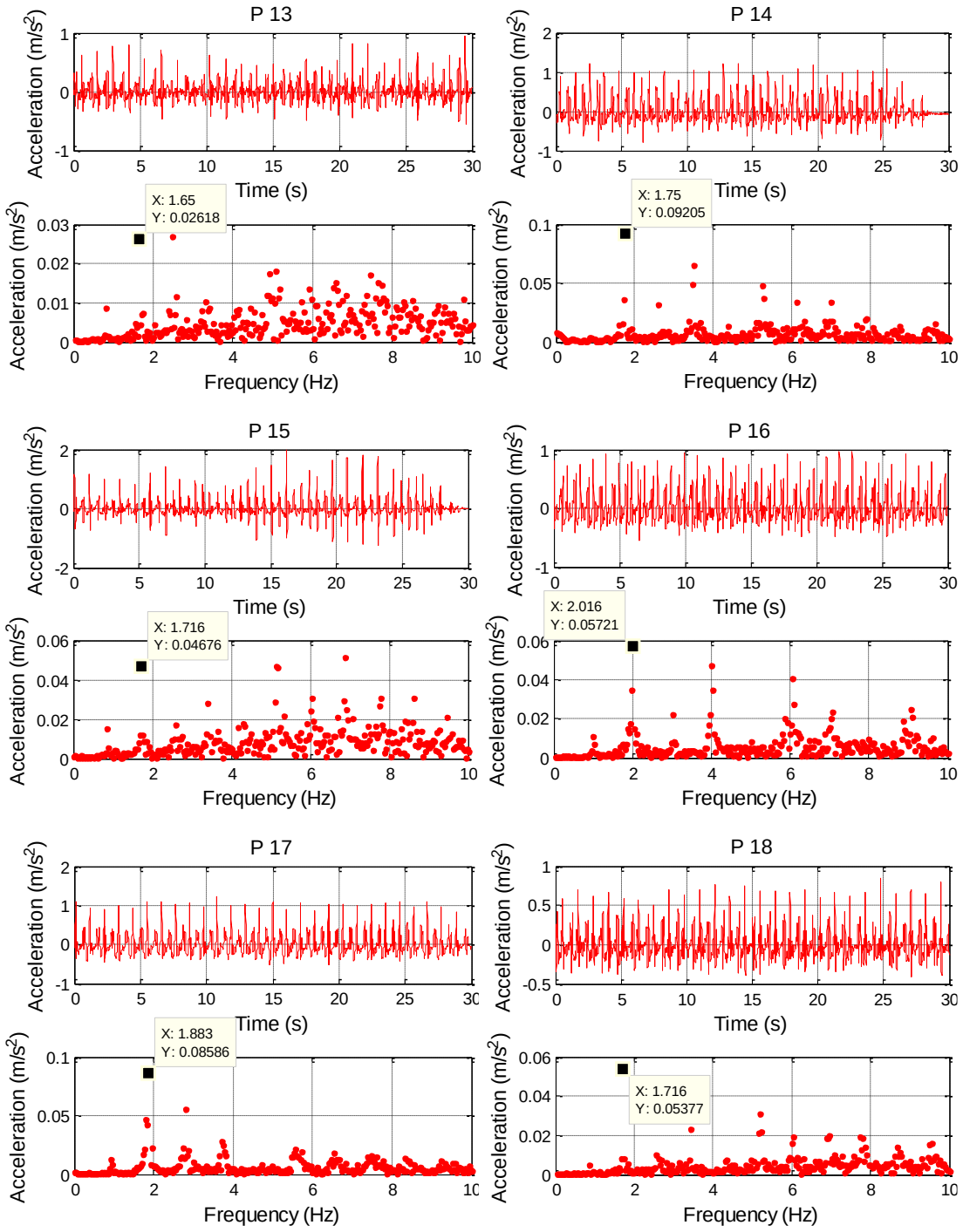
P 13
Acceleration (m/s²)
Time (s)
X: 1.65
Y: 0.02618
Frequency (Hz)
P 14
X: 1.75
Y: 0.09205
P 15
X: 1.716
Y: 0.04676
P 16
X: 2.016
Y: 0.05721
P 17
X: 1.883
Y: 0.08586
P 18
X: 1.716
Y: 0.05377

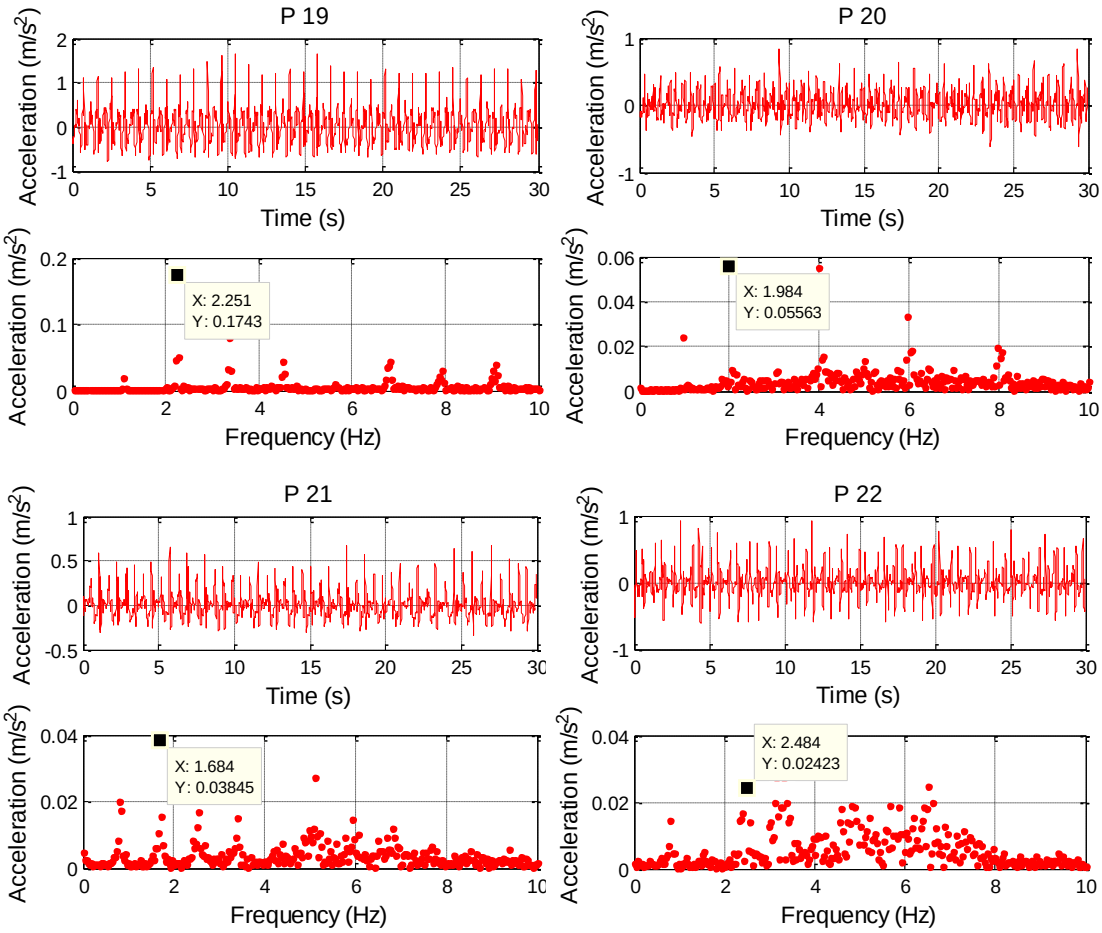
P 19
Acceleration (m/s²)
Time (s)
X: 2.251
Y: 0.1743
Frequency (Hz)
P 20
X: 1.984
Y: 0.05563
P 21
X: 1.684
Y: 0.03845
P 22
X: 2.484
Y: 0.02423

ii. Hip-motion signal during running

The spectra of the hip-motion signal during running analysed from 22 non-hip replacement patients.

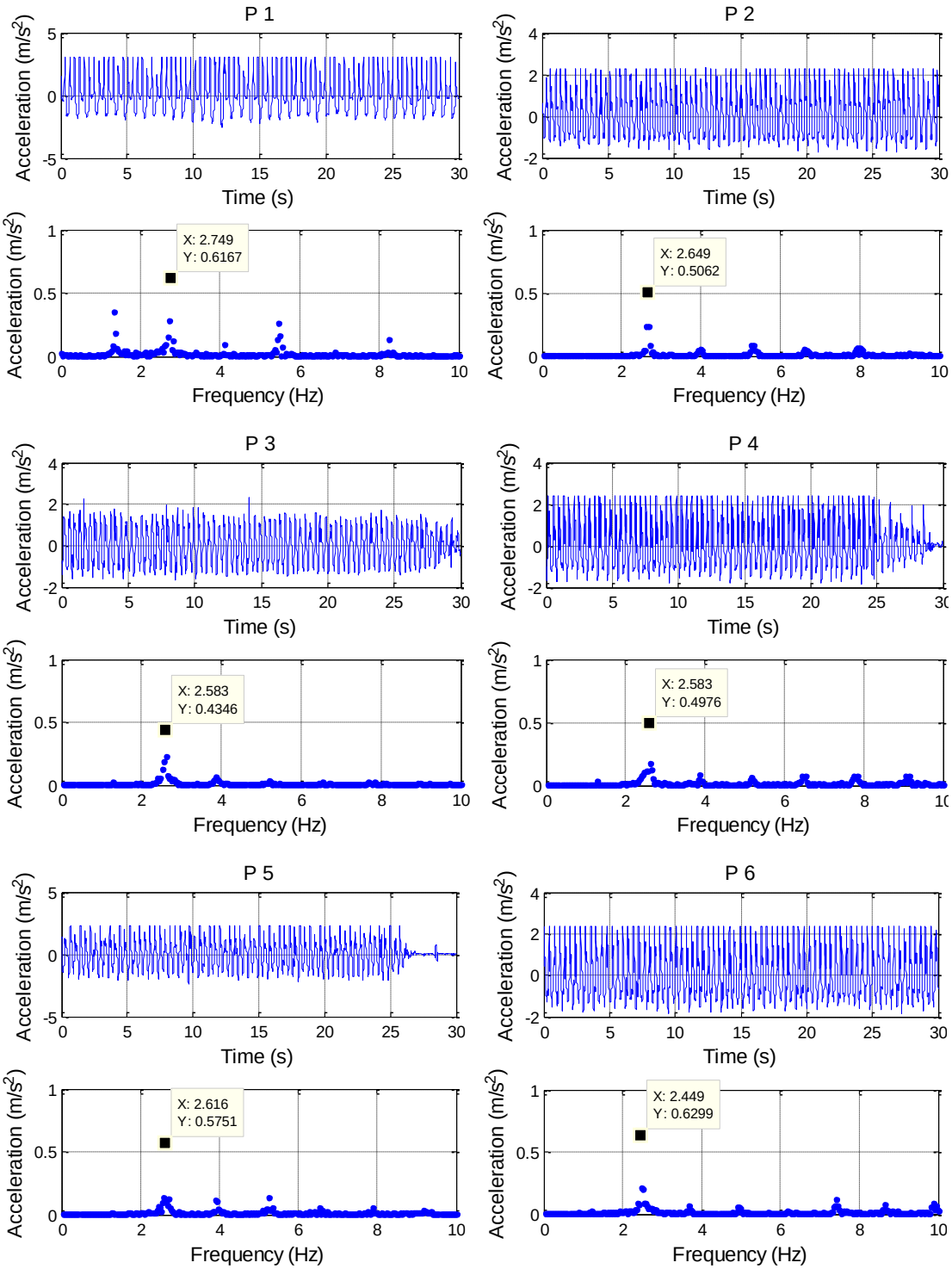

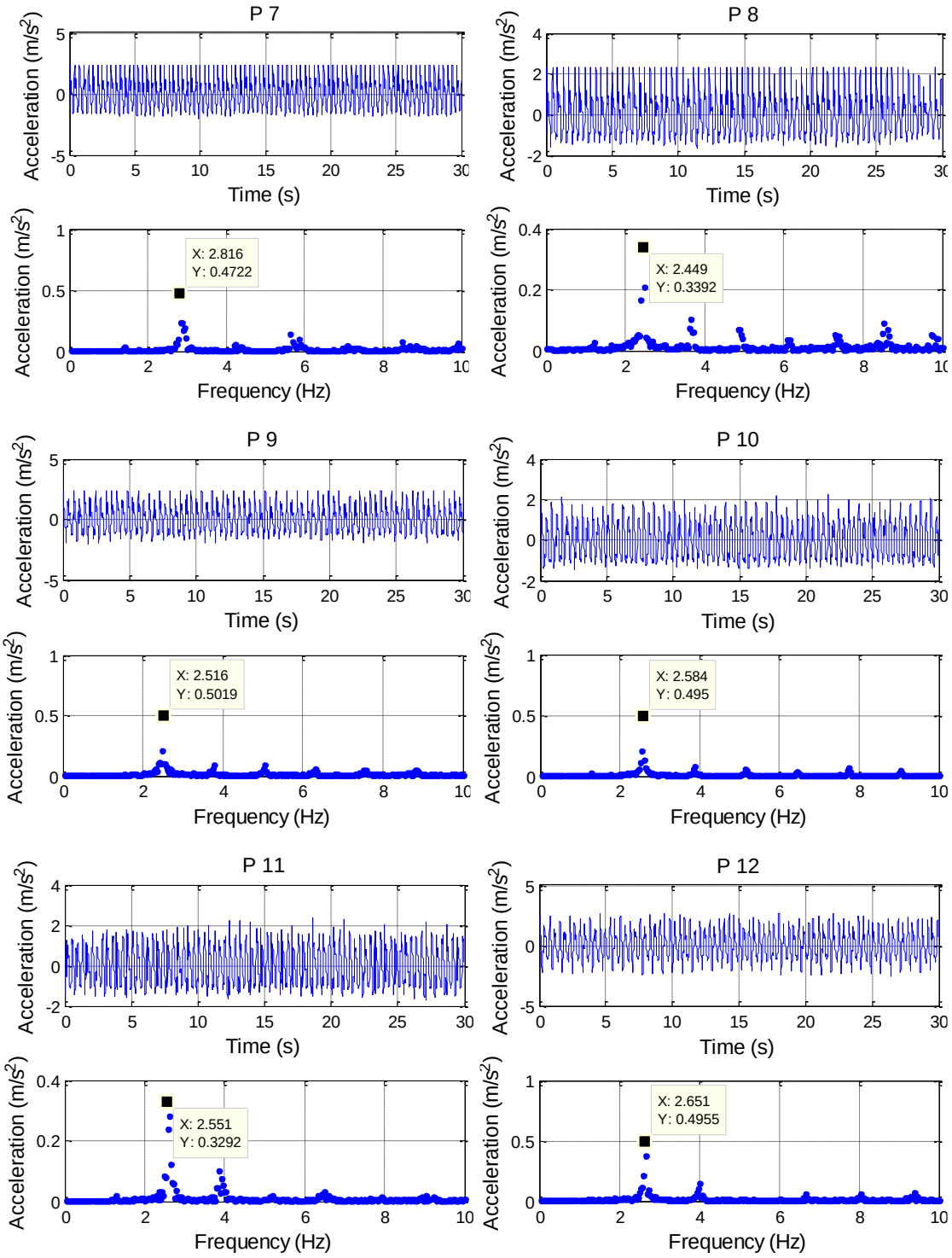
P 7
Acceleration (m/s²)
Time (s)
X: 2.816
Y: 0.4722
Frequency (Hz)
P 8
X: 2.449
Y: 0.3392
P 9
X: 2.516
Y: 0.5019
P 10
X: 2.584
Y: 0.495
P 11
X: 2.551
Y: 0.3292
P 12
X: 2.651
Y: 0.4955

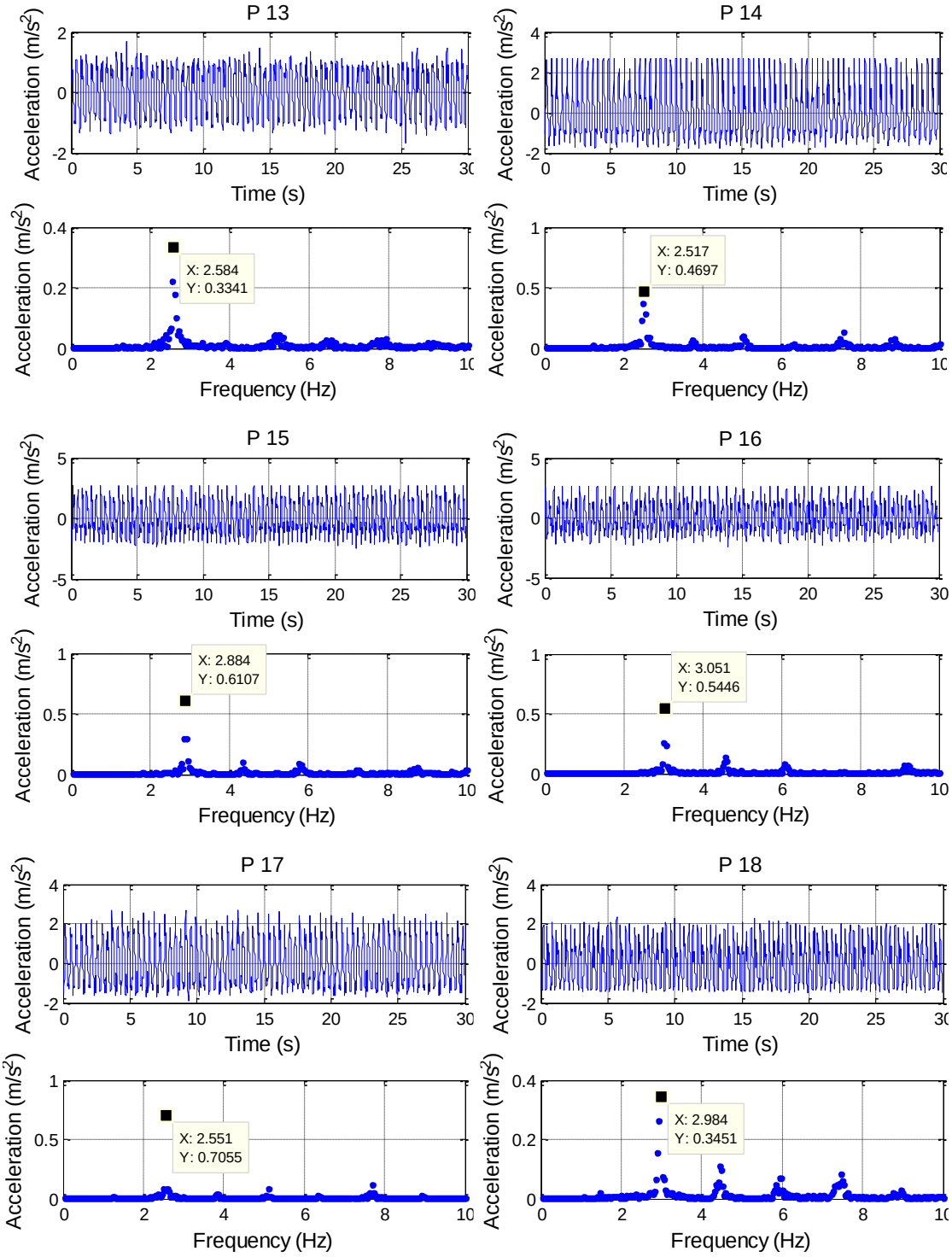
P 13
Acceleration (m/s²)
Time (s)
X: 2.584
Y: 0.3341
Frequency (Hz)
P 14
X: 2.517
Y: 0.4697
P 15
X: 2.884
Y: 0.6107
P 16
X: 3.051
Y: 0.5446
P 17
X: 2.551
Y: 0.7055
P 18
X: 2.984
Y: 0.3451

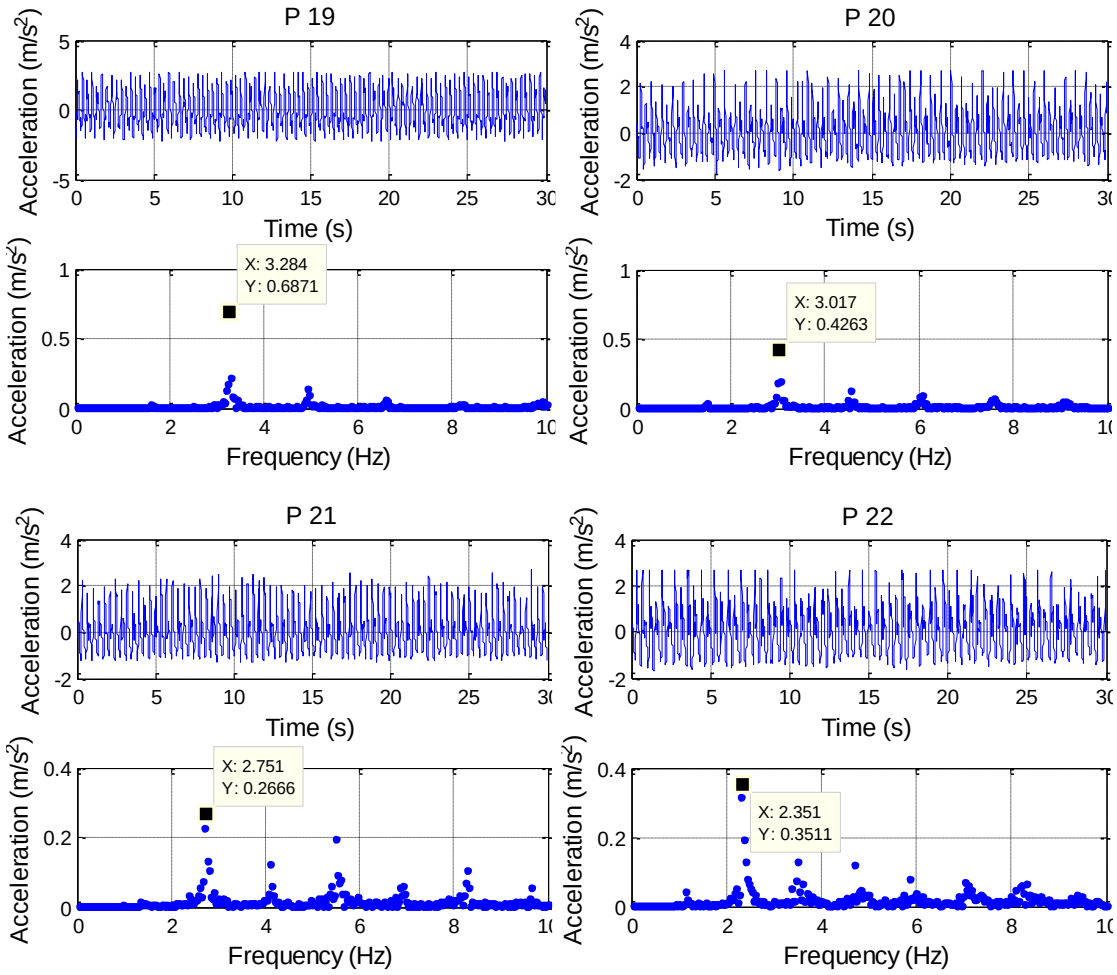
P 19
Acceleration (m/s²)
Time (s)
X: 3.284
Y: 0.6871
Frequency (Hz)
P 20
X: 3.017
Y: 0.4263
P 21
X: 2.751
Y: 0.2666
P 22
X: 2.351
Y: 0.3511

Appendix D
Block diagram of Simulink model for SMH

Block diagram of the Matlab/Simulink model for SMH.

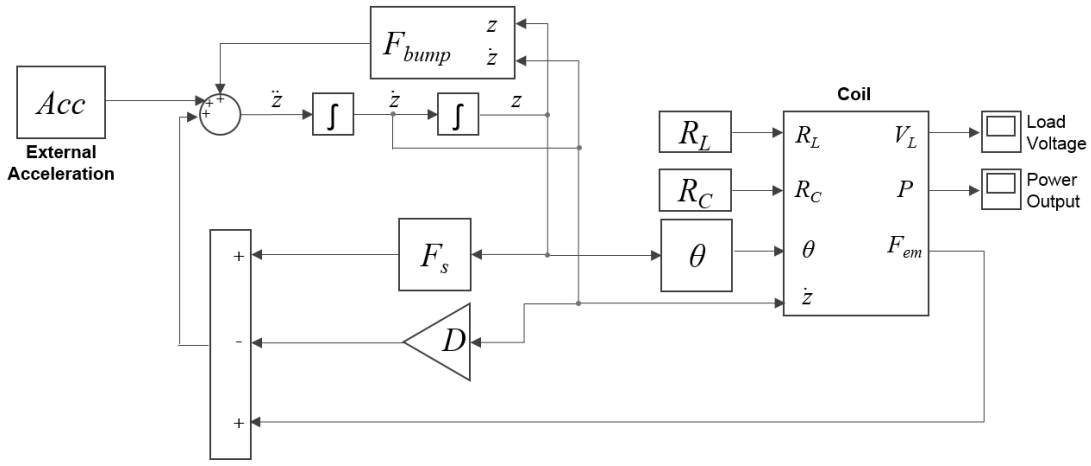

Appendix E
Temperature dependence

I. Curve fitting on the magnetic restoring forces

The polynomial fit has been applied on the magnetic restoring forces F_S as shown in Figure.1. The result of polynomial expansions is presented in Table 1.

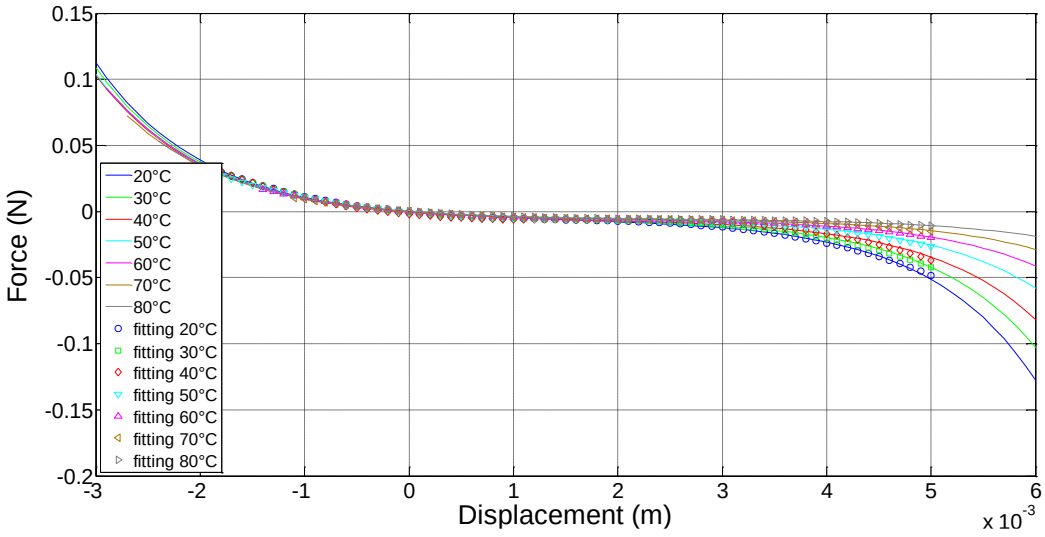

Figure.1 The curve fitting on the magnetic forces at different temperatures.

Table 1 The polynomial expansions of force-displacement curves.

Temperature	z^3	z^2	z^1	z^0
20°C	-833844.0283	3755.451266	-7.494303267	-0.000592863
30°C	-813634.8015	3906.201334	-7.441319928	-0.00092614
40°C	-845979.7011	4302.427261	-7.354845779	-0.00193796
50°C	-588988.3477	3359.023612	-7.262607462	-0.000437754
60°C	-454591.6369	2865.933576	-6.939243244	4.80197E-05
70°C	-347932.2447	2402.409255	-6.318461113	0.000118443
80°C	-247647.9073	1932.077884	-5.707279781	0.0002867

II. Dependence of Induced Voltage on Magnetic Flux Density

The induced voltage in the equation (6.21) is rewritten in term of the total force on the magnet $F_T = F_S - F_G$:

$$V_{emf} = -NBl\frac{Y}{2\zeta}\sqrt{\frac{2\zeta F_T}{Ym}} \tag{E.1}$$

Simplifying the equations (6.11) and (6.12) based on the simple diagram of force analysis in Figure 6.3, the total force F_T is given by

$$F_T = \frac{3(\pi M R_1^2 L_1)^2}{8}[g(d) - g(d+L_2) - g(D-d-L_1) - g(D-d-L_1+L_2)] - F_G \tag{E.2}$$

where R_1 is the radius of moving magnet, L_1 and L_2 are the length of moving magnet and fixed magnet respectively d is the distance between moving magnet and fixed magnet, D is the distance between fixed magnets, and F_G is the gravitational force which is small enough to be ignored. Substituting (E.2) into (E.1) produces the induced voltage in term of the magnetic flux density B in (6.22).

Appendix F Simulation parameters

I. Parameters for power and displacement estimation in section 3.4.2

Parameter	Value	Unit
Moving mass, *Mass*	1 - 5	g
Linear resonant frequency, *Freq*	1 - 10	Hz
Damping ratio, *Damp*	0.05 – 0.25	-
Nonlinear spring stiffness, k_3	$1e^3$ – $10e^3$	N/m^3

II. Parameters for design optimisation in section 4.3

Parameter	Value	Unit
Length of glass tube	20	mm
Outer diameter of glass tube	7	mm
Coil fill factor	0.64	-
Electrical resistivity of Copper coil	1.68×10^{-8}	Ω·m
Diameter of magnet	4	mm
NdFeB cylindrical magnet grade	N35	-
Remanence, B_r	1200	mT

III. Parameters for simulation of frequency response in section 4.5

Parameter	Value	Unit
Excitation level, F	0.1-0.5	g
Excitation frequency, ω_d	2-20	Hz
Damping ratio, ζ	0.02-0.18	-
Moving mass of SMH, m	$1.53e^{-3}$	kg
Linear stiffness, k_1, for SMH	7.13	N/m

Parameter	Value	Unit
Nonlinear stiffness, k_3, for SMH	3.1e^5	N/m^3
Linear resonance frequency of SMH, ω_0	10.86	Hz
Moving mass of CMH, m_1	1.52e^{-3}	kg
Moving mass of CMH, m_2	0.59e^{-3}	kg
Linear stiffness of M_1, k_1, for CMH	5.94	N/m
Nonlinear stiffness of M_1, k_3, for CMH	1.38e^6	N/m^3
Linear stiffness of M_2, k_1, for CMH	14.39	N/m
Nonlinear stiffness of M_2, k_3, for CMH	1.74e^6	N/m^3
Linear resonant frequency of M_1, ω_1	9.95	Hz
Linear resonant frequency of M_2, ω_2	13.14	Hz

IV. Parameters for simulation of induced voltage and moving-mass displacement in section 5.2

Parameter	Value	Unit
Excitation level, F, for section 5.2.2.1	0.1-0.5	g
Damping ratio, ζ (shown in Table 5.3)	0.05-0.12	-
Moving mass of SMH, m	1.53e^{-3}	kg
Linear stiffness, k_1, for SMH	7.13	N/m
Nonlinear stiffness, k_3, for SMH	3.1e^5	N/m^3
Linear resonance frequency of SMH, ω_0	10.86	Hz
Moving mass of CMH, m_1	1.52e^{-3}	kg
Moving mass of CMH, m_2	0.59e^{-3}	kg
Linear stiffness of M_1, k_1, for CMH	5.94	N/m
Nonlinear stiffness of M_1, k_3, for CMH	1.38e^6	N/m^3
Linear stiffness of M_2, k_1, for CMH	14.39	N/m
Nonlinear stiffness of M_2, k_3, for CMH	1.74e^6	N/m^3
Linear resonant frequency of M_1, ω_1	9.95	Hz
Linear resonant frequency of M_2, ω_2	13.14	Hz
Coil resistance, R_C	2558	Ω
Load resistance, R_L, for SMH	2662	Ω
Load resistance, R_L, for CMH	2661	Ω

Bibliography

[1] F. Birrell, O. Johnell, and A. Silman, "Projecting the need for hip replacement over the next three decades : influence of changing demography and threshold for surgery," *Ann. Rheum. Dis.*, vol. 58, no. 9, pp. 569–572, 1999.

[2] National Joint Registry, "National Joint Registry for England, Wales,Northern Ireland and the Isle of Man," *12th annual report*, 2015. [Online]. Available: http://www.njrcentre.org.uk/.

[3] A. Patel, G. Pavlou, R. E. Mújica-Mota, and A. D. Toms, "The epidemiology of revision total knee and hip arthroplasties in England and Wales," *Bone Jt. J.*, vol. 97–B, no. 8, pp. 1076–1081, 2015.

[4] M. Newman and K. Barker, "Rehabilitation of revision total hip replacement : A multi - centre survey of current practice," *Musculoskeletal Care*, pp. 1–9, 2017.

[5] P. B. Pynsent, S. R. Carter, and C. J. Bulstrode, "The total cost of hip-joint replacement; a model for purchasers.," *J. Public Health Med.*, vol. 18, no. 2, pp. 157–68, 1996.

[6] N.-B. Kandala *et al.*, "Setting benchmark revision rates for total hip replacement: analysis of registry evidence," *Bmj*, vol. 350, no. mar09 1, pp. h756–h756, 2015.

[7] C. E. Carlson, R. W. Mann, and W. H. Harris, "A Radio Telemetry Device for Monitoring Cartilage Surface Pressures in the Human Hip," *IEEE Trans. Biomed. Eng.*, vol. BME-21, no. 4, pp. 257–264, Jul. 1974.

[8] M. Kilvington and R. M. F. Goodman, "In Vivo Hip Joint Forces Recorded on a Strain Gauged 'English' Prosthesis Using an Implanted Transmitter," *Eng. Med.*, vol. 10, no. 4, pp. 175–187, Oct. 1981.

[9] F. Graichen and G. Bergmann, "Four-channel telemetry system for in vivo measurement of hip joint forces," vol. 13, pp. 370–374, 1991.

[10] F. Graichen, G. Bergmann, and a Rohlmann, "Hip endoprosthesis for in vivo measurement of joint force and temperature.," *J. Biomech.*, vol. 32, no. 10, pp. 1113–1117, 1999.

[11] C. a McGibbon, D. E. Krebs, C. a Trahan, S. B. Trippel, and R. W. Mann, "Cartilage degeneration in relation to repetitive pressure: case study of a unilateral hip hemiarthroplasty patient.," *J. Arthroplasty*, vol. 14, no. 1, pp. 52–58, 1999.

[12] R. Puers *et al.*, "A telemetry system for the detection of hip prosthesis loosening by vibration analysis," *Sensors Actuators A Phys.*, vol. 85, no. 1–3, pp. 42–47, 2000.

[13] P. Damm, F. Graichen, A. Rohlmann, A. Bender, and G. Bergmann, "Total hip joint prosthesis for in vivo measurement of forces and moments.," *Med. Eng. Phys.*, vol. 32, no. 1, pp. 95–100, Jan. 2010.

[14] P. D. Mitcheson, E. M. Yeatman, G. K. Rao, A. S. Holmes, and T. C. Green, "Energy harvesting from human and machine motion for wireless electronic devices," *Proc. IEEE*, vol. 96, no. 9, pp. 1457–1486, 2008.

[15] T. Starner, "Human-powered wearable computing," *IBM Syst. J.*, vol. 35, no. 3.4, pp. 618–629, 1996.

[16] P. Niu, P. Chapman, R. Riemer, and X. Zhang, "Evaluation of motions and actuation methods for biomechanical energy harvesting," *PESC Rec. - IEEE Annu. Power Electron. Spec. Conf.*, vol. 3, no. December 2014, pp. 2100–2106, 2004.

[17] R. Amirtharajah and A. P. Chandrakasan, "Self-powered signal processing using vibration-based power generation," *IEEE J. Solid-State Circuits*, vol. 33, no. 5, pp. 687–695, 1998.

[18] T. von Büren, "Body-Worn Inertial Electromagnetic Micro-Generators," SWISS FEDERAL INSTITUTE OF TECHNOLOGY ZURICH, 2006.

[19] R. Sarpeshkar *et al.*, "An ultra-low-power programmable analog bionic ear processor," *IEEE Trans. Biomed. Eng.*, vol. 52, no. 4, pp. 711–727, 2005.

[20] S. Saati, R. Lo, P.-Y. Li, E. Meng, R. Varma, and M. S. Humayun, "Mini drug pump for ophthalmic use.," *Curr. Eye Res.*, vol. 35, no. 3, pp. 192–201, 2010.

[21] S. Kenneth, "Low power circuits and systems for wireless neural stimulation," Massachusetts Institute of Technology, 2011.

[22] L. S. Y. Wong, S. Hossain, A. Ta, J. Edvinsson, D. H. Rivas, and H. N????s, "A very low-power CMOS mixed-signal IC for implantable pacemaker applications," *IEEE J. Solid-State Circuits*, vol. 39, no. 12, pp. 2446–2456, 2004.

[23] F. S.F.J., "Alternative Power Sources for Portables & Wearables Part 1: Power Generation & Part 2: Energy Storage," 2005.

[24] R. Tashiro *et al.*, "Development of an Electrostatic Generator that Harnesses the Motion of a Living Body. Generation Using Heartbeat.," *Trans. Japan Soc. Mech. Eng. Ser. C*, vol. 67, no. 659, pp. 2307–2313, 2001.

[25] R. Tashiro, N. Kabei, K. Katayama, F. Tsuboi, and K. Tsuchiya, "Development of an electrostatic generator for a cardiac pacemaker that harnesses the ventricular wall motion," *J. Artif. Organs*, vol. 5, no. 4, pp. 239–245, 2002.

[26] P. Miao, P. D. Mitcheson, A. S. Holmes, E. M. Yeatman, T. C. Green, and B. H. Stark, "Mems inertial power generators for biomedical applications," *Microsyst. Technol.*, vol. 12, no. 10–11, pp. 1079–1083, 2006.

[27] Y. ARAKAWA, Y. SUZUKI, and N. Kasagi, "Micro Seismic Power Generator Using Electret Polymer Film," *Proc. Natl. Symp. Power Energy Syst.*, vol. 2004.9, pp. 37–38, 2004.

[28] Y. Naruse, N. Matsubara, K. Mabuchi, M. Izumi, and S. Suzuki, "Electrostatic micro power generation from low-frequency vibration such as human motion," *J. Micromechanics Microengineering*, vol. 19, no. 9, p. 094002, 2009.

[29] B. Jaffe, W. R. C. Jr., and H. Jaffe, *Piezoelectric ceramics*. New York: Academic Press London, 1971.

[30] A. Almusallam, K. Yang, Z. Cao, D. Zhu, J. Tudor, and S. P. Beeby, "Improving the dielectric and piezoelectric properties of screen-printed Low temperature PZT / polymer composite using cold isostatic pressing," *Phys. Conf. Ser.*, vol. 557, p. 012083, 2014.

[31] A. Almusallam, Z. Luo, A. Komolafe, K. Yang, and A. Robinson, "Nano Energy Flexible piezoelectric nano-composite fi lms for kinetic energy harvesting from textiles," *Nano Energy*, vol. 33, no. December 2016, pp. 146–156, 2017.

[32] L. Wu *et al.*, "Enhancement of PVDF ' s piezoelectricity by VGCF and MWNT," *Adv. Compos. Mater.*, vol. 22, no. 1, pp. 49–63, 2013.

[33] J. C. Park, S. Member, J. Y. Park, and Y. Lee, "Modeling and Characterization of Piezoelectric d 33 -Mode MEMS Energy Harvester," *Microelectromechanical Syst.*, vol. 19, no. 5, pp. 1215–1222, 2010.

[34] J. C. Park and J. Y. Park, "Micromachined Piezoelectric Energy Harvester with Low Vibration," in *Applications of Ferroelectrics*, 2009.

[35] N. Maluf and K. Williams, *An Introduction to Microelectromechanical Systems Engineering*. Artech House, 2004.

[36] J. F. Nye, *Physical Properties of Crystals*. Oxford University Press, 1985.

[37] J. Kymissis, C. Kendall, J. Paradiso, and N. Gershenfeld, "Parasitic power harvesting in shoes," in *Digest of Papers. Second International Symposium on Wearable Computers (Cat. No.98EX215)*, 1998, pp. 132–139.

[38] N. S. Shenck and J. A. Paradiso, "Energy scavenging with shoe-mounted piezoelectrics," *IEEE Micro*, vol. 21, no. 3, pp. 30–42, 2001.

[39] D. Han and V. Kaajakari, "Microstructured polymer for shoe power generation," in *TRANSDUCERS 2009 - 2009 International Solid-State Sensors, Actuators and Microsystems Conference*, 2009, pp. 1393–1396.

[40] D. Fourie, "Shoe-Mounted PVDF Piezoelectric Transducer for Energy Harvesting," *MIT Undergrad. Res. J.*, vol. 19, no. 1, pp. 66–70, 2010.

[41] L. Moro and D. Benasciutti, "Harvested power and sensitivity analysis of vibrating shoe-mounted piezoelectric cantilevers," *Smart Mater. Struct.*, vol. 19, no. 11, p. 115011, 2010.

[42] Z. Luo *et al.*, "Energy harvesting study on single and multilayer ferroelectret foams under compressive force," *IEEE Trans. Dielectr. Electr. Insul.*, vol. 22, no. 3, pp. 1360–1368, 2015.

[43] M. Renaud, T. Sterken, P. Fiorini, R. Puers, K. Baert, and C. Van Hoof, "Scavenging energy from human body:design of a piezoelectric transducer," *Dig. Tech. Pap. - Int. Conf. Solid State Sensors Actuators Microsystems, TRANSDUCERS '05*, vol. 1, pp. 784–787, 2005.

[44] S. R. Platt, S. Farritor, K. Garvin, and H. Haider, "The use of piezoelectric ceramics for electric power generation within orthopedic implants," *IEEE/ASME Trans. Mechatronics*, vol. 10, no. 4, pp. 455–461, 2005.

[45] P. Zeng, H. Chen, Z. Yang, and A. Khaligh, "Unconventional wearable energy harvesting from human horizontal foot motion," *Conf. Proc. - IEEE Appl. Power Electron. Conf. Expo. - APEC*, pp. 258–264, 2011.

[46] P. Zeng and A. Khaligh, "A permanent-magnet linear motion driven kinetic energy harvester," *IEEE Trans. Ind. Electron.*, vol. 60, no. 12, pp. 5737–5746, 2013.

[47] S. Kwon, J. Park, and K. Law, "Electromagnetic energy harvester with repulsively stacked multilayer magnets for low frequency vibrations," vol. 055007.

[48] K. Ylli, D. Hoffmann, P. Becker, A. Willmann, B. Folkmer, and Y. Manoli, "Human Motion Energy Harvesting for AAL Applications," *J. Phys. Conf. Ser.*, vol. 557, p. 012024, 2014.

[49] Y. Choi *et al.*, "Low Frequency Vibration Energy Harvester Using Spherical Permanent Magnet with Non-uniform Mass Distribution," *J. Phys. Conf. Ser.*, vol. 476, p. 012123, Dec. 2013.

[50] M. Han, G. Qiu, W. Liu, B. Meng, X. Zhang, and H. Zhang, "Note: A cubic electromagnetic harvester that convert vibration energy from all directions," *Rev. Sci. Instrum.*, vol. 85, no. 7, p. 076109, Jul. 2014.

[51] A. Haroun, I. Yamada, and S. Warisawa, "Micro electromagnetic vibration energy harvester based on free/impact motion for low frequency–large amplitude operation," *Sensors Actuators A Phys.*, vol. 224, pp. 87–98, 2015.

[52] A. Haroun, I. Yamada, and S. Warisawa, "Study of electromagnetic vibration energy harvesting with free/impact motion for low frequency operation," *J. Sound Vib.*, vol. 349, pp. 389–402, 2015.

[53] A. Khaligh, P. Zeng, X. Wu, and Y. Xu, "A hybrid energy scavenging topology for human-powered mobile electronics," *Proc. - 34th Annu. Conf. IEEE Ind. Electron. Soc. IECON 2008*, pp. 448–453, 2008.

[54] B. L. Ooi and J. M. Gilbert, "Design of wideband vibration-based electromagnetic generator by means of dual-resonator," *Sensors Actuators, A Phys.*, vol. 213, pp. 9–18, 2014.

[55] B. C. Lee, M. A. Raman, and G. S. Chung, "Design, fabrication and characterization of a low frequency driven electromagnetic energy harvester," in *PowerMEMS*, 2012, pp. 452–455.

[56] B. Lee, M. A. Rahman, S. Hyun, and G.-S. Chung, "Low frequency driven electromagnetic energy harvester for self-powered system," *Smart Mater. Struct.*, vol. 21, no. 12, p. 125024, Dec. 2012.

[57] C. R. Saha, T. O'Donnell, N. Wang, and P. McCloskey, "Electromagnetic generator for harvesting energy from human motion," *Sensors Actuators A Phys.*, vol. 147, no. 1, pp. 248–253, Sep. 2008.

[58] A. R. M. Foisal, B.-C. Lee, and G.-S. Chung, "Fabrication and performance optimization of an AA size electromagnetic energy harvester using magnetic spring," *2011 IEEE SENSORS Proc.*, pp. 1125–1128, Oct. 2011.

[59] A. R. M. Foisal and G. Chung, "Design and Analysis of a Vibration-driven AA Size Electromagnetic Energy Harvester Using Magnetic Spring," *Trans. Electr. Electron. Mater.*, vol. 13, no. 3, pp. 125–128, Jun. 2012.

[60] A. Munaz, B. Lee, and G. Chung, "Sensors and Actuators A : Physical A study of an electromagnetic energy harvester using multi-pole magnet," *Sensors Actuators A. Phys.*, vol. 201, pp. 134–140, 2013.

[61] D. F. Berdy, D. J. Valentino, and D. Peroulis, "Kinetic energy harvesting from human walking and running using a magnetic levitation energy harvester," *Sensors Actuators A Phys.*, vol. 222, pp. 262–271, 2015.

[62] Q. Zhang, Y. Wang, and E. S. Kim, "Power generation from human body motion through magnet and coil arrays with magnetic spring," *J. Appl. Phys.*, vol. 115, no. 6, 2014.

[63] X. Y. Wang, S. Palagummi, L. Liu, and F. G. Yuan, "A magnetically levitated vibration energy harvester," vol. 055016, 2013.

[64] S. Palagummi and F. G. Yuan, "A vibration energy harvester using diamagnetic levitation," vol. 8688, pp. 1–12, 2013.

[65] S. Palagummi and F. G. Yuan, "An optimal design of a mono-stable vertical diamagnetic levitation based electromagnetic vibration energy harvester," *J. Sound Vib.*, vol. 342, pp. 330–345, 2015.

[66] Z. Ye, Z. Duan, and K. Takahata, "Motion characteristics and output voltage analysis of micro- vibration energy harvester based on diamagnetic levitation," pp. 91–100, 2015.

[67] S. Kim, S. Bang, and K. Chun, "Temperature effect on the vibration-based electrostatic energy harvester," *IEEE Reg. 10 Annu. Int. Conf. Proceedings/TENCON*, pp. 1317–1320, 2011.

[68] M. V. V. de Araujo and R. Nicoletti, "Electromagnetic harvester for lateral vibration in rotating machines," *Mech. Syst. Signal Process.*, vol. 52–53, pp. 685–699, 2015.

[69] Y. Rao, S. Cheng, and D. P. Arnold, "An energy harvesting system for passively generating power from human activities," *J. Micromechanics Microengineering*, vol. 23, no. 11, p. 114012, 2013.

[70] S. P. Beeby, M. J. Tudor, and N. M. White, "Energy harvesting vibration sources for microsystems applications," *Meas. Sci. Technol.*, vol. 17, no. 12, pp. R175–R195, Dec. 2006.

[71] D. Zhu, S. Roberts, M. J. Tudor, and S. P. Beeby, "Design and experimental characterization of a tunable vibration-based electromagnetic micro-generator," *Sensors Actuators A Phys.*, vol. 158, no. 2, pp. 284–293, Mar. 2010.

[72] C. Peters, D. Maurath, W. Schock, F. Mezger, and Y. Manoli, "A closed-loop wide-range tunable mechanical resonator for energy harvesting systems," *J. Micromechanics Microengineering*, vol. 19, no. 9, p. 094004, 2009.

[73] Z. Xu, X. Shan, D. Chen, and T. Xie, "A Novel Tunable Multi-Frequency Hybrid Vibration Energy Harvester Using Piezoelectric and Electromagnetic Conversion Mechanisms," *Appl. Sci.*, vol. 6, no. 1, p. 10, 2016.

[74] a Cammarano, S. G. Burrow, D. a W. Barton, a Carrella, and L. R. Clare, "Tuning a resonant energy harvester using a generalized electrical load," *Smart Mater. Struct.*, vol. 19, no. 5, p. 055003, 2010.

[75] K. Ashraf, M. H. Md Khir, J. O. Dennis, and Z. Baharudin, "Improved energy harvesting from low frequency vibrations by resonance amplification at multiple frequencies," *Sensors Actuators A Phys.*, vol. 195, pp. 123–132, Jun. 2013.

[76] A. Rahimi, Ö. Zorlu, A. Muhtaroğlu, and H. Külah, "An electromagnetic energy harvesting system for low frequency applications with a passive interface ASIC in standard CMOS," *Sensors Actuators, A Phys.*, vol. 188, pp. 158–166, 2012.

[77] M. a. Halim and J. Y. Park, "A non-resonant, frequency up-converted electromagnetic energy harvester from human-body-induced vibration for hand-held smart system applications," *J. Appl. Phys.*, vol. 115, no. 9, 2014.

[78] M. A. Halim and J. Y. Park, "Modeling and experiment of a handy motion driven , frequency up-converting electromagnetic energy harvester using transverse impact by spherical ball," *Sensors Actuators A. Phys.*, vol. 229, pp. 50–58, 2015.

[79] S. Türkyilmaz, Ö. Zorlu, A. Muhtaroğlu, and H. Külah, "An electromagnetic micro-power generator for low frequency vibrations with tunable resonance," *Procedia Eng.*, vol. 25, pp. 729–732, 2011.

[80] Ö. Zorlu, S. Türkyilmaz, A. Muhtaroğlu, and H. Külah, "An electromagnetic energy harvester for low frequency and low-g vibrations with a modified frequency up conversion method," *Proc. IEEE Int. Conf. Micro Electro Mech. Syst.*, pp. 805–808, 2013.

[81] Q. Tang, Y. Yang, and X. Li, "Repulsively driven frequency-increased-generators for durable energy harvesting from ultra-low frequency vibration," vol. 045004, pp. 1–6, 2014.

[82] N. S. Yuksek, Z. C. Feng, and M. Almasri, "Broadband electromagnetic power harvester from vibrations via frequency conversion by impact oscillations," *Appl. Phys. Lett.*, vol. 105, no. 11, p. 113902, 2014.

[83] I. Sari, T. Balkan, and H. Kulali, "A wideband electromagnetic micro power generator for wireless microsystems," *TRANSDUCERS EUROSENSORS '07 - 4th Int. Conf. Solid-State Sensors, Actuators Microsystems*, pp. 275–278, 2007.

[84] P. Podder, A. Amann, and S. Roy, "FR4 Based Bistable Electromagnetic Vibration Energy Harvester," *Procedia Eng.*, vol. 87, pp. 767–770, 2014.

[85] T. Petropoulos, E. M. Yeatman, and P. D. Mitcheson, "MEMS coupled resonators for power generation and sensing," in *Micromechanics Europe*, 2004, vol. 13, no. 3, pp. 429–440.

[86] I. Abed, N. Kacem, N. Bouhaddi, and M. L. Bouazizi, "Multi-modal vibration energy harvesting approach based on nonlinear oscillator arrays under magnetic levitation," *Smart Mater. Struct.*, vol. 25, no. 2, p. 025018, 2016.

[87] B. P. Mann and N. D. Sims, "Energy harvesting from the nonlinear oscillations of magnetic levitation," *J. Sound Vib.*, vol. 319, no. 1–2, pp. 515–530, Jan. 2009.

[88] a Cammarano, S. a Neild, S. G. Burrow, and D. J. Inman, "The bandwidth of optimized nonlinear vibration-based energy harvesters," *Smart Mater. Struct.*, vol. 23, no. 5, p. 055019, 2014.

[89] S. G. Burrow, L. R. Clare, a. Carrella, and D. Barton, "Vibration energy harvesters with non-linear compliance," *Proc. SPIE*, vol. 6928, pp. 692807-692807–10, 2008.

[90] S. G. Burrow and L. R. Clare, "A Resonant Generator with Non-Linear Compliance for Energy Harvesting in High Vibrational Environments GENERATORSElectro-Mechanical includ inge or ezo ESpring," pp. 715–720, 2007.

[91] A. Marin, J. Turner, and D. Sam, "Wideband , low-frequency springless vibration energy harvesters : part I."

[92] D. Zhu, "Vibration Energy Harvesting: Machinery Vibration, Human Movement and Flow Induced Vibration," in *Sustainable Energy Harvesting Technologies - Past, Present and Future*, no. Viv, InTech, 2011.

[93] S. Beeby and N. White, *Energy Harvesting for Autonomous Systems*. Norwood: Artech House, 2010.

[94] F. Graichen, R. Arnold, A. Rohlmann, and G. Bergmann, "Implantable 9-channel telemetry system for in vivo load measurements with orthopedic implants.," *IEEE Trans. Biomed. Eng.*, vol. 54, no. 2, pp. 253–261, 2007.

[95] R. Morais *et al.*, "Permanent magnet vibration power generator as an embedded mechanism for smart hip prosthesis," *Procedia Eng.*, vol. 5, pp. 766–769, Jan. 2010.

[96] R. Morais *et al.*, "Double permanent magnet vibration power generator for smart hip prosthesis," *Sensors Actuators A Phys.*, vol. 172, no. 1, pp. 259–268, Dec. 2011.

[97] N. Silva, P. Santos, J. Ferreira, M. Santos, M. Reis, and R. Morais, "Multi-purpose and Multi-source Energy Management System for Biomedical Implants," *Procedia Eng.*, vol. 47, pp. 722–725, Jan. 2012.

[98] N. M. Silva *et al.*, "Power management architecture for smart hip prostheses comprising multiple energy harvesting systems," *Sensors Actuators A Phys.*, vol. 202, pp. 183–192, Nov. 2013.

[99] D. C. Bock, A. C. Marschilok, K. J. Takeuchi, and E. S. Takeuchi, "Batteries used to Power Implantable Biomedical Devices.," *Electrochim. Acta*, vol. 84, pp. 155–164, Dec. 2012.

[100] J. Reis *et al.*, "A new piezoelectric actuator induces bone formation in vivo: a preliminary study.," *J. Biomed. Biotechnol.*, vol. 2012, p. 613403, Jan. 2012.

[101] S. Almouahed, M. Gouriou, C. Hamitouche, E. Stindel, and C. Roux, "The Use of Piezoceramics As Electrical Energy Implant During Walking," vol. 16, no. 5, pp. 799–807, 2011.

[102] N. Silva, P. Santos, J. Ferreira, M. Santos, M. Reis, and R. Morais, "Multi-purpose and multi-source energy management system for biomedical implants," *Procedia Eng.*, vol. 47, pp. 722–725, 2012.

[103] OrthoLoad Team, "Orthoload: Loaing of Orthopaedic Implants." [Online]. Available: http://www.orthoload.com/.

[104] H. Huang, "Human-Powered Inertial Energy Harvesters: The Effect of Orientation, Location and Activity on the Obtainable Electrical Power," 2014.

[105] A. Cammarano, S. A. Neild, S. G. Burrow, D. J. Wagg, and D. J. Inman, "Optimum resistive loads for vibration-based electromagnetic energy harvesters with a stiffening nonlinearity," *J. Intell. Mater. Syst. Struct.*, vol. 25, no. 14, pp. 1757–1770, 2014.

[106] A. Cammarano, S. a Neild, S. G. Burrow, and D. J. Inman, "The bandwidth of optimized nonlinear vibration-based energy harvesters," *Smart Mater. Struct.*, vol. 23, no. 5, p. 055019, 2014.

[107] S. Beeby and N. White, *Energy Harvesting for Autonomous Systems*. Norwood: Artech House, 2010.

[108] H. Xiao, X. Wang, and S. John, "A multi-degree of freedom piezoelectric vibration energy harvester with piezoelectric elements inserted between two nearby oscillators," *Mech. Syst. Signal Process.*, vol. 68–69, pp. 138–154, 2016.

[109] Z. J. Wong, J. Yan, K. Soga, and A. A. Seshia, "A MULTI-DEGREE-OF-FREEDOM ELECTROSTATIC MEMS POWER HARVESTER," no. 1, pp. 300–303, 2009.

[110] L. Tang and Y. Yang, "A multiple-degree-of-freedom piezoelectric energy harvesting model," *J. Intell. Mater. Syst. Struct.*, vol. 23, no. 14, pp. 1631–1647, 2012.

[111] S. Rao, *Mechanical Vibrations*, 5th ed. 2011.

[112] D. Spreemann and M. Yiannos, *Electromagnetic Vibration Energy Harvesting Devices: Architectures, Design, Modeling and Optimization*. Springer Science & Business Media, 2012.

[113] J. Yang, Y. P. Xiong, and J. T. Xing, "Power flow behaviour and dynamic performance of a nonlinear vibration absorber coupled to a nonlinear oscillator," *Nonlinear Dyn.*, pp. 1063–1079, 2014.

[114] F. F. Cap, "Averaging method for the solution of non-linear differential equations with periodic non-harmonic solutions," *Int. J. Non. Linear. Mech.*, vol. 9, no. 6, pp. 441–450, Dec. 1974.

[115] W. T. Thomson, *Theory of vibration with application*, 4th ed. Nelson Thornes Ltd, 2003.

[116] N. G. Stephen, "On energy harvesting from ambient vibration," *J. Sound Vib.*, vol. 293, no. 1–2, pp. 409–425, May 2006.

[117] Magnet Expert Ltd., "Grades Of Neodymium Magnets." [Online]. Available: http://www.first4magnets.com/tech-centre-i61/information-and-articles-i70/neodymium-magnet-information-i82. [Accessed: 20-Apr-2015].

[118] J. Pyrhonen, T. Jokinen, and V. Hrabovcova, *Design of Rotating Electrical Machines*. West Sussex: John Wiley & Sons, Ltd, 2008.

[119] P. Glynne-Jones, M. J. Tudor, S. P. Beeby, and N. M. White, "An electromagnetic, vibration-powered generator for intelligent sensor systems," *Sensors Actuators, A Phys.*, vol. 110, no. 1–3, pp. 344–349, 2004.

[120] S. Miki *et al.*, "Electromagnetic energy harvester by using buried NdFeB," *Proc. IEEE Int. Conf. Micro Electro Mech. Syst.*, no. February, pp. 1221–1224, 2012.

[121] J. Hu, X. C. Kou, and H. Kronmüller, "Investigation of the temperature dependence of the coercive fields in NdFeB magnets," *Phys. Status Solidi*, vol. 138, no. 1, pp. K41–K44, Jul. 1993.

[122] K. Bertsche, J.-F. Ostiguy, and W. B. Foster, "Temperature considerations in the design of a permanent magnetstorage ring," *Proc. Part. Accel. Conf.*, vol. 2, pp. 1381–1383, 1995.

[123] M.-D. Calin and E. Helerea, "Temperature influence on magnetic characteristics of NdFeB permanent magnets," *2011 7Th Int. Symp. Adv. Top. Electr. Eng.*, pp. 1–6, 2011.

[124] Y. Luo and N. Zhang, "Temperature variation of domain structure and magnetization in NdFeB magnets," *J. Appl. Phys.*, vol. 61, no. 8, pp. 3445–3447, 1987.

[125] Eclipse Magnetics, "Magnetic Materials & Assemblies," 2014. [Online]. Available: http://www.eclipsemagnetics.com/row/magnet-materials-and-assemblies/. [Accessed: 22-Sep-2016].

[126] NdFeB Specialist E-Magnets UK, "Temperature Ratings." [Online]. Available: http://www.ndfeb-info.com/temperature_ratings.aspx. [Accessed: 22-Sep-2016].

[127] E. Bonisoli, A. Canova, F. Freschi, S. Moos, M. Repetto, and S. Tornincasa, "Dynamic simulation of an electromechanical energy scavenging device," *IEEE Trans. Magn.*, vol. 46, no. 8, pp. 2856–2859, 2010.

[128] J. Fraden, *Handbook of Modern Sensors: Physics, Designs, and Applications*, 4th ed. Springer-Verlag New York, 2010.

[129] J. M. D. Coey, *Rare-Earth Iron Permanent magnets*. New York: Oxford science publications, 1996.

[130] T. Vaimann, A. Kallaste, A. Kilk, and A. Belahcen, "Magnetic properties of reduced Dy NdFeB permanent magnets and their usage in electrical machines," in *2013 Africon*, 2013, pp. 1–5.

[131] J. Karlsson, "Review of Magnetic Materials Along With a Study of the Magnetic Stability and Solidity of Y40," no. June, 2012.

[132] A. R. Jha, *Rare Earth Materials: Properties and Applications*. CRC Press, 2014.

[133] J. M. Camacho and V. Sosa, "Alternative method to calculate the magnetic field of permanent magnets with azimuthal symmetry," *Rev. Mex. Fis. E*, vol. 59, no. 1, pp. 8–17, 2013.

[134] K. Halbach, "Design of permanent multipole magnets with oriented rare earth cobalt material," *Nucl. Instruments Methods*, vol. 169, no. 1, pp. 1–10, Feb. 1980.

[135] S. Constantinides and D. Gulick, "NdFeB for High Temperature Motor Applications," in *SMMA Fall Technical Conference*, 2004, pp. 1–33.

[136] S. R. Trout and Y. Zhilichev, "Effective use of neodymium iron boron magnets, case studies," *Proc. Electr. Insul. Conf. Electr. Manuf. Coil Wind. Conf. (Cat. No.99CH37035)*, no. October, 1999.

[137] S. H. Kim and C. Doose, "Temperature compensation of NdFeB permanent magnets," *Proc. 1997 Part. Accel. Conf. (Cat. No.97CH36167)*, vol. 3, pp. 3227–3229, 1997.

[138] M. Balato, L. Costanzo, and M. Vitelli, "Resonant electromagnetic vibration harvesters: Determination of the equivalent electric circuit parameters and simplified closed-form analysis for the identification of the optimal diode bridge rectifier DC load," *Int. J. Electr. Power Energy Syst.*, vol. 84, pp. 111–123, 2017.

[139] E. Varguez-Villanueva, V. Rodriguez-Zermeno, and V. Sosa, "Calculation of vertical force between finite, cylindrical magnets and superconductors," *Rev. Mex. física*, vol. 54, no. 4, pp. 293–298, 2008.

[140] B. A. D. Piombo, A. Vigliani, and E. Bonisoli, "Dynamics of suspensions with rare-earth permanent magnets," in *Smart Structures and Materials 2003: Damping and Isolation*, 2003, vol. 5052, pp. 106–115.

[141] S. Stoupin and Y. V. Shvyd'Ko, "Thermal expansion," *Phys. Rev. Lett.*, vol. 104, no. 8, 2010.

[142] A. Technologies, "Material Expansion Coefficients," *Laser Opt. User's Man.*, pp. 17-1 to 17-12, 2002.

[143] Bal Seal Engineering, "Coefficient of Thermal Expansion for Various Materials," vol. 18, pp. 1–6, 2004.

[144] M. Mizuno and D. G. Chetwynd, "Investigation of a resonance microgenerator," *J. Micromechanics Microengineering*, vol. 13, no. 2, pp. 209–216, 2003.

[145] J. H. Dellinger, *The temperature coefficient of resistance of copper*. Govt. Print. Off.,

1911.

[146] D. F. Berdy, D. J. Valentino, and D. Peroulis, "Design and Optimization of a Magnetically Sprung Block Magnet Vibration Energy Harvester," *Sensors Actuators A Phys.*, vol. 218, pp. 69–79, 2014.

[147] Q. Zhang, Y. Wang, and E. S. Kim, "Electromagnetic Energy Harvester with Flexible Coils and Magnetic Spring for 1-10 Hz Resonance," *J. Microelectromechanical Syst.*, vol. 24, no. 4, pp. 1193–1206, 2015.

[148] S. P. Beeby *et al.*, "A micro electromagnetic generator for vibration energy harvesting," vol. 17, pp. 1257–1265, 2007.

[149] K. Sun, G. Q. Liu, and X. Y. Xu, "Nonlinear Resonant Generator for Harvesting Energy from Human Wrist Vertical Shaking," *Appl. Mech. Mater.*, vol. 128–129, pp. 923–927, Oct. 2011.

[150] M. Gutierrez, A. Shahidi, D. Berdy, and D. Peroulis, "Design and characterization of a low frequency 2-dimensional magnetic levitation kinetic energy harvester," *Sensors Actuators, A Phys.*, vol. 236, pp. 1–10, 2015.

[151] S. Li, H. Shang, F. Liu, M. Ma, and A. Zhang, "Toxic Effects of Copper (II) Ions on Bovine Hemoglobin: A Spectroscopic Investigation," *Spectrosc. Lett.*, vol. 7010, no. October, p. 00387010.2017.1335754, 2017.

[152] F. Lagarde and M. Leroy, "Metabolism and toxicity of tungsten in humans and animals.," *Met. Ions Biol. Syst.*, vol. 39, pp. 741–59, Mar. 2002.

[153] L. M. Gaetke, H. S. Chow-Johnson, and C. K. Chow, "Copper: toxicological relevance and mechanisms," *Arch. Toxicol.*, vol. 88, no. 11, pp. 1929–1938, 2014.

[154] J. G. Davies and H. Siddons, "Experience with Implanted Pacemakers: Technical Considerations," *Thorax*, vol. 20, pp. 128–134, 1965.

[155] R. Gerdsen, H. W. Kaiser, K. Friedrich, E. Rabe, and T. Bieber, "Annular erythema caused by impending pacemaker extrusion.," *Acta Derm. Venereol.*, vol. 79, no. 5, pp. 385–7, Sep. 1999.

[156] Y.-H. Joung, "Development of Implantable Medical Devices: From an Engineering Perspective," *Int. Neurourol. J.*, vol. 17, no. 3, p. 98, 2013.

[157] C. Peters, F. Henrici, M. Ortmanns, and Y. Manoli, "High-bandwidth floating gate CMOS rectifiers with reduced voltage drop," *Proc. - IEEE Int. Symp. Circuits Syst.*, pp. 2598–2601, 2008.

[158] Y. Lam, W. Ki, and C. Tsui, "Integrated Low-Loss CMOS Active Rectifier for Wirelessly Powered Devices," *IEEE Trans. Circuits Syst. II Express Briefs*, vol. 53, no. 12, pp. 1378–1382, Dec. 2006.

[159] S. Dwari and L. Parsa, "An efficient AC-DC step-up converter for low-voltage energy harvesting," *IEEE Trans. Power Electron.*, vol. 25, no. 8, pp. 2188–2199, 2010.

[160] G. Yang, B. H. Stark, S. J. Hollis, and S. G. Burrow, "Challenges for energy harvesting systems under intermittent excitation," *IEEE J. Emerg. Sel. Top. Circuits Syst.*, vol. 4, no. 3, pp. 364–374, 2014.

[161] V. Luciano, E. Sardini, M. Serpelloni, and G. Baronio, "An energy harvesting converter to power sensorized total human knee prosthesis," *Meas. Sci. Technol.*, vol. 25, no. 2, p. 025702, Feb. 2014.

[162] E. Akman, A. Demir, T. Canel, and T. Sinmazçelik, "Laser welding of Ti6Al4V titanium alloys," *J. Mater. Process. Technol.*, vol. 209, no. 8, pp. 3705–3713, 2009.

[163] T. Kramár, I. Michalec, and P. Kovačócy, "The laser beam welding of titanium grade 2 alloy," *GRANT*, vol. 1, no. 1, pp. 77–79, 2012.

[164] Valtronic Technologies, "Improvements in Glass Encapsulation Technology Offer Significant Advantages for Implantable Medical Devices," *Medical Technology*, Sep-2014.

[165] F. Mauron, "Encapsulating smaller and smarter implantables is a GLASS ACT," *Medical design*, 2013.

[166] D. Styblo and P. Klavora, "The Next Generation of Smart Implants," in *MEPTEC Symposium*, 2013, pp. 124–143.

[167] M. N. Helmus, D. F. Gibbons, and D. Cebon, "Biocompatibility: Meeting a Key Functional Requirement of Next-Generation Medical Devices," *Toxicol. Pathol.*, vol. 36, no. 1, pp. 70–80, Jan. 2008.